МИСИС
УНИВЕРСИТЕТ

ISSN 1997-308X
eISSN 2412-8767

ИЗВЕСТИЯ ВУЗОВ
ПОРОШКОВАЯ МЕТАЛЛУРГИЯ И ФУНКЦИОНАЛЬНЫЕ ПОКРЫТИЯ

POWDER METALLURGY AND FUNCTIONAL COATINGS

2025
Том Vol. 19 № No. 5
powder.misis.ru

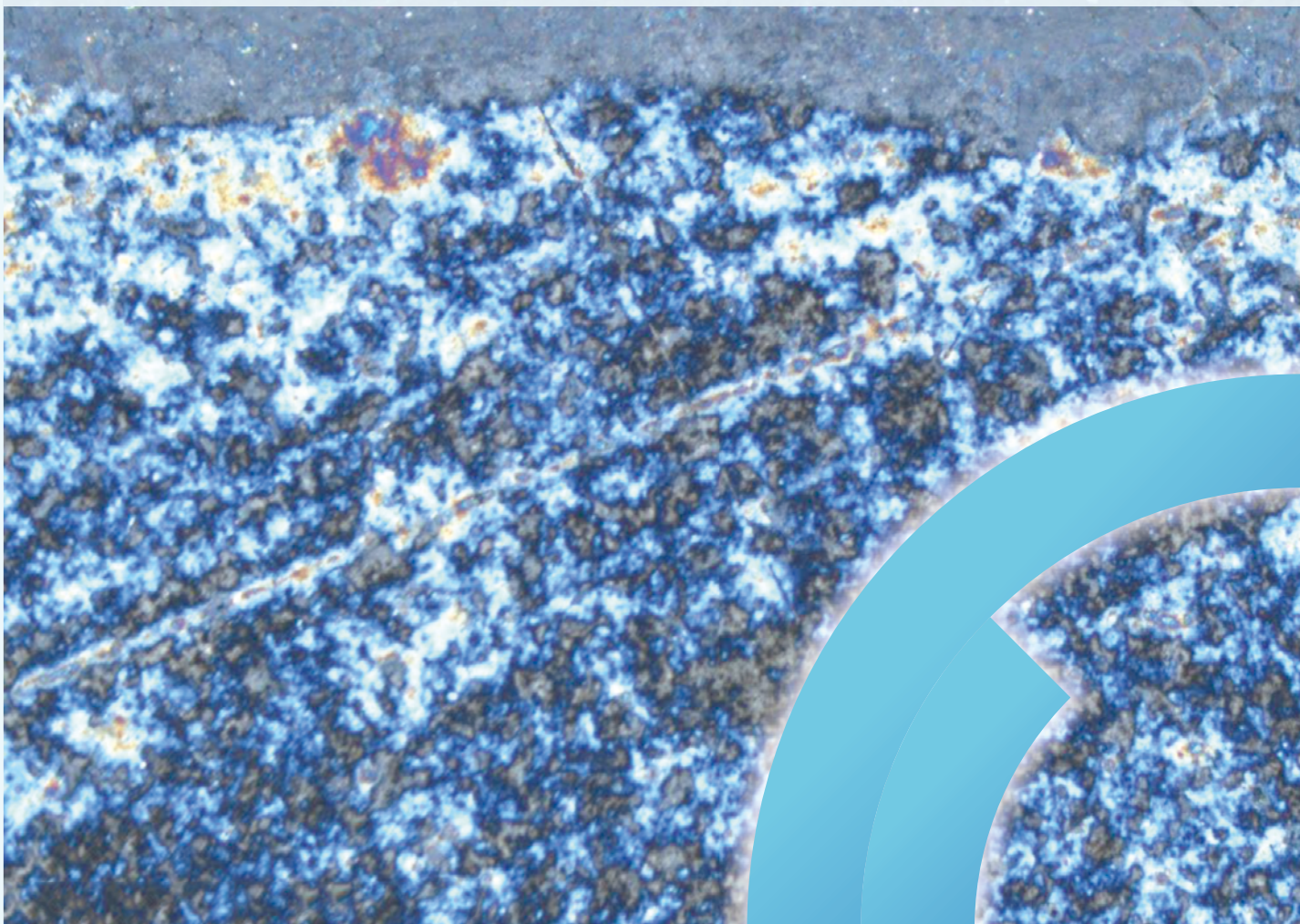

ISSN 1997-308X
eISSN 2412-8767

POWDER METALLURGY AND FUNCTIONAL COATINGS

Scientific and Technical Journal
Founded in 2007
Six issues per year

2025
Том Vol. 19 № No. 5

ИЗВЕСТИЯ ВУЗОВ ПОРОШКОВАЯ МЕТАЛЛУРГИЯ И ФУНКЦИОНАЛЬНЫЕ ПОКРЫТИЯ

Научно-технический журнал
Основан в 2007 г.
Выходит 6 раз в год

POWDER METALLURGY AND FUNCTIONAL COATINGS

ISSN 1997-308X
eISSN 2412-8767

Scientific and Technical Journal
Founded in 2007
Six issues per year

http://powder.misis.ru

Founder: MISIS University of Science and Technology

National University of Science and Technology "MISIS"
Address: 1 Bld, 4 Leninskiy Prosp., Moscow 119049, Russian Federation
http://www.misis.ru

Journal is included into the List of peer-reviewed scientific publications recommended by the Highest Attestation Commission of the Ministry of Education and Science of the Russian Federation for publishing the results of doctoral and candidate dissertations.
Abstracting/Indexing: Scopus, Russian Science Citation Index (RSCI), Ulrich's Periodicals Directory, VINITI Database (Abstract Journal).

Certificate of registration **No. FS77-27955** (12.04.2007)
Re-registration **PI No. FS77-79230** (25.09.2020)

Signed print 21.10.2025. Format 60×90 1/8
Offset paper No. 1. Digital printing. Quires 11.75
Order 23328. Free price
Printed in the printing house of the MISIS Publish House
1 Bld, 4 Leninskiy Prosp., Moscow 119049, Russian Federation
Phone/fax: +7 (499) 236-76-17

ИЗВЕСТИЯ ВУЗОВ
ПОРОШКОВАЯ МЕТАЛЛУРГИЯ
И ФУНКЦИОНАЛЬНЫЕ ПОКРЫТИЯ

НАУЧНО-ТЕХНИЧЕСКИЙ ЖУРНАЛ
ОСНОВАН В 2007 Г.
ВЫХОДИТ 6 РАЗ В ГОД

http://powder.misis.ru

ISSN 1997-308X
eISSN 2412-8767

Учредитель:

ФГАОУ ВО Национальный исследовательский технологический университет «МИСИС»
Адрес: 119049, Москва, Ленинский пр-т, 4, стр. 1
https://www.misis.ru

Журнал включен в Перечень рецензируемых научных изданий, рекомендованных ВАК Минобрнауки РФ для публикации результатов диссертаций на соискание ученых степеней.
Журнал включен в базы данных: Scopus, Russian Science Citation Index (RSCI), Ulrich's Periodicals Directory, РИНЦ, БД/РЖ ВИНИТИ.

Редакция журнала

Адрес: 119049, Москва,
Ленинский пр-т, 4, стр. 1. НИТУ МИСИС

Тел.: +7 (495) 638-45-35. ***Эл. почта:*** izv.vuz@misis.ru

Свидетельство о регистрации № **ФС77-27955** от 12.04.2007 г.
Перерегистрация 25.09.2020 г. **ПИ № ФС77-79230**

Ведущий редактор: А.А. Кудинова
Выпускающий редактор: О.В. Соснина
Дизайн и верстка: В.В. Расенець

Подписано в печать 21.10.2025. Формат 60×90 $^1/_8$
Бум. офсетная № 1. Печать цифровая. Усл. печ. л. 11,75
Заказ 23328. Цена свободная
Отпечатано в типографии Издательского Дома МИСИС
119049, г. Москва, Ленинский пр-т, 4, стр. 1
Тел./факс: +7 (499) 236-76-17

Contents

Содержание

Theory and Processes of Formation and Sintering of Powder Materials

Knyazeva A.G., Korosteleva E.N., Safronova V.S.
Sintering and thermokinetic modeling of the phase evolution in thermite powder mixtures under controlled heating 5

Self-Propagating High-Temperature Synthesis

Sanin V.N., Ikornikov D.M., Sivakova A.O., Kovalev D.Yu., Silyakov S.L., Panova M.D.
Synthesis of refractory high-entropy alloys based on Mo–Nb–Ta–(Cr, V, Zr, Hf) using centrifugal SHS metallurgy and investigation of their oxidation resistance 17

Uvarova I.A., Amosov A.P., Titova Yu.V., Ermoshkin A.A.
Polytetrafluoroethylene-activated azide self-propagating high-temperature synthesis of a highly dispersed TiN–SiC powder composition 36

Refractory, Ceramic, and Composite Materials

Khazin M.L., Apakashev R.A., Adas V.E.
Structure and properties of an aluminum-matrix composite reinforced with zirconium carbide particles 51

Antropova K.A., Cherkasova N.Yu., Aleksandrova N.S., Khabirov R.R., Miller A.A., Agafonov M.Yu.
Effect of spark plasma sintering temperature on the structure and properties of alumina ceramics containing barium hexaaluminate 60

Nanostructured Materials and Functional Coatings

Afanas'ev A.V., Bykov Yu.O., Lebedev A.O., Markov A.V., Sharenkova N.V., Latnikova N.M.
Titanium carbide coating for high-temperature graphite components 70

Materials and Coatings Fabricated Using the Additive Manufacturing Technologies

Bubnenkov B.B., Zharmukhambetov A.S., Ivanov I.A., Sharapov I.S., Veselkov S.N.
Densification of porous SLS SiC preforms through polymer infiltration, pyrolysis, and liquid silicon infiltration 80

Теория и процессы формования и спекания порошковых материалов

Князева А.Г., Коростелева Е.Н., Сафронова В.С.
Спекание и термокинетическое моделирование эволюции состава термитных смесей в условиях регулируемого нагрева 5

Самораспространяющийся высокотемпературный синтез

Санин В.Н., Икорников Д.М., Сивакова А.О., Ковалев Д.Ю., Силяков С.Л., Панова М.Д.
Синтез высокоэнтропийных сплавов на основе тугоплавких металлов Mo–Nb–Ta–(Cr, V, Zr, Hf) методами центробежной СВС-металлургии и исследование их окислительной стойкости 17

Уварова И.А., Амосов А.П., Титова Ю.В., Ермошкин А.А.
Применение политетрафторэтилена в азидном самораспространяющемся высокотемпературном синтезе высокодисперсной смеси керамических порошков TiN–SiC 36

Тугоплавкие, керамические и композиционные материалы

Хазин М.Л., Апакашев Р.А., Адас В.Е.
Структура и свойства алюмоматричного материала, упрочненного частицами карбида циркония 51

Антропова К.А., Черкасова Н.Ю., Александрова Н.С., Хабиров Р.Р., Миллер А.А., Агафонов М.Ю.
Влияние температуры электроискрового спекания на структуру и свойства алюмооксидной керамики, содержащей гексаалюминат бария 60

Наноструктурированные материалы и функциональные покрытия

Афанасьев А.В., Быков Ю.О., Лебедев А.О., Марков А.В., Шаренкова Н.В., Латникова Н.М.
Покрытие из карбида титана для графитовой арматуры высокотемпературных процессов 70

Материалы и покрытия, получаемые методами аддитивных технологий

Бубненков Б.Б., Жармухамбетов А.С., Иванов И.А., Шарапов И.С., Веселков С.Н.
Повышение плотности пористых СЛС-заготовок из карбида кремния пропиткой, пиролизом и силицированием 80

Theory and Processes of Formation and Sintering of Powder Materials
Теория и процессы формования и спекания порошковых материалов

UDC 536.421.5
https://doi.org/10.17073/1997-308X-2025-5-5-16

Research article
Научная статья

Sintering and thermokinetic modeling of the phase evolution in thermite powder mixtures under controlled heating

A. G. Knyazeva, E. N. Korosteleva, V. S. Safronova

Institute of Strength Physics and Materials Science, Siberian Branch, Russian Academy of Sciences
8/2 Akademicheskii Prosp., Tomsk 634055, Russia

l9627826013@yandex.ru

Abstract. The behavior of compacted mixtures of metal powders (Al, Ti) and recycled metalworking wastes ($Fe + Fe_2O_3 + C$) during vacuum sintering under controlled heating was investigated to assess the possibility of producing in situ metal–matrix composites containing oxide strengthening particles. The starting materials were titanium and aluminum powders (particle size <160 μm and <100 μm, respectively) and a powder produced from recycled steel chips (<300 μm). The resulting samples exhibited a heterogeneous phase composition, which was examined by *X*-ray diffraction (CuK_α radiation, XRD-6000 diffractometer) and optical microscopy (Axiovert 200MAT). A pronounced difference was observed between the aluminum- and titanium-based systems: the former exhibited a distinct thermal peak, whereas the latter showed smooth temperature behavior without thermal spikes. A thermokinetic model describing the multi-stage reactions in both systems was developed. The model incorporates metallothermic reduction and intermetallic formation reactions. Formal kinetic parameters were estimated using a semi-empirical approach and refined by comparison with experimental data. The governing equations, including the heat balance equation and the system of kinetic rate equations, were solved numerically using a semi-implicit Euler method, while mass conservation and atomic balance were verified. The initial composition of the samples was varied in the calculations – accounting for oxygen, carbon, and the Fe/Fe_2O_3 ratio in the steel-chippowder – to reproduce the experimentally observed product compositions. The calculated and experimental results showed qualitative agreement.

Keywords: metal-matrix composite, vacuum sintering, metallothermic reactions, intermetallics, thermokinetic model

Acknowledgements: This work was carried out within the framework of the Fundamental Research Program of the Institute of Strength Physics and Materials Science, Siberian Branch of the Russian Academy of Sciences (ISPMS SB RAS): Project FWRW-2022-0003 (theoretical part) and Project FWRW-2021-0005 (experimental part).

For citation: Knyazeva A.G., Korosteleva E.N., Safronova V.S. Sintering and thermokinetic modeling of the phase evolution in thermite powder mixtures under controlled heating. *Powder Metallurgy and Functional Coatings*. 2025;19(5):5–16.
https://doi.org/10.17073/1997-308X-2025-5-5-16

Спекание и термокинетическое моделирование эволюции состава термитных смесей в условиях регулируемого нагрева

А. Г. Князева, Е. Н. Коростелева, В. С. Сафронова

Институт физики прочности и материаловедения Сибирского отделения РАН
Россия, 634055, г. Томск, пр. Академический, 8/2

l9627826013@yandex.ru

Аннотация. Проанализировано поведение прессовок из смесей порошков металлов (Al, Ti) и переработанных отходов металлообработки (Fe + Fe_2O_3 + C) в условиях вакуумного спекания при регулируемом нагреве для исследования возможности получения *in situ* металломатричных композиционных материалов с упрочняющими оксидными частицами. В качестве исходных материалов использованы порошки титана и алюминия с фракциями $d < 160$ мкм и <100 мкм соответственно, а также порошок переработанной стружки из стали размером менее 300 мкм. В результате проведенного эксперимента обнаружен неоднородный фазовый состав образцов, который исследовали с помощью рентгеновского дифрактометра XRD-6000 с CuK_α-излучением и оптического микроскопа «Axiovert 200MAT». Продемонстрировано существенное различие в поведении систем на основе алюминия и титана: первая система характеризуется ярко выраженным термическим пиком, а во второй – превращения идут в спокойном режиме. Предложена термокинетическая модель процесса, учитывающая стадийность превращений для обеих систем. Учтены металлотермические реакции и реакции образования интерметаллидов. Дана оценка формально-кинетическим параметрам реакций с помощью полуэмпирического подхода. Полученные параметры корректировались при сравнении с экспериментом. Модель реализована численно с помощью полунеявного метода Эйлера. Проверялись закон сохранения массы и неизменность числа атомов. Начальный состав образцов в расчетах варьировался (за счет учета присутствия кислорода, углерода и соотношения железа и оксида железа в стружке) таким образом, чтобы в результате синтеза получить состав продуктов, максимально приближенный к результатам эксперимента. Получено качественное соответствие теории и эксперимента.

Ключевые слова: металломатричный композит, вакуумное спекание, металлотермические реакции, интерметаллиды, термокинетическая модель

Благодарности: Работа выполнена по программе фундаментальных научных исследований ИФПМ СО РАН: проекты FWRW-2022-0003 (теоретическая часть) и FWRW-2021-0005 (экспериментальная часть).

Для цитирования: Князева А.Г., Коростелева Е.Н., Сафронова В.С. Спекание и термокинетическое моделирование эволюции состава термитных смесей в условиях регулируемого нагрева. *Известия вузов. Порошковая металлургия и функциональные покрытия*. 2025;19(5):5–16. https://doi.org/10.17073/1997-308X-2025-5-5-16

Introduction

The *in-situ* formation of strengthening particles in metal–matrix composites (MMCs) has become a focal point in powder-processing technologies owing to applications across the aerospace, automotive, and energy sectors, and it continues to attract sustained interest from diverse research groups [1–4]. The spectrum of MMCs obtainable by powder routes is broad – in terms of both matrix chemistries and sets of strengthening phases. Of particular interest are systems built from chemically reactive powder components, where reactions between constituents synthesize the strengthening phases *in-situ* as micron-scale inclusions. This is largely characteristic of combustion-synthesis routes that rely on metallothermic reactions [5–9]. Such reactions are typically strongly exothermic, which helps sustain the synthesis process. Creating the strengthening particles directly during composite fabrication is advantageous for interfacial bonding with the surrounding matrix. However, when a mixture permits metallothermic reduction (one metal reducing another), the presence of additional constituents can markedly redirect reaction pathways because local interaction conditions vary across different regions of the compact [10].

The problem becomes even less straightforward if one component of the powder mixture is itself a complex material – namely, a metallic base containing oxide inclusions – produced by recycling steel chips [11].

Here, the feasibility of producing metal–matrix composites from Al–Fe_2O_3–Fe and Ti–Fe_2O_3–Fe powder mixtures (optionally containing carbon) under sintering in a vacuum chamber is assessed, together with a theoretical description based on a thermokinetic model that accounts for the kinetics of the principal reactions.

1. Experimental

1.1. Materials and methods

Phase evolution under vacuum sintering with a controlled heating program (sintering temperature 1173–1473 K; 60-min hold) was examined for powder systems based on Ti–Al–Fe_2O_3/(Fe + C) using the following representative mixtures (from several possible combinations): Al + (Fe + Fe_2O_3 + C) and Ti + (Fe + Fe_2O_3 + C). Titanium powder TPP-8 (main fraction $d < 160$ μm) and aluminum powder PA-4 ($d < 100$ μm) were used to prepare the mixtures. As an analogue of the Fe + Fe_2O_3 + C composition, a powder produced from recycled steel 45 chips with a particle size not exceeding 300 μm was employed; its characteristics are described in detail in [11]. The component ratios in the mixtures were calculated to be sufficient both for metallothermic reduction and for intermetallic formation. The quantitative compositions of the powder mixtures under study are given in Table 1.

Selection of proportions for the aluminum-containing mixtures was guided by the binary Al–Fe phase diagram. The first option corresponds to the α-$AlFe_3$ field, while the second lies predominantly in the Al_3Fe/AlFe phase region. Both options imply exothermic reactions.

The titanium-containing mixture comprised 75 wt. % Ti and 25 wt. % steel chips, which favors the formation of a matrix basis in the resulting composite as a solid solution of iron and oxygen in titanium.

Microstructural characterization was performed by optical microscopy, scanning electron microscopy (SEM), and *X*-ray diffraction (XRD). The following instruments were used: Axiovert 200MAT optical microscope (Carl Zeiss, Germany), Mira 3 LMU SEM (Tescan, Czech Republic), and XRD-600 (Shimadzu, Japan) and DRON-8 (Russia) diffractometers with CuK_α radiation. Phase identification employed the PDF-4+ database and POWDER CELL 2.4 for full-profile analysis.

According to [11], chips oxidized in water and then milled form oxide-coated steel-chip fragments with an Fe core, containing dissolved carbon (≈1.5 wt. %).

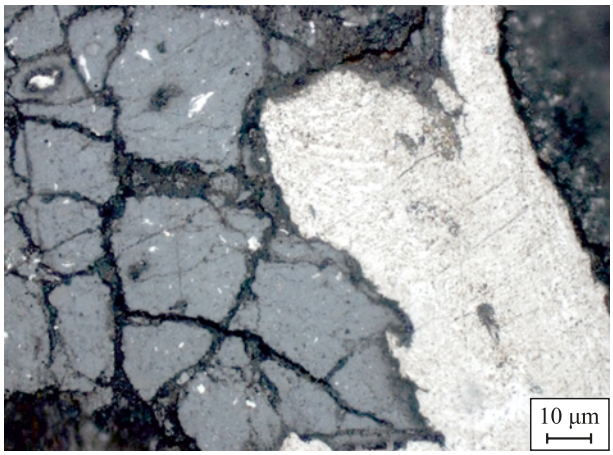

Fig. 1. Microstructure of the recycled steel 45 chips after oxidation and crushing

Light areas correspond to the steel core, dark areas to the iron oxide layer

Рис. 1. Микроструктура переработанной стружки из стали 45 после процедур окисления и дробления

Светлая область – стальная сердцевина, темная – слой из оксидов железа

Although carbide phases were not detected by XRD, the presence of carbon in the steel-chip particles was confirmed by energy-dispersive *X*-ray spectroscopy (EDS). Carbon content, measured with a LECO ONH-836 gas-impurity analyzer (USA), showed a broad distribution (0.8–1.6 wt. %), reflecting the substantial heterogeneity of the processed steel-chip–derived particles. Their surfaces bear iron-oxide regions (Fe_3O_4/Fe_2O_3/FeO) [11], with the oxide fraction reaching ≈50–70 %. Because these oxide layers are highly nonuniform (Fig. 1), the contact between a chip-derived particle and Al or Ti powder depends on the local surface domain encountered. Within the same mixture, the second component can therefore contact metallic iron (carbon steel) and iron oxides simultaneously.

1.2. Experimental results

Under vacuum sintering at T_s = 1273 K, a heterogeneous phase assemblage was identified for both Al + (Fe + Fe_2O_3 + C) formulations [12]. The pressed compacts of aluminum powder with milled, oxidized

Table 1. **Composition of the investigated powder mixtures, wt. %**

Таблица 1. **Состав исследуемых порошковых смесей, мас. %**

Mixture	Composition	Ti	Al	Recycled steel chips (Fe + Fe_2O_3 + C)
1	Al + (Fe + Fe_2O_3 + C)	–	25	75
		–	60	40
2	Ti + (Fe + Fe_2O_3 + C)	75	–	25

steel chips lost structural integrity and disintegrated into separate fragments. The selected sintering conditions were sufficient to initiate a cascade of reactions, yielding Fe–Al intermetallics together with oxide strengthening particles. Residual (unreacted) iron was also detected in the products (Fig. 2). Oxygen was transferred almost entirely from the iron oxides to aluminum, forming Al_2O_3, and FeAl constituted the dominant volumetric fraction of the product.

With increasing aluminum content in the compact, the reaction products contained a substantial fraction of residual, unreacted constituents, attributable to a decrease in the overall exothermicity of the reactions.

The second formulation, Ti + (Fe + Fe_2O_3 + C), is less exothermic. Since the solubility of iron in β-Ti reaches 22 at. % at T_s = 1358 K and drops to 0.34 at. % in α-Ti at 673 K, it was expected that part of the iron would react with titanium to form intermetallics. It was also anticipated that titanium would be sufficient to interact with oxide inclusions present in the recycled steel-chip powder. Experimentally, the steel-chip powder in the Ti + (Fe + Fe_2O_3 + C) mixture exhibited good sinterability, with predominantly diffusional interaction with iron and oxygen migration from iron oxides into the titanium matrix. It is plausible that carbon contained in the chips enhances sintering via diffusion into titanium; however, its amount is too low to produce titanium carbide at levels detectable by *X*-ray diffraction. Interaction of free iron with titanium in the presence of oxide inclusions does not impede interdiffusion. The phase set and phase fractions depend on the sintering temperature; nevertheless, in all cases the products are dominated by a titanium-based solid solution (Fig. 3). At lower temperatures, the products contain a nonstoichiometric TiO_2-based oxide (18 wt. %) and residual Fe_2O_3 (32 wt. %) originating from the steel-chip particles. Iron from these particles reacts with titanium to yield up to 20 wt. % of the equiatomic intermetallic TiFe. At a higher sintering temperature (1473 K), no unreacted constituents remain, and two types of α-Ti–based solid solutions form with different dissolved Fe and O contents; small inclusions of Ti_2Fe, $TiFe_2$, or TiFe are also observed. Oxides are not detected as a separate phase under these conditions (Fig. 3).

The results reported in [13; 14] provided the basis for constructing thermokinetic models that capture the staged nature of phase formation.

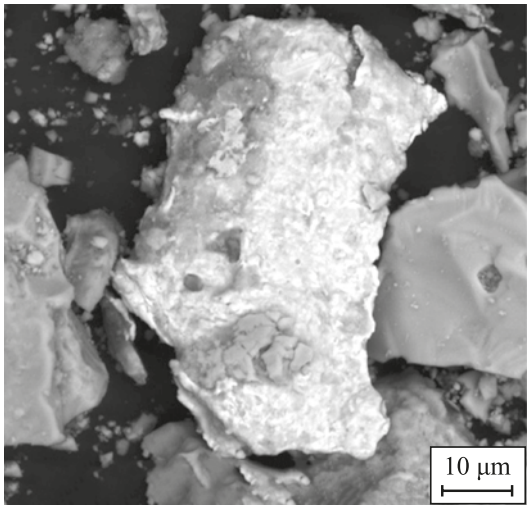

Fig. 2. Microstructure of a fragment of the sintered material 25 % Al + 75 % (Fe + Fe_2O_3 + C)

Рис. 2. Микроструктура фрагмента спеченного материала 25 % Al + 75 % (Fe + Fe_2O_3 + C)

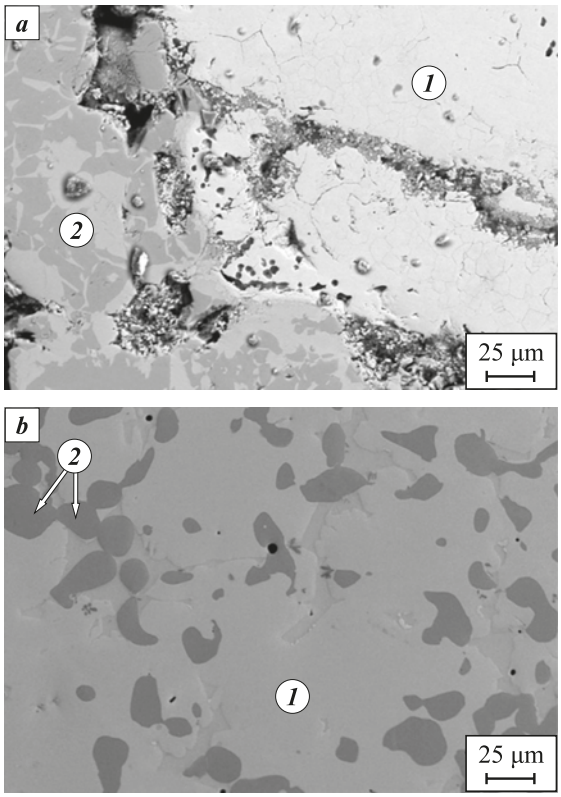

Fig. 3. Microstructure of sintered compacts from the mixture 75 % Ti + 25 % (Fe + Fe_2O_3 + C) at temperatures T_s = 1173 K (***a***) and 1473 K (***b***)

a: ***1*** – regions of residual iron with oxide inclusions; ***2*** – α-Ti of variable composition with TiFe inclusions; ***b***: ***1*** – α-Ti of variable composition with dissolved iron and oxygen, with small $TiFe_2$ or TiFe inclusions; ***2*** – α-Ti regions depleted in iron with small of Ti_2Fe inclusions

Рис. 3. Микроструктура спеченных прессовок из смеси 75 % Ti + 25 % (Fe + Fe_2O_3 + C) при температурах T_s = 1173 K (***a***) и 1473 K (***b***)

a: ***1*** – область остатков железа с оксидными включениями; ***2*** – α-Ti переменного состава с включениями TiFe; ***b***: ***1*** – α-Ti переменного состава с растворенными железом и кислородом, небольшими включениями $TiFe_2$ или TiFe; ***2*** – области α-Ti, обедненные железом с небольшими включениями Ti_2Fe

2. Sintering model with detailed kinetics

2.1. Heat balance

The thermokinetic model accounts for the sample temperature change arising from the controlled external heating program and from heat release by chemical reactions. Owing to the small sample size, temperature gradients within the compact are neglected (a lumped-capacitance assumption); estimates justifying this approximation are given in [15]. The heat-balance equation has the form

$$Vc\rho\frac{dT}{dt} = VW_{ch} + \sigma\varepsilon S\left(T_W^4 - T^4\right) - \alpha S\left(T - T_e\right), \quad (1)$$

where T is the temperature; t is time; V and S are the compact volume and surface area; c and ρ are the heat capacity and density of the pressed powder mixture; W_{ch} is the total heat release due to chemical reactions; σ is the Stefan–Boltzmann constant; ε is the surface emissivity of the compact; α is the heat-transfer coefficient (in vacuum it may be taken as zero); T_e is the ambient temperature (if Newton cooling is included).

The vacuum-chamber wall temperature T_W follows a linear law:

$$T_W = T_0 + at, \text{ for } T < T_s,$$

and

$$T_W = T_s, \text{ for } T \geq T_s, \quad (2)$$

where a is the heating rate and T_s is the sintering temperature.

Within the interval T_{min}–T_{max}, melting is assumed to occur, with the liquid-phase fraction (η_L) varying from 0 to 1:

$$\eta_L = 0 \text{ for } T \leq T_{min},$$
$$\eta_L = \left(\frac{T - T_{min}}{T_{max} - T_{min}}\right)^2 \text{ for } T_{min} < T \leq T_{max}, \quad (3)$$
$$\eta_L = 1 \text{ for } T > T_{max}.$$

Here, T_{min} is the lowest melting temperature among the reagents and reaction products in the chosen system, and T_{max} is the highest one (see Table 2).

Within the melting interval, the (specific) heat capacity is given by

$$c = \left(c_S + \frac{Q_{eff}}{m}\frac{\partial\eta}{\partial T}\right)(1 - \eta_L) + c_L\eta_L, \quad (4)$$

Table 2. **Melting points of the starting substances and selected reaction products**

Таблица 2. **Температуры плавления исходных веществ и некоторых продуктов**

Phase (compound)	T_m, K	Phase (compound)	T_m, K
Al	903,3	Ti–Al*	1513–1733
Fe	1811	Ti–Fe*	1273–1723
Ti	1941	Al–Fe*	825–1583
Fe_2O_3	1838	$FeAl_2O_4$	1713
Al_2O_3	2345	Ti_3FeO_2	–**
TiO_2	2116	TiC	3473

* Intermetallic phases in the corresponding binary system.
** An unstable compound that decomposes before melting (at T = 1273 K).

where c_S is the heat capacity of the mixture in the solid state, c_L is the heat capacity of the mixture in the liquid state; Q_{eff} is the effective enthalpy of fusion (J/mol); m is the mean molar mass of the mixture of reagents and reaction products.

Heat release from chemical reactions is given by

$$W_{ch} = \sum_{i=1}^{n} Q_i\Phi_i, \quad (5)$$

where n is the number of reactions; Φ_i are the reaction rates; Q_i are the reaction enthalpies (heat effects).

2.2. Model of phase composition evolution during sintering

Because the detailed mechanisms of most solid-state reactions are rarely known and the steps involved often comprise a mix of physicochemical processes, it is most appropriate to use a reduced-chemistry model that explicitly tracks the formation of the experimentally observed phases.

In the Al-containing system (where aluminum has the lowest melting temperature), the dominant exothermic step is expected to be the aluminothermic reduction of iron oxide:

$$2Al + Fe_2O_3 = Al_2O_3 + 2Fe. \quad (I)$$

The reduced iron then reacts with excess aluminum to form intermetallic phases. Owing to the large reaction enthalpies, phase formation is expected to occur predominantly in the liquid phase and to be accompanied by the appearance of agglomerates [16]. At the same time, as noted in [17], direct reaction

between aluminum and iron oxides during combustion is preceded by the partial decomposition sequence $Fe_2O_3 \rightarrow Fe_3O_4 \rightarrow FeO$. Thin plates of $FeAl_2O_4$, have been observed in [17] as a result of the interaction between FeO and the amorphous Al_2O_3 film that invariably coats aluminum:

$$FeO + Al_2O_3 \rightarrow FeAl_2O_4. \quad (II)$$

Iron aluminates such as $FeAl_2O$ and $FeAl_2O_4$ commonly appear in the Al–Fe_2O_3 system, which is unfavorable for further reduction of iron oxides – especially in the presence of Al_2O_3 [18].

In the Al–Fe_2O_3 system, an additional step may occur

$$2Fe_2O_3 \rightarrow 4FeO + O_2 \quad (III)$$

followed by oxidation of aluminum:

$$4Al + 3O_2 = 2Al_2O_3. \quad (IV)$$

The Al–Fe phase diagram contains several intermetallic phases (Fig. 4). The diagram was constructed using the Thermo-Calc Software (open version) with the TCBIN: TC Binary Solutions v1.1 database.

Formation of intermetallic phases proceeds via the reactions

$$Al + Fe = FeAl, \quad (V)$$

$$FeAl + Al = FeAl_2, \quad (VI)$$

$$FeAl + 2Fe = Fe_3Al, \quad (VII)$$

$$FeAl_2 + Al = FeAl_3, \quad (VIII)$$

$$FeAl_2 + FeAl_3 = Fe_2Al_5. \quad (IX)$$

The FeAl intermetallic is not shown on the diagram; however, it is known to form by ordering of the α-Fe(Al) solid solution. Fe_3Al is a metastable phase that appears via a second-order phase transformation from FeAl [19]. Carbon present in the processed chips could, in principle, participate in the synthesis of aluminum carbide (Al_4C_3), but the sintering schedule and mixture composition do not provide sufficient carbon or temperature to initiate the corresponding reaction.

In the second case (Ti–Fe_2O_3–Fe–C system), iron is the lowest-melting component (see Table 2). According to [20], the thermite reaction Ti–Fe_2O_3 proceeds through several steps – reduction of Fe_2O_3 by Ti to form Fe and TiO_2, followed by the formation of the metastable intermetallic Ti_2Fe. Allowing for partial decomposition of iron oxide, the presence of carbon, and the formation of intermetallic phases (Fig. 4, *b*), the reaction set can be written as:

$$3Ti + 2Fe_2O_3 = 3TiO_2 + 4Fe, \quad (I')$$

$$Ti + Fe = TiFe, \quad (II')$$

$$TiFe + Ti = Ti_2Fe, \quad (III')$$

$$TiFe + Fe = TiFe_2, \quad (IV')$$

$$Ti + C = TiC, \quad (V')$$

$$2Fe_2O_3 \rightarrow 4FeO + O_2, \quad (VI')$$

$$Ti + O_2 = TiO_2, \quad (VII')$$

$$TiO_2 + Ti_2Fe = Ti_3FeO_2. \quad (VIII')$$

The notation for species concentrations (C_k) for each system is given in Tables 3 and 4.

For each reaction network, the kinetic equations can be written as

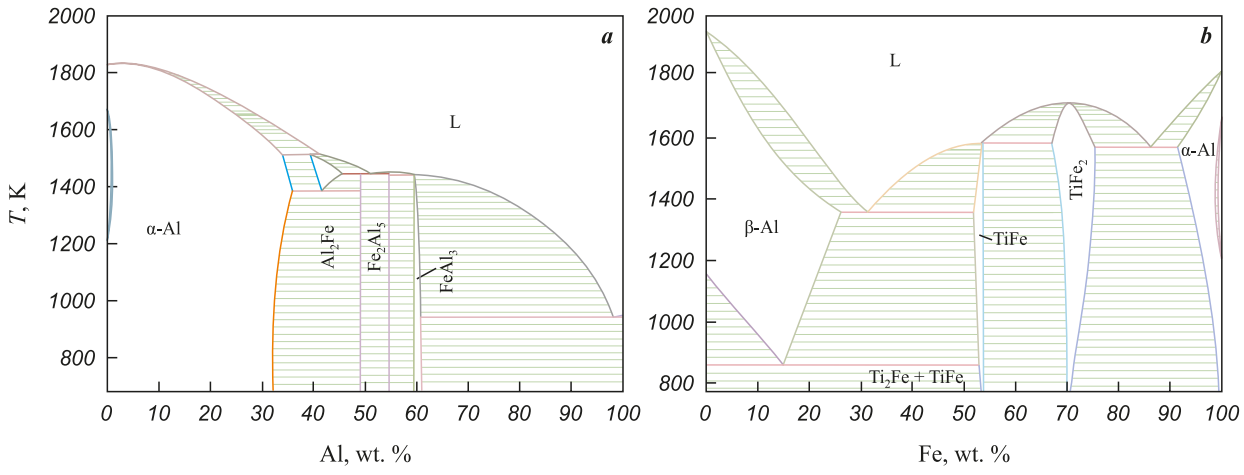

Fig. 4. Phase diagrams of the Al–Fe (***a***) and Ti–Fe (***b***) systems

Рис. 4. Диаграммы состояния Al–Fe (***a***) и Ti–Fe (***b***)

$$\frac{dC_k}{dt} = \sum_{k=1}^{r} \nu_{ki}\Phi_i, \quad (6)$$

where ν_{ki} are the stoichiometric coefficients of component k in reaction i; r is the number of reactions, Φ_i are the reaction rates. We assume that the reaction rates follow an Arrhenius temperature dependence and depend on concentrations according to the law of mass action:

$$\Phi_i = k_i(T)\prod_k C_k^{n_{ki}}. \quad (7)$$

Here, n_{ki} are the exponents equal in absolute value to the corresponding stoichiometric coefficients;

$$k_i = k_{i0}\exp\left(-\frac{E_i}{RT}\right), \quad (8)$$

where k_{i0} are the pre-exponential factors; E_i are the activation energies; R is the universal gas constant. The rate expressions for all reactions are given in Table 5.

Thus, for the first system we require 27 formal kinetic parameters k_{i0}, E_i, Q_i, and for the second – 24. Using published parameters for overall reactions in SHS-type mixtures [21] is not feasible. One reason is the strong dependence of parameters on the determination method, mixture processing, heating rate, etc. Another is the lack of data for most steps. Even for one of the most studied thermite mixtures (Al–Fe_2O_3), published values are inconsistent [22], including the reaction enthalpies. For example, for reaction (VI) in the Al-containing system, [23] gives: ΔH = –851.4 kJ/mol, whereas [16] reports $\Delta H \approx$ –752 kJ/mol.

The entropies and enthalpies of reactions were obtained using Hess's law:

$$\Delta H^0_{298} = \sum_{\text{products}} \nu_{ki}\Delta H^0_{298} - \sum_{\text{reagents}} \nu_{ki}\Delta H^0_{298}, \quad (9)$$

$$\Delta S^0_{298} = \sum_{\text{products}} \nu_{ki}\Delta S^0_{298} - \sum_{\text{reagents}} \nu_{ki}\Delta S^0_{298}, \quad (10)$$

where the first terms on the right-hand side are sums of the parameters for the reaction products, and the second terms are the parameters for the reactants (reagents in the formula). However, tabulated values

Table 3. **Concentration designations for the Al + (Fe + Fe_2O_3) system**

Таблица 3. **Обозначения концентраций для системы Al + (Fe + Fe_2O_3)**

Species	Concentration	Species	Concentration
Al	C_1	Fe_2Al_5	C_7
Fe	C_2	Al_2O_3	C_8
FeAl	C_3	Fe_2O_3	C_9
$FeAl_2$	C_4	FeO	C_{10}
Fe_3Al	C_5	O_2	C_{11}
$FeAl_3$	C_6	$FeAl_2O_4$	C_{12}

Table 4. **Concentration designations for the Ti + (Fe_2O_3 + Fe + C) system**

Таблица 4. **Обозначения концентраций для системы Ti + (Fe_2O_3 + Fe + C)**

Species	Concentration	Species	Concentration
Ti	C_1	$TiFe_2$	C_7
Fe	C_2	TiC	C_8
Fe_2O_3	C_3	FeO	C_9
TiO_2	C_4	O_2	C_{10}
TiFe	C_5	Ti_3FeO_2	C_{11}
Ti_2Fe	C_6		

Table 5. **Reaction rate expressions**

Таблица 5. **Скорости реакций**

Al-containing system	Reaction rate	Ti-containing system	Reaction rate
1) Al + Fe = FeAl	$\Phi_1 = k_1C_1C_2$	1) $3Ti + 2Fe_2O_3 = 3TiO_2 + 4Fe$	$\Phi_1 = k_1C_1^3C_3^2$
2) FeAl +Al = $FeAl_2$	$\Phi_2 = k_2C_1C_3$	2) Ti + Fe = TiFe	$\Phi_2 = k_2C_1C_2$
3) FeAl + 2Fe = Fe_3Al	$\Phi_3 = k_3C_2^2C_3$	3) TiFe + Ti = Ti_2Fe	$\Phi_3 = k_3C_1C_5$
4) $FeAl_2$ + Al = $FeAl_3$	$\Phi_4 = k_4C_1C_4$	4) TiFe + Fe = $TiFe_2$	$\Phi_4 = k_4C_2C_5$
5) $FeAl_2$ + $FeAl_3$ = Fe_2Al_5	$\Phi_5 = k_5C_4C_6$	5) Ti + C = TiC	$\Phi_5 = k_5C_1C_8$
6) $2Al + Fe_2O_3 = Al_2O_3 + 2Fe$	$\Phi_6 = k_6C_1^2C_9$	6) $2Fe_2O_3 \rightarrow 4FeO + O_2$	$\Phi_6 = k_6C_3^2$
7) $2Fe_2O_3 \rightarrow 4FeO + O_2$	$\Phi_7 = k_7C_9^2$	7) $Ti + O_2 = TiO_2$	$\Phi_7 = k_7C_1C_{11}$
8) $FeO + Al_2O_3 = FeAl_2O_4$	$\Phi_8 = k_8C_9C_{10}$	8) $TiO_2 + Ti_2Fe = Ti_3FeO_2$	$\Phi_8 = k_8C_4C_6$
9) $4Al + 3O_2 = 2Al_2O_3$	$\Phi_9 = k_9C_1^4C_{11}^3$		

are not available in the literature for all compounds. For this reason, approximate semi-empirical methods were used to obtain preliminary estimates of the formal kinetic parameters (Table 6). The parameter-estimation procedure is described in detail in [15].

For each system, the problem (which comprised 10 and 9 ordinary differential equations of the form (6) for the Al- and Ti-containing systems, respectively, plus the heat-balance equation (1)) was solved numerically using a semi-implicit Euler method. In every run, mass conservation and atomic balance were verified. Calculations were performed at constant ΔS^0_{298} and ΔH^0_{298}. The reaction orders were adjusted during the numerical solution. For the first system, we obtained:

$$k_{01} = 10^{17},\ k_{02} = 10^{22},\ k_{03} = 3\cdot10^{22},\ k_{04} = 10^{22},$$

$$k_{05} = 10^{22},\ k_{06} = 8\cdot10^{19},\ k_{07} = 6\cdot10^{15},$$

$$k_{08} = 10^{15},\ k_{09} = 10^{24}\ \text{s}^{-1}.$$

For the second system, the adjustments affected two pre-exponential factors and the activation energy of one reaction:

$$k_{05} = 3\cdot10^{19}\ \text{c}^{-1},\ k_{06} = 6\cdot10^{23}\ \text{s}^{-1},$$

$$E_6 = 150{,}255\ \text{J/mol}.$$

A single scaling factor applied to all reactions was 10^{-17} for the Al-containing system and $7.5\cdot10^{-13}$ for the Ti-containing system. The criterion for selecting this factor was the characteristic reaction time under the experimental conditions.

2.3. Numerical analysis results

Calculated temperature and composition profiles for reactive sintering of the studied systems are shown in Figs. 5–7. The typical temperature curves differ for the Al- and Ti-containing mixtures (Fig. 5). In the former, a temperature spike appears upon reaction initiation at T = 700–900 K. In the latter, there is no pronounced spike, although a wavy temperature curve is observed.

Such behavior is often ascribed to thermocouple sensitivity; however, the calculations indicate that it may also arise from the interplay of coupled physicochemical processes.

As noted above, the exact oxide composition in the chips is unknown. Accordingly, the modeling allows for different choices of initial data (Table 7). We assume the presence of two iron oxides – FeO and Fe_2O_3. Fe_3O_4 can, to first approximation, be treated as a combination of FeO and Fe_2O_3 and is therefore not included explicitly. In addition, the numerical experiment accounts for adsorbed oxygen and alumina on particle surfaces. Only under this assumption does the model reproduce the amount of Al_2O_3 observed experimentally in the products. The numerical study further enables exploration over a wide range of initial compositions, which is difficult to achieve experimentally.

No such complications arose for the Ti system, although the initial composition of the powder mixture can likewise be varied numerically.

Composition-evolution results for different initial data are presented in Figs. 6 and 7. We find that

***Table 6.* Formal kinetic parameters obtained using a semi-empirical approach**

***Таблица 6.* Формально-кинетические параметры, найденные с помощью полуэмпирического подхода**

Al + (Fe + Fe_2O_3)					Ti + (Fe_2O_3 + Fe + C)				
Reaction No.	ΔS^0_{298}	k_{0i}	E	ΔH^0_{298}	Reaction No.	ΔS^0_{298}	k_{0i}	E	ΔH^0_{298}
1	–26.10	10^{15}	32,104.53	–30.7	*1*	–0.36	$9\cdot10^{13}$	15,710.04	–1155.0
2	–25.15	10^{15}	31,218.18	–33.7	*2*	–3.47	10^{14}	18,730.20	–44.6
3	–36.10	$3\cdot10^{15}$	36,638.25	–93.0	*3*	–40.92	10^{16}	78,275.70	–49.1
4	–26.38	10^{15}	32,365.77	–37.6	*4*	–40.43	10^{16}	77,496.60	–45.4
5	–24.95	10^{15}	47,960.92	–161.5	*5*	–161.62	$3\cdot10^{22}$	17,970.00	–209.0
6	–38.48	$8\cdot10^{15}$	43,655.07	–760.0	*6*	274.20	$6\cdot10^{26}$	15,255.54	584.0
7	274.30	$6\cdot10^{26}$	15,260.94	584.0	*7*	–183.32	10^{22}	10,348.02	–933.0
8	–5.40	10^{14}	22,621.50	–122.0	*8*	10.60	$2\cdot10^{14}$	32,147.00	–173.3
9	–626.86	10^{45}	34,299.18	–3164.0					

N o t e s . Units: $[\Delta S^0_{298}]$ = J/(mol·K); $[k_{0i}]$ = s^{-1}; $[E]$ = J/mol; $[\Delta H^0_{298}]$ = kJ/mol.
Reaction numbers follow Table 5.

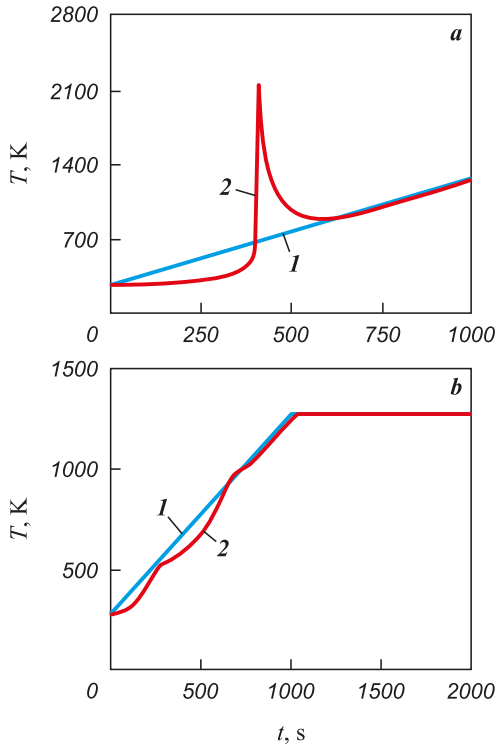

Fig. 5. Typical temperature curves for the composition with (***a***) and titanium (***b***)

Mixtures compositions *2* from Table 7
Sintering temperature T_s = 1273 K
1 – heater temperature; ***2*** – sample temperature

Рис. 5. Типичное поведение температурных кривых для состава с алюминием (***a***) и титаном (***b***)

Составы смесей *2* из табл. 7
Температура спекания T_s = 1273 K
1 – температура нагревателя; ***2*** – температура образца

the product composition can vary substantially. For the Al-containing system (Fig. 6), the products always contain Fe_3Al and $FeAl_3$ intermetallics in different proportions, as well as Al_2O_3. The reduction of iron is the fastest reaction. FeAl is not observed in the products. The mixed oxide appears only when the initial mixture contains Al_2O_3, FeO, and oxygen; in that case, Fe_2Al_5 is also present. The experimental data are best matched by Composition *2*, which includes oxygen and oxide in the starting mixture.

The phase composition of the Ti compact also evolves (Fig. 7). All reactions proceed actively over a time interval shorter than the total sintering time. For all initial compositions, the products always contain the intermetallic Ti_2Fe and unreacted Ti. TiFe appears as an intermediate during sintering. In three variants, the product contains Ti_3FeO_2. In the second variant, the starting mixture contains a small amount of iron oxide, hence its role is minor; however, Fe_2O_3 most closely reflects the experimental conditions. Under the experimental conditions, the product contains 91 wt. % of α-Ti solid solution + Ti_2Fe and α-Ti solid solution + TiFe. In this case, Fe_2O_3 is insufficient to form TiO_2. In the other three variants, TiO_2 appears as an intermediate that is consumed rapidly to form the complex oxide.

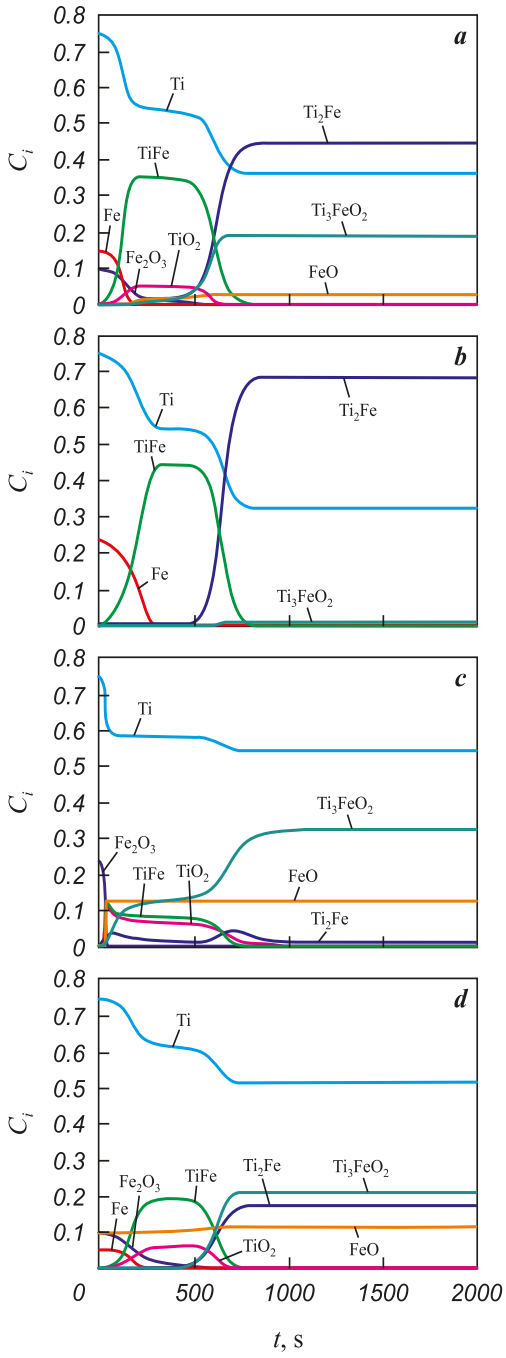

Fig. 6. Phase composition evolution of the aluminium compact during sintering

The nitial composition corresponds to Table 7
Al-based mixtures: ***a*** – composition *1*, ***b*** – *2*, ***c*** – *3*, ***d*** – *4*

Рис. 6. Изменение фазового состава прессовки с алюминием в условиях спекания
Начальный состав соответствует табл. 7
Составы с Al: ***a*** – состав *1*, ***b*** – *2*, ***c*** – *3*, ***d*** – *4*

Table 7. **Initial data for calculations**

Таблица 7. **Начальные данные для расчетов**

Composition No. (numerical experiment)	Initial composition of the Al-containing mixture, wt. %						Initial composition of the Ti-containing mixture, %				
	Al	Fe_2O_3	Fe	FeO	O_2	Al_2O_3	Ti	Fe_2O_3	Fe	FeO	C
1	0.25	0.45	0.30	–	–	–	0.75	0.100	0.150	–	–
2	0.25	0.20	0.30	0.15	0.05	0.05	0.75	0.010	0.239	–	0.001
3	0.25	0.15	0.30	0.20	0.50	0.05	0.75	0.239	0.010	–	0.001
4	0.60	0.20	0.20	–	–	–	0.75	0.100	0.050	0.10	–

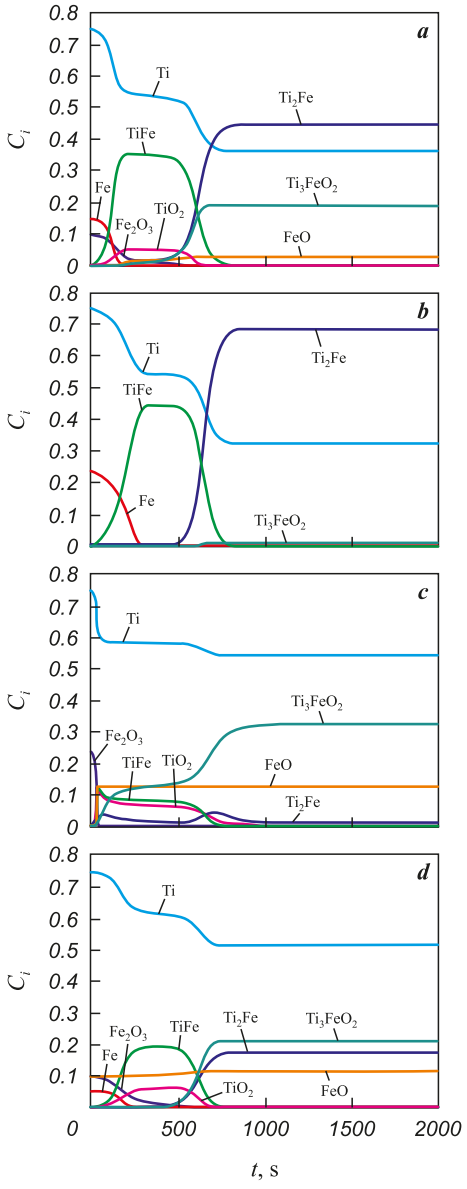

Fig. 7. Phase composition evolution of the titanium compact during sintering

The initial composition corresponds to Table 7
Ti-based mixtures: ***a*** – composition *1*, ***b*** – *2*, ***c*** – *3*, ***d*** – *4*

Рис. 7. Изменение фазового состава прессовки с титаном в условиях спекания

Начальный состав соответствует табл. 7
Составы с Ti: ***a*** – состав *1*, ***b*** – *2*, ***c*** – *3*, ***d*** – *4*

Conclusion

This study demonstrates good agreement between the proposed thermokinetic model and experimental data for multicomponent powder mixtures – recycled steel-chip powder with aluminum or titanium – under vacuum sintering. Consistent with the experiments, the calculations predict substantial heat release upon heating Al + (Fe + Fe_2O_3 + C) mixtures, whereas Ti + (Fe + Fe_2O_3 + C) sinters in a steady regime. In the former case, aluminum carbide was not included in the model because of the low sintering temperature; in the latter, titanium carbide formed only in trace amounts. No carbides were detected experimentally in either system.

References / Список литературы

1. Yeh C.L., Li R.F. Formation of TiAl–Ti_5Si_3 and TiAl–Al_2O_3 *in situ* composites by combustion synthesis. *Intermetallics*. 2008;16(1):64–70. https://doi.org/10.1016/j.intermet.2007.07.016
2. Zhang X., Li X., Wang J., Liu L., Li S., Li B., Hou X., Gao J., Kariya S., Umeda J., Kondoh K., Li S. Synthesis mechanism and interface contribution towards the strengthening effect of *in-situ* Ti_5Si_3 reinforced Al matrix composites. *Materials Science and Engineering: A*. 2024; 918:147427. https://doi.org/10.1016/j.msea.2024.147427
3. Yang Y.F., Mu D.K., Jiang Q.C. A simple route to fabricate TiC–TiB_2/Ni composite via thermal explosion reaction assisted with external pressure in air. *Materials Chemistry and Physics*. 2014;143(2):480–485. https://doi.org/10.1016/j.matchemphys.2013.10.003
4. Lemboub S., Boudebane S., Gotor F.J., Haouli S., Mezrag S., Bouhedja S., Hesser G., Chadli H., Chouchane T. Core-rim structure formation in TiC–Ni based cermets fabricated by a combined thermal explosion/hot-pressing process. *International Journal of Refractory Metals and Hard Materials*. 2018;70:84–92. https://doi.org/10.1016/j.ijrmhm.2017.09.014
5. Yeh C.L., Ke C.Y. Synthesis of TiB_2–Al_2O_3–FeAl composites via self-sustaining combustion with Fe_2O_3/TiO_2-based thermite mixtures. *Ceramics International*. 2018;44(13): 16030–16034. https://doi.org/10.1016/j.ceramint.2018.06.040

6. Zhang K., Fen W., Zhu J., Wu H. Mechanical properties and microstructure of Al_2O_3/TiAl *in situ* composites doped with Cr and V_2O_5. *Science of Sintering*. 2012;44(1):73–80. https://doi.org/10.2298/SOS1201073Z
7. Motlagh E.B., Nasiri H., Khaki J.V., Sabzevar M.H. Formation of metal matrix composite reinforced with nano sized Al_2O_3+Ni–Al intermetallics during coating of Al substrate via combustion synthesis. *Surface & Coatings Technology*. 2011;205(23-24):5515–5520. https://doi.org/10.1016/j.surfcoat.2011.06.026
8. Kim J.-W., Lee J.-M., Lee J.-H., Lee J.-C. Role of excess Al on the combustion reaction in the Al–TiO_2–C system. *Metals and Materials International*. 2014;20(6): 1151–1156. https://doi.org/10.1007/s12540-014-6020-8
9. Miloserdov P.A., Gorshkov V.A., Andreev D.E., Yukhvid V.I., Miloserdova O.M., Golosova O.A. Metallothermic SHS of Al_2O_3–Cr_2O_3 + TiC ceramic composite material. *Ceramics International*. 2023;49(14):24071–24076. https://doi.org/10.1016/j.ceramint.2023.04.145
10. Korosteleva E.N., Knyazeva A.G., Nikolaev I.O. Phase formation in reactive sintering with reduction. *Physical Mesomechanics*. 2023;26(1):39–47. https://doi.org/10.1134/S1029959923010058
11. Korosteleva E.N., Nikolaev I.O. Evolution of the structural-phase state of steel swarf during its processing into a powdered product. *Powder Metallurgy and Functional Coatings*. 2024;18(4):6–16. https://doi.org/10.17073/1997-308X-2024-4-6-16

    Коростелева Е.Н., Николаев И.О. Эволюция структурно-фазового состояния стальной стружки в процессе ее переработки в порошкообразный продукт. *Известия вузов. Порошковая металлургия и функциональные покрытия*. 2024;18(4):6–16. https://doi.org/10.17073/1997-308X-2024-4-6-16
12. Korosteleva E.N., Nikolaev I.O., Baranovsky A.V. Synthesis and evolution of the structural and phase state of powder materials Al–Fe–Fe_2O_3 under heating conditions. In: *Collection of materials of the XVII Minsk International Heat and Mass Transfer Forum* (20–24 May 2024). Minsk: Institute of Heat and Mass Transfer n.a. Lykov of the NAS of Belarus, 2024. P. 746–748. (In Russ.).

    Коростелева Е.Н., Николаев И.О., Барановский А.В. Синтез и эволюция структурно-фазового состояния порошковых материалов Al–Fe–Fe_2O_3 в условиях нагрева. В сб.: *Материалы XVII Минского международного форума по тепло- и массообмену* (20–24 мая 2024 г.). Минск: Институт тепло- и массообмена им. А.В. Лыкова НАН Беларуси, 2024. С. 746–748.
13. Miedema A.R., de Châtel P.F, de Boer F.R., de Chatel P.F. Cohesion in alloys – fundamental of a semi-empirical model. *Physica B + C*. 1980;100(1):1–28. https://doi.org/10.1016/0378-4363(80)90054-6
14. Binnewies M., Milke E. Thermochemical data of elements and compounds. Wiley-VCH Verlag GmbH, 2008. 928 p. https://doi.org/10.1002/9783527618347
15. Safronova V.S., Knyazeva A.G., Korosteleva E.N. A theoretical and experimental study of phase formation in Ti–CuO powder mixtures under reactive sintering conditions. *New Journal of Chemistry*. 2025;49(3):893–909. https://doi.org/10.1039/d4nj03751k
16. Podergin V.A. Metallothermal systems. Moscow: Metallurgiya, 1992. 272 p. (In Russ.).

    Подергин В.А. Металлотермические системы. М.: Металлургия, 1992. 272 с.
17. Korchagin M.A., Podergin V.A. Investigation of chemical transformations in the combustion of condensed systems. *Combustion, Explosion, and Shock Waves*. 1979;15(3):325–329. https://doi.org/10.1007/BF00785065

    Корчагин М.А., Подергин В.А. Исследование химических превращений при горении конденсированных систем. *Физика горения и взрыва*. 1979;(3):48–53.
18. Liu W., Ismail M., Dunstan M.T., Hu W., Zhang Z., Fennell P.S., Scott S.A., Dennis J.S. Inhibiting the interaction between FeO and Al_2O_3 during chemical looping production of hydrogen. *RSC Advances*. 2015;5(3):1759–1771. https://doi.org/10.1039/C4RA11891J
19. Liu Y., Watanabe M., Okugawa M., Hagiwara T., Sato T., Seguchi Y., Adachi Y., Minamino Y., Koizumi Y. Resolving the long-standing discrepancy in Fe_3Al ordering mobilities: A synergistic experimental and phase-field study. *Acta Materialia*. 2024;273:119958. https://doi.org/10.1016/j.actamat.2024.119958
20. Lin Y.-C., Shteinberg A.S., McGinn P.J., Mukasyan A.S. Kinetics study in Ti–Fe_2O_3 system by electro-thermal explosion method. *International Journal of Thermal Sciences*. 2014;84:369–378. https://doi.org/10.1016/j.ijthermalsci.2014.06.008
21. Mukasyan A.S., Shuck C.E. Kinetics of SHS reactions: A review. *International Journal of Self-Propagating High-Temperature Synthesis*. 2017;26(3):145–165. https://doi.org/10.3103/S1061386217030049
22. Durães L., Costa B.F.O., Santos R., Correia A., Campos J., Portugal A. Fe_2O_3/aluminum thermite reaction intermediate and final products characterization. *Materials Science and Engineering: A*. 2007;465(1-2):199–210. https://doi.org/10.1016/j.msea.2007.03.063
23. Bodaghi M., Zolfonoon H., Tahriri M., Karimi M. Synthesis and characterization of nanocrystalline α-Al_2O_3 using Al and Fe_2O_3 (hematite) through mechanical alloying. *Solid State Sciences*. 2009;11(2):496–500. https://doi.org/10.1016/j.solidstatesciences.2008.06.021

Information about the Authors

Anna G. Knyazeva – Chief Researcher, Laboratory of Nonlinear Mechanics of Metamaterials and Multilevel Systems, Institute of Strength Physics and Materials Science, Siberian Branch of the Russian Academy of Sciences (ISPMS SB RAS)
ORCID: 0000-0002-9765-7695
E-mail: anna-knyazeva@mail.ru

Elena N. Korosteleva – Senior Researcher, Laboratory of Physics of Powder Materials Consolidation of the ISPMS SB RAS
ORCID: 0000-0002-4363-3604
E-mail: elenak@ispms.ru

Valeriya S. Safronova – Research Assistant, Laboratory of Nonlinear Mechanics of Metamaterials and Multilevel Systems of the ISPMS SB RAS
ORCID: 0009-0004-7423-5897
E-mail: l9627826013@yandex.ru

Сведения об авторах

Анна Георгиевна Князева – гл. науч. сотрудник лаборатории нелинейной механики метаматериалов и многоуровневых систем Института физики прочности и материаловедения (ИФПМ) СО РАН
ORCID: 0000-0002-9765-7695
E-mail: anna-knyazeva@mail.ru

Елена Николаевна Коростелева – ст. науч. сотрудник лаборатории физики консолидации порошковых материалов ИФПМ СО РАН
ORCID: 0000-0002-4363-3604
E-mail: elenak@ispms.ru

Валерия Сергеевна Сафронова – лаборант-исследователь лаборатории нелинейной механики метаматериалов и многоуровневых систем ИФПМ СО РАН
ORCID: 0009-0004-7423-5897
E-mail: l9627826013@yandex.ru

Contribution of the Authors

A. G. Knyazeva – development of the main concept, formulation of the research objectives and tasks, model formulation, preparation of the text, and formulation of conclusions.
E. N. Korosteleva – experimental testing of the samples and preparation of the manuscript.
V. S. Safronova – development of the computational program, performing calculations, and analysis of the research results.

Вклад авторов

А. Г. Князева – формирование основной концепции, постановка цели и задачи исследования, формулировка модели, подготовка текста, формулировка выводов.
Е. Н. Коростелева – проведение испытаний образцов, подготовка текста статьи.
В. С. Сафронова – написание программы, проведение расчетов, анализ результатов исследований.

Received 23.03.2025
Revised 24.04.2025
Accepted 28.04.2025

Статья поступила 23.03.2025 г.
Доработана 24.04.2025 г.
Принята к публикации 28.04.2025 г.

Self-Propagating High-Temperature Synthesis
Самораспространяющийся высокотемпературный синтез

UDC 621.762
https://doi.org/10.17073/1997-308X-2025-5-17-35

Research article
Научная статья

Synthesis of refractory high-entropy alloys based on Mo–Nb–Ta–(Cr, V, Zr, Hf) using centrifugal SHS metallurgy and investigation of their oxidation resistance

V. N. Sanin[1], D. M. Ikornikov[1] ✉, A. O. Sivakova[1], D. Yu. Kovalev[1], S. L. Silyakov[1], M. D. Panova[2]

[1] Merzhanov Institute of Structural Macrokinetics and Materials Science of the Russian Academy of Sciences
8 Academician Osip'yan Str., Chernogolovka, Moscow Region 142432, Russia
[2] JSC "State Scientific Research and Design Institute of the Rare Metal Industry "Giredmet"
2 Elektrodnaya Str., Moscow 111524, Russia

✉ denis-ikornikov@yandex.ru

Abstract. Refractory high-entropy alloys (RHEAs) based on refractory metals exhibit a combination of outstanding properties, such as high strength and thermal stability at elevated temperatures. These alloys typically contain costly refractory elements, including Mo, Nb, Ta, W, and Hf. In addition to their high cost, RHEA production is associated with a number of technological challenges. Well-established commercial methods used for nickel-based superalloys are generally unsuitable due to the higher melting points and increased chemical reactivity of the components. To address this issue, the present study explores the feasibility of synthesizing cast RHEAs using centrifugal self-propagating high-temperature synthesis (SHS) metallurgy – a technological approach within the broader field of SHS. For the first time, cast RHEAs based on the Mo–Nb–Ta system, alloyed *in situ* with 3*d* metals (Cr, V, Zr, Hf), were successfully synthesized via SHS. It was demonstrated that crystallization of the ingots occurs from the molten state, ensuring homogeneous distribution of Mo, Nb, Ta, Cr, V, Zr, and Hf. The phase composition of the synthesized RHEAs was found to depend on the alloying elements. Co-reduction of group V (Nb, Ta, V) and group VI (Cr, Mo) metals resulted in nearly single-phase alloys with a body-centered cubic (BCC) structure typical for these elements. The addition of Zr and Hf – metals with a hexagonal crystal structure – to the quaternary MoNbTaCr alloy significantly altered the phase composition of the ingots. In addition to BCC-phase reflections, the *X*-ray diffraction patterns exhibited intense reflections of face-centered cubic (FCC) phases and weak reflections of two hexagonal close-packed (HCP) phases. The proposed synthesis method considerably simplifies the otherwise complex technological process of producing cast, multicomponent RHEAs with a desired composition. Oxidation resistance tests revealed that the Mo–Nb–Ta–Cr–V composition is the most promising for further investigation. Compared to other compositions, this alloy demonstrated superior oxidation resistance, making it a competitive candidate for high-temperature applications.

Keywords: self-propagating high-temperature synthesis (SHS); centrifugal SHS metallurgy; thermite-type SHS systems; high-entropy alloys (HEAs); refractory high-entropy alloys (RHEAs); multimetallic alloy synthesis; oxidation resistance of HEAs

Acknowledgements: The research was supported by the Russian Science Foundation (Project No. 24-13-00065, https://rscf.ru/project/24-13-00065/

For citation: Sanin V.N., Ikornikov D.M., Sivakova A.O., Kovalev D.Yu., Silyakov S.L., Panova M.D. Synthesis of refractory high-entropy alloys based on Mo–Nb–Ta–(Cr, V, Zr, Hf) using centrifugal SHS metallurgy and investigation of their oxidation resistance. *Powder Metallurgy and Functional Coatings*. 2025;19(5):17–35. https://doi.org/10.17073/1997-308X-2025-5-17-35

Синтез высокоэнтропийных сплавов на основе тугоплавких металлов Mo–Nb–Ta–(Cr, V, Zr, Hf) методами центробежной СВС-металлургии и исследование их окислительной стойкости

В. Н. Санин[1], Д. М. Икорников[1] ✉, А. О. Сивакова[1], Д. Ю. Ковалев[1], С. Л. Силяков[1], М. Д. Панова[2]

[1] Институт структурной макрокинетики и проблем материаловедения им. А.Г. Мержанова РАН
Россия, 142432, Московская обл., г. Черноголовка, ул. Академика Осипьяна, 8
[2] АО «Государственный научно-исследовательский и проектный институт редкометаллической промышленности «Гиредмед»
Россия, 111524, г. Москва, ул. Электродная, 2

✉ denis-ikornikov@yandex.ru

Аннотация. Высокоэнтропийные сплавы на основе тугоплавких металлов (ТВЭС) (англ. *RHEAs – refractory high-entropy alloys*) обладают набором замечательных свойств – такими, как высокая прочность и термическая стабильность при высоких температурах. В состав этих сплавов входит ряд дорогостоящих тугоплавких элементов: Mo, Nb, Ta, W, Hf и др. Помимо высокой стоимости, получение ТВЭС характеризуется рядом технологических трудностей. Успешно действующие коммерческие технологии для никелевых жаропрочных сплавов здесь практически не применимы вследствие более высоких температур плавления компонентов и их высокой химической активности. Для решения этой проблемы в настоящей работе исследована возможность получения литых ТВЭС методом центробежной СВС-металлургии – одним из технологических направлений в области самораспространяющегося высокотемпературного синтеза (СВС). Используя данный метод, впервые были получены литые ТВЭС на основе базовой системы, состоящей из тугоплавких металлов Mo–Nb–Ta, легированные 3*d*-металлами (Cr, V, Zr, Hf) непосредственно (*in situ*) путем СВС. Показано, что кристаллизация слитков происходит из жидкого состояния, в котором обеспечивается гомогенное распределение элементов Mo–Nb–Ta–(Cr, V, Zr, Hf). Выявлено, что фазовый состав синтезируемых слитков ТВЭС зависит от сплавляемых компонентов. При совместном восстановлении металлов V (Nb, Ta, V) и VI (Cr, Mo) групп формируются практически однофазные сплавы, имеющие кристаллическую структуру ОЦК, характерную для металлов этих групп. Введение в 4-компонентный сплав MoNbTaCr элементов Zr и Hf, имеющих гексагональную кристаллическую структуру, приводит к существенному изменению фазового состава слитков с рефлексами ОЦК-фазы на дифрактограмме, где присутствуют интенсивные рефлексы ГЦК-фазы, а также слабые рефлексы двух ГПУ-фаз. Показано, что применение предлагаемого метода существенно упрощает сложную технологическую задачу по получению литых многокомпонентных ТВЭС заданного состава. Изучением окислительной стойкости полученных материалов установлено, что состав Mo–Nb–Ta–Cr–V наиболее перспективен для дальнейшего исследования и, в сравнении с другими составами, имеет хорошие показатели по жаростойкости, что делает данный материал конкурентоспособным для высокотемпературного использования.

Ключевые слова: самораспространяющийся высокотемпературный синтез (СВС), центробежная СВС-металлургия, СВС-системы термитного типа, высокоэнтропийные сплавы (ВЭС), сплавы на основе тугоплавких металлов, получение полиметаллических сплавов, окислительная стойкость ВЭС

Благодарности: Работа выполнена за счет гранта Российского научного фонда № 24-13-00065, https://rscf.ru/project/24-13-00065/

Для цитирования: Санин В.Н., Икорников Д.М., Сивакова А.О., Ковалев Д.Ю., Силяков С.Л., Панова М.Д. Синтез высокоэнтропийных сплавов на основе тугоплавких металлов Mo–Nb–Ta–(Cr, V, Zr, Hf) методами центробежной СВС-металлургии и исследование их окислительной стойкости. *Известия вузов. Порошковая металлургия и функциональные покрытия*. 2025;19(5):17–35. https://doi.org/10.17073/1997-308X-2025-5-17-35

Introduction

Since the first studies published in 2004 [1; 2], a new paradigm based on multicomponent alloy design has been introduced into materials science, laying the foundation for the development of a novel class of metallic materials. These materials, referred to as high-entropy alloys (HEAs), have remained the focus of intense research interest over the past two decades. In addition to their multicomponent nature, a defining feature of HEAs is their tendency to form predominantly single-phase, thermodynamically stable, disordered substitutional solid solutions with high-symmetry crystal lattices – typically face-centered cubic (FCC) or body-centered cubic (BCC) [3–6].

Initial investigations proposed that the high configurational entropy of mixing, arising from the pre-

sence of multiple principal elements in equiatomic or near-equiatomic ratios, would favor the formation of disordered solid solutions over ordered intermetallic phases. As a result, these high-entropy solid solutions were expected to simultaneously exhibit high strength and sufficient ductility. However, subsequent studies revealed that entropy alone is not always the dominant factor governing the formation of disordered solid solutions in real alloy systems. It has since been established that the phase composition of HEAs is determined primarily by the specific atomic properties of the constituent elements rather than their number [7–12].

It is anticipated that HEAs will surpass the performance of conventional commercial structural alloys [13–16] owing to rational composition design (including deviations from strict equiatomicity) and the development of advanced microstructural control tools, such as novel synthesis techniques and post-processing via thermal or mechanical treatments. Numerous HEAs have already been identified that exhibit superior physicochemical properties compared to traditional alloys [4; 7; 11–17].

Among the various families of HEAs [18], a special place is held by refractory high-entropy alloys (RHEAs), which are designed for high-temperature service and are composed mainly of high-melting-point elements such as niobium (Nb), molybdenum (Mo), tantalum (Ta), tungsten (W), rhenium (Re), and hafnium (Hf) [14; 18–23]. Refractory metals are known for their high strength and resistance to deformation at elevated temperatures, making them ideal candidates for the development of RHEAs.

Early studies [22; 23] reported that BCC-structured RHEAs such as NbMoTaW and VNbMoTaW demonstrate good strengthening behavior at room temperature and structural stability up to 1400 °C. Remarkably, these alloys retained yield strengths of 405 and 477 MPa, respectively, even at 1600 °C, clearly indicating their promising potential for practical high-temperature applications. As a result, RHEAs are being actively explored for use in the aerospace and aviation industries, particularly for components in high-temperature gas turbine systems where there is a demand to increase operating temperatures beyond the limits of current nickel-based superalloys (up to 1100 °C) [24; 25].

The main drawbacks of the earliest RHEAs – based on refractory elements such as Mo, Nb, Ta, W, and V – were their very high density and low oxidation resistance [23]. To address these issues, subsequent efforts focused on substituting or partially replacing these elements with lighter and more accessible ones, such as Cr, Ti, Zr, Co, Mn, and Al [18; 26–38]. The incorporation of such elements improves specific strength, oxidation and corrosion resistance, thermal shock resistance, creep resistance, and high-temperature deformation behavior. Most RHEA studies to date have focused on understanding structure–property relationships, while comparatively little attention has been paid to developing new, effective synthesis methods that offer precise control over alloy composition and the designed distribution of structural constituents.

At the same time, expanding the range of elements used in RHEA design introduces significant technological challenges. These stem from the extremely high melting points of key components (e.g., W, Mo, Nb, Re, Hf), the large differences in melting temperatures between base and alloying elements (e.g., Al, Ti, V, Cr, Fe), and the high chemical reactivity of certain constituent elements, as well as other factors.

Numerous laboratory-scale methods have been proposed currently for RHEA synthesis [18; 38], including mechanochemical approaches (mechanical alloying, MA), combinations of MA with spark plasma sintering (SPS), electrochemical techniques [39], additive 3D manufacturing, and melting-based metallurgical processes. However, most of these methods share common drawbacks: the requirement for high-purity elemental feedstock, high energy consumption, and low productivity – factors that are acceptable for research purposes but not for industrial-scale production (with the exception of melting techniques). Among all available methods, casting remains the most promising for producing RHEAs [18; 38]. The most common techniques include vacuum arc remelting (VAR), vacuum induction melting (VIM), and, less frequently, electron beam melting (EBM). However, melting modes suitable for conventional alloys are inadequate for RHEAs. The presence of refractory elements (W, Mo, Ta, Nb, Hf) demands significantly higher temperatures and extended holding times in the molten state to ensure full intermixing and dissolution. To avoid elemental segregation and macrosegregation, multiple melting cycles (up to 5–6) are typically required. Furthermore, RHEAs produced via VAR often have relatively coarse grain structures (ranging from 100 to 300 μm), which limits the grain boundary strengthening effect.

We previously demonstrated the feasibility of synthesizing cast HEAs based on 3*d* metals (Co–Cr–Fe–Ni–Mn) using centrifugal SHS metallurgy [40; 41] – a direction within the broader, energy-efficient class of self-propagating high-temperature synthesis (SHS) technologies. Subsequently, *in situ* SHS was used to produce composite materials based on these HEAs, incorporating strengthening structural precipitates such as $Mo(Nb)_5SiB_2$, $Mo(Nb)_3Si$, and $MoSi_2$ [42].

The aim of the present study was to investigate the possibility of synthesizing cast RHEAs based on the Mo–Nb–Ta system alloyed with 3*d* metals (Cr, V, Zr, Hf, Ti) using centrifugal SHS metallurgy and to examine the influence of the alloying system on a key performance characteristic – oxidation resistance.

The ability to produce cast RHEAs without furnace equipment and high energy input offers significant potential for practical applications. SHS metallurgy relies on oxide raw materials (metal oxides) and the chemical energy released during highly exothermic reactions initiated in a combustion front through a compacted powder charge. The SHS process requires no external energy input. This approach may prove substantially more cost-effective than traditional melting of pure metals. Moreover, the high synthesis temperature (above 2300 °C) and the action of centrifugal forces (*g*-forces) enable enhanced dissolution of alloying components, improved metal reduction completeness, and more efficient separation of metallic and oxide phases [40–44].

1. Starting powder components and experimental scheme for RHEA synthesis

As previously demonstrated [40–44], the use of highly exothermic thermite-type SHS mixtures makes it possible to reach temperatures sufficient for producing reaction products in the molten state (above 2500 °C), and thereby obtain the synthesized material in a cast form, including cast HEAs [40–42].

The synthesis was carried out using thermite-type SHS systems containing powder oxides of the target elements (MoO_3, Nb_2O_5, Ta_2O_5, Cr_2O_3, V_2O_5, TiO_2), Zr–Mo and Hf–Mo master alloys, a metallic reducing agent (Al), and functional additives (fluxing agents CaO and CaF_2). Selected characteristics of the primary powder reagents used are listed in Table 1.

All starting oxide powders were pre-dried to remove adsorbed moisture in SNOL-type drying ovens (t = 90 °C, τ = 1 h). After weighing the components (calculated to achieve the target alloy composition), the reagents were mixed in an MP4/5.0 planetary mill with a drum volume of up to 5 L for 15–20 min at a ball-to-charge mass ratio of 1:10. The elements Zr and Hf were introduced into the reaction mixture in the form of Zr–Mo and Hf–Mo master alloys, custom-fabricated for this purpose.

The charge composition was determined based on the stoichiometry of the following main reactions:

$$MoO_3 + 2Al = Mo + Al_2O_3, \quad (1)$$

$$3Nb_2O_5 + 10Al = 6Nb + 5Al_2O_3, \quad (2)$$

$$3Ta_2O_5 + 10Al = 6Ta + 5Al_2O_3, \quad (3)$$

$$Cr_2O_3 + 2Al = 2Cr + Al_2O_3, \quad (4)$$

$$3V_2O_5 + 10Al = 6V + 5Al_2O_3, \quad (5)$$

$$3TiO_2 + 4Al = 3Ti + 2Al_2O_3. \quad (6)$$

The experiments used powder charges designed to produce five alloy compositions (S1–S5), as shown in Table 2.

Table 1. **Selected characteristics of the primary powder components**

Таблица 1. **Некоторые характеристики основных исходных порошковых компонентов**

Component	Grade	GOST/Technical specification (TU)	Particle size	Chemical composition, wt. %
MoO_3	Analytical reagent (ChDA)	TU 6-09-01-269-85	–	99.9
Nb_2O_5	Extra pure (OSCh (8-2))	TU 6-09-4047-86	–	99.9
Ta_2O_5	–	TU 48-4-408-78	<70 μm	99.9
Cr_2O_3	Pure (Ch)	TU 6-09-4272-84	<20 μm	99.0
V_2O_5	–	TU 6-09-4093-75	–	–
TiO_2	–	TU 6-09-2166-77	–	99.8
Zr–Mo	–	Custom-made	<3 mm	Zr – 40.0 Mo – balance
Hf–Mo	–	Custom-made	<3 mm	Hf – 40.0 Mo – balance
Al	Aluminum powder (PA-4)	GOST 60-58-73	<130 μm	98.8

When Zr–Mo and Hf–Mo master alloys were introduced into the charge, the composition was adjusted based on the total molybdenum content. Aluminum served as the reducing agent, while CaO and CaF_2 were used as fluxing additives. The required amount of flux to bind Al_2O_3 and form a low-melting-point slag system during melting was calculated from the total amount of aluminum oxide generated in reactions (1)–(6). The mass of the starting mixture was constant across all experiments and amounted to 600 g. The concentration of the added flux varied from 2 to 5 wt. %. To synthesize the alloys in combustion mode, hollow cylindrical refractory molds made of sintered electrolytic corundum (Al_2O_3) were used. These molds had an inner diameter of 80 mm and a height of 170 mm and were pre-dried for at least 1 h at 90 °C. During the filling process, the powder charge (500 g) was compacted by vibration into the mold. The loaded mold was then placed on the rotor of a centrifugal SHS setup. Combustion synthesis of the prepared mixtures was carried out in a custom-designed centrifugal SHS unit [43; 45], specifically developed for producing cast materials via centrifugal SHS metallurgy. It was previously shown [43] that the optimal range of centrifugal acceleration (hereinafter referred to as overload) for synthesizing alloys based on refractory metals is between 55 and 65*g*.

To generate the required centrifugal acceleration, the rotor was driven by an electric motor to a preset rotational speed, producing a *g*-force within the specified range. The reaction mixture was then ignited using a short laser pulse focused on the sample surface. Combustion proceeded at a constant rotor speed in an open-type reaction mold under atmospheric pressure. The combustion temperature exceeded 3000 K, which was higher than the melting points of the final products. After the reaction, the molten products (the alloy and the alumina-based slag) separated due to their mutual immiscibility and the action of centrifugal forces and then solidified upon cooling. Cooling of the reaction mass was forced through a water-cooled jacket of the reaction chamber. The combustion products formed a two-layer ingot with a well-defined interface. The upper part of the ingot (slag layer) consisted of fused corundum, while the lower part was the target RHEA alloy.

Table 2. **Calculated chemical composition, wt. %**

Таблица 2. **Расчетный химический состав, мас. %**

Composition	Mo	Nb	Ta	Cr	V	Zr	Hf
S1	34.35	33.26	32.39	–	–	–	–
S2	31.46	30.47	28.77	9.30	–	–	–
S3	28.29	27.39	25.69	13.06	5.57	–	–
S4	23.30	22.57	35.16	10.10	–	8.87	–
S5	21.82	22.82	32.92	9.46	–	–	12.98

The application of overload during the combustion stage of thermite-type SHS mixtures made it possible to significantly reduce, or even completely suppress, the dispersion of combustion products. It also ensured intensive mixing of the high-temperature melt behind the combustion front, enabling high conversion of the starting mixture directly within the combustion zone. The action of overload during the gravitational separation and subsequent cooling stages led to a high yield of the metallic phase in the ingot – approaching the theoretical value – and facilitated the removal of gaseous reaction products. In addition, overload promotes homogeneous distribution of the chemical elements throughout the volume of the resulting ingot, which is critically important for the synthesis of multimetallic alloys. The combustion process was recorded using a video camera mounted on the rotor of the centrifugal SHS setup.

Phase composition was analyzed using an ARL X'TRA *X*-ray diffractometer. Elemental distribution within the structural constituents of the synthesized RHEAs, as well as energy-dispersive spectroscopy (EDS) analysis, were performed using a Zeiss Ultra Plus ultra-high-resolution field emission scanning electron microscope (based on the Ultra 55 platform), equipped with an EDS detector capable of generating elemental mapping across the sample surface.

2. Results and discussion

2.1. Thermodynamic analysis

An important parameter in the development of SHS system formulations is the thermodynamic assessment of the maximum achievable synthesis temperature (adiabatic temperature) at various ratios of starting components. This evaluation helps determine the range of component ratios that meet the necessary conditions for obtaining cast final synthesis products. One such condition is that the adiabatic temperature of synthesis must exceed the melting points of the final and intermediate reaction products. It is important to note that the calculated combustion temperature is always somewhat higher than the actual experimental synthesis temperature. This discrepancy arises from heat losses due to thermal exchange with the mold material, incomplete chemical reactions (i.e., partial conversion of the reactants), shifts in component concentrations caused by partial gas evolution (primarily suboxides), and possible ejection of reaction products during

the high-temperature interaction of the initial components in the combustion front.

To theoretically assess the maximum achievable synthesis temperature (adiabatic temperature) as a function of the initial component ratios, a thermodynamic analysis of the synthesis processes was performed using the THERMO software package developed at ISMAN. This software allows thermodynamic equilibrium calculations in complex multicomponent heterophase systems. It includes a database of thermodynamic data for equilibrium calculations and features a function for adding data for new compounds [46; 47]. The calculation results include the equilibrium composition of reaction products (both condensed and gaseous) and the adiabatic temperature. The software enables thermodynamic calculations under isobaric, isochoric, or isothermal conditions, depending on the selected mode. The studied systems can be either gas-free or contain any amount of gaseous phase.

The results of the thermodynamic analysis of the adiabatic temperature (T_{ad}) and the total concentrations of the gas (gas), metallic (ingot), and oxide (oxide) phases in the reaction products for the investigated systems S1–S5 (see Table 2) are presented in Fig. 1.

Analysis of the obtained data revealed that for systems S1–S3, the combustion temperature of the mixtures can reach or exceed 3000 K (3427–2935 K), which is higher than the melting points of all alloy components (T_{melt}, K: Nb – 2741, Mo – 2896, Cr – 2163, Zr – 2125, V – 2170, Hf – 2506), with the exception of tantalum (Ta – 3290 K). However, the presence of a high-temperature liquid phase formed by these components is likely to promote rapid dissolution of finely dispersed solid-phase tantalum particles that form in the combustion front. In the case of system S5, the adiabatic combustion temperature is somewhat lower (T_{ad} = 2890.8 K), which may result in Ta and Nb remaining partially in the solid state. Nonetheless, as in the previous systems, the presence of molten phases from other alloy components should enable their rapid and complete dissolution in the resulting alloy ingot. This assumption will be tested in the experimental section of this study.

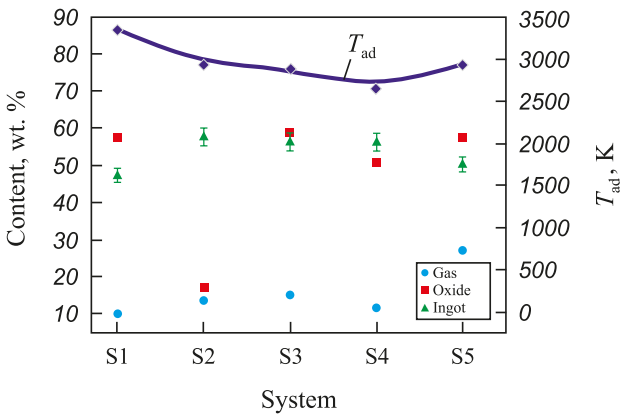

Fig. 1. Thermodynamic analysis of the adiabatic temperature (T_{ad}) and the relative amounts of gaseous, metallic, and oxide phases in the combustion products for systems S1–S5

Рис. 1. Термодинамический анализ адиабатической температуры ($T_{ад}$) и соотношения в продуктах горения газовой, металлической и оксидной фаз для систем S1–S5

Across all the studied systems, the mass fractions of oxide and metallic phases vary only slightly (see Fig. 1), which is a favorable factor for their comparative evaluation in the experimental work.

The analysis of the calculated adiabatic temperatures and component concentrations under thermodynamic equilibrium conditions showed that the combustion temperature can reach up to 3427 K for systems S1–S3 (see Table 2), and up to 2935 K for system S5. Thus, it can be concluded that there are no thermodynamic limitations to producing cast materials in the studied systems (S1–S5); the combustion temperatures are sufficient to obtain materials with the desired (target) composition.

2.2. Effect of centrifugal acceleration (overload) on the composition and microstructure formation of RHEAs

As shown in previous studies [40–44], the level of overload can have a significant impact on the macroscopic kinetics of the synthesis process and, consequently, on the resulting composition and microstructure of cast alloys. In the case of alloys based on refractory metals, the lifetime of the high-temperature melt in its liquid state is relatively short, as these systems have considerably higher crystallization temperatures compared to transition-metal-based alloys. Therefore, to ensure proper formation of the ingot in the bottom part of the mold, it is essential to accelerate the phase separation between the metallic (ingot) and oxide (Al_2O_3-based corundum) phases. The most effective way to achieve this is by applying centrifugal forces generated by centrifugal SHS units during both the combustion stage and the phase separation of synthesis products.

Fig. 2 presents data for the base system S1 (Mo, Nb, Ta), showing how the combustion rate (U_c), the metallic phase yield in the ingot (η_1), and the loss of combustion products due to dispersion (η_2) depend on the applied centrifugal acceleration g. The results clearly demon-

strate that the combustion rate of the base composition increases significantly under overload, particularly in the range of 1 to 50*g*. Notably, the metallic phase yield also increases within this range, approaching a saturation level at values exceeding 100*g*. These findings indicate that applying overloads in the range of 50 to 100*g* is optimal for synthesizing the studied alloys.

Visual examination of the resulting samples confirmed that all of them exhibited a cast structure. Applying an overload greater than 50*g* ensured the formation of ingots with well-defined phase separation. At overloads below 50*g*, the ingots developed an irregular macrostructure, with gas inclusions observed in their upper sections. As a result, an overload of 60*g* was selected for synthesizing the target compositions S2–S5.

Video analysis of the combustion process for S2–S5 showed no significant increase (exceeding 15 %) in the combustion rate.

2.3. Chemical and phase analysis of the synthesized RHEAs

The cast RHEA samples (S1–S5), after removal from the refractory mold, were sectioned transversely and subjected to analysis. Elemental composition analysis (Table 3), performed by *X*-ray fluorescence spectroscopy, confirmed the presence of the target elements Mo, Nb, Ta, Cr, V, Zr, and Hf in the synthesized alloys. The deviation of their concentrations from the calculated values did not exceed 1 wt. %. It should be noted that the use of Zr–Mo and Hf–Mo master alloys helped minimize the interaction of chemically active components (Zr and Hf) within the combustion front, thus enabling their incorporation into the alloy at concentrations close to the theoretical values.

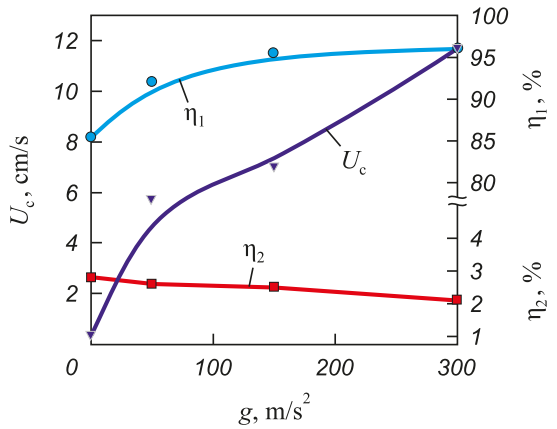

Fig. 2. Effect of overload (g) on the combustion rate (U_c), the yield of the metallic phase in the ingot (η_1), and the combustion product loss (η_2) for the base S1 system (see Table 2)

Рис. 2. Влияние величины перегрузки (g) на скорость горения ($U_г$), полноту выхода металлической фазы в слиток (η_1) и величину потерь продуктов горения (η_2) для базовой системы S1 (см. табл. 2)

For comparative analysis, a binary Mo–Nb alloy designated as S0 was synthesized. The *X*-ray diffraction patterns of the RHEA samples (S0–S5) are shown in Fig. 3.

The results of *X*-ray diffraction (XRD) analysis for the S0–S5 alloys are summarized in Table 4. The phase composition of the metallic ingots depends on the specific combination of alloying elements. The co-reduction and subsequent alloying of group V metals (Nb, Ta, V) with group VI metals (Cr, Mo) result in the formation of nearly single-phase alloys with a body-centered cubic (BCC) crystal structure, which is typical for these elements. It is well established that one of the key conditions for the formation of a single-phase solid solution is that the constituent metals share the same crystal structure type.

The XRD pattern of the binary S0 (Mo + Nb) alloy (Fig. 3) confirms the formation of the MoNb phase (space group *Im*-3*m*, PDF2 card #65-5786). Indeed, the Mo–Nb binary system exhibits unlimited mutual solubility and conforms to the Hume–Rothery rules for the formation of substitutional solid solutions. A small amount of impurity phases, such as Al_2O_3 and NbO, was also detected, likely due to incomplete phase separation during ingot formation.

The addition of a third component (Ta) to alloy S1 also results in the formation of a BCC solid solution phase, MoNbTa. The diffraction peaks of this phase are shifted toward lower angles, indicating an increase in its unit cell parameter compared to the binary MoNb solid solution. This increase is attributed to the larger atomic radius of Ta (1.430 Å) relative to Mo (1.362 Å) and Nb (1.429 Å) [14]. Weak diffraction peaks of the $Al_2Nb_3Mo_3$ phase with a cubic structure (space

Table 3. **Chemical composition of synthesized RHEAs ingots (wt. %)**

Таблица 3. **Химический состав синтезированных слитков ТВЭС (мас. %)**

Alloy	Mo	Nb	Ta	Cr	V	Zr	Hf
S0	50.8	49.2	–	–	–	–	–
S1	34.7	33.4	31.9	–	–	–	–
S2	31.9	30.9	28.1	9.1	–	–	–
S3	28.6	27.9	25.1	12.7	5.7	–	–
S4	23.7	22.8	35.2	9.7	–	8.6	–
S5	22.5	23.6	32.2	9.3	–	–	12.4

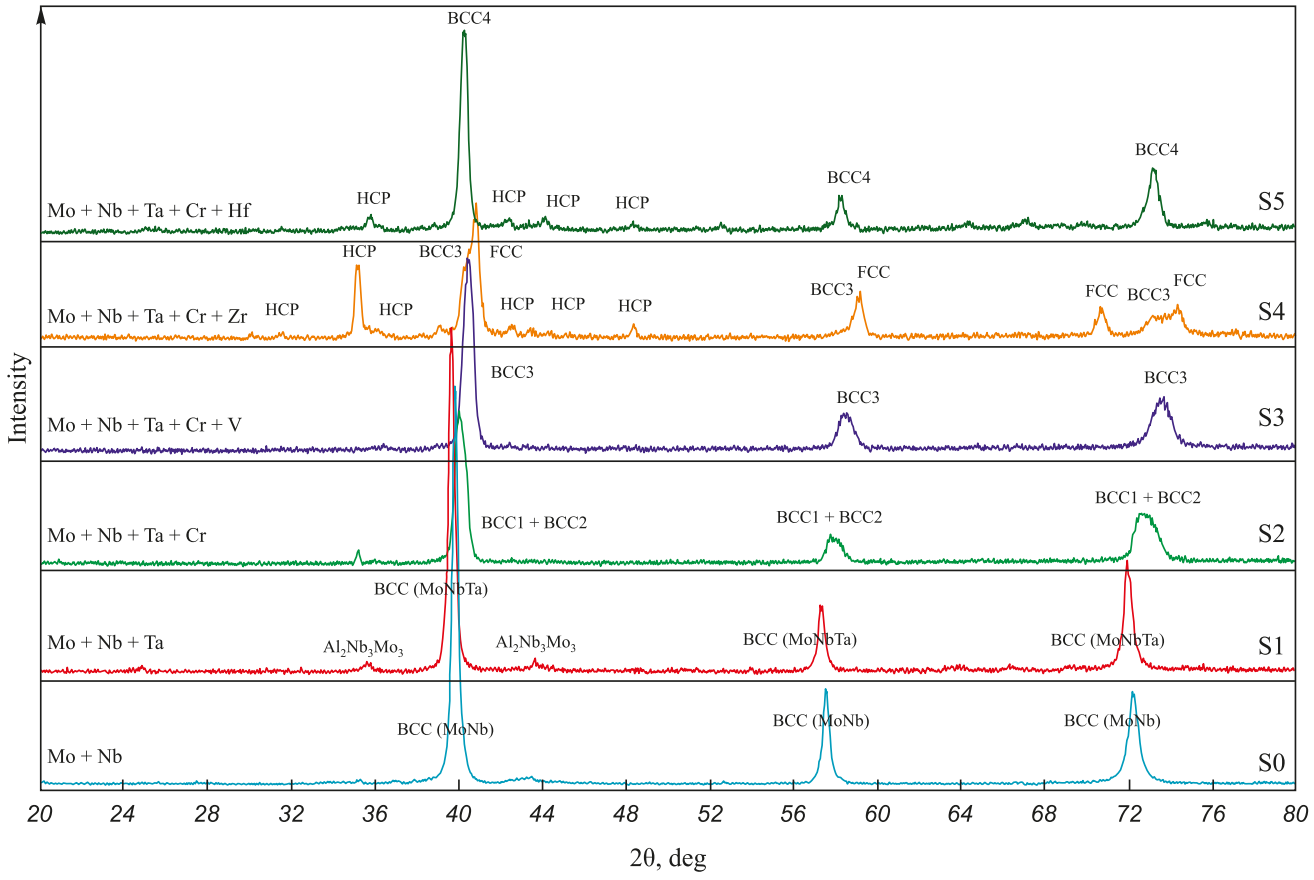

Fig 3. XRD patterns of the synthesized RHEA samples (S0–S5)

Рис. 3. Дифрактограммы синтезированных образцов ТВЭС (S0–S5)

Table 4. **Phase composition of RHEAs ingots**

Таблица 4. **Фазовый состав слитков ТВЭС**

Alloy	Main phases	Secondary phases	Impurity phases
S0	MoNb	–	Al_2O_3, NbO
S1	MoNbTa (BCC solid solution)	$Al_2Nb_3Mo_3$	–
S2	MoNbTaCr (BCC1 + BCC2 solid solution)	–	TaO
S3	MoNbTaCrV (BCC3 solid solution)	–	NbO
S4	MoNbTaCrZr (FCC + BCC3 solid solution)	HCP	–
S5	MoNbTaCrHf (BCC4 solid solution)	HCP	–

group *Pm*-3*n*, PDF2 card #65-4465) are also observed in the XRD pattern of alloy S1 (Fig. 4).

The addition of a fourth component (Cr) to alloy S2 leads to the formation of two BCC solid solution phases with similar unit cell parameters, designated as BCC1 and BCC2 in Fig. 3. The corresponding diffraction peaks are significantly broadened due to the overlap of reflections from both phases. Notably, the peaks are shifted toward higher angles, indicating a reduction in the unit cell parameter. This can be attributed to the presence of Cr in the solid solution, as Cr has a substantially smaller atomic radius (1.249 Å) than the other elements in the alloy. The difference in unit cell parameters between BCC1 and BCC2 suggests varying Cr content in the two phases, as confirmed by the microanalysis data shown in Fig. 5. Crystallization occurs from the melt, where a homogeneous distribution of Mo, Nb, Ta, and Cr is established. It is likely that the two-phase structure forms over a temperature range in which the Cr-depleted, refractory-rich phase (Mo–Nb–Ta) solidifies first, followed by a Cr-enriched, lower-melting phase. It is known that in multicomponent systems, the formation of a single-phase solid solution requires that the atomic radius

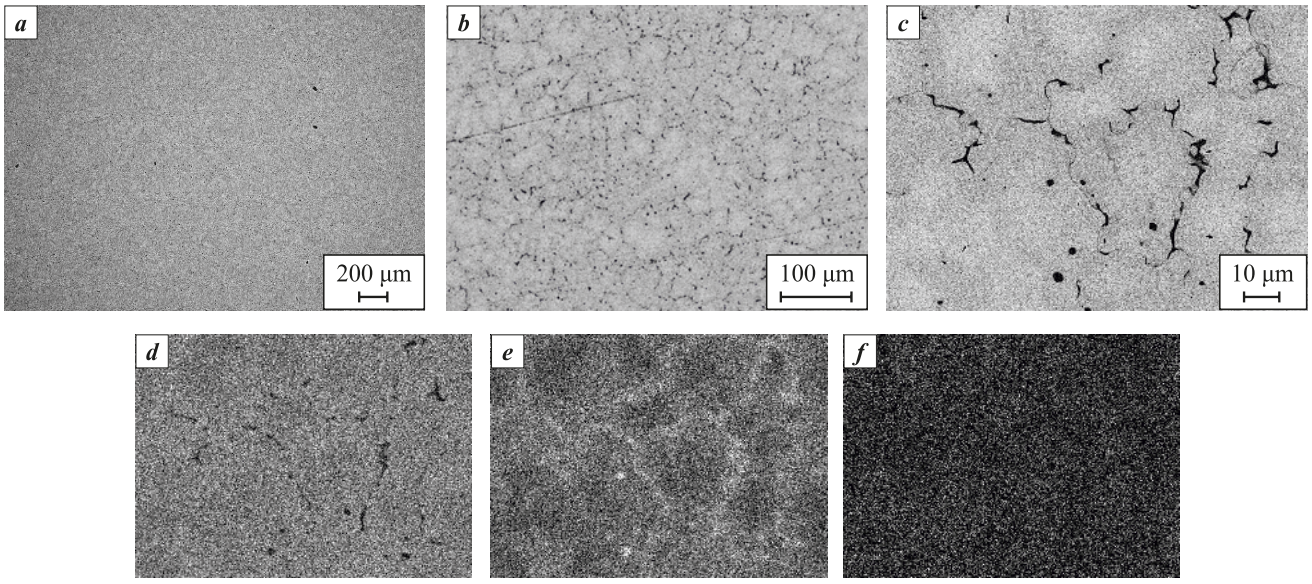

Fig. 4. Microstructure of alloy S1 (***a***, ***b***) and elemental distribution maps of the obtained alloy (***c***–***f***)
c – combined image of elemental distribution map, ***d*** – Mo, ***e*** – Nb, ***f*** – Ta

Рис. 4. Микроструктура сплава состава S1 (***a***, ***b***) и карты распределения элементов полученного сплава (***c***–***f***)
c – комбинированное изображение карты распределения элементов, ***d*** – Mo, ***e*** – Nb, ***f*** – Ta

difference between constituent elements not exceed 4 %. This condition is not met with Cr addition, which explains the formation of a two-phase alloy.

Introducing a fifth component (V) into alloy S3 results in the formation of a group of BCC phases, collectively referred to as BCC3 in the XRD pattern. The observed reflections are symmetric but significantly broadened, indicating the presence of multiple BCC phases with different elemental compositions and corresponding unit cell parameters. Although the atomic radius of V (1.316 Å) is larger than that of Cr, the criteria for single-phase formation are still not satisfied. The peak shift toward higher angles is the most pronounced in this alloy, suggesting that the average unit

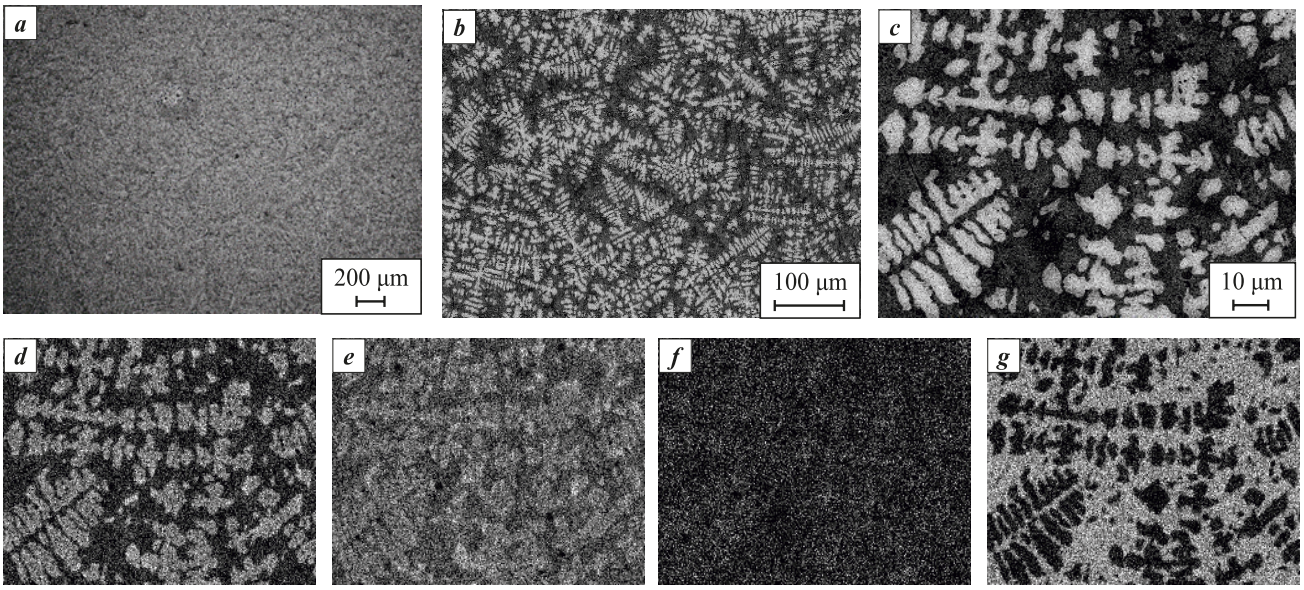

Fig. 5. Microstructure of alloy S2 (***a***, ***b***) and elemental distribution maps of the obtained alloy (***c***–***g***)
c – combined image of elemental distribution map, ***d*** – Mo, ***e*** – Nb, ***f*** – Ta, ***g*** – Cr

Рис. 5. Микроструктура сплава состава S2 (***a***, ***b***) и карты распределения элементов полученного сплава (***c***–***g***)
c – комбинированное изображение карты распределения элементов, ***d*** – Mo, ***e*** – Nb, ***f*** – Ta, ***g*** – Cr

cell parameter of the BCC phases in the five-component system is the lowest among the MoNb, MoNbTa, and MoNbTaCr alloys.

The addition of group IV elements (Zr and Hf), which have a hexagonal crystal structure, to the four-component alloy S2 (MoNbTaCr) causes significant changes in the phase composition of alloys S4 and S5, respectively. In the Zr-containing five-component alloy S4, the XRD pattern shows, in addition to BCC reflections, strong peaks of an FCC phase (space group *Fm*-3*m*) and weak peaks of two hexagonal (HCP) phases (space groups *P*-6*m*2 and $P6_3/mmc$). The PDF2 Realize 2022 diffraction database does not list compounds containing these elements in the observed combinations with these specific space groups. For the Hf-containing alloy S5, intense reflections of a BCC4 phase are observed, with angular positions close to those of the BCC3 phase, indicating similar unit cell parameters. As in the Zr-containing alloy, weak reflections of two HCP phases are also present. Clearly, the formation of multiphase structures in alloys S4 and S5 is a result of the differing crystal structures of the alloying elements – BCC for group V and VI metals (Mo, Nb, Ta, Cr) and HCP for group IV metals (Zr and Hf). Moreover, the atomic radii of Zr (1.603 Å) and Hf (1.578 Å) are significantly larger than those of the BCC-forming elements.

2.4. Microstructure of the synthesized RHEAs (S1–S5)

Microstructural analysis was performed on pre-polished cross-sections of the cast RHEA samples (S1–S5). Elemental distribution maps were obtained using energy-dispersive *X*-ray spectroscopy (EDS). The results are shown in Figs. 4–8.

Microstructural analysis of the cast RHEA samples (S1–S5) revealed that the addition of modifying elements (Cr, V, Zr, and Hf) leads to the formation of new structural features.

The base alloy S1 (Fig. 4, *a*, *b*) exhibits a fairly uniform elemental distribution, indicating a single-phase microstructure, which is consistent with the XRD results. Elemental mapping (Fig. 4, *c–f*) shows only slight Nb enrichment at the grain boundaries, a common characteristic of cast materials.

The introduction of Cr into the base composition (Fig. 5) causes noticeable structural changes in alloy S2. The micrographs reveal a two-phase microstructure, which agrees with the XRD data. This structure comprises two BCC solid solutions (see Fig. 3): one forms a Cr-rich matrix, and the other is a Mo-based dendritic phase.

With the addition of both Cr and V to the base alloy (Fig. 6), alloy S3 exhibits a similar dendritic structure. However, the dendrite arm size is slightly reduced, ranging from 5 to 10 μm.

The combined addition of Cr and Zr to the base composition leads to significant changes in the phase composition of alloy S4. According to the XRD data (Fig. 3), three distinct phases form: two BCC solid solutions and one FCC solid solution. However, microstructural examination (Fig. 7) shows two clearly distinguishable components: the first (Fig. 7, *c–h*, bright regions) exhibits an equiaxed grain structure and is based on a Mo–Ta solid solution, while the second forms an intergranular network enriched in Cr and Zr.

In the case of alloy S5, where both Cr and Hf are introduced, XRD analysis (Fig. 3) indicates the formation of a single-phase BCC solid solution. Microstructural observations (Fig. 8) confirm a relatively homogeneous distribution of the primary elements. Nevertheless, elemental mapping (Fig. 8, *c–h*) reveals localized Hf-rich precipitates with sizes of 3–5 μm. Chromium is present as dispersed intragranular particles and thin bands along grain boundaries.

The fine-dispersed microstructure observed in alloys S2–S5 is expected to contribute to enhanced mechanical properties.

The objective of this study did not include measuring the physicochemical or mechanical properties of the alloys, as the primary goal was to confirm the feasibility of synthesizing such RHEAs based on three refractory components (Mo–Nb–Ta) by centrifugal SHS metallurgy using oxide feedstock. This feasibility was successfully demonstrated, and the next stage of research will focus on establishing structure–property relationships.

2.5. Oxidation resistance of the synthesized alloys S2–S5

The oxidation resistance of the synthesized refractory high-entropy alloys (RHEAs) S1–S5 (see Table 2) was investigated under cyclic heating and holding at 1000 °C in an air atmosphere. It is worth noting that most studies on RHEA oxidation behavior are conducted under isothermal conditions. While such conditions are suitable for evaluating oxidation kinetics and mechanisms, they do not adequately simulate the repeated heating–cooling cycles that these materials typically experience in real-world service environments.

Disk-shaped samples with a diameter of 8 mm and a height of 4 mm were cut from the cast ingots using a GX-320L electrical discharge machine (CHMER

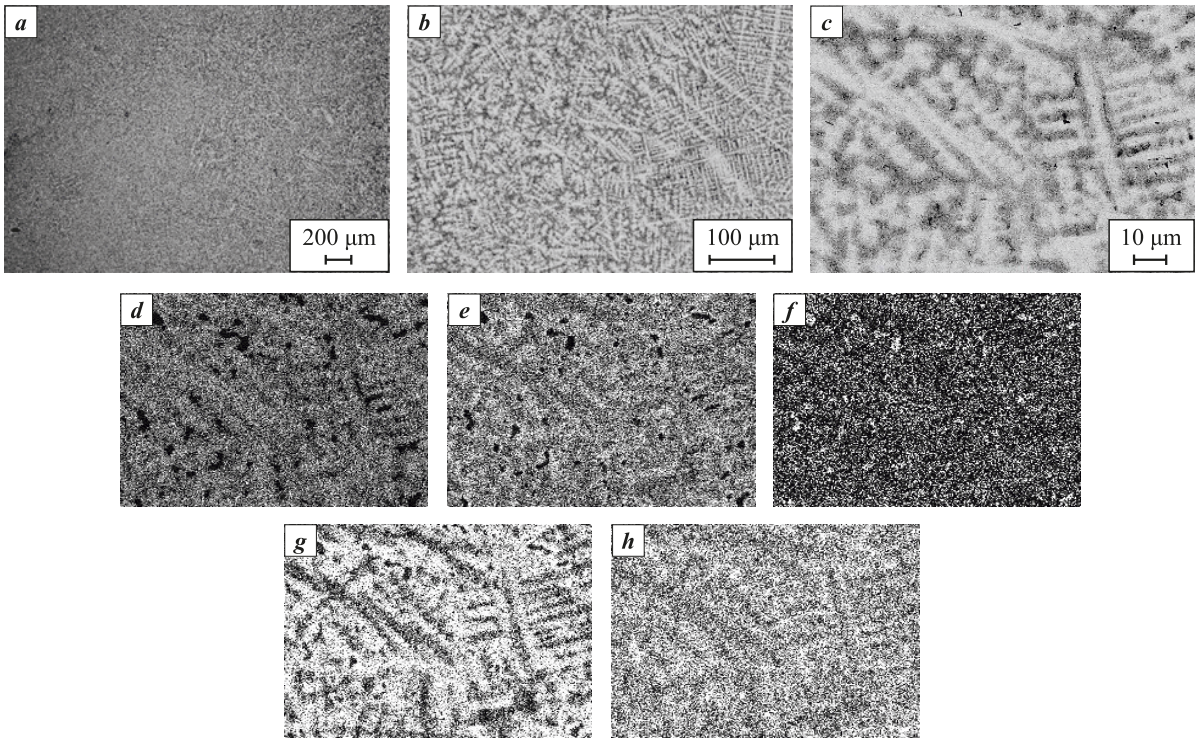

Fig. 6. Microstructure of alloy S3 (***a***, ***b***) and elemental distribution maps of the obtained alloy (***c***–***h***)
c – combined image of elemental distribution map, ***d*** – Mo, ***e*** – Nb, ***f*** – Ta, ***g*** – Cr, ***h*** – V

Рис. 6. Микроструктура сплава состава S3 (***a***, ***b***) и карты распределения элементов полученного сплава (***c***–***h***)
c – комбинированное изображение карты распределения элементов, ***d*** – Mo, ***e*** – Nb, ***f*** – Ta, ***g*** – Cr, ***h*** – V

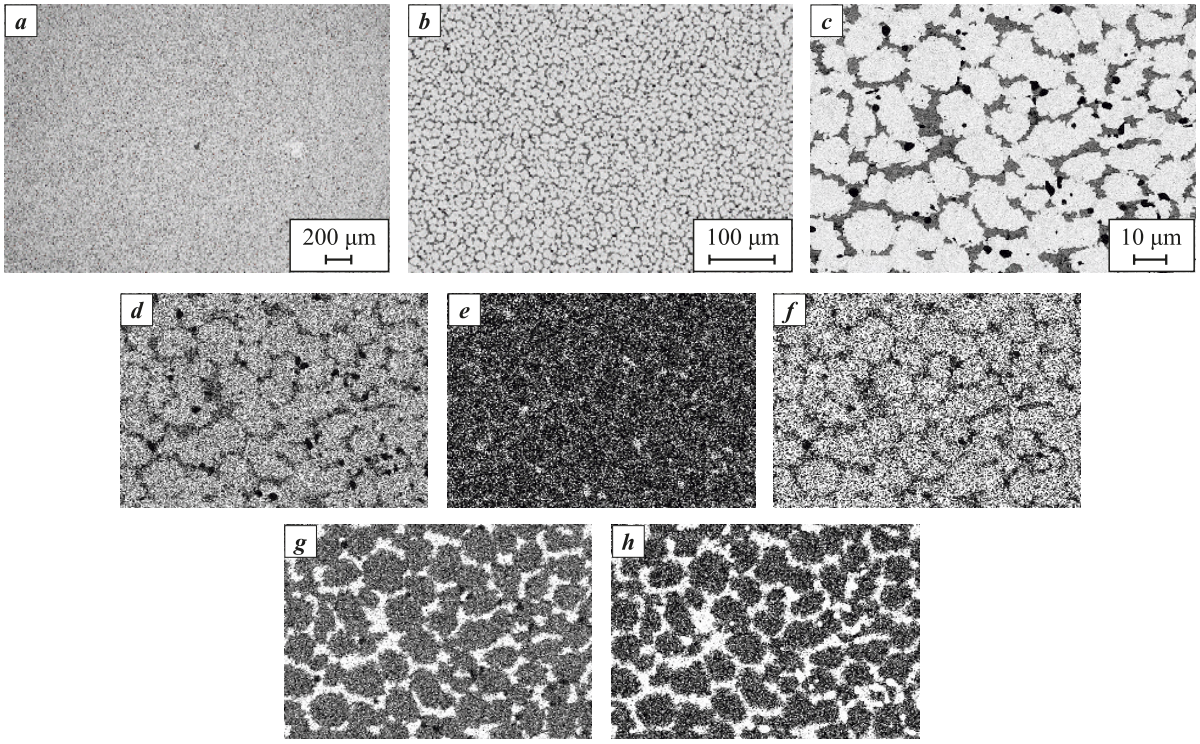

Fig. 7. Microstructure of alloy S4 (***a***, ***b***) and elemental distribution maps of the obtained alloy (***c***–***h***)
c – combined image of elemental distribution map, ***d*** – Mo, ***e*** – Nb, ***f*** – Ta, ***g*** – Cr, ***h*** – Zr

Рис. 7. Микроструктура сплава состава S4 (***a***, ***b***) и карты распределения элементов полученного сплава (***c***–***h***)
c – комбинированное изображение карты распределения элементов, ***d*** – Mo, ***e*** – Nb, ***f*** – Ta, ***g*** – Cr, ***h*** – Zr

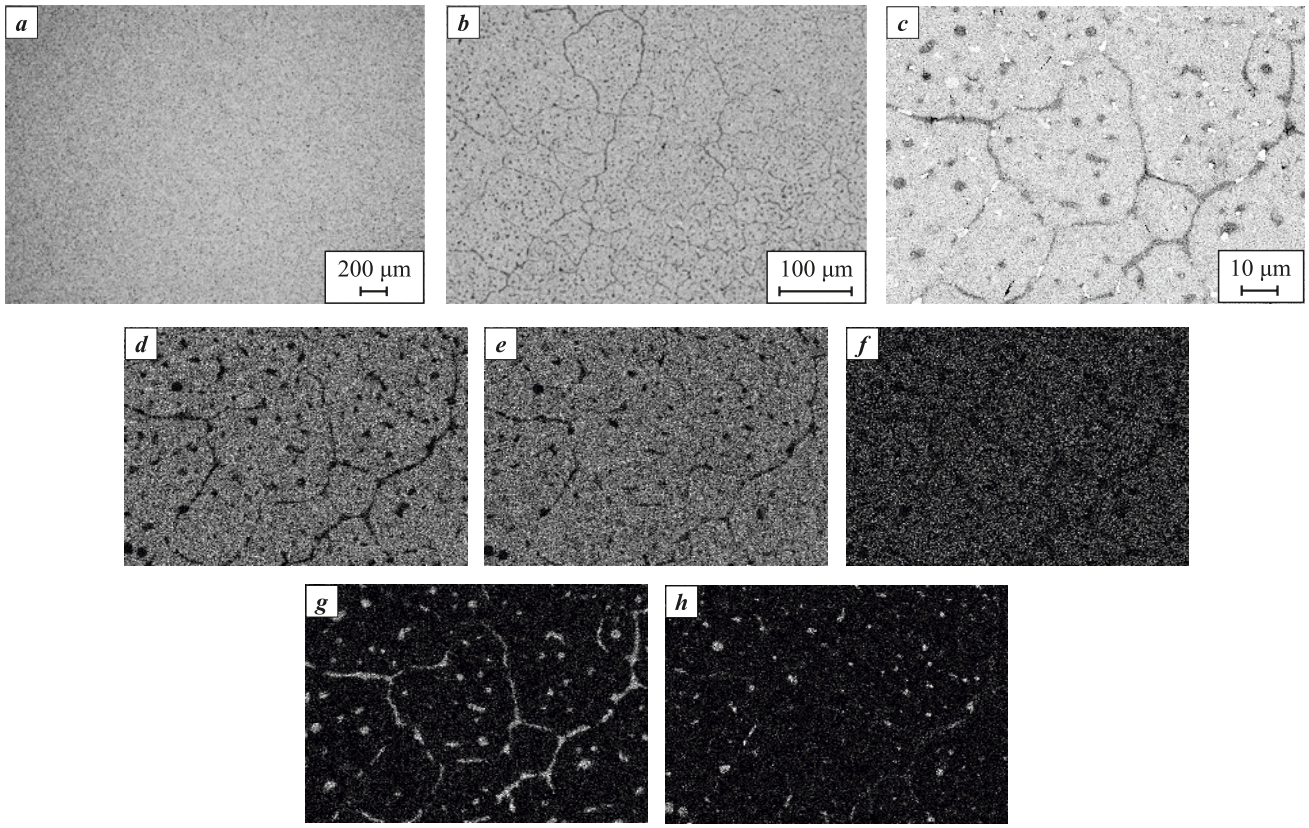

Fig. 8. Microstructure of alloy S5 (***a***, ***b***) and elemental distribution maps of the obtained alloy (***c***–***h***)
c – combined image of elemental distribution map, ***d*** – Mo, ***e*** – Nb, ***f*** – Ta, ***g*** – Cr, ***h*** – Hf

Рис. 8. Микроструктура сплава состава S5 (***a***, ***b***) и карты распределения элементов полученного сплава (***c***–***h***)
c – комбинированное изображение карты распределения элементов, ***d*** – Mo, ***e*** – Nb, ***f*** – Ta, ***g*** – Cr, ***h*** – Hf

EDM, China). The samples were then ground to a surface roughness of R_z = 5, followed by ultrasonic cleaning in isopropanol.

The oxidation annealing tests were carried out in a programmable muffle furnace. The samples were placed on alumina ceramic supports and arranged in a "cassette" fixture to enable convenient and rapid insertion/removal from the furnace. The cassette was loaded into a preheated furnace and held according to the following schedule: 30 min per cycle during the first hour, followed by 1 h cycles until a total annealing time of 10 h was reached. After each oxidation cycle, the samples were air-cooled to room temperature and weighed using an analytical balance with a precision of 0.1 mg. The mass gain per unit surface area over time was determined. Oxidation kinetics curves were constructed based on the experimental data. The appearance of the samples after 10 h of oxidation is shown in Fig. 9.

Visual examination revealed that the S1, S4, and S5 alloys underwent complete structural degradation. In contrast, the S2 alloy showed only partial loss of structural integrity, while the S3 alloy retained its original shape and developed only a dense oxide layer on its surface.

Since alloy S3 exhibited the lowest degree of oxidation, a cross-section of its sample was prepared to investigate the structure of the oxidized and transitional zones. The remaining samples were pulverized, and their powders were subjected to XRD analysis (Table 5). The results indicate that in the oxidized alloys S4 and S5, the primary oxidation product is the rutile-type phase $CrTaO_4$, which forms via a reaction between Cr_2O_3 and Ta_2O_5. According to the literature [48], unlike conventional oxides such as Al_2O_3 and Cr_2O_3 – which typically form dense, continuous surface layers during high-temperature oxidation of heat-resistant alloys – $CrTaO_4$ tends to form as discontinuous flakes. Although it does not prevent internal oxidation, it effectively hinders the outward diffusion of metallic cations. In contrast, another rutile-type oxide, $CrNbO_4$, is known to enhance oxidation resistance [49], which is consistent with our experimental observations: in alloy S2 (Mo–Nb–Ta–Cr), $CrNbO_4$ was identified as the predominant oxidation phase. As shown in Fig. 9, the S2 sample partially retained its shape, in contrast to the S1, S4, and S5 alloys.

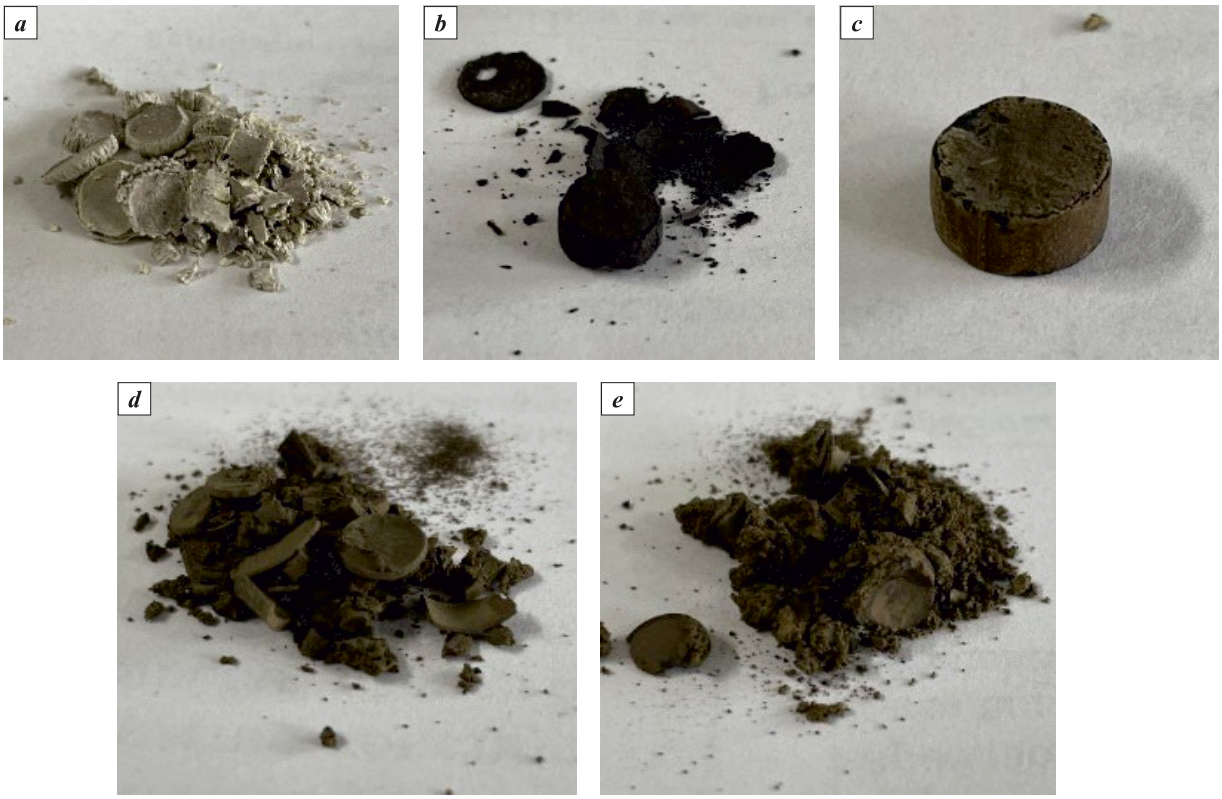

Fig. 9. Appearance of the tested RHEA samples after oxidation annealing (T = 1273 K, τ = 10 h)
a – S1 (Mo–Nb–Ta); ***b*** – S2 (Mo–Nb–Ta–Cr); ***c*** – S3 (Mo–Nb–Ta–Cr–V); ***d*** – S4 (Mo–Nb–Ta–Cr–Zr); ***e*** – S5 (Mo–Nb–Ta–Cr–Hf)

Рис. 9. Внешний вид испытуемых образцов ТВЭС после проведения окислительного отжига (T = 1273 К, τ = 10 ч)
a – S1 (Mo–Nb–Ta); ***b*** – S2 (Mo–Nb–Ta–Cr); ***c*** – S3 (Mo–Nb–Ta–Cr–V); ***d*** – S4 (Mo–Nb–Ta–Cr–Zr); ***e*** – S5 (Mo–Nb–Ta–Cr–Hf)

The mass change data for the tested samples are shown in Figs. 10 and 11. Analysis of these data revealed anomalous behavior in the single-phase base alloy S1 (Mo–Nb–Ta). This sample exhibited a significant mass loss during annealing (Fig. 10), especially within the first 5 h.

It is well established that Mo-based alloys are susceptible to oxidation at temperatures above 773 K due to the formation of volatile MoO_3. The Mo content in alloy S1 is the highest among all samples (34.35 wt. %), and notably, it lacks chromium, which can form protective complex oxides. As a result, the intense oxidation

Table 5. **Phase composition of oxidation products after annealing (T = 1273 K, τ = 10 h)**
Таблица 5. **Фазовый состав окисленных продуктов после отжига (T = 1273 К, τ = 10 ч)**

Alloy	Composition	Main phase	Secondary phases	Oxidation
S1	Mo–Nb–Ta	$MoTa_{12}O_{33}$ (PDF2 card #000-89-6894)	–	Complete
S2	Mo–Nb–Ta–Cr	$CrNbO_4$ (PDF2 card #000-81-0909)	$Mo_{13}O_{33}$ (PDF2 card #000-82-1930), MoNb (BCC, space group *Im*-3*m*, PDF2 card #000-65-5786)	Partial
S4	Mo–Nb–Ta–Cr–Zr	$CrTaO_4$ (PDF2 card #000-39-1428)	$TaZr_{2.75}O_8$ (PDF2 card #000-42-0060), $Mo_{13}O_{33}$ (PDF2 card #000-82-1930)	Complete
S5	Mo–Nb–Ta–Cr–Hf	$CrTaO_4$ (PDF2 card #000-39-1428)	$Nb_4Ta_2O_{15}$ (PDF2 card #000-15-0114), HfO_2 (PDF2 card #000-53-0560)	Complete

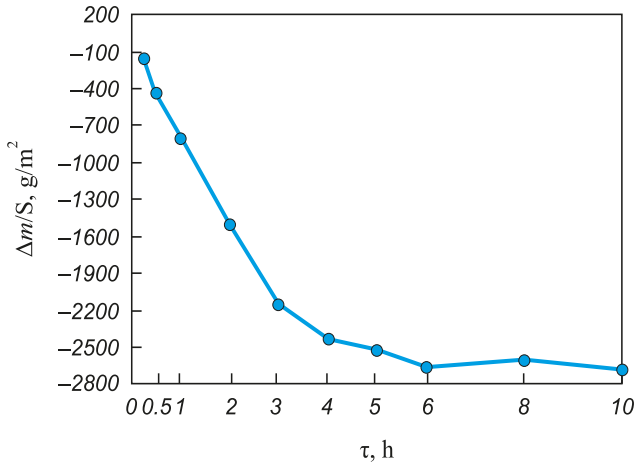

Fig. 10. Mass change of the S1 alloy (Mo–Nb–Ta) sample during oxidation annealing (T = 1273 K, τ = 10 h)

Рис. 10. Изменение массы испытуемого образца сплава S1 (Mo–Nb–Ta) при окислительном отжиге (T = 1273 K, τ = 10 ч)

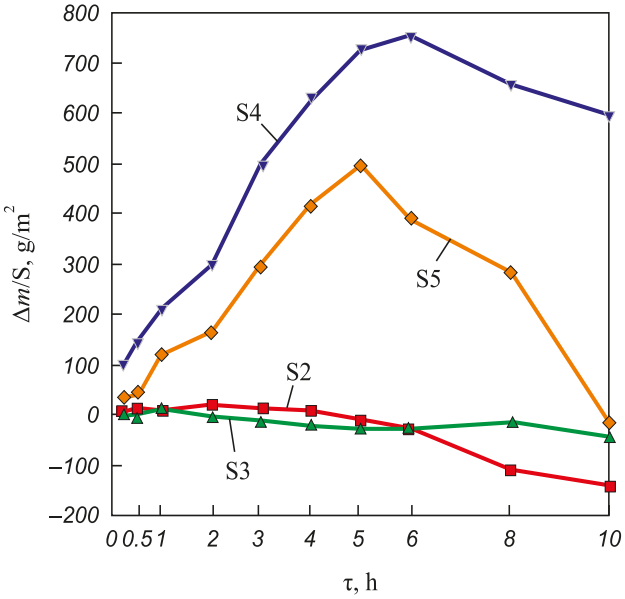

Fig. 11. Mass change curves for the S2–S5 alloy samples during oxidation annealing (T = 1273 K, τ = 10 h)

Compositions: Mo–Nb–Ta–Cr (S2); Mo–Nb–Ta–Cr–V (S3); Mo–Nb–Ta–Cr–Zr (S4); Mo–Nb–Ta–Cr–Hf (S5)

Рис. 11. Кривые изменения массы испытуемых образцов S2–S5 при окислительном отжиге (T = 1273 K, τ = 10 ч)

Составы: Mo–Nb–Ta–Cr (S2); Mo–Nb–Ta–Cr–V (S3); Mo–Nb–Ta–Cr–Zr (S4); Mo–Nb–Ta–Cr–Hf (S5)

of molybdenum leads to considerable mass loss due to the volatilization of Mo. This assumption is supported by the XRD data.

Analysis of the data presented in Fig. 11 shows that the oxidation behavior of the alloys varies both qualitatively (mass gain or loss) and quantitatively depending on their composition. Alloys S4 and S5 exhibited the greatest mass gain during the first 5 h of exposure; thereafter, a non-monotonic oxidation trend was observed, and at τ > 5 h, they began to lose mass. Among all tested samples, alloy S3 showed the smallest mass change, which made the investigation of its structure near the oxidation zone particularly relevant.

Microstructural analysis based on cross-sectional micrographs (Fig. 12) reveals that the interface between the oxidized layer and the bulk alloy is well defined. A distinct transition zone is practically absent. Elemental distribution data (Fig. 12, *c–h*) indicate that the most significant compositional change in the oxidized layer is observed for Mo, whose concentration is minimized due to the volatility of the molybdenum oxide. The other elements (Nb, Ta, Cr, and V), according to the XRD data, retain their concentrations while transitioning to oxidized states and forming complex oxides.

These findings suggest that the S3 alloy (Mo–Nb–Ta–Cr–V) is the most promising candidate for further research. Compared to other compositions reported in the literature, it demonstrates superior oxidation resistance [50]. With further optimization of the alloying system, its oxidation resistance could be improved even more, making this material a strong contender for high-temperature applications. As previously noted, oxidation resistance is just one of the key performance parameters for refractory high-entropy alloys (RHEAs), and future studies will aim to evaluate other relevant properties.

Conclusion

This study experimentally demonstrated the feasibility of producing cast refractory high-entropy alloys (RHEAs) by self-propagating high-temperature synthesis (SHS) metallurgy – one of the technological approaches within the SHS field. Using this method, cast RHEAs based on the Mo–Nb–Ta system, alloyed with 3d-transition metals (Cr, V, Zr, Hf), were obtained for the first time directly *in situ* via SHS. Microstructural analysis confirmed that all target elements were successfully incorporated and homogeneously distributed throughout the ingot volume. The overall elemental concentrations showed only minor deviations from the calculated chemical composition, indicating that the synthesis parameters were appropriately selected.

The introduction of modifying elements (Cr, V, Zr, and Hf) was found to induce the formation of new structural features, offering broad opportunities for tailoring the microstructure at the synthesis stage.

The experimental data confirm the potential of the investigated cast refractory high-entropy alloys (RHEAs) based on the Mo–Nb–Ta system and sup-

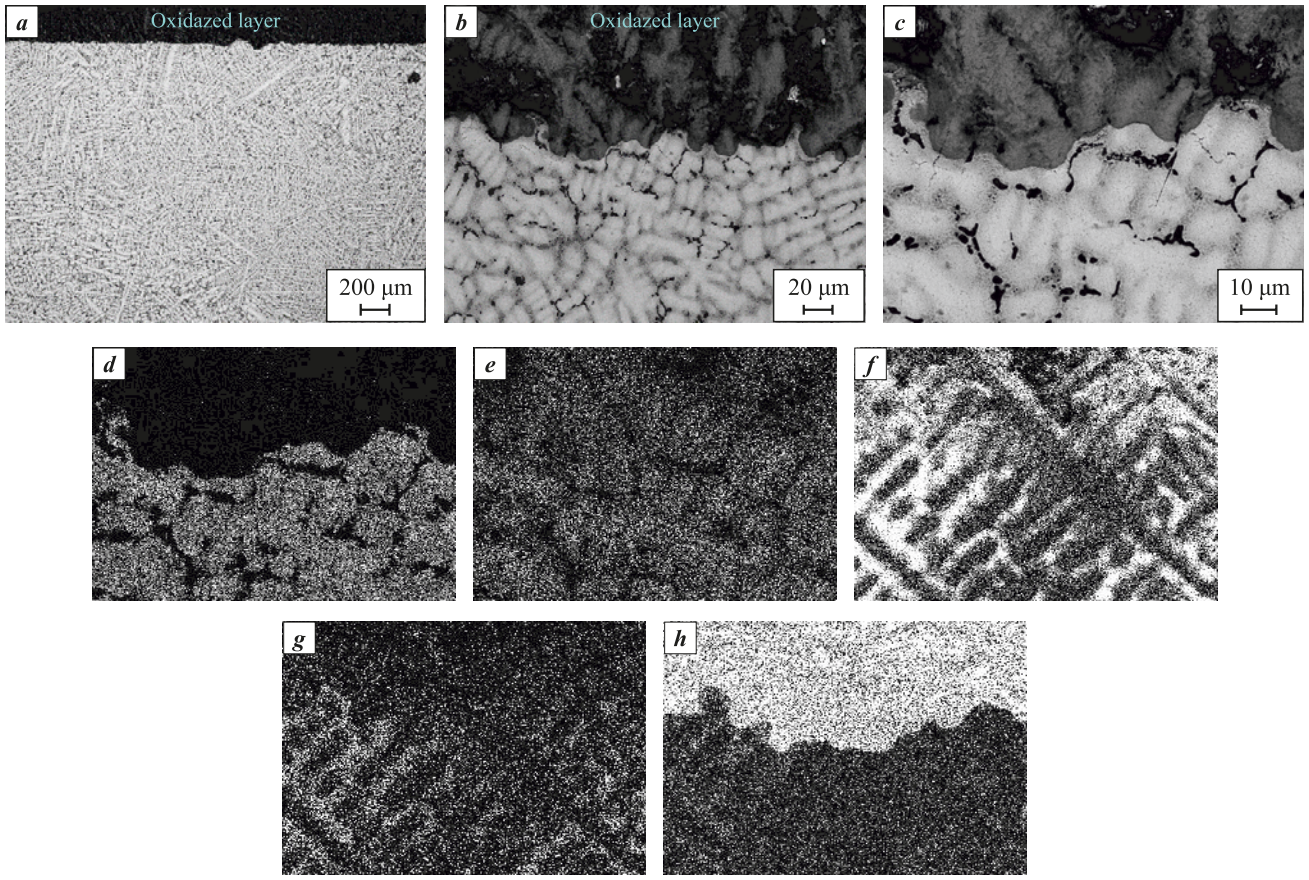

Fig. 12. Microstructure (***a***, ***b***) of the surface layer of alloy S3 (Mo–Nb–Ta–Cr–V) after annealing (T = 1273 K, τ = 10 h) and elemental distribution maps (***c***–***h***)

c – combined image of elemental distribution map,
d – Mo, ***e*** – Ta, ***f*** – Cr, ***g*** – V, ***h*** – O_2

Рис. 12. Микроструктура (***a***, ***b***) поверхностного слоя сплава S3 (Mo–Nb–Ta–Cr–V) после отжига (T = 1273 K, τ = 10 ч) и карты распределения элементов (***c***–***h***)

c – комбинированное изображение карты распределения элементов,
d – Mo, ***e*** – Ta, ***f*** – Cr, ***g*** – V, ***h*** – O_2

port the feasibility of the proposed alloy formation method via combustion synthesis using thermite-type SHS mixtures. This approach may serve as an effective alternative to energy-intensive vacuum electrometallurgical techniques. In light of increasingly stringent environmental regulations for metallurgical production – including the need for improved energy efficiency and reduced carbon footprint – the SHS-based centrifugal metallurgy method explored in this study fully aligns with these objectives.

It enables the production of cast RHEAs with high chemical homogeneity. The proposed method significantly simplifies the complex technological challenge of producing multicomponent cast RHEAs with controlled composition and targeted microstructural distribution. This can contribute to expanding the scientific basis for designing novel high-temperature metallic materials based on HEAs and for developing next-generation high-performance engineering systems.

Oxidation resistance testing revealed that alloy S3 (Mo–Nb–Ta–Cr–V) shows the greatest potential for further investigation. Compared to compositions reported by other researchers, it exhibited superior oxidation resistance, making it a promising candidate for high-temperature applications.

References / Список литературы

1. Cantor B., Chang I.T.H., Knight P., Vincent A.J.B. Microstructural development in equiatomic multicomponent alloys. *Journal of Materials Science and Engineering: A*. 2004;375–377:213–218. http://doi.org/10.1016/j.msea.2003.10.257
2. Yeh J.W., Chen S.K., Lin S.J., Gan J.Y., Chin T.S., Shun T.T., Tsau C.H., Chang S.Y. Nanostructured high-entropy alloys with multiple principal elements: Novel alloy design concepts and outcomes. *Advanced Engineering Materials*. 2004;6(5):299–303. https://doi.org/10.1002/adem.200300567

3. Yeh J.-W., Lin S.-J., Chin T.-S., Gan J.-Y., Chen S.-K., Shun T.-T., Tsau C.-H., Chou S.-Y. Formation of simple crystal structures in Cu–Co–Ni–Cr–Al–Fe–Ti–V alloys with multiprincipal metallic elements. *Metallurgical and Materials Transactions: A*. 2004;35A:2533–2536. https://doi.org/10.1007/s11661-006-0234-4
4. Otto F., Yang Y., Bei H., George E.P.P. Relative effects of enthalpy and entropy on the phase stability of equiatomic high-entropy alloys. *Acta Materialia*. 2013;61(7):2628–2638. https://doi.org/10.1016/j.actamat.2013.01.042
5. Zhang Y., Zuo T.T., Tang Z., Gao M.C., Dahmen K.A., Liaw P.K., Lu Z.P. Microstructures and properties of high-entropy alloys. *Progress in Materials Science*. 2014; 61:1–93. https://doi.org/10.1016/j.pmatsci.2013.10.001
6. Lu Y., Dong Y., Guo S., Jiang L., Kang H., Wang T., Wen B., Wang Z., Jie J., Cao Z., Ruan H., Li T. A promising new class of high-temperature alloys: Eutectic high-entropy alloys. *Scientific Reports*. 2014;4:6200. https://doi.org/10.1038/srep06200
7. Murty B.S., Yeh J.W., Ranganathan S., Bhattacharjee P.P. High-entropy alloys. London: Elsevier, 2014. 213 p.
8. Gorban F.F., Krapivka N.A., Firstov S.A. High-entropy alloys: Interrelations between electron concentration, phase composition, lattice parameter, and properties. *The Physics of Metals and Metallography*. 2017;118:970–981. https://doi.org/10.1134/S0031918X17080051

   Горбань Ф.Ф., Крапивка Н.А., Фирстов С.А. Высокоэнтропийные сплавы – электронная концентрация – фазовый состав – параметр решетки – свойства. *Физика металлов и металловедение*. 2017;118(10):1017–1029.
9. Brechtl J., Liaw P.K. (Eds.). High-entropy materials: Theory, experiments, and applications. Springer, 2021. https://doi.org/10.1007/978-3-030-77641-1
10. Gorban V.F., Krapivka N.A., Firstov S., Kurilenko D.V Role of various parameters in the formation of the physicomechanical properties of high-entropy alloys with bcc lattices. *Physics of Metals and Metallography*. 2018;119(5):477–481. https://doi.org/10.1134/S0031918X18050046

    Горбань В.Ф., Крапивка Н.А., Фирстов С.А., Куриленко Д.В. Роль различных параметров в формировании физико-механических свойств высокоэнтропийных сплавов с ОЦК-решеткой. *Физика металлов и металловедение*. 2018;119(5):504–509. https://doi.org/10.7868/S0015323018050108
11. Gorsse S., Miracle D.B., Senkov O.N. Mapping the world of complex concentrated alloys. *Acta Materialia*. 2017;135:177–187. https://doi.org/10.1016/j.actamat.2017.06.027
12. Zhang F., Zhang C., Chen S.L., Zhu J., Cao W. S., Kattner U.R. An understanding of high entropy alloys from phase diagram calculations. *Calphad*. 2014;45:1–10. https://doi.org/10.1016/j.calphad.2013.10.006
13. Tsai M.-H., Yeh J.-W. High-entropy alloys: A critical review. *Materials Research Letters*. 2014;2(3):107–123. https://doi.org/10.1080/21663831.2014.912690
14. Miracle D.B., Senkov O.N. A critical review of high entropy alloys and related concepts. *Acta Materialia*. 2017;122:448–511. https://doi.org/10.1016/j.actamat. 2016.08.081
15. Miracle D.B., Miller J.D., Senkov O.N., Woodward C., Uchic M.D., Tiley J. Exploration and development of high entropy alloys for structural applications. *Entropy*. 2014;16:494–525. https://doi.org/10.3390/e16010494
16. Ghasemi A., Eivani A.R., Abbasi S.M., Jafarian H.R., Ghosh M., Anijdan S.H.M. Al–Co–Cr–Fe–Ni–Ti high entropy alloys: A review of microstructural and mechanical properties at elevated temperatures. *Journal of Alloys and Compounds*. 2025;1010:178216. https://doi.org/10.1016/j.jallcom.2024.178216
17. Zamani M.R., Mirzadeh H., Malekan M., Weißensteiner I., Roostaei M. Unveiling the strengthening mechanisms of as-cast micro-alloyed CrMnFeCoNi high-entropy alloys, *Journal of Alloys and Compounds*. 2023;957:170443. https://doi.org/10.1016/j.jallcom.2023.170443
18. Nene S.S., Sinha S., Yadav D.K., Dutta A. Metallurgical aspects of high entropy alloys. *Journal of Alloys and Compounds*. 2024;1005:175849. https://doi.org/10.1016/j.jallcom.2024.175849
19. Xiong W., Guo A.X.Y., Zhan S., Liu C.-T., Cao S.C. Refractory high-entropy alloys: A focused review of preparation methods and properties. *Journal of Materials Science and Technology*. 2023;142:196–215. https://doi.org/10.1016/j.jmst.2022.08.046
20. Senkov O.N., Miracle D.B., Chaput K.J., Couzinie J.-P. Development and exploration of refractory high entropy alloys – A review. *Journal of Materials Research*. 2018;33(19):3092–3128. https://doi.org/10.1557/jmr.2018.153
21. Zheng W., Lü S., Wu S., Chen X., Guo W. Development of MoNbVTa$_x$ refractory high entropy alloy with high strength at elevated temperature. *Materials Science and Engineering: A*. 2022;850:143554. https://doi.org/10.1016/j.msea.2022.143554
22. Senkov O.N., Wilks G.B., Miracle D.B., Chuang C.P., Liaw P.K. Refractory high-entropy alloys. *Intermetallics*. 2010;18(9):1758–1765. https://doi.org/10.1016/j.intermet.2010.05.014
23. Senkov O.N., Wilks G.B., Scott J.M., Miracle D.B. Mechanical properties of $Nb_{25}Mo_{25}Ta_{25}W_{25}$ and $V_{20}Nb_{20}Mo_{20}Ta_{20}W_{20}$ refractory high entropy alloys. *Intermetallics*. 2011;19(5): 698–706. https://doi.org/10.1016/j.intermet.2011.01.004
24. Carter T.J. Common failures in gas turbine blades. *Engineering Failure Analysis*. 2005;12(2):237–247. https://doi.org/10.1016/j.engfailanal.2004.07.004
25. Tancret F., Sourmail T., Yescas M.A., Evans R.W., McAleese C., Singh L., Smeeton T., Bhadeshia H.K.D.H. Design of creep-resistant nickel-base superalloy for power plant applications. *Materials Science and Technology*. 2003;19:291–302.
26. Das S., Robi P.S. A novel refractory WMoVCrTa high-entropy alloy possessing fine combination of compressive stress-strain and high hardness properties. *Advanced Powder Technology*. 2020;31(12):4619–4631. https://doi.org/10.1016/j.apt.2020.10.008
27. Moser M., Dine S., Vrel D., Perriere L., Pires-Brazuna R., Couque H., Bernard F. Elaboration and characterization of WMoTaNb high entropy alloy prepared by powder

metallurgy processes. *Materials.* 2022;15(15):5416. https://doi.org/10.3390/ma15155416

28. Cao Y., Liu Y., Liu B., Zhang W. Precipitation behavior during hot deformation of powder metallurgy Ti–Nb–Ta–Zr–Al high entropy alloys. *Intermetallics*. 2018;100:95–103. https://doi.org/10.1016/j.intermet.2018.06.007

29. Cao Y., Liu Y., Li Y., Liu B., Fu A., Nie Y. Precipitation behavior and mechanical properties of a hot-worked $TiNbTa_{0.5}ZrAl_{0.5}$ refractory high entropy alloy. *International Journal of Refractory Metals and Hard Materials*. 2020;86:105132. https://doi.org/10.1016/j.ijrmhm.2019.105132

30. Guo W., Liu B., Liu Y., Li T., Fu A., Fang Q., Nie Y. Microstructures and mechanical properties of ductile NbTaTiV refractory high entropy alloy prepared by powder metallurgy. *Journal of Alloys and Compounds*. 2019;776:428–436. https://doi.org/10.1016/j.jallcom.2018.10.230

31. Dirras G., Gubicza J., Heczel A., Lilensten L., Couzinié J.-P., Perriére L., Guillot I., Hocini A. Microstructural investigation of plastically deformed $Ti_{20}Zr_{20}Hf_{20}Nb_{20}Ta_{20}$ high entropy alloy by *X*-ray diffraction and transmission electron microscopy. *Materials Characterization*. 2015;108:1–7. https://doi.org/10.1016/j.matchar.2015.08.007

32. Jia Y., Wang G., Wu S., Mu Y., Yi Y., Jia Y., Liaw P.K., Zhang T., Liu C.-T. A lightweight refractory complex concentrated alloy with high strength and uniform ductility. *Applied Materials Today*. 2022;27:101429. https://doi.org/10.1016/J.APMT.2022.101429.

33. Yurchenko N., Panina E., Zherebtsov S., Stepanov N. Design and characterization of eutectic refractory high entropy alloys. *Materialia*. 2021;16:101057. https://doi.org/10.1016/J.MTLA.2021.101057

34. Stepanov N.D., Yurchenko N.Yu., Skibin D.V., Tikhonovsky M.A., Salishchev G.A., Structure and mechanical properties of the $AlCr_xNbTiV$ (x = 0, 0.5, 1, 1.5) high entropy alloys. *Journal of Alloys and Compounds*. 2015;652:266–280. https://doi.org/10.1016/j.jallcom.2015.08.224

35. Yurchenko N., Panina E., Tikhonovsky M., Salishchev G., Zherebtsov S., Stepanov N. A new refractory Ti–Nb–Hf–Al high entropy alloy strengthened by orthorhombic phase particles. *International Journal of Refractory Metals and Hard Materials*. 2020;92:105322. https://doi.org/10.1016/J.IJRMHM.2020.105322

36. Senkov O.N., Senkova S.V., Woodward C., Miracle D.B. Low-density, refractory multi-principal element alloys of the Cr–Nb–Ti–V–Zr system: Microstructure and phase analysis. *Acta Materialia*. 2013;61(5):1545–1557. https://doi.org/10.1016/j.actamat.2012.11.032

37. Senkov O.N., Senkova S.V., Miracle D.B., Woodward C. Mechanical properties of low-density, refractory multi-principal element alloys of the Cr–Nb–Ti–V–Zr system. *Journal of Materials Science and Engineering*. 2013;565:51–62. https://doi.org/10.1016/j.msea.2012.12.018

38. Ren X., Li Y., Qi Y., Wang B. Review on preparation technology and properties of refractory high entropy alloys. *Materials*. 2022;15(8):2931. https://doi.org/ 10.3390/ma15082931

39. Shojaei Z., Khayati G.R, Darezereshki E. Review of electrodeposition methods for the preparation of high-entropy alloys. *International Journal of Minerals, Metallurgy and Materials*. 2022;29:1683–1696. https://doi.org/10.1007/s12613-022-2439-y

40. Sanin V.N., Yukhvid V.I., Ikornikov D.M., Andreev D.E., Sachkova N.V., Alymov M.I. SHS metallurgy of high-entropy transition metal alloys. *Doklady Physical Chemistry*. 2016;470:145–149. https://doi.org/10.1134/S001250161610002X

Санин В.Н., Юхвид В.И., Икорников Д.М., Андреев Д.Е., Сачкова Н.В., Алымов М.И. СВС-металлургия литых высокоэнтропийных сплавов на основе переходных металлов. *Доклады Академии наук*. 2016;470(4):421–426. https://doi.org/10.7868/S0869565216280124

41. Sanin V.N., Ikornikov D.M., Golosova O.A., Andreev D.E., Yukhvid V.I. Centrifugal metallothermic SHS of cast Co–Cr–Fe–Ni–Mn–(*X*) alloys. *Russian Journal of Non-Ferrous Metals*. 2020;61(4):436–445. https://doi.org/10.3103/S1067821220040070

Санин В.Н., Икорников Д.М., Голосова О.А., Андреев Д.Е., Юхвид В.И. Центробежная СВС-металлургия легированных высокоэнтропийных литых сплавов на основе системы Co–Cr–Fe–Ni–Mn–(*X*). *Известия вузов. Цветная металлургия*. 2020;(3):59–71. https://doi.org/10.17073/0021-3438-2020-3-59-71

42. Sanin V.N., Ikornikov D.M., Golosova O.A., Andreev D.E., Yukhvid V.I. Centrifugal SHS metallurgy of cast Co–Cr–Fe–Ni–Mn high-entropy alloys strengthened by precipitates based on Mo and Nb borides and silicides. *Physical Mesomechanics*. 2021;24(6):692–700. https://doi.org/10.1134/S1029959921060072

Санин В.Н., Икорников Д.М., Голосова О.А., Андреев Д.Е., Санин В.В., Юхвид В.И. Центробежная СВС-металлургия литых высокоэнтропийных сплавов системы Co–Cr–Fe–Ni–Mn, упрочняемых структурными выделениями на основе боридов и силицидов Mo и Nb. *Физическая мезомеханика*. 2021;24(4):73–82. https://doi.org/10.24412/1683-805X-2021-4-73-82

43. Kubanova A.N., Ikornikov D.M., Sanin V.D., Martynov D.A. Cast Mo–Cr, W–Cr, and Cr–Al master alloys by gravity-assisted SHS metallurgy. *International Journal of Self-Propagating High-Temperature Synthesis*. 2024;33(4):295–302. https://doi.org/10.3103/S1061386224700274

44. Sanin V., Andreev D., Ikornikov D., Yukhvid V. Cast intermetallic alloys and composites based on them by combined centrifugal casting – SHS process. *Open Journal of Metal*. 2013;3(2B):12–24. https://doi.org/10.4236/ojmetal.2013.32A2003

45. Martynov D.A., Sanin V.N. A centrifugal installation for the production of cast materials by centrifugal SHS-casting methods: Patent 2814351 (RF). 2024.

Мартынов Д.А., Санин В.Н. Центробежная установка для получения литых материалов методами центробежного СВС-литья: Патент 2814351 (РФ). 2024.

46. Shiryaev A.A. Thermodynamic of SHS: modern approach. *International Journal of Self-Propagating High-Temperature Synthesis*. 1995;4(4):351–362.

47. Shiryaev A.A. Distinctive features of thermodynamic analysis in SHS investigations. *Journal of Engineering Physics and Thermophysics*. 1993;65:957–962. https://doi.org/101007/BF00862765

Шариев А.А. Особенности использования метода термодинамического анализа при исследовании процессов СВС. *Инженерно-физический журнал*. 1993;65(4):412–419.

48. Gorr B., Schellert S., Müller F., Christ H.J., Kauffmann A., Heilmaier M. Current status of research on the oxidation behavior of refractory high entropy alloys. *Advanced Engineering Materials*. 2021;23(5):2001047. https://doi.org/10.1002/adem.202001047

49. Waseem O.A., Ryu H.J. Combinatorial synthesis and analysis of $Al_xTa_yV_z$–$Cr_{20}Mo_{20}Nb_{20}Ti_{20}Zr_{10}$ and $Al_{10}CrMo_xNbTiZr_{10}$ refractory high-entropy alloys: Oxidation behavior. *Journal of Alloys and Compounds*. 2020;828:154427. https://doi.org/10.1016/j.jallcom.2020.154427

50. Yurchenko N., Panina E., Zherebtsov S., Stepanov N. Oxidation behaviour of refractory $(HfCo)_{100-x}(NbMo)_x$ high-entropy alloys with a bcc+B2 structure. *Applied Sciences*. 2023;13(16):9336. https://doi.org/10.3390/app13169336

Information about the Authors

Vladimir N. Sanin – Dr. Sci. (Eng.), Chief Researcher of the Laboratory of liquid-phase SHS processes and cast materials of Merzhanov Institute of Structural Macrokinetics and Materials Science of the Russian Academy of Sciences (ISMAN)
ORCID: 0000-0001-8402-4605
E-mail: svn@ism.ac.ru

Denis M. Ikornikov – Research Engineer, Junior Researcher of the Laboratory of liquid-phase SHS processes and cast materials, ISMAN
ORCID: 0000-0002-8082-4442
E-mail: denis-ikornikov@yandex.ru

Alina O. Sivakova – Postgraduate Student, Junior Researcher of the Laboratory of physical materials science, ISMAN
ORCID: 0009-0000-7292-5887
E-mail: sivakovaalina@yandex.ru

Dmitry Yu. Kovalev – Dr. Sci. (Phys.-Math.), Head of the Laboratory of *X*-ray investigation, Chief Researcher, ISMAN
ORCID: 0000-0002-8285-5656
E-mail: kovalev@ism.ac.ru

Sergey L. Silyakov – Cand. Sci. (Eng.), Senior Researcher of the Laboratory of liquid-phase SHS processes and cast materials, ISMAN
E-mail: ssl@ism.ac.ru

Milena D. Panova – Junior Researcher of the Laboratory of metallurgical processes of JSC "State Scientific Research and Design Institute of the Rare Metal Industry "Giredmet"
E-mail: MDPanova@rosatom.ru

Сведения об авторах

Владимир Николаевич Санин – д.т.н., гл. науч. сотрудник лаборатории жидкофазных СВС-процессов и литых материалов Института структурной макрокинетики и проблем материаловедения им. А.Г. Мержанова Российской академии наук (ИСМАН)
ORCID: 0000-0001-8402-4605
E-mail: svn@ism.ac.ru

Денис Михайлович Икорников – инженер-исследователь, мл. науч. сотрудник лаборатории жидкофазных СВС-процессов и литых материалов ИСМАН
ORCID: 0000-0002-8082-4442
E-mail: denis-ikornikov@yandex.ru

Алина Олеговна Сивакова – аспирант, мл. науч. сотрудник лаборатории физического материаловедения ИСМАН
ORCID: 0009-0000-7292-5887
E-mail: sivakovaalina@yandex.ru

Дмитрий Юрьевич Ковалев – д.ф-м.н., заведующий лабораторией рентгеноструктурных исследований, гл. науч. сотрудник ИСМАН
ORCID: 0000-0002-8285-5656
E-mail: kovalev@ism.ac.ru

Сергей Леонидович Силяков – к.т.н., ст. науч. сотрудник лаборатории жидкофазных СВС-процессов и литых материалов ИСМАН
E-mail: ssl@ism.ac.ru

Милена Денисовна Панова – мл. науч. сотрудник лаборатории металлургических процессов АО «Государственный научно-исследовательский и проектный институт редкометаллической промышленности «Гиредмет»
E-mail: MDPanova@rosatom.ru

Contribution of the Authors

V. N. Sanin – developed the main concept, defined the aims and objectives of the study, supervised the research, organized the work, discussed the findings, and prepared the manuscript.

D. M. Ikornikov – performed the thermodynamic analysis, conducted alloy synthesis experiments, collected and analyzed experimental data, processed the results, and contributed to manuscript preparation.

A. O. Sivakova – carried out microstructural analysis of the synthesized alloys, analyzed and processed the data, and contributed to manuscript preparation.

Вклад авторов

В. Н. Санин – формирование основной концепции, определение целей и задач исследования, руководство исследованием, организация работ, обсуждение результатов исследования, подготовка текста статьи.

Д. М. Икорников – термодинамический анализ, проведение исследований по синтезу сплавов, сбор и анализ экспериментальных данных, обработка результатов, подготовка текста статьи.

А. О. Сивакова – микроструктурной анализ синтезированных сплавов, анализ данных, обработка результатов, подготовка текста статьи.

D. Yu. Kovalev – conducted *X*-ray phase analysis of the synthesized alloys, processed and interpreted the data, and contributed to manuscript preparation.
S. L. Silyakov – collected and analyzed experimental data, processed the results, and prepared them for inclusion in the manuscript.
M. D. Panova – investigated the oxidation resistance of the synthesized alloys, processed and interpreted the data, and contributed to manuscript preparation.

Д. Ю. Ковалев – рентгенофазовый анализ синтезированных сплавов, аналитическая обработка полученных данных, обработка результатов, подготовка текста статьи.
С. Л. Силяков – сбор и анализ экспериментальных данных, обработка результатов и их подготовка для статьи.
М. Д. Панова – исследование окислительной стойкости синтезированных сплавов, аналитическая обработка полученных данных, обработка результатов, подготовка текста статьи.

Received 26.02.2025
Revised 15.04.2025
Accepted 17.04.2025

Статья поступила 26.02.2025 г.
Доработана 15.04.2025 г.
Принята к публикации 17.04.2025 г.

Self-Propagating High-Temperature Synthesis
Самораспространяющийся высокотемпературный синтез

UDC 544.452 + 621.762.2 + 666.3

https://doi.org/10.17073/1997-308X-2025-5-36-50

Research article
Научная статья

Polytetrafluoroethylene-activated azide self-propagating high-temperature synthesis of a highly dispersed TiN–SiC powder composition

I. A. Uvarova[1], A. P. Amosov[1] ✉, Yu. V. Titova[1], A. A. Ermoshkin[2]

[1] Samara State Technical University
244 Molodogvardeiskaya Str., Samara 443100, Russia
[2] IT-Service LLC
52/55 Ulyanovskaya/Yarmarochnaya Str., Samara 443001, Russia

✉ egundor@yandex.ru

Abstract. Silicon carbide (SiC) and titanium nitride (TiN) are widely used non-oxide ceramics characterized by low density and high melting point, hardness, wear resistance, high-temperature strength, and corrosion resistance. However, single-phase silicon carbide ceramics have a number of drawbacks that limit their wider application. The main reason for developing TiN–SiC composite ceramics lies in the introduction of an electrically conductive TiN phase into the electrically non-conductive silicon carbide phase, which makes it possible to significantly reduce the high specific electrical resistivity of SiC while improving the sinterability, as well as the physical and mechanical properties of SiC-based composite ceramics. This study focuses on improving a simple and energy-efficient method of azide self-propagating high-temperature synthesis (SHS) for producing highly dispersed (<1 μm) TiN–SiC powder compositions from charge mixtures consisting of sodium azide (NaN_3), titanium, silicon, and carbon powders, through the use of powdered polytetrafluoroethylene (PTFE) as an activating and carbiding additive. The bulk and pressed charges were combusted in a reactor under a nitrogen pressure of 3 MPa. The maximum pressure and the yield of solid combustion products were measured. The morphology and phase composition of the combustion products were determined using scanning electron microscopy (SEM) and *X*-ray diffraction (XRD). The use of the PTFE additive eliminated the shortcomings of the traditional azide SHS of TiN–SiC compositions involving halide salts ($(NH_4)_2TiF_6$, Na_2SiF_6, and $(NH_4)_2SiF_6$). While maintaining the high dispersity of the synthesized TiN–SiC powder compositions, their phase composition became much closer to the theoretical one: the silicon carbide content in the synthesized TiN–SiC product increased substantially, while the amount of the secondary phase of silicon nitride (Si_3N_4) decreased or was completely eliminated.

Keywords: titanium nitride, silicon carbide, powder compositions, self-propagating high-temperature synthesis (SHS), sodium azide, polytetrafluoroethylene (PTFE), combustion products, composition, structure

Acknowledgements: The work was supported by the Russian Science Foundation under grant No. 23-29-00680.

For citation: Uvarova I.A., Amosov A.P., Titova Yu.V., Ermoshkin A.A. Polytetrafluoroethylene-activated azide self-propagating high-temperature synthesis of a highly dispersed TiN–SiC powder composition. *Powder Metallurgy and Functional Coatings*. 2025;19(5):36–50. https://doi.org/10.17073/1997-308X-2025-5-36-50

Применение политетрафторэтилена в азидном самораспространяющемся высокотемпературном синтезе высокодисперсной смеси керамических порошков TiN–SiC

И. А. Уварова[1], А. П. Амосов[1] ✉, Ю. В. Титова[1], А. А. Ермошкин[2]

[1] Самарский государственный технический университет
Россия, 443100, г. Самара, ул. Молодогвардейская, 244
[2] ООО «ИТ-Сервис»
Россия, 443001, г. Самара, ул. Ульяновская/Ярмарочная, 52/55

✉ egundor@yandex.ru

Аннотация. Карбид кремния (SiC) и нитрид титана (TiN) относятся к широко используемым неоксидным керамическим материалам с малой плотностью и высокими значениями температуры плавления, твердости, износостойкости, жаропрочности, коррозионной стойкости. Однако керамика из однофазного карбида кремния имеет ряд недостатков, препятствующих ее более широкому применению. Наиболее важная причина создания композиционной керамики TiN–SiC заключается в добавлении электропроводной фазы TiN в неэлектропроводную фазу карбида кремния для существенного снижения его высокого удельного электрического сопротивления с улучшением при этом спекаемости, физических и механических свойств композиционной керамики на основе SiC. Работа посвящена усовершенствованию простого энергосберегающего метода азидного самораспространяющегося высокотемпературного синтеза (СВС) композиций высокодисперсных (<1 мкм) порошков TiN–SiC из смесей исходных порошковых реагентов (шихт) азида натрия (NaN_3), титана, кремния и углерода за счет использования активирующей и карбидизирующей добавки порошкового политетрафторэтилена (ПТФЭ). Эти шихты в насыпном и прессованном виде сжигались в реакторе с давлением газообразного азота 3 МПа. Измерялись максимальное давление и выход твердых продуктов горения. С применением сканирующей электронной микроскопии и рентгенофазового анализа определялись морфология и фазовый состав продуктов горения. Использование добавки ПТФЭ позволило устранить недостатки традиционного азидного СВС композиций TiN–SiC с применением галоидных солей $(NH_4)_2TiF_6$, Na_2SiF_6 и $(NH_4)_2SiF_6$. При сохранении высокой дисперсности синтезированных композиций порошков TiN–SiC их фазовый состав стал значительно ближе к теоретическому составу, существенно увеличилось содержание карбида кремния в синтезированном продукте TiN–SiC при уменьшении содержания или полном устранении примеси побочной фазы нитрида кремния Si_3N_4.

Ключевые слова: нитрид титана, карбид кремния, композиции порошков, самораспространяющийся высокотемпературный синтез, азид натрия, политетрафторэтилен, продукты горения, состав, структура

Благодарности: Работа выполнена при поддержке Российского научного фонда в рамках гранта № 23-29-00680.

Для цитирования: Уварова И.А., Амосов А.П., Титова Ю.В., Ермошкин А.А. Применение политетрафторэтилена в азидном самораспространяющемся высокотемпературном синтезе высокодисперсной смеси керамических порошков TiN–SiC. *Известия вузов. Порошковая металлургия и функциональные покрытия*. 2025;19(5):36–50.
https://doi.org/10.17073/1997-308X-2025-5-36-50

Introduction

Silicon carbide (SiC) is one of the most widely used non-oxide ceramic materials due to its low density (3100 kg/m^3) and high values of such properties as melting point (refractoriness), hardness, wear resistance, thermal conductivity, dimensional thermal stability, high-temperature strength, heat resistance, and corrosion resistance. As a result, its application range extends from traditional uses – abrasive and cutting tool materials, mechanical seals, brake discs, turbine components, catalyst supports, heating elements, carbon and silicon sources for steelmaking, filters for molten metals and gases, and foundry crucibles – to modern applications such as composite armor for military vehicles and bulletproof vests, semiconductor processing components, mirror substrates for astronomical telescopes and other optical systems, matrices and claddings for nuclear fuel particles, and power electronic devices [1; 2].

However, single-phase silicon carbide ceramics have several drawbacks that limit their practical use [3]. First, SiC exhibits relatively low flexural strength (on average 450 MPa) and fracture toughness (2.8 MPa·m$^{1/2}$), which makes it brittle under impact loading. It is generally believed that increasing impact strength would enable silicon carbide to compete with structural materials based on silicon nitride, which exhibit higher flexural strength (around 750 MPa) and fracture toughness (approximately 5.3 MPa·m$^{1/2}$) [4; 5]. Second,

the extremely high melting point of silicon carbide (2730–2830 °C, with decomposition) caused by strong covalent bonding and low atomic self-diffusion results in poor sinterability of SiC powders. Therefore, very high temperatures of 2100–2200 °C are required during pressureless solid-state sintering, which leads to a coarser microstructure and deterioration of mechanical properties [4; 6]. Third, the high specific electrical resistivity of silicon carbide (10^6–10^{11} Ω·cm), typical of a semiconductor, prevents the fabrication of complex-shaped components by the cost-effective method of electrical discharge machining (EDM). Instead, mechanical machining of high-hardness SiC (20–30 GPa) requires expensive diamond tools, which also restricts its broader application [4; 7]. Moreover, when SiC ceramics are used as the friction pair in mechanical face seals, the specific (volume) electrical resistivity must be below ~10^3 Ω·cm to prevent triboelectric charge accumulation generated by rubbing of the mating end-faces during operation, which can trigger electrochemical corrosion and accelerate wear [8].

To date, extensive efforts have been made to overcome the aforementioned drawbacks of single-phase SiC ceramics by introducing secondary-phase additives, applying various processing and sintering technologies, using silicon carbide powders of different polytypes (α-SiC and β-SiC modifications) and dispersities, as well as adopting other approaches [1–9]. As a result, the most effective solution has been found to be the incorporation of secondary phases, i.e., the transition from single-phase SiC ceramics to SiC-based composite ceramics. Numerous studies have demonstrated that the addition of oxide, carbide, boride, and nitride phases enhances the sinterability and improves the physical and mechanical properties of SiC-based ceramics [6; 9].

Two main sintering methods for SiC ceramics involving additives are solid-state sintering and liquid-phase sintering. Solid-state sintering requires additives that reduce the energy barrier for SiC densification [6]. Carbon, boron, aluminum, titanium carbide (TiC), boron carbide (B_4C), and titanium diboride (TiB_2) are among the most widely used additives in this system [8–13]. However, even with these additives, the sintering temperature remains high, and achieving full densification of SiC continues to be a challenging task [6; 9]. Moreover, SiC ceramics containing carbon or graphene are unsuitable for semiconductor-processing components because carbon contamination adversely affects subsequent chemical vapor deposition (CVD) procedures. Similarly, aluminum-containing additives may be get into finished semiconductor products and worsen their performance characteristics [7].

Liquid-phase sintering is the most common method for producing SiC components. A liquid phase promotes faster mass transport, shortens sintering time, and lowers the sintering temperature to 1800–1900 °C [4; 6]. The final product generally exhibits a homogeneous, fine-grained microstructure and acceptable physical and mechanical properties. A widely used additive is an alumina–yttria mixture with the $5Al_2O_3{:}3Y_2O_3$ stoichiometry; under sintering conditions it forms a transient liquid that crystallizes to yttrium aluminum garnet (YAG, $Al_5Y_3O_{12}$), promoting densification and lowering the sintering temperature. Consequently, YAG formation increases density and enhances the mechanical properties of SiC ceramics through several toughening mechanisms, including crack deflection, crack bridging, phase transformation, grain-boundary strengthening, and a shift of the fracture mode from intergranular to transgranular [6]. In recent years, in addition to the Al_2O_3–Y_2O_3 system, other additives have been used to further improve the mechanical and physical properties and refine the microstructure of SiC-based ceramics. These include MgO, CaO, TiO_2, La_2O_3, and SiO_2 from the oxide group; TiC from the carbide group; TiB_2 and ZrB_2 from the boride group; and AlN and TiN from the nitride group [4; 6; 9]. Each of these additives imparts specific characteristics to SiC ceramics, generally inhibiting matrix grain growth, enhancing mechanical performance, and activating toughening mechanisms.

One of the most promising approaches for producing SiC ceramics suitable for electrical discharge machining is nitrogen doping (N-doping) of the SiC crystal lattice [7]. Nitrogen doping through the liquid phase can reduce the specific (volume) electrical resistivity of sintered SiC ceramics by up to ten orders of magnitude (from 10^8 to 10^{-2} Ω·cm) [14]. N-doping can be achieved either by sintering in a nitrogen atmosphere or by introducing nitride additives as a nitrogen source. However, gaseous N_2 inhibits mass transport and results in low density of sintered SiC ceramics [15], making the use of nitride-phase additives more promising. Importantly, adding 1 wt. % AlN lowers the specific (volume) electrical resistivity of SiC ceramics by four orders of magnitude – from $1.7\cdot10^5$ to $8.3\cdot10^1$ Ω·cm – but introduces undesirable aluminum impurities into the SiC matrix [16]. In contrast, the addition of 50 vol. % TiN decreases the specific electrical resistivity by nine orders of magnitude – from $2.0\cdot10^5$ Ω·cm (0 % TiN) to $2.0\cdot10^{-4}$ Ω·cm in the SiC–50 vol. % TiN composite – due to the combined beneficial effects of N-doping and the electrically conductive TiN grain boundaries [4; 17].

Given these considerations, let us focus more closely on the use of titanium nitride (TiN) powder as an additive – that is, on TiN–SiC ceramic composites. Like silicon carbide, titanium nitride has a high melting point (2950 °C), good corrosion resistance, and rela-

tively high hardness (20 GPa). However, TiN differs fundamentally from SiC in its very low specific electrical resistivity ($2.2 \cdot 10^{-5}$ Ω·cm) [18]. This key distinction determines the main interest in using an electrically conductive TiN ceramic phase as an additive to the non-conductive SiC ceramic matrix – to significantly reduce its high specific electrical resistivity (10^6–10^{11} Ω·cm) to below 10^3 Ω·cm, while simultaneously improving the sinterability and the physical and mechanical properties of SiC-based ceramics [6; 7; 9].

The first studies in this area investigated the effect of nano-TiN additions on sintering behavior, microstructure, and mechanical properties of SiC ceramics [19; 20]. A powder mixture consisting of α-SiC (particle size 0.5–1.0 μm) as the matrix, 0–15 wt. % TiN nanoparticles (average particle size 20 nm) as the reinforcing phase, and 10 wt. % of sintering additives ($5Al_2O_3 + 3Y_2O_3$) was cold-isostatically pressed at 250 MPa into rectangular bars and subsequently liquid-phase-sintered at 1950 °C for 15 min and then at 1850 °C for 1 h [19]. It was shown that the addition of TiN nanoparticles suppressed grain growth in the ceramics, and that reactions of TiN with SiC and of Al_2O_3 with the formation of new TiC and AlN phases, within a certain range of TiN content, improved the properties of SiC ceramics. The composition containing 5 wt. % nano-TiN exhibited the most homogeneous microstructure, the highest density, and a flexural strength of 686 MPa. The beneficial effect of nano-TiN addition was also demonstrated in another study [20] for pressureless-sintered SiC ceramics: the Vickers hardness increased from 18.19 to 26.65 GPa, flexural strength varied from 416 to 1122.81 MPa, and the maximum fracture toughness reached 8.69 MPa·$m^{1/2}$.

However, later research indicated that the use of nanopowders in fabricating SiC-based ceramics complicates processing and increases production costs due to the high price of the initial nanopowders [4; 13; 21]. Therefore, studies began to employ coarser and more affordable highly dispersed TiN powders with particle sizes up to 1 μm. SiC-based ceramic samples were produced by hot pressing at 2000 °C for 3 h under a nitrogen gas pressure of 40 MPa from a powder mixture of β-SiC (~0.5 μm), 2 or 4 vol. % TiN (~1 μm), and 2 vol. % Y_2O_3 as a sintering aid [21]. Phase-composition and microstructural analyses of the sintered samples revealed predominantly β-SiC grains with traces of α-SiC and Ti_2CN clusters located between β-SiC grains. The highly conductive *in-situ*-formed Ti_2CN clusters significantly reduced the specific electrical resistivity of the SiC ceramics to $2.4 \cdot 10^{-3}$ and $1.8 \cdot 10^{-4}$ Ω·cm for 2 and 4 vol. % TiN, respectively. In a subsequent study by the same group [17], SiC–Ti_2CN composites were fabricated by pressureless sintering at 1950 °C in a nitrogen atmosphere from powder mixtures containing 0, 3, 12, 20, and 25 vol. % TiN. All ceramic composite samples were sintered to a density of at least 98 % of the theoretical value, and their specific electrical resistivity decreased with increasing TiN content, reaching a minimum of $8.6 \cdot 10^{-4}$ Ω·cm at 25 vol. % TiN. The high electrical conductivity of the composites was attributed to *in-situ* synthesis of the conductive Ti_2CN phase and to grain growth of nitrogen-doped SiC during pressureless sintering. The sample containing 25 vol. % TiN exhibited a flexural strength of 430 MPa, fracture toughness of 4.9 MPa·$m^{1/2}$, and Vickers hardness of 23.1 GPa at room temperature.

In [4], SiC-based ceramic composites were fabricated by hot pressing at 1900 °C from SiC powder (~0.7 μm) with various TiN contents (0–50 wt. %, 0.8–1.2 μm), using Al_2O_3 and Y_2O_3 as sintering additives. The resulting composites reached densities above 98 % of the theoretical value. The specific electrical resistivity decreased from $2.0 \cdot 10^5$ Ω·cm (0 % TiN) with increasing TiN content and reached a plateau at $2.0 \cdot 10^{-4}$ Ω·cm for 40–50 wt. % TiN. At the same time, flexural strength gradually increased with the TiN content, attaining a maximum of 921 MPa at 40 wt. % TiN compared with 616 MPa for the original SiC (0 % TiN).

Additional results on the use of TiN additives were obtained for SiC ceramics produced by solid-state pressureless sintering in a graphite resistance furnace at a significantly higher temperature of 2100 °C for 2 h in a flowing argon atmosphere. The samples were prepared from pre-pressed powder mixtures of α-SiC (~0.5 μm) + 1–10 wt. % TiN (~1 μm) + 2.5 % C + 0.7 % B_4C (~0.5 μm) [7]. A TiN content up to 1 wt. % resulted in relative densities above 97 %, whereas further increase in TiN concentration led to the formation of large residual pores and a sharp decrease in relative density. For example, at ≥5 wt. % TiN, the density dropped to about 60 %, presumably due to the detrimental effect of excessive N_2 evolution during TiN decomposition. Nitrogen doping derived from TiN reduced the specific electrical resistivity by only one order of magnitude – to $9.0 \cdot 10^6$ Ω·cm at 1 wt. % TiN.

Thus, the effect of TiN addition on the properties of SiC-based ceramics strongly depends on the fabrication method, the composition of the initial powder mixtures, and the amount of TiN added. The most positive results – namely, a substantial decrease in specific electrical resistivity and improvement of mechanical properties – were achieved by hot pressing and pressureless sintering in a nitrogen atmosphere at temperatures not exceeding 2000 °C, using mixtures of highly

dispersed SiC and TiN powders (≤1–2 μm) with Al_2O_3 and Y_2O_3 as sintering additives and TiN contents from 1 to 50 wt. %.

In all the above studies, SiC–TiN ceramic composites were produced using the simplest and most common *ex situ* approach, which involves mechanical mixing of pre-synthesized SiC and TiN powders, followed by compaction and sintering. However, fine ceramic powders are costly; for instance, industrial-scale production of highly dispersed TiN powders requires complex equipment and energy-intensive plasma-chemical or vapor-phase reduction processes, in which titanium tetrachloride vapors are reduced by ammonia at 900–1000 °C [22; 23]. Furthermore, pre-synthesized fine powders are difficult to mix mechanically into a homogeneous composition because their particles tend to form strong agglomerates that are hard to break apart. For these reasons, an *in-situ* approach – based on the chemical synthesis of SiC and TiN powder particles directly within the composite from inexpensive starting reagents with uniform mixing – is considered more promising for the production of highly dispersed SiC–TiN composite powders [24–26]. To be fair, *in-situ* methods are currently used only under laboratory conditions and have not yet been adopted in industrial practice, where single-phase ceramic powders are still manufactured and composite powders are obtained by the traditional *ex-situ* route of mechanical mixing and milling of their single-phase components [25; 26]. Nevertheless, *in-situ* chemical synthesis methods for composite highly dispersed powders are considered advanced and strategically important, warranting further development and industrial implementation. Once this goal is achieved, high-quality composite highly dispersed powders will become commercially available, leading to significant improvements in the performance characteristics of the resulting composite ceramics [25; 26].

Among *in-situ* chemical synthesis methods for producing highly dispersed ceramic powders and their composites, the self-propagating high-temperature synthesis (SHS) method stands out for its simplicity and energy efficiency. It is based on the combustion of mixtures of inexpensive starting reagents [27–29]. Reference [29] presents earlier results, obtained with the participation of the present authors, on the application of the azide variant of SHS to Si–Ti–C–NaN_3–halide-salt systems. The charge mixtures consisted of silicon (Si), titanium (Ti), technical carbon (C), and sodium azide (NaN_3) as the nitriding reagent, with halide salts – $(NH_4)_2TiF_6$, Na_2SiF_6, and $(NH_4)_2SiF_6$ – serving as activating and gasifying additives. To synthesize highly dispersed TiN–SiC powder compositions at five molar ratios of the target phases – TiN:SiC = 4:1, 2:1, 1:1, 1:2, and 1:4 – the corresponding stoichiometric equations were formulated, for example

$$2Si + Ti + 6NaN_3 + (NH_4)_2TiF_6 + 2C =$$
$$= 2TiN + 2SiC + 6NaF + 4H_2 + 9N_2.$$

Of the 15 stoichiometric equations derived, only one is shown here for brevity – the equation using the halide salt $(NH_4)_2TiF_6$ corresponding to the TiN:SiC = 1:1 molar ratio of the target phases. The charge mixtures of the starting reagents corresponding to these 15 stoichiometries were combusted in bulk in an azide SHS reactor under a nitrogen pressure of 4 MPa. After cooling, the combustion products were removed from the reactor, disintegrated to a bulk powder form in a porcelain mortar, and washed with water to remove the by-product sodium fluoride (NaF). In most cases, the combustion product was a highly dispersed powder of complex composition, consisting of a mixture of submicron (0.1–1.0 μm) equiaxed particles and fibers. The phase composition of the washed combustion products is summarized in Table 1, in comparison with the theoretical composition of the TiN–SiC target phases at various molar ratios according to the 15 stoichiometric equations.

According to Table 1, the phase compositions of the synthesized TiN–SiC powders differed markedly from the theoretical predictions. The content of silicon carbide was much lower – or even absent – ranging from 0 to 49.4 wt. % instead of the theoretical 13.9–72.1 wt. %. In addition, a considerable amount of the secondary silicon nitride phase (12.3–54.2 wt. %) in α- and β-modifications was observed, despite its absence in the theoretical composition. The formation of SiC was especially limited, or completely suppressed, when the halide salt $(NH_4)_2TiF_6$ was used. It is also noteworthy that the azide SHS products contained only minor amounts of free silicon and carbon (≤1.4 wt. %) or none at all.

Reference [29] also reports that using the traditional azide SHS route with gasifying halide activators – $(NH_4)_2SiF_6$, AlF_3, and NH_4F – to synthesize AlN–SiC powders led to systematic deviations between the experimental and theoretical phase compositions across AlN:SiC molar ratios of 4:1, 2:1, 1:1, 1:2, and 1:4. On average, the SiC content was approximately half of the theoretical value, and substantial amounts of the undesired secondary phase Si_3N_4 were detected. These issues were recently addressed in our study [30] by replacing the halide activators with powdered polytetrafluoroethylene (PTFE, $(C_2F_4)_n$) used as an activating carbiding additive in the azide SHS synthesis of AlN–SiC powders. Partially substituting 0.1 mol of carbon with 0.05 mol of PTFE in the carbiding mixture ($0.9C + 0.05C_2F_4$), together with sodium azide as

the activating nitriding agent in an amount sufficient to neutralize the fluorine released upon complete PTFE decomposition, preserved the high dispersity of the synthesized AlN–SiC powders and brought their phase composition – particularly for pressed charges – much closer to the theoretical one. The SiC phase fraction increased substantially, and the undesired silicon nitride phases were eliminated.

A similar approach – partial substitution of 0.3 mol of carbon with 0.15 mol of PTFE in the carbiding mixture ($0.7C + 0.15C_2F_4$) – was used in our recently published work [31] to synthesize highly dispersed Si_3N_4–SiC powder compositions by azide SHS, yielding a phase composition close to the theoretical stoichiometry.

Considering these results, in the present study – aiming to bring the composition of the synthesized highly dispersed TiN–SiC powder mixture closer to the theoretical one by increasing the SiC phase content and removing the undesired secondary Si_3N_4 phase – we analogously used partial substitution of carbon with PTFE, instead of halide salt additives, in the initial Azide SHS reagent mixture, and investigated the combustion products of the Si–Ti–NaN_3–C–C_2F_4 system.

Research methodology

The following starting reagents were used in the study (hereafter in wt. %): silicon powder, grade Kr00 (main component ≥99.9 %, mean particle size d = 40 μm); titanium powder, grade PTOM-1 (98.0 %, d = 30 μm); sodium azide powder, analytical grade (≥98.71 %, d = 100 μm); polytetrafluoroethylene (PTFE) powder, grade PN-40 (≥99.0 %, d = 40 μm); and technical carbon black, grade P701 (≥88.0 %, d = 70 nm, agglomerates up to 1 μm).

As in [30; 31] and following [32; 33], to increase the silicon carbide content in the synthesized TiN–SiC composites, technical carbon was partially replaced by PTFE in amounts of 5, 10, and 15 %. This corresponded to the following carbiding mixtures of carbon and PTFE, each equivalent to one mole of carbiding carbon:

$$0.9C + 0.05C_2F_4, \quad (A)$$

$$0.8C + 0.1C_2F_4, \quad (B)$$

$$0.7C + 0.15C_2F_4. \quad (C)$$

Table 1. **Theoretical and experimental phase composition of washed solid products of azide SHS of the TiN–SiC composition [29]**

Таблица 1. **Теоретический и экспериментальный фазовые составы промытых твердых продуктов азидного СВС композиции TiN–SiC [29]**

TiN:SiC (mol)	Content, wt. %							
	Theoretical		Experimental					
	TiN	SiC	TiN	SiC	α-Si_3N_4	β-Si_3N_4	Si	C
Halide salt $(NH_4)_2TiF_6$								
4:1	86.1	13.9	87.7	–	5.6	6.7	–	–
2:1	75.6	24.4	80.0	–	14.0	6.0	–	–
1:1	60.7	39.3	45.8	–	49.8	4.4	–	–
1:2	43.6	56.4	41.2	6.4	43.9	7.6	0.9	–
1:4	27.9	72.1	28.8	19.9	42.5	7.4	1.4	–
Halide salt $(NH_4)_2SiF_6$								
4:1	86.1	13.9	61.0	4.0	27.0	7.0	1.0	–
2:1	75.6	24.4	71.0	–	18.0	9.0	1.2	0.8
1:1	60.7	39.3	54.7	16.0	17.4	11.9	–	–
1:2	43.6	56.4	40.0	31.0	19.0	9.0	1.0	–
1:4	27.9	72.1	24.2	49.4	21.1	5.0	0.3	–
Halide salt Na_2SiF_6								
4:1	86.1	13.9	76.0	–	19.0	5.0	–	–
2:1	75.6	24.4	64.0	10.0	17.0	9.0	–	–
1:1	60.7	39.3	54.0	20.0	15.0	11.0	–	–
1:2	43.6	56.4	42.0	34.0	16.0	8.0	–	–
1:4	27.9	72.1	23.0	49.0	21.0	6.0	1.0	–

Sodium azide (NaN_3) was added to the charge in an amount sufficient to neutralize the fluorine released during complete PTFE decomposition and to bind it into water-soluble sodium fluoride (NaF), which can be readily removed from the azide SHS product by washing with water. Consequently, the stoichiometric equations of azide SHS for the TiN–SiC target phases at five molar ratios (TiN:SiC = 4:1, 2:1, 1:1, 1:2, and 1:4) were derived for carbiding mixtures (*A*)–(*C*) containing PTFE, assuming combustion in gaseous nitrogen, as follows:

for carbiding mixture (*A*):

$$4Ti + Si + 0.9C + 0.05C_2F_4 + 0.2NaN_3 + 1.7N_2 = 4TiN + SiC + 0.2NaF, \quad (1)$$

$$2Ti + Si + 0.9C + 0.05C_2F_4 + 0.2NaN_3 + 0.7N_2 = 2TiN + SiC + 0.2NaF, \quad (2)$$

$$Ti + Si + 0.9C + 0.05C_2F_4 + 0.2NaN_3 + 0.2N_2 = TiN + SiC + 0.2NaF, \quad (3)$$

$$Ti + 2Si + 1.8C + 0.1C_2F_4 + 0.4NaN_3 = TiN + 2SiC + 0.4NaF + 0.1N_2, \quad (4)$$

$$Ti + 4Si + 3.6C + 0.2C_2F_4 + 0.8NaN_3 = TiN + 4SiC + 0.8NaF + 0.7N_2; \quad (5)$$

for carbiding mixture (*B*):

$$4Ti + Si + 0.8C + 0.1C_2F_4 + 0.4NaN_3 + 1.4N_2 = 4TiN + SiC + 0.4NaF, \quad (6)$$

$$2Ti + Si + 0.8C + 0.1C_2F_4 + 0.4NaN_3 + 0.4N_2 = 2TiN + SiC + 0.4NaF, \quad (7)$$

$$Ti + Si + 0.8C + 0.1C_2F_4 + 0.4NaN_3 = TiN + SiC + 0.4NaF + 0.1N_2, \quad (8)$$

$$Ti + 2Si + 1.6C + 0.2C_2F_4 + 0.8NaN_3 = TiN + 2SiC + 0.8NaF + 0.7N_2, \quad (9)$$

$$Ti + 4Si + 3.2C + 0.4C_2F_4 + 1.6NaN_3 = TiN + 4SiC + 1.6NaF + 1.9N_2; \quad (10)$$

for carbiding mixture (*C*):

$$4Ti + Si + 0.7C + 0.15C_2F_4 + 0.6NaN_3 + 1.1N_2 = 4TiN + SiC + 0.6NaF, \quad (11)$$

$$2Ti + Si + 0.7C + 0.15C_2F_4 + 0.6NaN_3 + 0.1N_2 = 2TiN + SiC + 0.6NaF, \quad (12)$$

$$Ti + Si + 0.7C + 0.15C_2F_4 + 0.6NaN_3 = TiN + SiC + 0.6NaF + 0.4N_2, \quad (13)$$

$$Ti + 2Si + 1.4C + 0.3C_2F_4 + 1.2NaN_3 = TiN + 2SiC + 1.2NaF + 1.3N_2, \quad (14)$$

$$Ti + 4Si + 2.8C + 0.6C_2F_4 + 2.4NaN_3 = TiN + 4SiC + 2.4NaF + 3.1N_2. \quad (15)$$

The reagent mixtures corresponding to equations (1)–(15), with masses ranging from 23 to 37 g (average 30 g), were combusted in a 4.5 L azide SHS reactor under an initial nitrogen pressure of P_0 = 3 MPa. Combustion was performed in two forms: as a bulk charge, placed in a tracing-paper crucible (30 mm in diameter and 45 mm in height), and as briquetted charges, compacted under 7 MPa into cylindrical pellets measuring 30 mm in diameter and approximately 22 mm in height. (The nitrogen pressure of 3 MPa and the briquette compaction pressure of 7 MPa for a 30 mm charge diameter were selected according to [33], which demonstrated that under these conditions partial replacement of carbon with PTFE ensures the complete course of the silicon carburization reaction and the formation of SiC particles with an average size of about 200 nm). Combustion was initiated using a tungsten spiral heater. The maximum gas pressure (P_{max}) in the reactor during combustion was recorded using a manometer. After cooling, the combustion products were removed from the reactor, disintegrated to a bulk powder form in a porcelain mortar, and washed with water to remove the byproduct sodium fluoride (NaF). The dried and washed combustion product was weighed, and the mass loss (Δm, %) was determined as the difference between the initial charge mass (m_0) and the mass of the washed product (m_k). This mass loss was interpreted as the scattering of part of the solid synthesis products beyond the charge volume due to gases intensively released during combustion. (This estimation of product scattering is approximate, since it does not account for the formation of NaF in the products or for the consumption or release of gaseous nitrogen in the reactor according to equations (1)–(15). However, because this approach was used in our previous studies [30; 31], it is retained here to ensure comparability of the product-scattering data. The validity of this estimation will be discussed later in the following sections of the paper).

The phase composition of the synthesized products was analyzed using an ARL X'TRA powder *X*-ray diffractometer (Thermo Fisher Scientific, Switzerland) equipped with a Cu anode *X*-ray tube. The diffraction patterns were processed, and the phase composition was determined by the Rietveld refinement method

using the HighScore Plus software package and the COD-2024 crystallographic database. The morphology and particle size of the synthesized powders were examined with a JSM-6390A scanning electron microscope (JEOL, Japan).

Results and discussion

The experimentally determined maximum reactor pressure (P_{max}), mass loss (Δm) for the bulk and pressed powder charges of reactions (1)–(15), and the phase compositions of the washed solid combustion products are summarized in Table 2 as average values from three repeated experiments for each charge.

A comparison between the experimental phase compositions of the washed solid products of the Azide SHS reactions for TiN–SiC compositions (Tables 1 and 2) reveals a marked difference between the two sets of results. Table 2 shows that partial substitution of technical carbon with PTFE led to the formation of a considerably higher fraction of silicon carbide (13–72 %), compared to the use of halide salts (0–49.4 % SiC, Table 1). Whereas some compositions in Table 1 show complete absence of SiC (0 %), all samples in Table 2 contained measurable SiC. Notably, the experimentally obtained SiC contents (13–72 %) in Table 2 are very close to their theoretical values (13.9–72.1 %) calculated from the stoichiometric equations. A similar trend is observed for the secondary silicon nitride (Si_3N_4) phase in α- and β-modifications. While the total Si_3N_4 content in Table 1 reached 12.3–54.2 %, its amount in Table 2 was much lower (0–18 %) and, in several cases, completely absent, in line with theoretical predictions. Table 2 also indicates that free carbon impurities were entirely absent, and free silicon was either undetected or present in trace amounts, not exceeding a few tenths of a percent. Only four of the thirty analyzed samples contained 1.0–3.3 % Si. Overall, the data in Table 2 show that the experimental phase compositions of the TiN and SiC target phases obtained via azide SHS using PTFE correspond much more closely to the theoretical stoichiometric predictions than those achieved by the traditional Azide SHS process with halide additives $(NH_4)_2TiF_6$, Na_2SiF_6, and $(NH_4)_2SiF_6$ [29].

However, Table 2 also shows very large mass losses (product scattering) during combustion, particularly for bulk charges (42.0–88.7 %), with noticeably lower values for pressed charges (17.7–77.5 %). In contrast, in traditional azide SHS processes, these values were much smaller – for example, 4.2–10.4 % for Si_3N_4–SiC synthesis from bulk charges using the halide salt NH_4F [34]. The mass losses observed here for TiN–SiC are also significantly higher than those reported for AlN–SiC compositions synthesized using carbiding mixture (*A*) with PTFE – 0.2–38.9 % for bulk charges and 0.1–26.3 % for pressed charges [30]. Meanwhile, the mass losses of the solid products obtained for mixture (*C*) are comparable to those reported for Si_3N_4–SiC synthesized with the same mixture – 57.0–81.4 % for bulk charges and 12.6–80.4 % for pressed charges [31].

We now consider how including NaF formation in the products and the consumption or release of gaseous nitrogen in the reactor affects the calculated mass loss of the combustion products. First, consider reaction (1), which consumes gaseous nitrogen, using a bulk charge that showed a large product-scattering loss of 73.5 % (Table 2). For this reaction, the charge mass was $m_0 = 37.23$ g, and the mass of the washed product was $m_k = 9.83$ g. On the right-hand side of equation (1), 0.2 NaF corresponds to 2.92 %, or 0.29 g, relative to the mass of 4TiN + SiC equal to 9.83 g. Thus, the unwashed product mass equals 10.12 g, and when the NaF mass is taken into account, the product mass loss decreases from 73.5 to 72.8 %. The correction for nitrogen consumption is made based on the left-hand side of equation (1), where 1.7 N_2 accounts for 19.13 %, or 7.12 g, of the total charge mass of 37.23 g. When the consumed nitrogen is taken into account, the total mass of the initial reactants on the left-hand side of equation (1) increases to 44.35 g. Consequently, the estimated mass loss of the unwashed product – including the NaF mass – rises from 72.8 to 77.2 %. Thus, accounting for the mass of NaF formed in the product and for the nitrogen consumed in the reactor changes the approximate product mass loss value of 73.5 % to more accurate estimates of 72.8 and 77.2 %, respectively. However, this difference is negligible at high product-loss levels.

For the average product loss value in Table 2 – an approximate estimate of 29.5 % for reaction (11) with a pressed charge – similar calculations show that accounting for NaF formation in the product and for the mass of nitrogen consumed yields more accurate product-loss estimates of 23.3 and 30.8 %, respectively. When only NaF formation is taken into account, the calculated value of 23.3 % is noticeably lower than the approximate estimate of 29.5 %; however, when both factors (NaF and N_2) are included, the resulting value of 30.8 % differs insignificantly from the approximate estimate of 29.5 %.

For the minimum scattering-related mass loss – an approximate estimate of 17.7 % for reaction (3) with a pressed charge – accounting only for NaF formation likewise gives a noticeably lower value of 10.9 %. However, when both NaF formation and nitrogen consumption are taken into account, the resulting value

Table 2. **Combustion parameters of charge mixtures for reactions (1)–(15) and theoretical and experimental phase compositions of washed solid products for bulk and pressed charges**

Таблица 2. **Параметры горения шихт реакций (1)–(15) и теоретический и экспериментальный фазовые составы промытых твердых продуктов реакций для насыпных и прессованных шихт**

Reaction equation	TiN:SiC (mol)	P_{max}, MPa	Δm, %	Phase composition of reaction products, wt. %							
				Theoretical		Experimental					
				TiN	SiC	TiN	SiC	α-Si_3N_4	β-Si_3N_4	Si	Other
Bulk charges											
Carbiding mixture (*A*)											
(1)	4:1	5.33	73.5	86.1	13.9	71.3	13.0	–	–	–	15.7 Ti_2N
(2)	2:1	5.49	77.1	75.6	24.4	74.1	23.3	–	–	0.4	2.2 Ti
(3)	1:1	5.18	63.5	60.7	39.3	59.4	37.3	–	–	3.3	–
(4)	1:2	4.60	83.5	43.6	56.4	28.0	55.0	10.0	6.0	1.0	–
(5)	1:4	4.44	78.1	27.9	72.1	29.0	51.0	13.0	5.0	2.0	–
Carbiding mixture (*B*)											
(6)	4:1	5.71	57.0	86.1	13.9	86.5	13.5	–	–	–	–
(7)	2:1	5.75	57.6	75.6	24.4	75.0	22.0	–	–	3.0	–
(8)	1:1	5.62	81.9	60.7	39.3	59.5	33.3	–	6.3	0.9	–
(9)	1:2	5.25	85.4	43.6	56.4	38.9	53.3	2.3	5.0	0.5	–
(10)	1:4	5.49	87.6	27.9	72.1	17.0	72.0	4.8	6.0	0.2	–
Carbiding mixture (*C*)											
(11)	4:1	5.04	42.0	86.1	13.9	81.7	15.2	3.1	–	–	–
(12)	2:1	5.87	69.5	75.6	24.4	75.8	22.1	2.1	–	–	–
(13)	1:1	5.87	88.7	60.7	39.3	57.3	34.0	5.0	3.3	0.4	–
(14)	1:2	5.98	69.5	43.6	56.4	37.2	55.7	4.0	3.1	–	–
(15)	1:4	4.91	78.2	27.9	72.1	25.0	69.0	4.0	2.0	–	–
Pressed charges											
Carbiding mixture (*A*)											
(1)	4:1	5.30	38.3	86.1	13.9	88.7	11.3	–	–	–	–
(2)	2:1	5.15	36.3	75.6	24.4	72.3	17.3	10.1	–	0.3	–
(3)	1:1	4.76	17.7	60.7	39.3	60.4	30.0	9.6	–	–	–
(4)	1:2	4.45	39.2	43.6	56.4	23.0	65.0	10.0	2.0	–	–
(5)	1:4	4.58	58.6	27.9	72.1	25.0	61.5	11.0	2.5	–	–
Carbiding mixture (*B*)											
(6)	4:1	4.58	49.7	86.1	13.9	84.5	15.5	–	–	–	–
(7)	2:1	5.67	48.1	75.6	24.4	72.7	27.0	–	–	0.3	–
(8)	1:1	5.45	32.9	60.7	39.3	60.4	33.1	6.0	–	0.5	–
(9)	1:2	5.23	49.3	43.6	56.4	40.0	53.0	4.0	3.0	–	–
(10)	1:4	5.47	74.2	27.9	72.1	21.9	67.6	6.5	4.0	–	–
Carbiding mixture (*C*)											
(11)	4:1	5.21	29.5	86.1	13.9	83.0	14.0	3.0	–	–	–
(12)	2:1	5.54	32.6	75.6	24.4	73.4	22.5	4.3	–	–	–
(13)	1:1	5.67	35.5	60.7	39.3	56.7	34.0	7.3	–	0.2	–
(14)	1:2	5.75	45.5	43.6	56.4	39.8	55.5	5.3	–	–	–
(15)	1:4	5.74	77.5	27.9	72.1	26.2	69.9	3.6	–	–	–

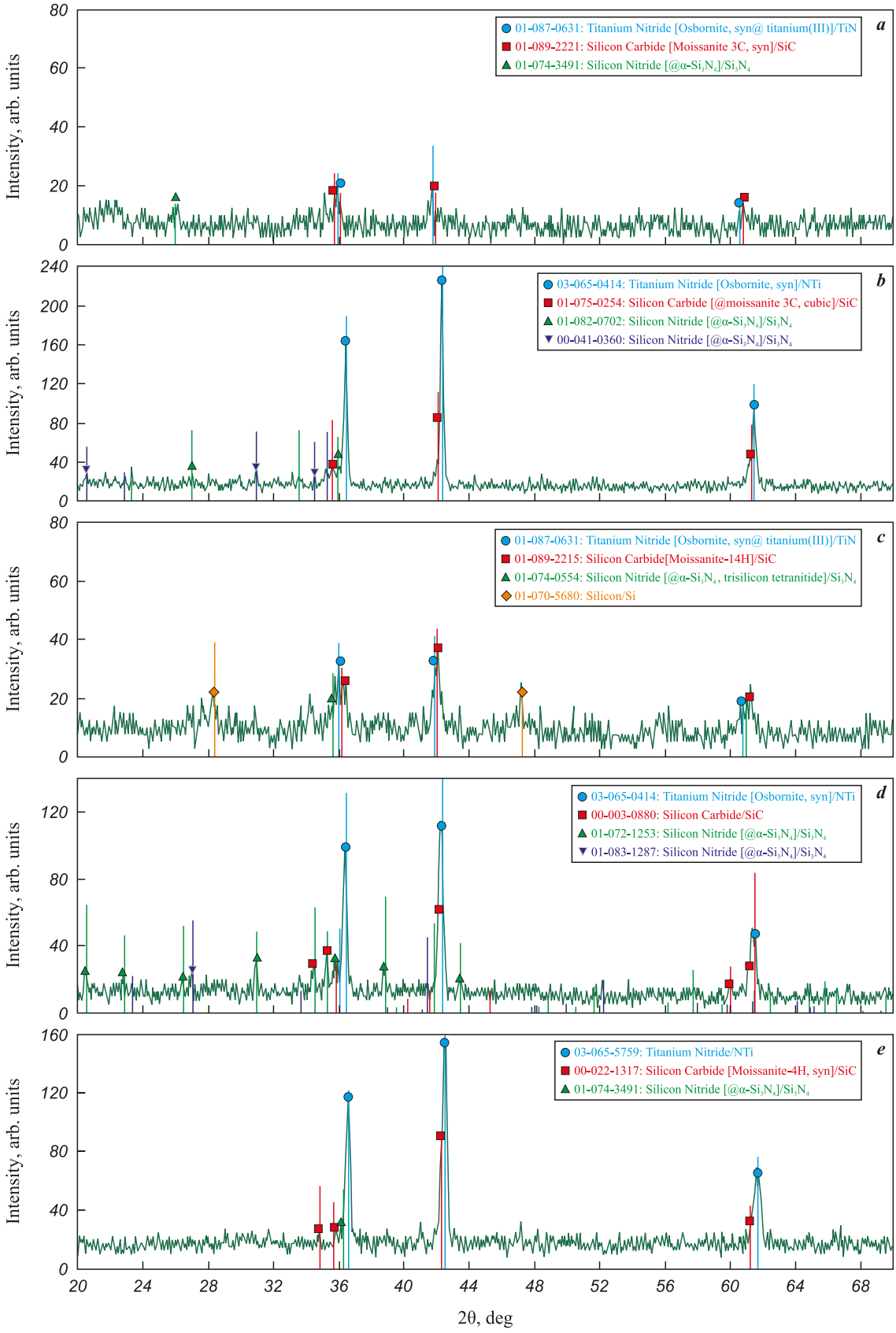

Fig. 1. XRD patterns of the washed combustion products of pressed charges from reaction equations (11)–(15)
a – (11), ***b*** – (12), ***c*** – (13), ***d*** – (14), ***e*** – (15)

Рис. 1. Рентгеновские дифрактограммы промытых продуктов горения прессованных шихт из уравнений реакций (11)–(15)
a – (11), ***b*** – (12), ***c*** – (13), ***d*** – (14), ***e*** – (15)

of 15.5 % differs only slightly from the approximate estimate of 17.7 %.

Thus, for reactions involving nitrogen consumption, the approximate estimates of solid product loss are close to the more accurate values obtained when both NaF formation and nitrogen consumption are fully taken into account, the latter increasing the total mass of the initial reactants. In contrast, for reactions accompanied by nitrogen release – where nitrogen appears on the right-hand side of the reaction equations – there is no need to consider it when evaluating the loss of solid products, since gaseous nitrogen is not part of the solid phase. In these cases, a more accurate loss estimate involves accounting only for NaF formation, whose mass is generally small compared with the other solid reaction products and can reduce the calculated loss value by approximately 10 %. For example, in reaction (8) from Table 2 (pressed charge), the approximate product loss is 32.9 %, while accounting for NaF formation gives 21.9 %. The relative difference between the two estimates is therefore significant (33.4 %), demonstrating how strongly NaF correction can reduce the calculated solid product loss in cases of small overall loss. Conversely, for reaction (15) with a very large product loss (approx. 77.5 %), accounting for NaF formation lowers the estimated loss to 67.3 %, where the relative difference is minor (13.2 %).

It was then necessary to select, from the 30 charge variants presented in Table 2, those corresponding to different TiN:SiC molar ratios that most closely matched the theoretical phase compositions calculated from the initial stoichiometric equations, while also exhibiting the lowest combustion-related losses. These optimal variants could then be recommended for further study and for assessing the feasibility of using the azide SHS process with PTFE to produce commercially viable highly dispersed TiN–SiC composite powders. The selection was based on a comparative assessment of the efficiency of bulk and pressed charges prepared with different carbiding mixtures (*A*, *B*, and *C*), using two parameters: the mass loss of the solid reaction products (Δm, %) and the total impurity content in these products (impurities, %). From the data in Table 2, the average values of these parameters for all variants were calculated as follows: for bulk charges, Δm = 72.9 % and impurities = 7.64 %; for pressed charges, Δm = 44.3 % and impurities = 6.22 %. Thus, in general, the use of bulk charges results in considerably higher product losses and greater contamination by impurities compared with pressed charges. Therefore, the search for the best synthesis conditions was continued among the pressed charges prepared with the three carbiding mixtures. Based on the results obtained with these mixtures (*A*, *B*, and *C*), the average

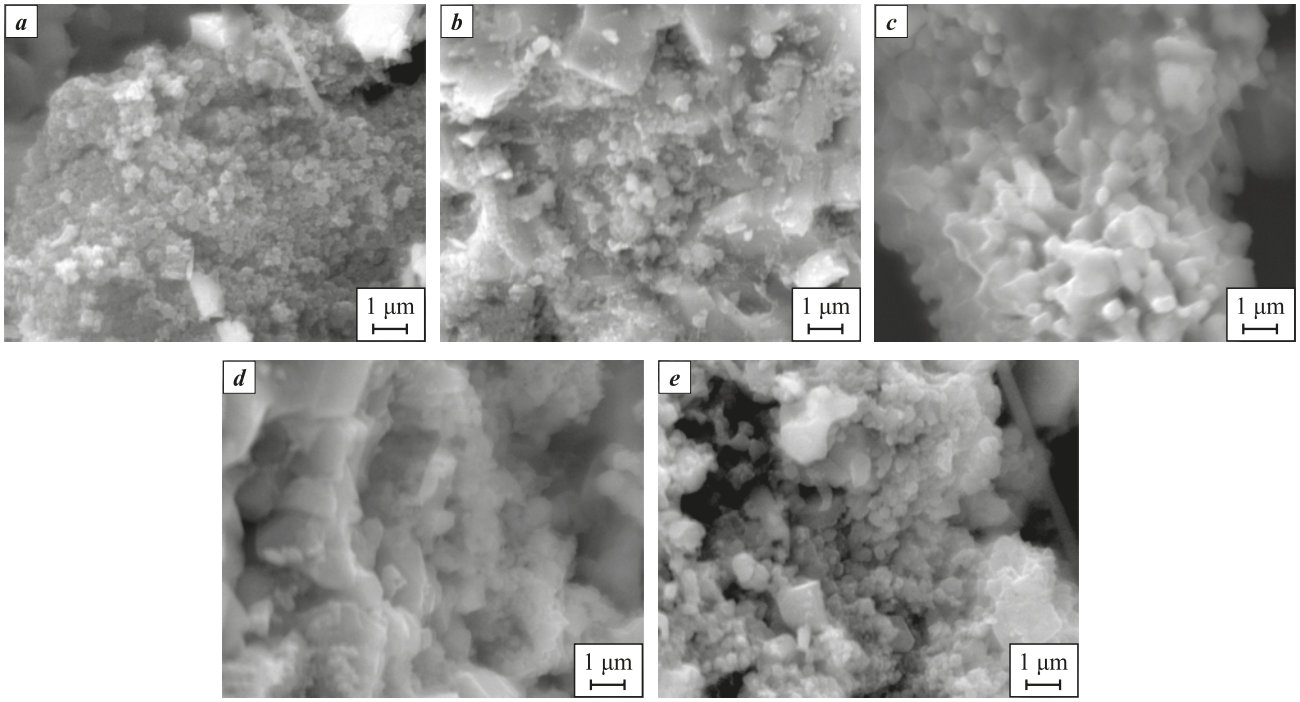

Fig. 2. SEM images of the washed combustion products of pressed charges from reaction equations (11)–(15)
a – (11), ***b*** – (12), ***c*** – (13), ***d*** – (14), ***e*** – (15)

Рис. 2. Морфология промытых продуктов горения прессованных шихт из уравнений реакций (11)–(15)
a – (11), ***b*** – (12), ***c*** – (13), ***d*** – (14), ***e*** – (15)

values of the parameters were as follows: Δm = 38.0, 50.8, and 44.1 %, and impurities = 9.1 %, 4.9 %, and 4.7 %, respectively. Mixture (*A*) provided the lowest mass loss (38.0 %) but also the highest impurity content (9.1 %). Mixture (*C*), in contrast, showed a slightly higher mass loss (44.1 %) yet a markedly lower impurity level (4.7 %), nearly twice as low as for mixture (*A*); therefore, mixture (*C*) was considered the most favorable option. Mixture (*B*) demonstrated a somewhat higher impurity level (4.9 %) and noticeably larger product losses (50.8 %) compared with mixture (*C*). Consequently, mixture (*C*) can be regarded as the most efficient carbiding composition for pressed charges. As a result of this systematic analysis, the best synthesis variants – those representing the optimal balance between product loss and impurity content – were identified for all five TiN:SiC molar ratios. These correspond to the pressed charges prepared with carbiding mixture (*C*) according to equations (11)–(15). Indeed, most of these variants exhibit some of the lowest product mass losses – 29.5, 32.6, 35.5, and 45.5 % for equations (11)–(14), respectively – and impurity levels of 3.0, 4.3, 5.3, and 3.6 % for equations (11), (12), (14), and (15), respectively. However, two issues remain: the relatively high impurity level (7.3 %) in the products of reaction (13) and the very large product loss (77.5 %) observed for reaction (15). These questions are discussed in the Conclusion section.

The *X*-ray diffraction patterns of the washed combustion products for the selected optimal synthesis variants of the TiN–SiC powder compositions are shown in Fig. 1.

The diffraction patterns in Fig. 1 exhibit strong reflections corresponding to the target phases TiN and SiC, along with weak reflections from minor impurities of free Si and secondary phases α-Si_3N_4 and β-Si_3N_4. In some cases, these impurity reflections are absent altogether. As seen from Fig. 1 and Table 2, silicon nitride forms predominantly in the α-Si_3N_4 modification.

The morphology of the TiN–SiC powder compositions for the selected best synthesis variants is presented in Fig. 2.

As shown in Fig. 2, all synthesized products are highly dispersed powders composed of equiaxed particles less than 1–2 μm in size, aggregated into agglomerates.

Conclusion

This study shows that replacing the halide activators $(NH_4)_2TiF_6$, Na_2SiF_6, $(NH_4)_2SiF_6$ with polytetrafluoroethylene (PTFE) as an activating, carbiding additive in azide SHS – together with partial substitution of technical carbon by 5–15 % – substantially increases the SiC phase fraction in the synthesized highly dispersed TiN–SiC powders, while reducing or completely eliminating the secondary Si_3N_4 phase. As a result, the experimental phase compositions obtained with PTFE agree much more closely with the theoretical stoichiometric predictions than those produced by the traditional azide SHS route using halide salts.

The drawback is that PTFE can lead to large mass losses of solid product (up to 88.7 %) due to scattering by vigorously evolving gases. Bulk charges showed higher losses on average (72.9 %) than pressed charges (44.3 %), and their products contained more impurities (average 7.64 % vs 6.22 %). The best balance of low loss and low impurity was achieved with 15 % PTFE replacing carbon in pressed charges across all five TiN:SiC ratios (4:1, 2:1, 1:1, 1:2, 1:4). The corresponding mass losses were 29.5, 32.6, 35.5, 45.5, 77.5 %, and the impurity contents were 3.0, 4.3, 5.3, 7.3, 3.6 %, respectively. These conditions are promising candidates for further study toward commercial production of composite, highly dispersed TiN–SiC powders by azide SHS with PTFE.

Further research should be conducted in pilot-scale SHS reactors (SHS-20 and SHS-30, with volumes of 20 and 30 L, respectively) capable of accommodating kilogram-scale charges, rather than in a small 4.5 L laboratory reactor limited to ≤50 g [27; 35]. Increasing the charge mass is expected to enhance self-heating during SHS, leading to a longer and higher thermal profile due to reduced specific heat losses from the surface compared with smaller charges (≤50 g). This effect should promote more complete formation of the TiN and SiC phases and reduce the total impurity content (Si + Si_3N_4) to well below 7.3 %. To reduce losses of the target powder products caused by scattering during vigorous gas evolution in combustion – reaching 77.5 % in one of the recommended variants – the charge should be placed in filtering assemblies when burned in pilot-scale reactors. These assemblies are hollow cylindrical frames made of metal mesh or thin steel sheet with numerous drilled perforations and gas-permeable inner liners of carbon fabric or fiberglass [35]. In addition, scattering-related mass loss can be further reduced by increasing the initial nitrogen pressure in the reactor. For example, in our previous study [31] on azide SHS of the Si_3N_4:SiC = 1:4 composition from a pressed PTFE-containing charge, raising the initial nitrogen pressure from 3 to 4 MPa led to a nearly twofold decrease in Δm – from 80.4 to 41.9 % – while maintaining a comparable phase composition of the washed combustion product. With these measures, scattering-related losses in the other recommended variants can be reduced to well below 30 %.

References / Список литературы

1. Kim Y.-W., Malik R. SiC ceramics, structure, processing and properties. In: *Encyclopedia of Materials: Technical Ceramics and Glasses*. Ed. M. Pomeroy. Oxford: Elsevier, 2021. Vol. 2. P. 150–164. https://doi.org/10.1016/B978-0-12-818542-1.00022-9
2. Ruys A.J. Silicon carbide ceramics. Structure, properties and manufacturing. 1st ed. Elsevier, 2023. 586 p.
3. Oguntuyi S.D., Nyembwe K., Shongwe M.B., Johnson O.T., Adewumi J.R., Malatji N., Olubambi P.A. Improvement on the fabrication of SiC materials: Processing, reinforcing phase, fabricating route – A review. *International Journal of Lightweight Materials and Manufacture*. 2023;6(2):225–237. https://doi.org/10.1016/j.ijlmm.2022.10.005
4. Wing Z.N. TiN modified SiC with enhanced strength and electrical properties. *Journal of the European Ceramic Society*. 2017;37(4):1373–1378. https://doi.org/10.1016/j.jeurceramsoc.2016.11.007
5. Bobovich B.B. Nonmetallic structural materials: Textbook. Moscow: MGIU, 2009. 384 p. (In Russ.).

   Бобович Б.Б. Неметаллические конструкционные материалы: Учеб. пос. М.: МГИУ, 2009. 384 с.
6. Khodaei M., Yaghobizadeh O., Alhosseini S.N., Esmaeeli S., Mousavi S.R. The effect of oxide, carbide, nitride and boride additives on properties of pressureless sintered SiC: A review. *Journal of the European Ceramic Society*. 2019;39(7):2215–2231. https://doi.org/10.1016/j.jeurceramsoc.2019.02.042
7. Malik R., Kim Y.W. Effect of nitride addition on the electrical and thermal properties of pressureless solid-state sintered SiC ceramics. *Journal of the Korean Ceramic Society*. 2022;59(5):589–594. https://doi.org/10.1007/s43207-022-00190-4
8. Cai N., Guo D., Wu G., Xie F., Tan S., Jiang N., Li H. Decreasing resistivity of silicon carbide ceramics by incorporation of graphene. *Materials*. 2020;13(16):3586. https://doi.org/10.3390/ma13163586
9. Faeghinia A. Comparing the effects of different sintering aids on spark plasma sintering of SiC ceramics. *Synthesis and Sintering*. 2024;4(2):79–86. https://doi.org/10.53063/synsint.2024.42187
10. Prochazka S., Scanlan R.M. Effect of boron and carbon on sintering of SiC. *Journal of the American Ceramic Society*. 1975;58(1-2):72. https://doi.org/10.1111/j.1151-2916.1975.tb18990.x
11. Sahani P., Karak S.K., Mishra B., Chakravarty D., Chaira D. Effect of Al addition on SiC–B_4C cermet prepared by pressureless sintering and spark plasma sintering methods. *International Journal of Refractory Metals and Hard Materials*. 2016;57:31–41. https://doi.org/10.1016/j.ijrmhm.2016.02.005
12. Zhang Z., Xu C., Du X., Li Z., Wang J., Xing W., Sheng Y., Wang W., Fu Z. Synthesis mechanism and mechanical properties of TiB_2–SiC composites fabricated with the B_4C–TiC–Si system by reactive hot pressing. *Journal of Alloys and Compounds*. 2015;619:26–30. https://doi.org/10.1016/j.jallcom.2014.09.030
13. Ahmoye D., Bucevac D., Krstic V.D. Mechanical properties of reaction sintered SiC–TiC composite. *Ceramics International*. 2018;44(12):14401–14407. https://doi.org/10.1016/j.ceramint.2018.05.050
14. Kim Y.W., Cho T.Y., Kim K.J. Efect of grain growth on electrical properties of silicon carbide ceramics sintered with gadolinia and yttria. *Journal of the European Ceramic Society*. 2015;35(15):4137–4142. https://doi.org/10.1016/j.jeurceramsoc.2015.08.006
15. Taki Y., Kitiwan M., Katsui H., Goto T. Effect of B doping on electrical and thermal properties of SiC bodies fabricated by spark plasma sintering. *Materials Today Proceedings*. 2019;16(1):211–215. https://doi.org/10.1016/j.matpr.2019.05.249
16. Malik R., Kim Y.W. Effect of AlN addition on the electrical resistivity of pressureless sintered SiC ceramics with B_4C and C. *Journal of the American Ceramic Society*. 2021; 104(12):6086–6091. https://doi.org/10.1111/jace.18003
17. Cho T.Y., Malik R., Kim Y.W., Kim K.J. Electrical and mechanical properties of pressureless sintered SiC–Ti_2CN composites. *Journal of the European Ceramic Society*. 2018;38(9):3064–3072. https://doi.org/10.1016/j.jeurceramsoc.2018.03.040
18. Samsonov G.V., Vinitskii I.M. Refractory compounds: Handbook. 2nd ed. Moscow: Metallurgiya, 1976. 558 p. (In Russ.).

   Самсонов Г.В., Виницкий И.М. Тугоплавкие соединения: Справочник. 2-е изд. М.: Металлургия, 1976. 558 с.
19. Guo X., Yang H., Zhang L., Zhu X. Sintering behavior, microstructure and mechanical properties of silicon carbide ceramics containing different nano-TiN additive. *Ceramics International*. 2010;36(1):161–165. https://doi.org/10.1016/j.ceramint.2009.07.013
20. Zhang L., Yang H., Guo X., Shen J., Zhu X. Preparation and properties of silicon carbide ceramics enhanced by TiN nanoparticles and SiC whiskers. *Scripta Materialia*. 2011;65(3):186–189. https://doi.org/10.1016/j.scriptamat.2011.03.034
21. Kim K.J., Lim K.-Y., Kim Y.-W. Electrically and thermally conductive SiC ceramics. *Journal of the Ceramic Society of Japan*. 2014;122(1431):963–966. https://doi.org/10.2109/jcersj2.122.963
22. Kiesler D., Bastuck T., Theissmann R., Kruis F.E. Plasma synthesis of titanium nitride, carbide and carbonitride nanoparticles by means of reactive anodic arc evaporation from solid titanium. *Journal of Nanoparticle Research*. 2015;17(3):152. https://doi.org/10.1007/s11051-015-2967-8
23. Dekker J.P., van der Put P.J., Veringa H.J., Schoonman J. Vapor-phase synthesis of titanium nitride powder. *Journal of Materials Chemistry*. 1994;4(5):689–694. https://doi.org/10.1039/JM9940400689
24. Basu B., Balani K. Advanced structural ceramics. Hoboken. New Jersey: John Wiley & Sons, Inc., 2011. 502 p.
25. Palmero P. Structural ceramic nanocomposites: A review of properties and powders' synthesis methods. *Nanomaterials*. 2015;5(2):656–696. https://doi.org/10.3390/nano5020656
26. Montanaro L., Palmero P. Advances in the field of nanostructured ceramic composites. *Ceramics*. 2019;2(2): 296–297. https://doi.org/10.3390/ceramics2020024

27. Rogachev A.S., Mukasyan A.S. Combustion for material synthesis. New York: CRC Press, 2014. 424 p. https://doi.org/10.1201/b17842

Рогачев А.С., Мукасьян А.С. Горение для синтеза материалов. М.: Физматлит, 2012. 400 с.

28. Levashov E.A., Mukasyan A.S., Rogachev A.S., Shtansky D.V. Self-propagating high-temperature synthesis of advanced materials and coatings. *International Materials Reviews*. 2016;62(4):1–37. https://doi.org/10.1080/09506608.2016.1243291

29. Amosov A.P., Titova Yu.V., Belova G.S., Maidan D.A., Minekhanova A.F. SHS of highly dispersed powder compositions of nitrides with silicon carbide. Review. *Powder Metallurgy and Functional Coatings*. 2022;16(4):34–57. https://doi.org/10.17073/1997-308X-2022-4-34-57

Амосов А.П., Титова Ю.В., Белова Г.С., Майдан Д.А., Минеханова А.Ф. СВС высокодисперсных порошковых композиций нитридов с карбидом кремния: Обзор. *Известия вузов. Порошковая металлургия и функциональные покрытия*. 2022;16(4):34–57. https://doi.org/10.17073/1997-308X-2022-4-34-57

30. Амосов А.П., Титова Ю.В., Уварова И.А., Белова Г.С. Азидный самораспространяющийся высокотемпературный синтез высокодисперсной порошковой композиции AlN–SiC с применением политетрафторэтилена. *Известия вузов. Порошковая металлургия и функциональные покрытия*. 2024;18(6):28–43. https://doi.org/10.17073/1997-308X-2024-6-28-43

Amosov A.P., Titova Yu.V., Uvarova I.A., Belova G.S. Azide self-propagating high-temperature synthesis of a highly dispersed AlN–SiC powder composition using polytetrafluoroethylene. *Powder Metallurgy and Functional Coatings*. 2024; 18(6):28–43. https://doi.org/10.17073/1997-308X-2024-6-28-43

31. Uvarova I.A., Amosov A.P., Titova Yu.V., Novikov V.A. Self-propagating high-temperature synthesis of a highly dispersed Si_3N_4–SiC ceramic powders composition using sodium azide and polytetrafluoroethylene. *Powder Metallurgy and Functional Coatings*. 2025;19(3):25–38. https://doi.org/10.17073/1997-308X-2025-3-25-38

Уварова И.А., Амосов А.П., Титова Ю.В., Новиков В.А. Самораспространяющийся высокотемпературный синтез высокодисперсной композиции керамических порошков Si_3N_4–SiC с применением азида натрия и политетрафторэтилена. *Известия вузов. Порошковая металлургия и функциональные покрытия*. 2025;19(3):25–38. https://doi.org/10.17073/1997-308X-2025-3-25-38

32. Khachatryan G.L., Arutyunyan A.B., Kharatyan S.L. Activated combustion of a silicon–carbon mixture in nitrogen and SHS of Si_3N_4–SiC composite ceramic powders and silicon carbide. *Combustion, Explosion, and Shock Waves*. 2006;42(5):543–548. https://doi.org/10.1007/S10573-006-0086-7

Хачатрян Г.Л., Арутюнян А.Б., Харатян С.Л. Активированное горение смеси кремний–углерод в азоте и СВС композиционных керамических порошков Si_3N_4/SiC и карбида кремния. *Физика горения и взрыва*. 2006;42(5):56–62.

33. Amirkhanyan N., Kirakosyan H., Zakaryan M., Zurnachyan A., Rodriguez M.A., Abovyan L., Aydinyan S. Sintering of silicon carbide obtained by combustion synthesis. *Ceramics International*. 2023;49(15):26129–26134. https://doi.org/10.1016/j.ceramint.2023.04.233

34. Amosov A.P., Belova G.S., Titova Yu.V., Maidan D.A. Synthesis of highly dispersed powder ceramic composition Si_3N_4–SiC by combustion of components in the Si–C–NaN_3–NH_4F system. *Russian Journal of Inorganic Chemistry*. 2022;67(2):123–130. https://doi.org/10.1134/S0036023622020024

Амосов А.П., Белова Г.С., Титова Ю.В., Майдан Д.А. Синтез высокодисперсной порошковой керамической композиции Si_3N_4–SiC при горении компонентов в системе Si–C–NaN_3–NH_4F. *Журнал неорганической химии*. 2022;67(2):139–147. https://doi.org/10.31857/S0044457X22020027

35. Amosov A.P., Bichurov G.V. Azide technology of self-propagating high-temperature synthesis of micro- and nanopowders of nitrides. Moscow: Mashinostroenie-1, 2007. 526 p. (In Russ.).

Амосов А.П., Бичуров Г.В. Азидная технология самораспространяющегося высокотемпературного синтеза микро- и нанопорошков нитридов. М.: Машиностроение-1, 2007. 526 с.

Information about the Authors

Irina A. Uvarova – Engineer of the Department of Metallurgy, Powder Metallurgy, Nanomaterials (MPMN), Samara State Technical University (SamSTU)
ORCID: 0000-0003-3023-3289
E-mail: mr.simple2@mail.ru

Aleksandr P. Amosov – Dr. Sci. (Phys.-Math.), Professor, Head of the Department of MPMN, SamSTU
ORCID: 0000-0003-1994-5672
E-mail: egundor@yandex.ru

Yuliya V. Titova – Cand. Sci. (Eng.), Associate Professor of the Department of MPMN, SamSTU
ORCID: 0000-0001-6292-280X
E-mail: titova600@mail.ru

Сведения об авторах

Ирина Александровна Уварова – инженер кафедры «Металловедение, порошковая металлургия, наноматериалы» (МПМН), Самарский государственный технический университет (СамГТУ)
ORCID: 0000-0003-3023-3289
E-mail: mr.simple2@mail.ru

Александр Петрович Амосов – д.ф.-м.н., профессор, заведующий кафедрой МПМН, СамГТУ
ORCID: 0000-0003-1994-5672
E-mail: egundor@yandex.ru

Юлия Владимировна Титова – к.т.н., доцент кафедры МПМН, СамГТУ
ORCID: 0000-0001-6292-280X
E-mail: titova600@mail.ru

Anton A. Ermoshkin – Cand. Sci. (Eng.), Head of the Testing Center of IT-Service LLC
ORCID: 0009-0005-6679-7133
E-mail: nerev89@yandex.ru

Антон Александрович Ермошкин – к.т.н., начальник Испытательного центра ООО «ИТ-Сервис»
ORCID: 0009-0005-6679-7133
E-mail: nerev89@yandex.ru

Contribution of the Authors

I. A. Uvarova – conducted combustion-mode synthesis experiments on powder compositions; prepared and formatted experimental results; participated in the analysis and discussion of the findings; contributed to writing the manuscript.
A. P. Amosov – defined the research objective; summarized the obtained results; wrote and edited the manuscript.
Yu. V. Titova – formulated the research tasks; planned the experiments; analyzed and discussed the results; contributed to writing the manuscript.
A. A. Ermoshkin – performed XRD analyses of synthesized powder compositions, participating in the analysis and discussion of the results.

Вклад авторов

И. А. Уварова – проведение экспериментов по синтезу порошковых композиций в режиме горения, подготовка и оформление результатов экспериментов, участие в анализе и обсуждении результатов, участие в написании статьи.
А. П. Амосов – определение цели работы, обобщение полученных результатов, написание и редактирование текста статьи.
Ю. В. Титова – постановка задач исследований, планирование экспериментов, анализ и обсуждение результатов, участие в написании статьи.
А. А. Ермошкин – проведение РФА-исследований синтезированных порошковых композиций, участие в анализе и обсуждении результатов.

Received 20.06.2025
Revised 11.08.2025
Accepted 18.08.2025

Статья поступила 20.06.2025 г.
Доработана 11.08.2025 г.
Принята к публикации 18.08.2025 г.

Refractory, Ceramic, and Composite Materials
Тугоплавкие, керамические и композиционные материалы

UDC 669.2
https://doi.org/10.17073/1997-308X-2025-5-51-59

Research article
Научная статья

Structure and properties of an aluminum-matrix composite reinforced with zirconium carbide particles

M. L. Khazin, R. A. Apakashev, V. E. Adas

Ural State Mining University
30 Kuibysheva Str., Ekaterinburg 620144, Russia

Khasin@ursmu.ru

Abstract. This study examines the structure and mechanical properties of aluminum-matrix composites (AMCs) with varying contents of the ZrC reinforcing phase, produced by powder metallurgy. Elemental mapping together with hardness measurements indicate a uniform distribution of ZrC particles in the matrix. The effects of mixing time (1–6 h), compaction pressure (636–1910 MPa), and sintering time (1–2 h) on density, porosity, and properties were investigated. With increasing ZrC content, the composite's mechanical properties improve, and correlations among density, porosity, hardness, and strength are observed. An increase in sintering time has little effect on density and porosity; after sintering, hardness decreases due to annealing. Local agglomeration of ZrC at grain boundaries may weaken interfacial bonding between aluminum and the reinforcement. Strengthening arises from load transfer, Orowan strengthening, and thermally induced dislocations due to the coefficient-of-thermal-expansion mismatch between the particles and the matrix. Efficient load transfer during compression testing requires good particle–matrix interfacial contact; dislocation–particle interactions generate Orowan loops, contributing to the observed strengthening.

Keywords: aluminum-matrix composites (AMCs), zirconium carbide, density, porosity, structure, morphology, hardness, strength, deformation

For citation: Khazin M.L., Apakashev R.A., Adas V.E. Structure and properties of an aluminum-matrix composite reinforced with zirconium carbide particles. *Powder Metallurgy and Functional Coatings*. 2025;19(5):51–59.
https://doi.org/10.17073/1997-308X-2025-5-51-59

Структура и свойства алюмоматричного материала, упрочненного частицами карбида циркония

М. Л. Хазин, Р. А. Апакашев, В. Е. Адас

Уральский государственный горный университет
Россия, 620144, г. Екатеринбург, ул. Куйбышева, 30

Khasin@ursmu.ru

Аннотация. Представлены результаты исследования структуры и физико-механических свойств дисперсно-упрочненных композиционных материалов на основе алюминия с различным содержанием упрочняющей фазы ZrC, полученных методом порошковой металлургии. Согласно картам распределения химических элементов наполнителя и значениям твердости, частицы карбида циркония распределены в матрице равномерно. Изучено влияние времени перемешивания (от 1 до 2 ч) и усилия прессования (от 636 до 1910 МПа) на плотность, пористость и свойства образцов. С повышением количества частиц карбида циркония механические свойства композита улучшаются. Отмечена корреляция плотности, пористости, твердости и прочности композитов. Показано, что увеличение времени спекания практически не оказало влияния на плотность и пористость образцов. После спекания твердость образцов уменьшается вследствие отжига. Кроме того, скопления частиц ZrC на границах зерен могут ослабить химическую связь между алюминием и материалом наполнителя. В исследуемых композитах упрочнение происходит за счет следующих механизмов: передача активной

нагрузки от матрицы к арматуре; усиления Орована; возникновение внутренних термических напряжений из-за разницы в коэффициентах теплового расширения между армирующими частицами и фазой матрицы. Эффективная передача нагрузки между пластичной матрицей и частицами жесткой керамической арматуры при испытаниях на сжатие происходит при наличии хорошего межфазного контакта между матрицей и арматурой. Взаимодействие между дислокациями и армирующими частицами увеличивает прочность композиционных материалов в соответствии с механизмом Орована. Благодаря наличию в матрице дисперсных частиц армирования, при взаимодействии дислокаций с армирующими частицами образуются дислокационные петли.

Ключевые слова: спеченный дисперсно-упрочненный композиционный материал, карбид циркония, плотность, пористость, структура, морфология, твердость, прочность, деформация

Для цитирования: Хазин М.Л., Апакашев Р.А., Адас В.Е. Структура и свойства алюмоматричного материала, упрочненного частицами карбида циркония. *Известия вузов. Порошковая металлургия и функциональные покрытия*. 2025;19(5):51–59. https://doi.org/10.17073/1997-308X-2025-5-51-59

Introduction

Modern mechanical engineering, including the mining industry, is increasingly characterized by the use of new materials. The growing demand for lightweight materials with high specific strength, excellent high-temperature strength, and corrosion resistance stimulates active research and development of advanced high-performance materials [1–4].

Among light-weight materials with low density, aluminum-matrix composites (AMCs) occupy a leading position. The use of aluminum and its alloys as a matrix material continues to expand, finding broad applications in numerous industrial sectors due to their high strength and ductility, excellent thermal conductivity and corrosion resistance [5–7], as well as their relatively low cost compared to other light metals such as Mg and Ti [4; 8].

The global market for metal-matrix composites was estimated at USD 224.82 billion in 2023. It is projected to grow from USD 239.21 billion in 2024 to USD 369.29 billion by 2032, demonstrating a compound annual growth rate (CAGR) of 5.58 %. The increasing demand for lightweight materials in the mechanical engineering, automotive, and aerospace industries is expected to further stimulate key market drivers and contribute to market expansion[1].

The main limiting factor for the use of aluminum alloys is their relatively low hardness. Therefore, various reinforcements are incorporated into the matrix to enhance the physical and mechanical properties of aluminum-based materials. Metal-matrix composites (MMCs) are produced by different methods, including stir casting, die casting, spray forming, hot pressing, dynamic compaction, ultrasonic cavitation, physical vapor deposition, mechanical alloying, liquid-metal infiltration, and powder metallurgy (PM) [1; 2; 9; 10]. Most commercial MMCs are produced by liquid-phase methods with mechanical stirring, which makes it possible to obtain components of various sizes and geometries. However, these techniques have several drawbacks: low wettability of reinforcement particles by the molten matrix and the difficulty of achieving a uniform composite structure. Upon cooling and cessation of stirring, the reinforcement particles tend to distribute non-uniformly in the aluminum matrix, often forming agglomerates [1; 11; 12]. As a result, the composite may exhibit nonuniform mechanical behavior.

Unlike liquid-phase techniques, PM methods provide a uniform distribution of the dispersed phase within the aluminum matrix, usually prevent the formation of undesirable phases, and ensure strong interfacial bonding between the matrix metal and the reinforcing particles.

The PM method is energy-efficient, cost-effective, and technologically versatile for producing both simple and complex components of required dimensions. In recent years, PM processing has proven to be efficient and competitive compared with conventional casting methods in the fabrication of metal-matrix composites reinforced with ceramic particles. Composites fabricated by powder metallurgy generally exhibit lower density and higher porosity than those produced by stir casting; however, the reinforcement particles are uniformly distributed in the metallic matrix, unlike in stir-cast materials.

Aluminum-matrix composites produced by various methods are widely used in mechanical engineering [13], shipbuilding [14], electrical engineering [15], medicine [16] the aerospace [17] and defense [18; 19] industries, and even in consumer products [20].

Reinforcements typically include oxides, carbides, nitrides, fly ash, and carbon powders [1–3; 21; 22]. The choice of reinforcing particles depends on the intended application of the composite. The most commonly used dispersoids are SiC, TiC, ZrC, TiB_2,

[1] Metal matrix composites market size & share report. URL: https://www.marketresearchfuture.com/reports/metal-matrix-composites-mmcs-market-8131 (accessed: 16.05.2025).

B_4C, Al_2O_3, and Si_3N_4. Among them, zirconium carbide (ZrC) is one of the most suitable reinforcing materials for wear-resistant applications, seals, bearings, crucibles in the nuclear industry, and electronic devices. ZrC is characterized by a high melting point, specific strength, hardness, and corrosion resistance [23]. However, there are very few studies examining the effect of ZrC addition on the physical and mechanical properties of aluminum-matrix materials [24].

The aim of the present study is to investigate the structure and physical and mechanical properties of dispersion-strengthened aluminum-matrix composites reinforced with zirconium carbide (ZrC) particles.

Research methodology

The objects of study were aluminum-matrix composites containing different amounts of the ZrC reinforcing phase. Aluminum powder grade GOST 6058-73; 99 % purity; 250–450 μm) was used as the matrix. Zirconium carbide (ZrC) powder (GOST 28377-89; 40–100 μm) was served as the reinforcement.

The aluminum and zirconium carbide powders were mixed in a polystyrene cylinder rotating at 100 rpm for 1–6 h, with the rotation direction reversed every 15 min to enhance homogeneity.

The homogeneous powder blend was cold-pressed in a PGR-400 uniaxial hydraulic press using a hardened 40Kh steel die (ID 10.2 mm); industrial oil was applied to lubricate the die walls. The green compacts were sintered at 640 °C for 1–2 h under a protective carbon-powder layer and then furnace-cooled to room temperature.

SEM micrographs and EDS elemental maps of the aluminum-matrix composite were acquired on a Vega LMS (Tescan, Czech Republic) scanning electron microscope equipped with an Xplore30 EDS system (Oxford Instruments, UK). The microstructure was also examined using an Olympus BX61 research optical microscope (Olympus Corp., Japan).

The actual density was determined by measuring mass on an AND GR-300 electronic analytical balance (A&D Company Ltd., Japan), with volume obtained geometrically from micrometer measurements. Vickers hardness was measured on the sample surfaces using an ITV-30-AM tester (Metotest LLC, Neftekamsk, Russia) tester under a 25 N load and 15 s dwell; in accordance with GOST R ISO 6507-1-2007, five indents were made per sample. Compressive strength was measured on a MIM 2-20-2 universal testing machine (GOST LLC, Moscow, Russia) at a crosshead speed of 0.2 mm/s (GOST 25.503-97), with simultaneous stress–strain curve acquisition.

Results and discussion

Density and porosity are primary parameters for many applications. After cold compaction of the initial powder blend, the density of the material was measured in both the compacted and sintered states and compared with the theoretical density calculated by the rule of mixtures. The actual density was determined from the mass-to-volume ratio. Porosity was determined as the ratio of the difference between the theoretical and actual densities to the theoretical density. In estimating porosity, the theoretical density was assumed to remain unchanged during sintering because the composite constituents are mutually insoluble.

To select the optimal compaction pressure, trial runs were performed (Table 1). At $P = 636$ MPa, the compacts were friable, weak, and failed under slight load. Beginning at $P = 950$ MPa, dense compacts were obtained. Further increases in compaction pressure produced only minor changes in density (γ); therefore, all subsequent experiments used 980 MPa.

Analysis of the effect of compaction pressure shows that density increases with increasing reinforcement (carbide-phase) fraction (Table 1), owing to the higher density of the ZrC particles. After sintering, the density decreases. Theoretical densities exceed the measured values due to residual porosity, which likewise increases with increasing reinforcement content in the matrix.

With increasing reinforcement content, the porosity of the compacts initially rises linearly and then slows down, stabilizing at 7–10 wt. % reinforcement. After sintering, the porosity increases due to the expansion of air trapped during mixing of the initial powder blend. This expansion enlarges the pore volume and causes a corresponding change in the linear dimensions of the samples. Excessive addition of reinforcement particles also leads to matrix swelling of the sintered samples. Such porosity variations are consistent with the findings reported by other authors [1; 11].

According to the experimental data, both the “green” and sintered densities are governed by the combined and interacting effects of several factors, including compaction pressure, sintering conditions, and the compressibility of the reinforcing particles. As a result, the green and sintered densities deviate from the theoretical density of the composites.

Increasing the sintering time from 60 to 120 min had almost no effect on density and porosity, whereas for aluminum-matrix composites reinforced with SiC or Al_2O_3, an increase in sintering time from 60 to 90 min was reported to enhance density [11].

***Table. 1.* Effect of compaction pressure on the density and porosity of the samples**

***Таблица 1.* Влияние величины давления формования на плотность и пористость образцов**

Sample	*P*, MPa	γ_{theor}, kg/m^3	γ_{act}, kg/m^3		Porosity, %	
			before sintering	after sintering	before sintering	after sintering
Al	636	2700	1718	1652	36.37	38.81
	750		2081	2073	22.92	23.22
	900		2478	2469	8.22	8.56
	950		2572	2564	4.74	5.04
	960		2584	2576	4.29	4.59
	980		2604	2596	3.56	3.85
	1273		2610	2602	3.33	3.63
	1910		2612	2601	3.26	3.67
Al–4%ZrC	636	2861	1840	1832	35.68	35.96
	900		2630	2622	8.07	8.35
	950		2747	2738	3.98	4.29
	980		2760	2752	3.53	3.81
	1273		2765	2757	3.35	3.63
	1910		2769	2761	3.22	3.49
Al–7%ZrC	636	2982	1914	1906	35.81	36.08
	980		2871	2865	4.62	4.81
	1273		2875	2864	3.59	3.96
	1910		2882	2872	3.35	3.69
Al–10%ZrC	636	3103	1947	1941	37.25	37.44
	980		2984	2978	3.86	4.03
	1273		2998	2987	3.38	3.74
	1910		3007	2998	3.09	3.38

The surface morphology and elemental distribution of the synthesized samples are shown in Figs. 1 and 2. In all cases, a smooth and relatively even surface was observed. The measured surface roughness of the sample cross section was R_a = 1.0–1.2, corresponding to fine turning. Elemental mapping confirmed a sufficiently uniform distribution of the constituent elements.

The high detected oxygen content, and correspondingly lower total aluminum content, are explained by the formation of an Al_2O_3 film on the aluminum surface exposed to air (2 mol Al → 3 mol O). According to the analysis, the ratio was 1.87 mol Al and 2.64 mol O. This oxygen amount oxidizes most of the surface aluminum (1.76 mol Al), leaving 0.11 mol Al unoxidized.

Hardness is one of the key parameters directly influencing the strength, impact toughness, fatigue strength, and wear resistance of metal-matrix composites. It is well known that hardness testing is one of the most informative and rapid methods for assessing mechanical properties.

For the composites investigated in this study, variation of the mixing time from 1 to 6 h had virtually no effect on hardness (Fig. 3).

Increasing the sintering time from 60 to 120 min caused a 3.7–8.6 % increase in hardness (Fig. 4). However, as the reinforcement content increased, the relative hardness change decreased, approaching a steady value of 3.7–3.8 %.

To assess the uniformity of particle distribution, hardness measurements were taken along the polished surface of the sintered samples at 2.5 mm intervals. The small variation in hardness (±2.6 %) confirmed uniform particle dispersion in the aluminum matrix, consistent with the elemental maps.

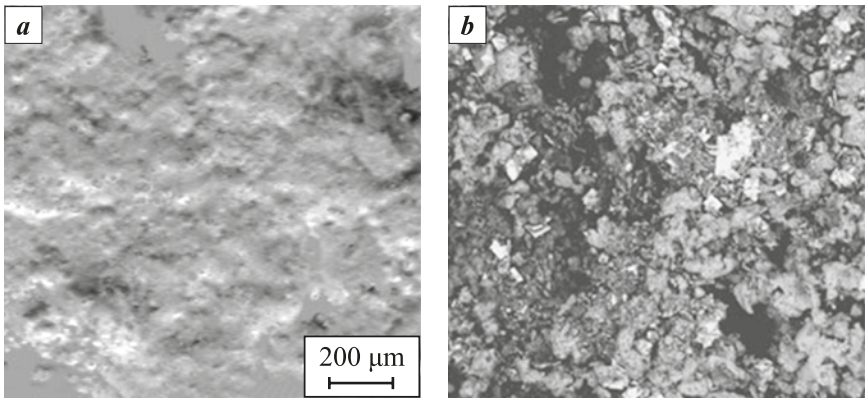

Fig. 1. SEM images of the surface of an Al–5%ZrC sample
a – SEM secondary-electron (SE) image; ***b*** – SEM backscattered-electron (BSE) image

Рис. 1. Морфология поверхности образца Al–5%ZrC
a – топо изображение; ***b*** – электронное изображение

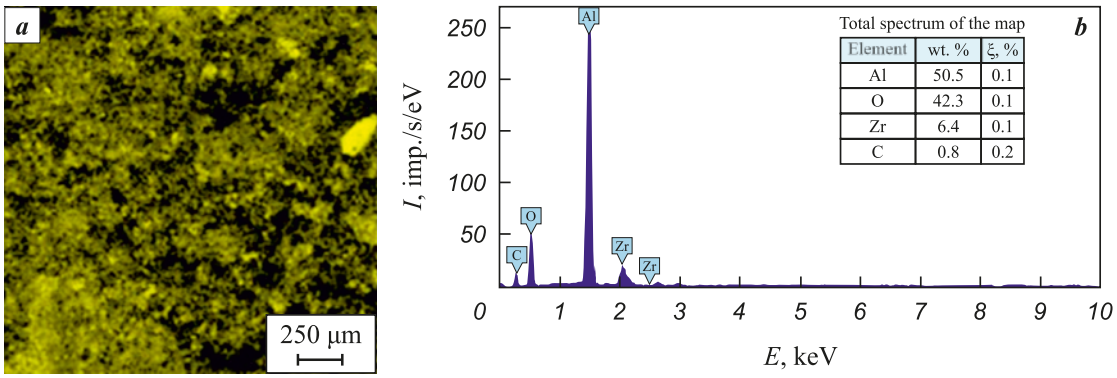

Fig. 2. Elemental distribution map and corresponding EDS spectrum
a – surface of the Al–4%ZrC sample; ***b*** – EDS spectrum showing elemental composition

Рис. 2. Карта распределения элементов
a – по поверхности образца Al–4%ZrC; ***b*** – суммарное распределение элементов

With increasing ZrC content in the aluminum matrix, the composite hardness increased (Table 2). After sintering, hardness decreased due to annealing. In addition, clustering of ZrC particles at grain boundaries may weaken interfacial bonding between aluminum and the reinforcement.

Previous studies have reported a correlation between hardness and density (or porosity) of the samples [1; 3; 6; 7]. A similar proportional relationship between hardness and density (porosity) was also observed in this study (Fig. 5).

The compressive strength of the composites was determined by compression testing. Unlike tension tests, not all materials can be brought to failure under compression, as ductile metals such as aluminum tend to deform into thin plates.

With increasing reinforcement content, the compressive strength increased similarly to hardness. Composites containing carbide particles exhibited a substantial strength improvement compared with the unreinforced aluminum matrix, indicating that ZrC particles provide a strong strengthening effect.

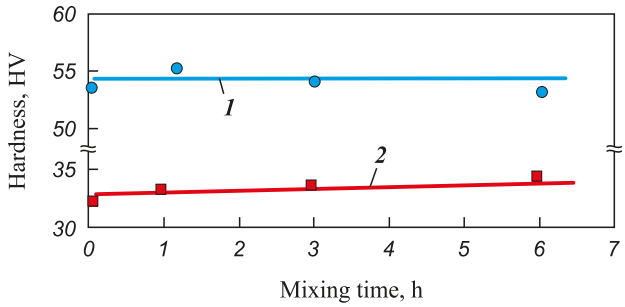

Fig. 3. Effect of mixing time on the hardness of Al–4%ZrC samples
1 – before sintering; ***2*** – after sintering

Рис. 3. Влияние времени перемешивания на твердость образцов Al–4%ZrC
1 – до спекания; ***2*** – после спекания

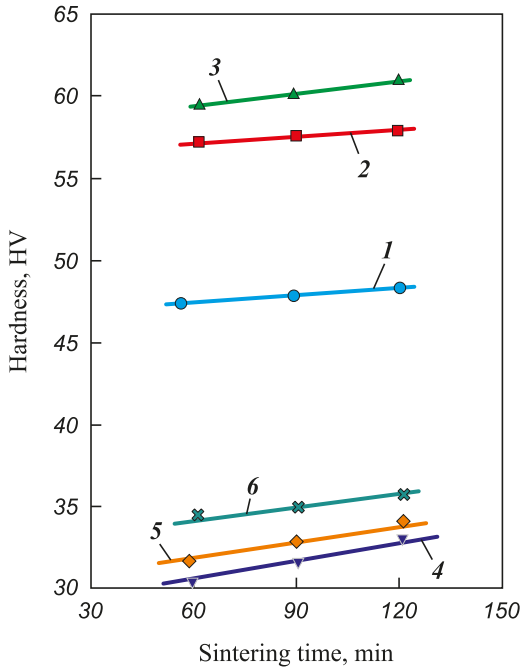

Fig. 4. Effect of sintering time on the hardness of the samples

1–3 – before sintering; ***4–6*** – after sintring
1, ***4*** – Al–0%ZrC; ***2***, ***5*** – Al–4%ZrC; ***3***, ***6*** – Al–10%ZrC

Рис. 4. Влияние времени спекания на твердость образцов

1–3 – до спекания; ***4–6*** – после спекания
1, ***4*** – Al–0%ZrC; ***2***, ***5*** – Al–4%ZrC; ***3***, ***6*** – Al–10%ZrC

As the ZrC content increased, both the ultimate strength and yield strength of the composites rose (Fig. 6). The strengthening can be attributed to the higher dislocation density and the role of carbide particles as barriers to dislocation motion.

The relative strength increase of the composites compared with the aluminum matrix ranged from 20 to 50 %. The addition of carbide particles to an aluminum alloy has a positive effect on mechanical properties. The obtained results are consistent with the reported compressive strength of Al–ZrC composites produced by powder metallurgy [24] and by friction stir processing method [25].

Table 2. **Effect of composition on the hardness of composites**

Таблица 2. **Влияние состава на твердость композитов**

Sample	Hardness, HV	
	before sintering	after sintering
Al–0%ZrC	48.38	31.44
Al–4%ZrC	57.42	32.76
Al–7%ZrC	59.75	33.57
Al–10%ZrC	60.42	34.88

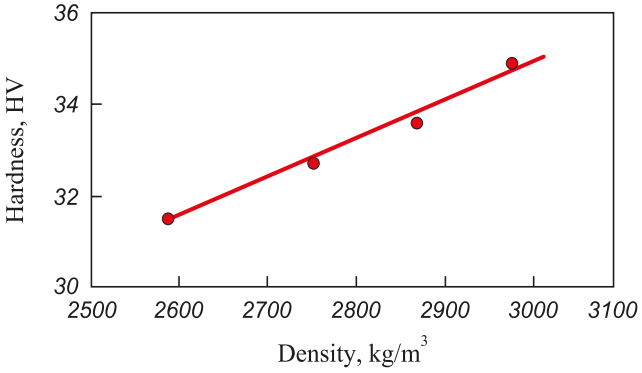

Fig. 5. Effect of density on the hardness of Al–ZrC samples after sintering

Рис. 5. Зависимость твердости от плотности образцов Al–ZrC после спекания

Several strengthening mechanisms contribute to the improved performance of metal-matrix composites, the most important being thermal-expansion mismatch and elastic-modulus mismatch between the matrix and the reinforcement (Hall–Petch relationship and Orowan mechanism).

In the studied composites, strengthening arises from load transfer from the matrix to the reinforcement, Orowan strengthening, and the generation of internal thermal stresses due to the difference in the coefficients of thermal expansion (CTE) between the reinforcement particles and the aluminum matrix. Effective load

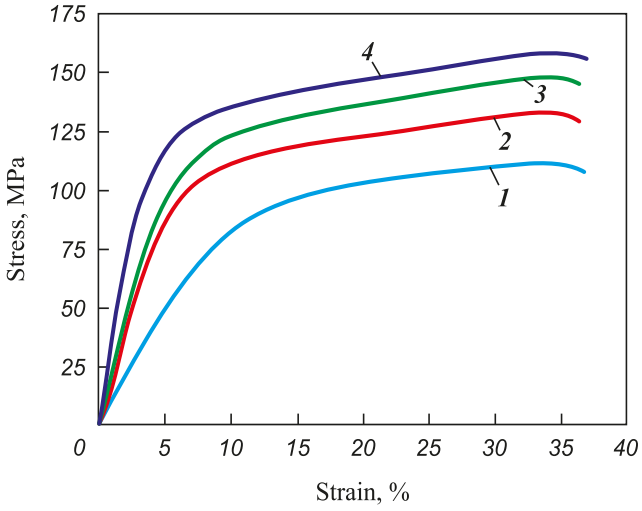

Fig. 6. Compression stress–strain curves of the samples

1 – Al–0%ZrC; ***2*** – Al–4%ZrC; ***3*** – Al–7%ZrC; ***4*** – Al–10%ZrC

Рис. 6. Диаграммы деформации образцов, полученные при испытаниях на сжатие

1 – Al–0%ZrC; ***2*** – Al–4%ZrC; ***3*** – Al–7%ZrC; ***4*** – Al–10%ZrC

transfer between the ductile matrix and hard ceramic reinforcement particles during tension or compression occurs when good interfacial contact exists between the two phases.

Interactions between dislocations and reinforcement particles enhance the composite strength according to the Orowan mechanism. The presence of dispersed reinforcement particles in the matrix leads to the formation of dislocation loops as dislocations bypass the particles.

Conclusion

Based on the results of the conducted study, the following conclusions can be drawn:

1. Fabrication of Al–ZrC composites by the powder metallurgy method ensures a uniform distribution of zirconium carbide particles within the aluminum matrix, as confirmed by microstructural observations and hardness measurements.

2. Increasing the zirconium carbide content from 0 to 10 wt. % leads to higher density and porosity of the aluminum-matrix composite. The porosity of the samples initially increases linearly with reinforcement content, followed by a slowdown and stabilization at 7–10 wt. % reinforcement.

3. The hardness and strength of the composites increase proportionally with reinforcement content. With a zirconium carbide content of up to 10 wt. %, the hardness and strength of the composites rise by 11 and 52 %, respectively.

4. Increasing the mixing time from 1 to 6 h has little effect on the hardness of the composite material: the relative change was 0.5–0.8 % for green compacts and 2.6–3.2 % for sintered samples.

5. With an increase in sintering time from 1 to 2 h, hardness of the samples rises from 3.7 to 8.6 %, but as the reinforcement content in the matrix increases, it decreases and approaches a steady value of 3.7–3.8 %.

References / Список литературы

1. Aynalem G.F. Processing methods and mechanical properties of aluminium matrix composites. *Advances in Materials Science and Engineering*. 2020;2020(2):1–19. https://doi.org/10.1155/2020/3765791
2. Konopatsky A.S., Yusupov Kh.U., Corthay S., Matveev A.T., Kovalskii A.M., Shtansky D.V. High-strength composite materials based on aluminum reinforced by micro and nanostructures (mini review). *Powder Metallurgy and Functional Coatings*. 2018;(4):62–72. (In Russ.). https://doi.org/10.17073/1997-308X-2018-4-62-72

   Конопацкий А.С., Юсупов Х.У., Corthay S., Матвеев А.Т., Штанский Д.В. Высокопрочные композиционные материалы на основе алюминия, упрочненные микро- и наноструктурами (миниобзор). *Известия вузов. Порошковая металлургия и функциональные покрытия*. 2018;(4):62–72. https://doi.org/10.17073/1997-308X-2018-4-62-72
3. Kumar S.R., Armstrong M., Sivaneswaran M., Prakash V.S., Prasad S.S., Vishnu Sankar B.P. Characteristics enhancement of mechanical properties of aluminum metal matrix composites reinforced with silicon carbide using stir casting technique. *SAE Technical Paper*. 2024;2023-01-5164. https://doi.org/10.4271/2023-01-5164
4. Ujah C.O., Von Kallon D.V. Trends in aluminium matrix composite development. *Crystals*. 2022;12(10):1357. https://doi.org/10.3390/cryst12101357
5. Mussatto A., Ahad I.U.I., Mousavian R.T., Delaure Y., Brabazon D. Advanced production routes for metal matrix composites. *Engineering Reports*. 2021;3(5):e12330. https://doi.org/10.1002/eng2.12330
6. Garg P., Jamwal A., Kumar D., Sadasivuni K.K., Hussain C.M., Gupta P. Advance research progresses in aluminium matrix composites: Manufacturing & applications. *Journal of Materials Research and Technology*. 2019;8(5): 4924–4939. https://doi.org/10.1016/j.jmrt.2019.06.028
7. Kar A., Sharma A., Kumar S. A critical review on recent advancements in aluminium-based metal matrix composites. *Crystals*. 2024;14:412. https://doi.org/10.3390/cryst14050412
8. Kurganova Yu.A., Kolmakov A.G. Structural metal matrix composite materials. Moscow: Publ. MSTU, 2015. 144 p. (In Russ.).

   Курганова Ю.А., Колмаков А.Г. Конструкционные металломатричные композиционные материалы. М.: Изд-во МГТУ, 2015. 144 с.
9. Parikh V.K., Patel V., Pandya D.P., Andersson J. Current status on manufacturing routes to produce metal matrix composites: State-of-the-art. *Heliyon*. 2023;9(2):e13558. https://doi.org/10.1016/j.heliyon.2023.e13558
10. Ruzic J., Simić M., Stoimenov N., Božić D., Stašić J. Innovative processing routes in manufacturing of metal matrix composite materials. *Metallurgical and Materials Engineering*. 2021;27(1):1–13. https://doi.org/10.30544/629
11. Nayak K.C., Rane K.K., Date P.P., Srivatsan T.S. Synthesis of an aluminum alloy metal matrix composite using powder metallurgy: Role of sintering parameters. *Applied Sciences*. 2022;12:8843. https://doi.org/10.3390/app12178843
12. Khazin M.L., Apakashev R.A., Davydov S.Ya. Obtaining aluminum-matrix composite materials particulate-reinforced with ceramic particles. *Refractories and Industrial Ceramics*. 2022;63(3):291–296. https://doi.org/10.1007/s11148-022-00719-4
13. Purohit R., Qureshi M., Jain A. Forming behaviour of aluminium matrix nano Al_2O_3 composites for automotive applications. *Advances in Materials and Processing Tech-*

nologies. 2020;6(6):272–283. https://doi.org/10.1080/2374068X.2020.1731665

14. Vinod B., Ramanathan S., Ananthi V., Selvakumar N. Fabrication and characterization of organic and in-organic reinforced A356 aluminium matrix hybrid composite by improved double-stir casting. *Silicon*. 2019;11:817–829. https://doi.org/10.1007/s12633-018-9881-5
15. Ujah C., Popoola A., Popoola O., Aigbodion V.S. Influence of CNTs addition on the mechanical, microstructural, and corrosion properties of Al alloy using spark plasma sintering technique. *International Journal of Advanced Manufacturing Technology*. 2020; 106:2961–2969. https://doi.org/10.1007/s00170-019-04699-7
16. Singh N., Belokar R.M. Tribological behavior of aluminum and magnesium-based hybrid metal matrix composites: A state-of-art review. *Materials Today: Proceedings*. 2021;44(1):460–466. https://doi.org/10.1016/j.matpr.2020.09.757
17. Kumar N., Das A. Ecofriendly energy efficient welding of aluminium matrix composites for aerospace applications: A state of art review. *Materials Today: Proceedings*. 2020;26(2):1666–1675. https://doi.org/10.1016/j.matpr.2020.02.352
18. Mohanavel V., Ravichandra, M., Kumar S.S. Tribological and mechanical properties of zirconium di-boride (ZrB_2) particles reinforced aluminium matrix composites. *Materials Today: Proceedings*. 2020;21(1):862–864. https://doi.org/10.1016/j.matpr.2019.07.603
19. Talalaeva G.V., Paznikova S.N. Modern composite materials: prospects and risks of their use in the field of integrated security and civil defense. *Tekhnologii grazhdanskoi bezopasnosti*. 2023;1(75):107–114. (In Russ.).

    Талалаева Г.В., Пазникова С.Н. Современные композиционные материалы: перспективы и риски применения их в области комплексной безопасности и гражданской обороны. *Технологии гражданской безопасности*. 2023;1(75):107–114.
20. Khan M., Zulfaqar M., Ali F., Subhani T. Hybrid aluminium matrix composites containing boron carbide and quasicrystals: Manufacturing and characterisation. *Materials Science and Technology*. 2017;33(16):1955–1963. https://doi.org/10.1080/02670836.2017.1342017
21. Ibrahim T.K., Yawas D.S., Thaddaeus J., Danasabe B, lliyasu I., Adebisi A.A., Ahmadu T.O. Development, modelling and optimization of process parameters on the tensile strength of aluminum, reinforced with pumice and carbonated coal hybrid composites for brake disc application. *Scietific Reports*. 2024;14:16999. https://doi.org/10.1038/s41598-024-67476-x
22. Seputra Y.E.A., Soegijono B. Engineering of aluminium matrix composite (AMC) reinforcement organoclay based on hotpress method using adaptive neuro-fuzzy inference system (ANFIS). *IOP Conference Series: Materials Science and Engineering*. 2019;509(1):012156. https://doi.org/10.1088/1757-899X/509/1/012156
23. Ağaoğullari D., Gökçe H., Genç A., Duman İ., Öveçoğlu M.L. Characterization of mechanically alloyed and sintered ZrC particulate reinforced Al matrix composites. In: *Proc. of 19th International Conference on Metallurgy and Materials* (METAL 2010). TANGER Ltd. Metal, 2010. P. 702–708.
24. Cug H., Zengin O. Investigation of microstructural and mechanical properties of zirconium carbide reinforced aluminum matrix nanocomposites. *Acta Physica Polonica Series A*. 2019;135(5):870–872. https://doi.org/10.12693/APhysPolA.135.870
25. Sundarrajan S., Satish Kumar T., Suganya Priyadharshini G. Production and characterization of Al6061/zirconium carbide surface composites. *International Journal of Materials Research*. 2020;111(8):639–644. https://doi.org/10.3139/146.111926

Information about the Authors

Mark L. Khazin – Dr. Sci. (Eng.), Professor, Department of Mining Equipment Operation, Ural State Mining University (USMU)
ORCID: 0000-0002-6081-4474
E-mail: Khasin@ursmu.ru

Rafail A. Apakashev – Dr. Sci. (Chem.), Professor, Department of Chemistry, USMU
ORCID: 0000-0002-9006-3667
E-mail: parknedra@yandex.com

Vitalii E. Adas – Senior Lecturer, Department of Mining Equipment Operation, USMU
ORCID: 0000-0001-7912-8047
E-mail: adas.v@m.ursmu.ru

Сведения об авторах

Марк Леонтьевич Хазин – д.т.н., профессор кафедры эксплуатации горного оборудования Уральского государственного горного университета (УГГУ)
ORCID: 0000-0002-6081-4474
E-mail: Khasin@ursmu.ru

Рафаил Абдрахманович Апакашев – д.х.н., профессор кафедры химии УГГУ
ORCID: 0000-0002-9006-3667
E-mail: parknedra@yandex.com

Виталий Егорович Адас – ст. преподаватель кафедры эксплуатации горного оборудования УГГУ
ORCID: 0000-0001-7912-8047
E-mail: adas.v@m.ursmu.ru

Contribution of the Authors

M. L. Khazin – scientific supervision, development of the main concept, formulation of the research objectives and tasks, manuscript preparation, and formulation of conclusions.
R. A. Apakashev – development of the main concept, formulation of the research objectives and tasks, preparation and revision of the manuscript, and revision of conclusions.
V. E. Adas – preparation and performance of experiments, and formulation of conclusions.

Вклад авторов

М. Л. Хазин – научное руководство, формирование основной концепции, постановка цели и задачи исследования, подготовка текста, формулировка выводов.
Р. А. Апакашев – формирование основной концепции, постановка цели и задачи исследования, подготовка текста, корректировка текста, корректировка выводов.
В. Е. Адас – подготовка эксперимента, проведение экспериментов, формулировка выводов.

Received 09.01.2025
Revised 16.05.2025
Accepted 20.05.2025

Статья поступила 09.01.2025 г.
Доработана 16.05.2025 г.
Принята к публикации 20.05.2025 г.

Refractory, Ceramic, and Composite Materials
Тугоплавкие, керамические и композиционные материалы

UDC 666.9-129
https://doi.org/10.17073/1997-308X-2025-5-60-69

Research article
Научная статья

Effect of spark plasma sintering temperature on the structure and properties of alumina ceramics containing barium hexaaluminate

K. A. Antropova, N. Yu. Cherkasova, N. S. Aleksandrova, R. R. Khabirov, A. A. Miller, M. Yu. Agafonov

Novosibirsk State Technical University
20 Karl Marks Prosp., Novosibirsk 630073, Russia

antropova.2017@stud.nstu.ru

Abstract. Alumina-based composite ceramics containing barium hexaaluminate are promising for various industrial applications, including the fabrication of replaceable cutting inserts. However, reports on such materials produced by spark plasma sintering (SPS) are scarce. This study aimed to evaluate the influence of sintering temperature on the structure and properties of alumina ceramics containing barium hexaaluminate. The materials were fabricated from highly dispersed Al_2O_3 and BaO powders by co-dispersion in an alcohol medium, followed by drying and spark plasma sintering at 1500, 1550, and 1600 °C. *X*-ray diffraction, scanning electron microscopy, and hydrostatic weighing were used to determine phase composition, microstructure, apparent density, and open porosity. Vickers hardness and fracture toughness were evaluated by indentation. The formation of α-Al_2O_3 and $Ba_{0.83}Al_{11}O_{17.33}$ phases was confirmed. The relative density of alumina ceramics without additive reached 99.72 ± 0.3 %, while that of ceramics containing barium hexaaluminate was 92.45 ± 0.5 %. The average Al_2O_3 grain size decreased from 4.27 ± 1.80 μm (without additive) to 1.49 ± 0.80, 1.89 ± 0.85, and 1.60 ± 0.63 μm at sintering temperatures of 1500, 1550, and 1600 °C, respectively. The barium hexaaluminate plates grew with increasing temperature, from 2.45 ± 0.22 μm at 1500 °C to 5.23 ± 0.46 μm at 1600 °C. The maximum fracture toughness (K_{Ic} = 5.00 ± 0.10 MPa·m$^{1/2}$) was obtained for the material containing barium hexaaluminate sintered at 1550 °C, which also exhibited a hardness of 2070 ± 43 HV_2.

Keywords: spark plasma sintering (SPS), alumina, barium hexaaluminate, phase formation, microstructure, fracture toughness

Acknowledgements: This research was funded by the Russian Science Foundation, grant No. 24-79-00256, https://rscf.ru/project/24-79-00256/. The experiments were carried out using the facilities of the Core Facilities Center “Structure, Mechanical and Physical Properties of Materials”, Novosibirsk State Technical University (NSTU).

For citation: Antropova K.A., Cherkasova N.Yu., Aleksandrova N.S., Khabirov R.R., Miller A.A., Agafonov M.Yu. Effect of spark plasma sintering temperature on the structure and properties of alumina ceramics containing barium hexaaluminate. *Powder Metallurgy and Functional Coatings*. 2025;19(5):60–69. https://doi.org/10.17073/1997-308X-2025-5-60-69

Влияние температуры электроискрового спекания на структуру и свойства алюмооксидной керамики, содержащей гексаалюминат бария

К. А. Антропова, Н. Ю. Черкасова, Н. С. Александрова, Р. Р. Хабиров, А. А. Миллер, М. Ю. Агафонов

Новосибирский государственный технический университет
Россия, 630073, г. Новосибирск, пр-т Карла Маркса, 20

antropova.2017@stud.nstu.ru

Аннотация. Композиционная керамика на основе оксида алюминия, содержащая гексаалюминат бария, является перспективной для применения в различных областях промышленности, в том числе для изготовления сменных режущих пластин. Работ, в которых отмеченные материалы получены электроискровым спеканием, практически не наблюдается. Целью данного исследования являлась оценка влияния температуры электроискрового спекания на структуру и свойства керамики на основе оксида алюминия, содержащей гексаалюминат бария. Исследуемые материалы получены из высокодисперсных порошков оксида алюминия и оксида бария путем совместного диспергирования спиртовых суспензий, их сушки и последующего электроискрового спекания при температурах (t_c) 1500, 1550 и 1600 °С. Проводили рентгенофазовый анализ, исследования структуры методом растровой электронной микроскопии, оценку кажущейся плотности и открытой пористости методом гидростатического взвешивания. Оценивали твердость по Виккерсу и трещиностойкость методом индентирования. Зафиксировано формирование фаз α-Al_2O_3 и $Ba_{0,83}Al_{11}O_{17,33}$. Относительная плотность от теоретической алюмооксидной керамики без добавок составляет 99,72 ± 0,3 %, при формировании гексаалюмината бария – 92,45 ± 0,5 %. Средний размер зерен оксида алюминия в материале без добавки находится в диапазоне 4,27 ± 1,80 мкм, а при формировании 15 мас. % гексаалюмината бария – 1,49 ± 0,80, 1,89 ± 0,85 и 1,60 ± 0,63 мкм при t_c = 1500, 1550 и 1600 °С соответственно. Размеры пластин гексаалюмината бария с ростом температуры спекания увеличиваются. При t_c = 1500 °С их длина составляет 2,45 ± 0,22 мкм, а при t_c = 1600 °С – 5,23 ± 0,46 мкм. Наиболее высокое значение критического коэффициента интенсивности напряжений (5,00 ± 0,10 МПа·м$^{1/2}$) зафиксировано для материала, содержащего гексаалюминат бария и спеченного при t_c = 1550 °С, твердость такого материала составляет 2070 ± 43 HV_2.

Ключевые слова: электроискровое спекание, оксид алюминия, гексаалюминат бария, фазообразование, структура, трещиностойкость

Благодарности: Исследование выполнено за счет гранта Российского научного фонда No. 24-79-00256, https://rscf.ru/project/24-79-00256/. Исследования проведены на оборудовании ЦКП «Структура, механические и физические свойства материалов» НГТУ.

Для цитирования: Антропова К.А., Черкасова Н.Ю., Александрова Н.С., Хабиров Р.Р., Миллер А.А., Агафонов М.Ю. Влияние температуры электроискрового спекания на структуру и свойства алюмооксидной керамики, содержащей гексаалюминат бария. *Известия вузов. Порошковая металлургия и функциональные покрытия*. 2025;19(5):60–69.
https://doi.org/10.17073/1997-308X-2025-5-60-69

Introduction

Research on alumina and alumina–zirconia ceramics continues to expand. Their combination of high mechanical performance and low weight, along with other advantageous properties, has driven adoption across medical [1], defence [2], and tooling [3] sectors. As performance requirements tighten, improving the service properties of oxide ceramics has become essential; in particular, boosting resistance to crack propagation remains a central challenge [4].

In modern materials science, an active approach is to reinforce alumina ceramics with alkali, alkaline-earth, and rare-earth metal hexaaluminates ($MeAl_{12}O_{19}$, magnetoplumbite; $MeAl_{11}O_{18}$, β-Al_2O_3)) [5]. In the structure of such materials, hexaaluminate grains are flattened hexagonal prisms that contribute to improved fracture toughness through various mechanisms [6–8]. The most frequently reported mechanisms include crack deflection, grain pull-out, crystal fracture in transverse – and less often longitudinal – directions, crack bridging, and crack branching. It has been noted that the overall material performance is significantly affected by the type of initial additive used for hexaaluminate formation [9] and on crystal size and volume fraction [6], which determine the strength of their bonding with the matrix grains and the mechanisms contributing to fracture toughness enhancement.

Numerous studies have reported that variations in hexaaluminate content lead to changes in key mate-

rial properties – such as density, porosity, hardness, strength, and fracture toughness. For instance, when up to 10 wt. % $CaAl_{12}O_{19}$ is formed in the structure of Al_2O_3–ZrO_2 ceramics, the fracture toughness increases from 5.8 to 6.3 MPa·m$^{1/2}$. Further increase in calcium hexaaluminate content results in a decrease in fracture toughness to 5.5 MPa·m$^{1/2}$, accompanied by reduced density and hardness [10]. A similar relationship was observed in [11], where the formation of 2.8 vol. % $LaAl_{11}O_{18}$ led to an increase in fracture toughness by approximately 1 MPa·m$^{1/2}$, whereas higher $LaAl_{11}O_{18}$ content reduced it to 2.7 MPa·m$^{1/2}$.

Notably, that hexaaluminates themselves exhibit a wide range of functional properties, including considerable catalytic activity and stability [12], luminescence [13], electrical conductivity [14], among others. Therefore, when selecting a hexaaluminate-forming additive for alumina ceramics, its choice should be guided by the intended application area. For example, calcium hexaaluminate is widely used in the production of medical ceramics [1]. The formation of barium hexaaluminate enhances thermal shock resistance, and compositions based on it remain among the least studied [8]. The relevance of researching the Al_2O_3–BaO system, along with its thermodynamic characteristics and the thermal stability of different phases, is discussed in the article [15]. It has also been reported that the barium hexaaluminate phase is the most thermally stable.

Barium hexaaluminate belongs to the β-Al_2O_3 structural family and forms as nonstoichiometric phases such as $Ba_{0.75}Al_{11}O_{17.25}$, $Ba_{2.33}Al_{21.33}O_{34.33}$, and $Ba_{0.83}Al_{11}O_{17.33}$ [5; 16]. Due to its plate-like morphology, it also contributes to improving the fracture toughness of alumina ceramics. In [8] 20.89 vol. % $Ba_{0.75}Al_{11}O_{17.25}$ in an Al_2O_3–ZrO_2 matrix increased fracture toughness by approximately 25 % relative to the additive-free material. Further increase in content to 41.38 vol. % yielded a smaller additional gain in toughness but markedly reduced hardness, strength, and density. Similar plate-mediated toughening has been reported for Al_2O_3 with up to 10 vol. % ZrO_2 [17], with effectiveness of toughness enhancement tied to the degree of material densification.

This study examines the effect of spark plasma sintering (SPS) parameters on the structure and properties of alumina ceramics with barium oxide additive. As noted in [3], spark plasma sintering enables the fabrication of ceramic workpieces for cutting-tool production. Therefore, the present work not only contributes to the body of knowledge on the Al_2O_3–BaO system but may also hold practical significance for developments in the tooling industry.

Materials and methods

High-purity alumina powder (99 %, average particle size 140 ± 50 nm, China) and barium oxide powder (99 %, average particle size 2.7 ± 0.6 μm, Russia; prepared in accordance with TU 6-09-5397-88) were used as starting materials. Alcohol suspensions were prepared using isopropyl alcohol (50 vol. %) as a dispersion medium for mixing the initial powders. The BaO content was set to 3 wt. % to form approximately 15 wt. % barium hexaaluminate. A relatively high barium hexaaluminate fraction was chosen to clearly evaluate its effect on the properties of the studied materials.

Dispersion was carried out in a ball mill for 10 h with periodic stops to cool the suspension. The rotation speed was 90 rpm. The drum of the mill was lined with polypropylene, and alumina grinding bodies 3 mm in diameter were used.

After dispersion, the powders were dried and consolidated by spark plasma sintering on an MS-1 unit at sintering temperatures (t_s) of 1500–1600 °C, under a pressure of 17 MPa, with a 5-minute holding time at maximum temperature. To prevent direct interaction between the powder and the tooling surfaces, graphite paper was placed between the powder and the die walls, as well as between the powder and the punch faces. Heating was provided by pulsed direct current passing through the graphite tooling. The temperature was measured using a pyrometer positioned in a side hole of the die assembly.

The apparent density and open porosity of the sintered materials were determined by the hydrostatic weighing method.

The apparent density was calculated as the ratio of the dry sample mass to the difference between the saturated and immersed masses:

$$\rho_{app} = \frac{M_{dry}}{M_{sat} - M_{liq}} \text{ [g/cm}^3\text{]},$$

where M_{dry} is the mass of the dry sample, g; M_{sat} is the mass of the sample saturated with liquid, g; M_{liq} is the mass of the sample immersed in liquid, g.

The relative density was calculated as

$$\rho_{rel} = \frac{\rho_{app}}{\rho_{theor}} \cdot 100 \text{ %}.$$

The theoretical density was determined using the literature values of the *X*-ray densities of the sintered components according to the formula:

$$\rho_{theor} = \left(\frac{m_i}{\rho_i} + \frac{m_n}{\rho_n} \right)^{-1} \cdot 100 \text{ % [g/cm}^3\text{]},$$

where ρ_i and ρ_n are the theoretical densities of the individual components, g/cm^3; m_i and m_n are their mass fractions in the composite, %.

The open porosity (P_o) was calculated as

$$P_o = \frac{M_{sat} - M_{dry}}{M_{sat} - M_{liq}} \cdot 100\ \%.$$

X-ray diffraction (XRD) analysis was performed using a PowDix600 diffractometer (ADWIN Smart Factory, Republic of Belarus) with Cu$K_{\alpha_{1+2}}$ radiation. The phases were identified using the ICDD PDF-4+ database. Polished sections for microstructural analysis were prepared using standard procedures, including grinding and polishing with diamond wheels and suspensions of various fineness. To reveal the grain structure, thermal etching was performed at a temperature 200 °C below the sintering temperature. Microstructural analysis was carried out using an EVO 50 scanning electron microscope (Carl Zeiss, Germany) equipped with an *X*-ray microanalysis attachment. Prior to examination, the polished sections were coated with a 40-nm copper layer to improve conductivity. Secondary electron detection was used for imaging. Grain sizes were measured using the JMicroVision 1.3.4 software. The alumina grain size was determined as the equivalent-circle diameter corresponding to the grain projection area in the microstructure image. For barium hexaaluminate grains, their length and width were measured, and the aspect ratio was calculated. At least 300 alumina grains and 100 barium hexaaluminate grains were analyzed for each composition.

The Vickers hardness and fracture toughness were evaluated by the indentation method under a 2-kg load using an SV-50A Vickers hardness tester (China). The fracture toughness, K_{Ic} (critical stress intensity factor), was calculated using the following equation [18]:

$$K_{Ic} = 0.048\left(\frac{c}{a}\right)^{-0.5}\left(\frac{HV}{E\Phi}\right)^{-0.4}\frac{HVa^{0.5}}{\Phi}\ [\text{MPa}\cdot\text{m}^{1/2}],$$

where HV is the hardness, GPa; a is the half-diagonal of the indentation, μm; c is the length of the radial crack measured from the indentation center, μm; $\Phi = 3$ is the constant.

The Young's modulus (E) of the composite materials was estimated by the rule of mixtures:

$$E = \left(\frac{m_i}{E_i} + \frac{m_j}{E_j}\right)^{-1} \cdot 100\ \%\ [\text{GPa}],$$

where E_i and E_j are the Young's moduli of Al_2O_3 (397 GPa) and $Ba_{0.83}Al_{11}O_{17.33}$ (226 GPa), respectively; m_i and m_j are their mass fractions (%). The modulus values were taken from the literature [19].

Results and discussion

Experimental materials were sintered from starting mixtures of alumina and barium oxide. The sintering temperature (t_s) was 1500, 1550, and 1600 °C. As a reference, an additive-free alumina ceramics was prepared.

X-ray diffraction patterns of the sintered materials are shown in Fig. 1. Regardless of the sintering temperature, the materials with BaO in the starting mixture display, in addition to α-Al_2O_3, diffraction peaks of $Ba_{0.83}Al_{11}O_{17.33}$. No other barium-containing phases were detected.

The apparent density and open porosity of the sintered materials were evaluated; the results are summarized in Table 1. The highest relative density (with respect to the theoretical density) was obtained for the additive-free alumina ceramics. Formation of barium hexaaluminate in the composite led to a decrease in relative density and an increase in open porosity, which is consistent with prior reports on hexaaluminate formation in alumina matrix [5; 11]. With increasing sintering temperature, density and porosity changed nonlinearly.

Microstructural studies were performed by scanning electron microscopy (SEM). In the SEM micro-

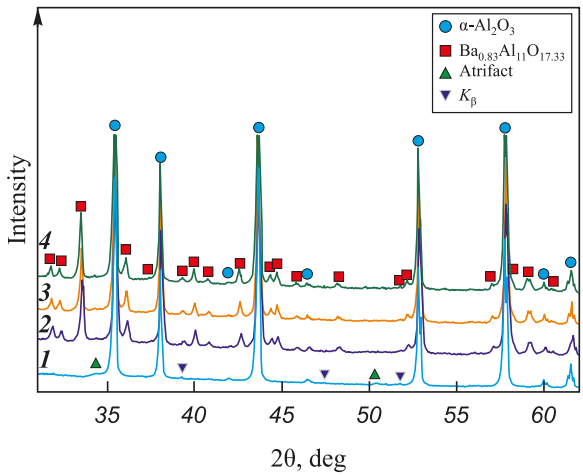

Fig. 1. *X*-ray patterns of the sintered materials
1 – alumina ceramics without additives, sintered at t_s = 1500 °C;
2–4 – ceramics of the composition Al_2O_3 + $Ba_{0.83}Al_{11}O_{17.33}$ ceramics, sintered at t_s = 1500 (***2***), 1550 (***3***), and 1600 (***4***) °C

Рис. 1. Рентгеновские дифрактограммы спеченных исследуемых материалов
1 – алюмооксидная керамика без добавок, спеченная при t_c = 1500 °C;
2–4 – керамика состава Al_2O_3 + $Ba_{0.83}Al_{11}O_{17.33}$, спеченная при t_c = 1500 (***2***), 1550 (***3***) и 1600 (***4***) °C

Table 1. **Apparent density and open porosity of the sintered materials**

Таблица 1. **Кажущаяся плотность и открытая пористость спеченных материалов**

Material	Sintering temperature, °C	Apparent density, g/cm^3	Relative density, % of theoretical	Open porosity, %
Al_2O_3	1500	3.98 ± 0.02	99.72 ± 0.3	0.26 ± 0.07
$Al_2O_3 + Ba_{0.83}Al_{11}O_{17.33}$	1500	3.70 ± 0.04	92.45 ± 0.5	4.75 ± 0.09
	1550	3.86 ± 0.03	96.41 ± 0.4	1.76 ± 0.08
	1600	3.86 ± 0.03	96.35 ± 0.4	2.08 ± 0.08

graphs (Fig. 2), the darker equiaxed grains correspond to the low-Z alumina phase, whereas the brighter elongated grains belong to the Ba-rich phase. SEM–EDS spot analyses conducted on the elongated grains confirmed the presence of Ba, Al, and O, identifying them as barium hexaaluminate (Fig. 2, *e*). Grains of both phases are distributed fairly uniformly, though local clusters of bright elongated grains are occasionally observed.

A detailed quantitative analysis of the structural constituents was performed, and the results are presented in Fig. 3 and Table 2. The average grain size of alu-

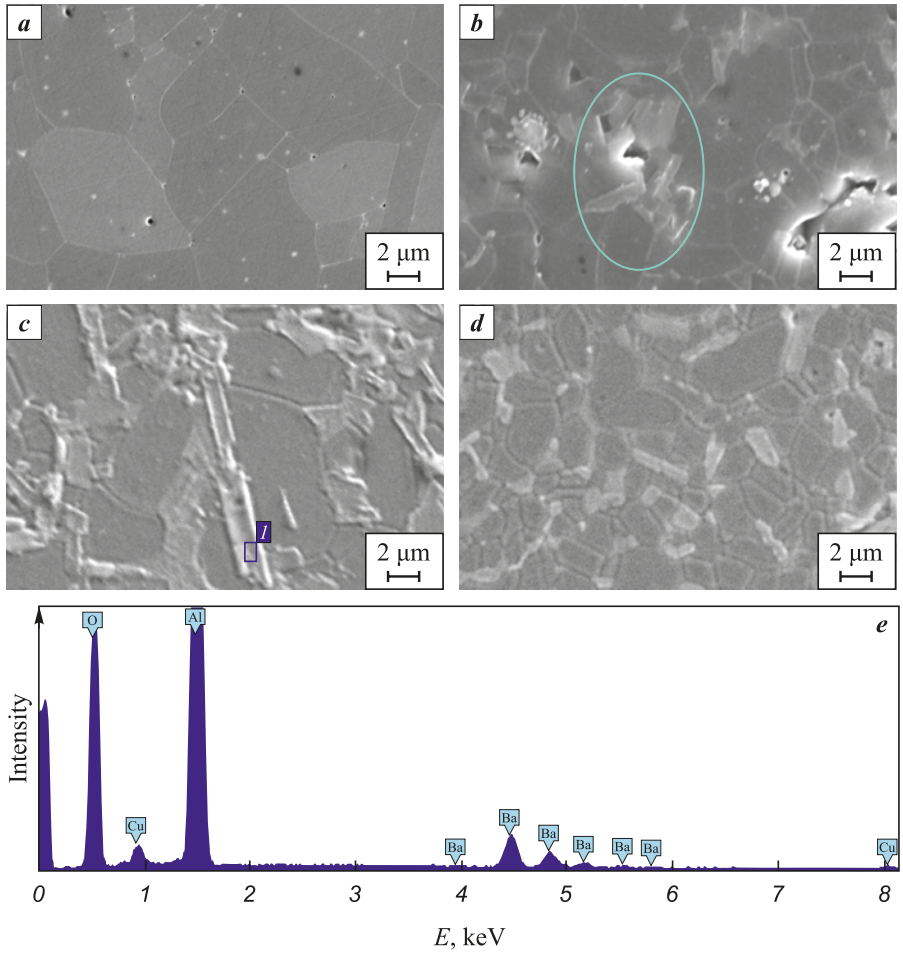

Fig. 2. Microstructure of the sintered materials

a – alumina ceramics without additives; ***b***–***d*** – ceramics containing barium hexaaluminate sintered at t_s, °C – 1500 (***b***), 1550 (***c***), 1600 (***d***); ***e*** – results of micro-*X*-ray spectral analysis obtained from region ***1*** marked in Fig. 2, *c*

Рис. 2. Структура спеченных материалов

a – алюмооксидная керамика без добавок; ***b***–***d*** – содержащая гексаалюминат бария; t_c, °C – 1500 (***b***), 1550 (***c***), 1600 (***d***); ***e*** – результаты микрорентгеноспектрального анализа, полученные с области ***1***, выделенной на рис. 2, *c*

mina in the additive-free material was 4.27 ± 1.80 μm. The alumina powder used in this study was highly dispersed, which provided high sinterability. In addition, the SPS technique and the presence of barium oxide contributed to the intensification of the sintering process. In materials containing BaO, the alumina grains were significantly smaller. For instance, under identical sintering conditions at t_s = 1500 °C, the alumina grain size decreased by about 65 % in the material containing barium hexaaluminate. This effect can be attributed to Ba segregation along alumina grain boundaries, which inhibits their migration and growth [20]. Furthermore, the growth of hexaaluminate grains of any chemical composition is usually accompanied by the consumption of alumina grains, which also leads to their size reduction – a behavior consistent with previously reported findings [21; 22].

The alumina ceramics exhibited the widest grain size distribution, whereas in the material containing barium hexaaluminate and sintered at t_s = 1600 °C, the distribution of Al_2O_3 grains was the narrowest, with a maximum grain size not exceeding 4 μm. It was also observed that the barium hexaaluminate plates increased in size with rising sintering temperature. At t_s = 1600 °C, both the length and width of the hexaaluminate plates increased. The aspect ratio of the barium hexaaluminate grains changed nonlinearly, reaching its minimum value at t_s = 1550 °C. This indicates that at the maximum sintering temperature, the most intensive growth of barium hexaaluminate plates occurs, accompanied by alumina grain consumption, which ultimately results in smaller alumina grains. Therefore, at t_s = 1600 °C, the decrease in alumina grain size is mainly associated with their participation in barium hexaaluminate formation rather than Ba segregation along grain boundaries.

The observed grain-structure features correlate with the changes in density and porosity of the studied materials. It was established that pores in the composite ceramics are predominantly concentrated in regions where barium hexaaluminate grains accumulate (highlighted by an oval in Fig. 2, *b*). Hence, the presence of pores is associated with the loose packing of plate-like grains, which explains the pronounced decrease in density and increase in porosity upon BaO addition in the materials sintered at t_s = 1500 °C. Further temperature increase promoted alumina grain growth. At t_s = 1550 °C, the average Al_2O_3 grain size reached approximately 1.89 ± 0.85 μm. The coarsening of alumina grains led to a reduction in open porosity and an increase in relative density. At this temperature, alumina grain growth likely inhibited the elongation of barium hexaaluminate plates. However, at t_s = 1600 °C, the growth of barium hexaaluminate plates dominated, resulting in longer plates, smaller alumina grains, and increased porosity.

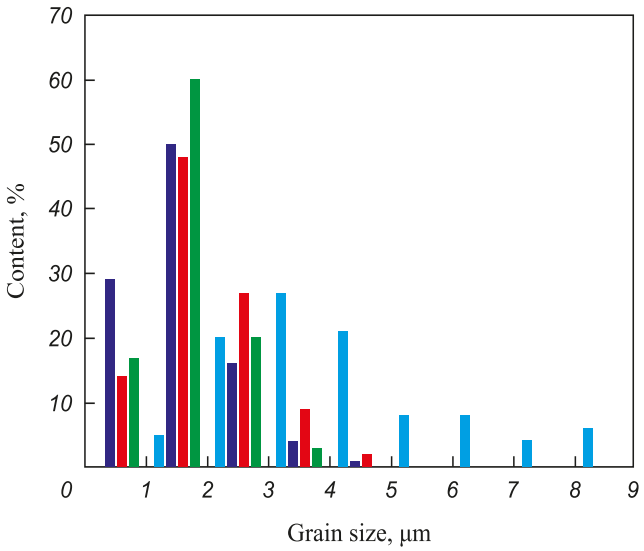

Fig. 3. Grain size distribution of alumina in the sintered materials

Рис. 3. Распределение размеров зерен оксида алюминия в спеченных материалах

Table 2. **Grain sizes of the sintered materials**

Таблица 2. **Размеры зерен спеченных материалов**

Material	Sintering temperature, °C	Average Al_2O_3 grain size, μm	$Ba_{0.83}Al_{11}O_{17.33}$ grains		
			Length, μm	Width, μm	Aspect ratio
Al_2O_3	1500	4.27 ± 1.80	–	–	–
Al_2O_3 + $Ba_{0.83}Al_{11}O_{17.33}$	1500	1.49 ± 0.80	2.45 ± 0.22	0.57 ± 0.05	1.0:4.3
	1550	1.89 ± 0.85	3.38 ± 0.21	0.93 ± 0.04	1.0:3.6
	1600	1.60 ± 0.63	5.23 ± 0.46	1.20 ± 0.06	1.0:4.4

Plate-like grains in the microstructure can significantly influence the mechanical properties of the material [19]. The results of Vickers hardness and fracture toughness measurements are summarized in Table 3. The materials containing barium hexaaluminate exhibited higher hardness compared with the additive-free alumina ceramics. For oxide ceramics, the incorporation of hexaaluminates more commonly results in hardness degradation [9–11]; in this case, however, the hardness increase is attributed to the substantial refinement of alumina grains. An improvement in fracture toughness was also observed in alumina ceramics containing barium hexaaluminate. The highest K_{Ic} value was recorded for the material sintered at t_s = 1550 °C. It is likely that this composition provides the most favorable combination of porosity and grain sizes of both alumina and barium hexaaluminate.

Fig. 4 shows a typical Vickers indentation with radial cracks emerging from the indentation diagonals and a magnified view of a crack propagating through the Al_2O_3–$BaAl_{12}O_{19}$ composite. The measured crack lengths, taken from the indentation center to the crack tip, correlate with the calculated K_{Ic} value. In the additive-free alumina, the average crack length reaches ~80 μm, whereas in the composite ceramics it ranges from 50 to 55 μm, with the maximum length not exceeding 65 μm.

Detailed examination of the crack path (Fig. 4, *b*) revealed intergranular fracture along alumina grain boundaries and transgranular fracture of barium hexaaluminate plates in both transverse (*1*) and longitudinal (*2*) sections. Crack propagation was further accompanied by deflection at plate interfaces and the formation of crack bridging (*3*).

Conclusions

1. Regardless of the sintering temperature, XRD analysis of materials containing barium oxide in

Table 3. **Hardness and fracture toughness of the investigated materials**

Таблица 3. **Твердость и трещиностойкость исследуемых материалов**

Material	Sintering temperature, °C	Hardness, HV_2	Fracture toughness, $MPa \cdot m^{1/2}$
Al_2O_3	1500	1990 ± 71	4.65 ± 0.14
$Al_2O_3 + Ba_{0.83}Al_{11}O_{17.33}$	1500	2085 ± 33	4.85 ± 0.08
	1550	2070 ± 43	5.00 ± 0.10
	1600	2120 ± 67	4.50 ± 0.18

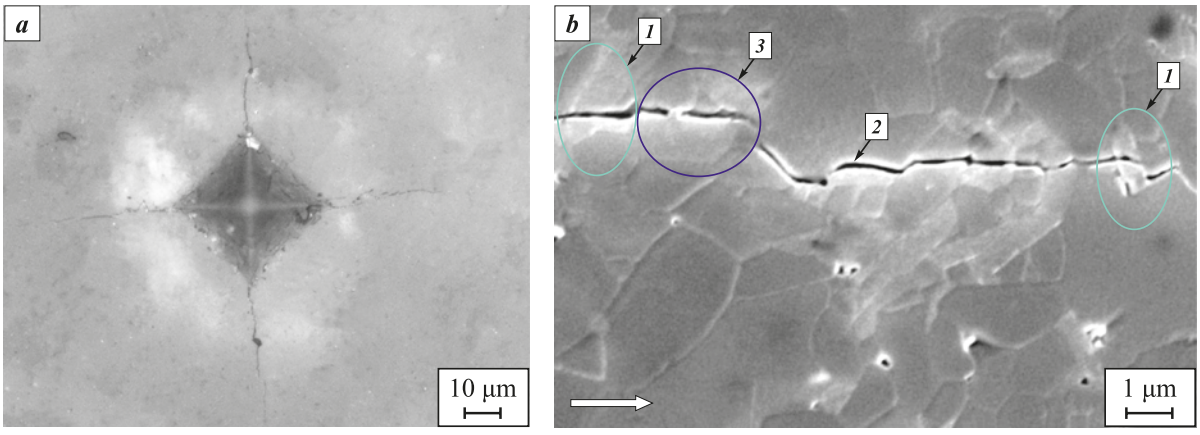

Fig. 4. Typical indentation (***a***) and propagating crack (***b***) in the investigated materials containing barium hexaaluminate

Numbers indicate the toughening mechanisms: ***1*** – plate fracture in the transverse direction; ***2*** – in the longitudinal direction with subsequent crack path deflection; ***3*** – crack bridging
The white arrow indicates the direction of crack propagation

Рис. 4. Типичный снимок отпечатка (***a***) и распространяющейся трещины (***b***) в исследуемых материалах, содержащих гексаалюминат бария

Цифрами обозначены механизмы повышения трещиностойкости: ***1*** – перерезание пластины в поперечном направлении; ***2*** – в продольном направлении с последующим отклонением траектории распространения; ***3*** – формирование мостиков
Белой стрелкой показано направление распространения трещины

the starting mixture revealed, in addition to α-Al_2O_3, the presence of $Ba_{0.83}Al_{11}O_{17.33}$ reflections.

2. The formation of barium hexaaluminate leads to a decrease in relative density and an increase in open porosity. With rising sintering temperature, density and porosity change non-uniformly due to the simultaneous growth and loose packing of plate-like barium-hexaaluminate grains and variation in alumina grain size.

3. The size of barium-hexaaluminate plates increases with sintering temperature: their average length rises from 2.45 ± 0.22 μm at 1500 °C to 5.23 ± 0.46 μm at 1600 °C.

4. The formation of barium hexaaluminate in the ceramic microstructure causes a reduction of alumina grain size by approximately 65 % under identical sintering conditions at t_s = 1500 °C.

5. The highest fracture toughness (K_{Ic} = 5.00 ± ± 0.10 MPa·$m^{1/2}$) was obtained for the material containing barium hexaaluminate and sintered at t_s = 1550 °C. The corresponding Vickers hardness was 2070 ± 43 HV_2.

References / Список литературы

1. Podzorova L.I., Volchenkova V.A., Il'icheva A.A., Andreeva N.A., Konovalov A.A., Penkina T.N., Pen'kova O.I. Chemical composition stability of corundum/zirconium dioxide composites in a biological media. *Inorganic Materials: Applied Research*. 2024;15(4):983–987. https://doi.org/10.1134/S2075113324700497
2. Garshin A.P., Kulik V.I., Nilov A.S. Shock-resistant materials based on commercial grade ceramic: achievements and prospects for improving their ballistic efficiency. *Refractories and Industrial Ceramics*. 2016;57(2):207–219. https://doi.org/10.1007/s11148-016-9955-0
3. Kuzin V.V., Grigor'ev N., Fedorov S.Y., Volosova M.A., Pinargote N.V.S. Spark plasma sintering of Al_2O_3-ceramic workpieces for small end milling cutters. *Refractories and Industrial Ceramics*. 2019;59(6):623–627. https://doi.org/10.1007/s11148-019-00285-2
4. Abyzov A.M. Aluminum oxide and alumina ceramics (review). Part 1. Properties of Al_2O_3 and commercial production of dispersed Al_2O_3. *Refractories and Industrial Ceramics*. 2019;60(1):24–32. https://doi.org/10.1007/s11148-019-00304-2
5. Tian M., Wang X.D., Zhang T. Hexaaluminates: a review of the structure, synthesis and catalytic performance. *Catalysis Science & Technology*. 2016;6(7):1984–2004. https://doi.org/10.1039/C5CY02077H
6. Kern F. A comparison of microstructure and mechanical properties of 12Ce–TZP reinforced with alumina and in situ formed strontium- or lanthanum hexaaluminate precipitates. *Journal of the European Ceramic Society*. 2014;34(2):413–423. https://doi.org/10.1016/j.jeurceramsoc.2013.08.03 7
7. Shi S., Cho S., Goto T., Sekino T. Role of $CeAl_{11}O_{18}$ in reinforcing Al_2O_3/Ti composites by adding CeO_2. *International Journal of Applied Ceramic Technology*. 2021;18(1):170–181. https://doi.org/10.1111/ijac.13629
8. Liu L., Takasu Y., Onda T., Chen Z.-C. Influence of *in-situ* formed Ba–β-Al_2O_3 on mechanical properties and thermal shock resistance of ZTA/Ba–β-Al_2O_3 composites. *Ceramics International*. 2020;46(3):3738–3743. https://doi.org/10.1016/j.ceramint.2019.10.095
9. Rivero-Antúnez P., Morales-Flórez V., Cumbrera F.L., Esquivias L. Rietveld analysis and mechanical properties of in situ formed La–β-Al_2O_3/Al_2O_3 composites prepared by sol-gel method. *Ceramics International*. 2022; 48(17):24462–24470. https://doi.org/10.1016/j.ceramint.2022.05.058
10. Sktani Z.D.I., Azhar A.Z.A., Ratnam M.M., Ahmad Z.A. The influence of in-situ formation of hibonite on the properties of zirconia toughened alumina (ZTA) composites. *Ceramics International*. 2014;40(4):6211–6217. https://doi.org/10.1016/j.ceramint.2013.11.076
11. Negahdari Z., Willert-Porada M., Pfeiffer C. Mechanical properties of dense to porous alumina/lanthanum hexaaluminate composite ceramics. *Materials Science and Engineering: A*. 2010;527(12):3005–3009. https://doi.org/10.1016/j.msea.2010.01.050
12. Kerzhentsev M.A., Podyacheva O.Yu., Shikina N.V., Mishanin S.V., Ismagilov Z.R., Deutschmann O., Russo G. Application of catalytic technologies for power plants based on high-temperature fuel cells. *Chemistry for Sustainable Development*. 2021;29(3):317–324. https://doi.org/10.15372/CSD2021309

    Керженцев М.А., Подъячева О.Ю., Шикина Н.В., Мишанин С.В., Исмагилов З.Р., Deutschmann O., Russo G. Применение каталитических технологий для энергоустановок на высокотемпературных топливных элементах. *Химия в интересах устойчивого развития*. 2021;29(3):326–333. https://doi.org/10.15372/KhUR2021309
13. Selyunina L.A., Mishenina L.N., Slizhov Y.G., Kozik V.V. Effect of citric acid and ethylene glycol on the formation of calcium aluminate via the sol-gel method. *Russian Journal of Inorganic Chemistry*. 2013;58(4):450–455. https://doi.org/10.1134/S0036023613040165

    Селюнина Л.А., Мишенина Л.Н., Слижов Ю.Г., Козик В.В. Влияние лимонной ксилоты и этиленгликоля на формирование алюмината кальция золь-гель методом. *Журнал неорганической химии*. 2013;58(4): 517–522. https://doi.org/10.7868/S0044457X1304017X
14. Zhdanok A.A., Berdnikova L.K., Korotaeva Z.A., Tolochko B.P., Bulgakov V.V., Mikhaylenko M.A. Specifics of obtaining a vacuum-tight weakly conductive ceramics based on barium aluminate. *Refractories and Industrial Ceramics*. 2023;64(4):407–412. https://doi.org/10.1007/s11148-024-00861-1

    Жданок А.А., Бердникова Л.К., Коротаева З.А., Толочко Б.П., Булгаков В.В., Михайленко М.А. Особенности получения вакуум-плотной слабопроводящей кера-

мики на основе алюмината бария. *Новые огнеупоры*. 2023;(8):14–20.
https://doi.org/10.17073/1683-4518-2023-8-14-20

15. Tyurnina N.G., Lopatin S.I., Balabanova E.A., Shugurov S.M., Tyurnina Z.G., Polyakova I.G. Thermodynamic properties of the $BaO–Al_2O_3$ system. *Journal of Alloys and Compounds*. 2023;969:172266.
https://doi.org/10.1016/j.jallcom.2023.172266
16. Nugroho S., Chen Z.-C., Kawasaki A., Jarligo M.O.D. Solid-state synthesis and formation mechanism of barium hexaaluminate from mechanically activated $Al_2O_3–BaCO_3$ powder mixtures. *Journal of Alloys and Compounds*. 2010;502(2):466–471.
https://doi.org/10.1016/j.jallcom.2010.04.198
17. Liu L., Maeda K., Onda T., Chen Z.-C. Effect of YSZ with different Y_2O_3 contents on toughening behavior of Al_2O_3/$Ba–\beta\text{-}Al_2O_3/ZrO_2$ composites. *Ceramics International*. 2019;45(14):18037–18043.
https://doi.org/10.1016/j.ceramint.2019.06.023
18. Niihara K., Morena R., Hasselman D.P.H. Evaluation of K_{Ic} of brittle solids by the indentation method with low crack-to-indent ratios. *Journal of Materials Science Letters*. 1982;1(1):13–16.
https://doi.org/10.1007/BF00724706
19. Chen Z., Chawla K., Koopman M. Microstructure and mechanical properties of in situ synthesized alumina/Ba–β-alumina/zirconia composites. *Materials Science and Engineering: A*. 2004;367(1–2):24–32.
https://doi.org/10.1016/j.msea.2003.09.070
20. Altay A., Gülgün M.A. Microstructural evolution of calcium-doped α-alumina. *Journal of the American Ceramic Society*. 2003;86(4):623–629.
https://doi.org/10.1111/j.1151-2916.2003.tb03349.x
21. Rani D.A., Yoshizawa Y., Hirao K., Yamauchi Y. Effect of rare-earth dopants on mechanical properties of alumina. *Journal of the American Ceramic Society*. 2004;87(2):289–292.
https://doi.org/10.1111/j.1551-2916.2004.00289.x
22. Sktani Z.D.I., Rejab N.A, Rosli A.F.Z, Arab A., Ahmad Z.A. Effects of La_2O_3 addition on microstructure development and physical properties of harder ZTA–CeO_2 composites with sustainable high fracture toughness. *Journal of Rare Earths*. 2021;39(7):844-849.
https://doi.org/10.1016/j.jre.2020.06.005

Information about the Authors

Kristina A. Antropova – Junior Researcher, Research Laboratory of Physical and Chemical Technologies and Functional Materials, Novosibirsk State Technical University (NSTU)
ORCID: 0000-0001-5482-3537
E-mail: antropova.2017@stud.nstu.ru

Nina Yu. Cherkasova – Cand. Sci. (Eng.), Senior Researcher, Research Laboratory of Physical and Chemical Technologies and Functional Materials, NSTU
ORCID: 0000-0002-5603-7852
E-mail: cherkasova.2013@corp.nstu.ru

Natalya S. Aleksandrova – Junior Researcher, Research Laboratory of Physical and Chemical Technologies and Functional Materials, NSTU
ORCID: 0000-0002-7619-525X
E-mail: aleksandrova.2017@corp.nstu.ru

Roman R. Khabirov – Junior Researcher, Center for Technological Excellence, NSTU
ORCID: 0000-0003-4720-2876
E-mail: xabirov.2016@stud.nstu.ru

Aleksandr A. Miller – Master's Student, Department of Materials Science in Mechanical Engineering, NSTU
ORCID: 0009-0008-0534-0879
E-mail: miller.2020@stud.nstu.ru

Mikhail Yu. Agafonov – Master's Student, Department of Materials Science in Mechanical Engineering, NSTU
ORCID: 0009-0008-8153-9118
E-mail: agafonov.2020@stud.nstu.ru

Сведения об авторах

Кристина Александровна Антропова – мл. науч. сотрудник научно-исследовательской лаборатории физико-химических технологий и функциональных материалов Новосибирского государственного технического университета (НГТУ)
ORCID: 0000-0001-5482-3537
E-mail: antropova.2017@stud.nstu.ru

Нина Юрьевна Черкасова – к.т.н., ст. науч. сотрудник научно-исследовательской лаборатории физико-химических технологий и функциональных материалов НГТУ
ORCID: 0000-0002-5603-7852
E-mail: cherkasova.2013@corp.nstu.ru

Наталья Сергеевна Александрова – мл. науч. сотрудник научно-исследовательской лаборатории физико-химических технологий и функциональных материалов НГТУ
ORCID: 0000-0002-7619-525X
E-mail: aleksandrova.2017@corp.nstu.ru

Роман Рафаэлович Хабиров – мл. науч. сотрудник Центра технологического превосходства НГТУ
ORCID: 0000-0003-4720-2876
E-mail: xabirov.2016@stud.nstu.ru

Александр Андреевич Миллер – магистрант кафедры материаловедения в машиностроении НГТУ
ORCID: 0009-0008-0534-0879
E-mail: miller.2020@stud.nstu.ru

Михаил Юрьевич Агафонов – магистрант кафедры материаловедения в машиностроении НГТУ
ORCID: 0009-0008-8153-9118
E-mail: agafonov.2020@stud.nstu.ru

Contribution of the Authors

K. A. Antropova – defined the research objectives, conducted the experiments, and wrote the manuscript.
N. Yu. Cherkasova – developed the concept and defined the objectives of the study, and contributed to writing the manuscript.
N. S. Aleksandrova – performed *X*-ray phase analysis, and participated in the discussion of the results.
R. R. Khabirov – carried out structural studies and participated in the discussion of the results.
A. A. Miller – prepared the mixtures and experimental samples, and participated in discussions of the results.
M. Yu. Agafonov – conducted the investigations and participated in the discussion of the results.

Вклад авторов

К. А. Антропова – определение цели работы, проведение экспериментов, написание статьи.
Н. Ю. Черкасова – определение концепции и цели работы, написание статьи.
Н. С. Александрова – проведение рентгенофазового анализа, участие в обсуждении результатов.
Р. Р. Хабиров – проведение структурных исследований, участие в обсуждении результатов.
А. А. Миллер – приготовление смесей и экспериментальных образцов, участвие в обсуждении результатов.
М. Ю. Агафонов – проведение исследований, участие в обсуждении результатов.

Received 14.03.2025
Revised 25.04.2025
Accepted 28.04.2025

Статья поступила 14.03.2025 г.
Доработана 25.04.2025 г.
Принята к публикации 28.04.2025 г.

Nanostructured Materials and Functional Coatings
Наноструктурированные материалы и функциональные покрытия

UDC 546.261 : 661.882 : 667.637.23
https://doi.org/10.17073/1997-308X-2025-5-70-79

Research article
Научная статья

Titanium carbide coating for high-temperature graphite components

A. V. Afanas'ev[1], Yu. O. Bykov[1], A. O. Lebedev[1, 2] ✉, A. V. Markov[1], N. V. Sharenkova[2], N. M. Latnikova[3]

[1] **V.I. Ulyanov (Lenin) Saint Petersburg State Electrotechnical University (LETI)**
5 Prof. Popova Str., Saint Petersburg 197022, Russia
[2] **A.F. Ioffe Physical Technical Institute**
26 Politekhnicheskaya Str., Saint Petersburg 194021, Russia
[3] **D.I. Mendeleev Central Research Institute of Materials**
8 Paradnaya Str., Saint Petersburg 191014, Russia

✉ aswan61@yandex.ru

Abstract. Titanium carbide (TiC) coatings were produced on the surface of graphite components using a low-cost liquid-phase technique involving application of a TiO_2-based reaction mixture followed by carbothermal annealing in vacuum at 1900 °C. Typical grades of structural graphite (GMZ, MPG-6, and I-3) commonly used in high-temperature graphite assemblies were employed as substrates for the protective coating. The resulting polycrystalline titanium carbide films (NaCl-type structure) exhibited an axial growth texture [111] and thermal stresses that depended on the graphite grade, caused by the difference in the coefficients of thermal expansion between titanium carbide and graphite. Typical coating thicknesses ranged from 10 to 20 μm. Graphite components with TiC coatings were successfully tested under high-temperature silicon carbide single-crystal growth conditions. The tribological properties of the coatings were also evaluated. The use of denser grades of isostatic graphite (I-3) is preferable due to the formation of a dense two-dimensional structure of the protective layer on the graphite surface.

Keywords: titanium oxide, titanium carbide, protective coating, structural characteristics

Acknowledgements: The authors express their gratitude to the staff of the International Scientific and Educational Center "BaltTribo-Polytechnic", Institute of Machinery, Materials, and Transport, Peter the Great St. Petersburg Polytechnic University, for conducting the tribological experiments.

For citation: Afanas'ev A.V., Bykov Yu.O., Lebedev A.O., Markov A.V., Sharenkova N.V., Latnikova N.M. Titanium carbide coating for high-temperature graphite components. *Powder Metallurgy and Functional Coatings*. 2025;19(5):70–79.
https://doi.org/10.17073/1997-308X-2025-5-70-79

Покрытие из карбида титана для графитовой арматуры высокотемпературных процессов

А. В. Афанасьев[1], Ю. О. Быков[1], А. О. Лебедев[1, 2] ✉, А. В. Марков[1], Н. В. Шаренкова[2], Н. М. Латникова[3]

[1] **Санкт-Петербургский государственный электротехнический университет «ЛЭТИ» им. В.И. Ульянова (Ленина)**
Россия, 197022, г. Санкт-Петербург, ул. Проф. Попова, 5
[2] **Физико-технический институт им. А.Ф. Иоффе Российской академии наук**
Россия, 194021, г. Санкт-Петербург, ул. Политехническая, 26
[3] **Центральный научно-исследовательский институт материалов им. Д.И. Менделеева**
Россия, 191014, г. Санкт-Петербург, ул. Парадная, 8

✉ aswan61@yandex.ru

Аннотация. Покрытия из карбида титана (TiC) создавали на поверхности графитовых изделий посредством дешевого «жидкофазного» способа, включающего нанесение жидкой реакционной смеси на основе TiO_2 и ее последующий карботермический отжиг в вакууме при температуре 1900 °C. В качестве основы для нанесения защитного покрытия выбраны типовые марки конструкционных графитов, используемых в промышленности для создания элементов высокотемпературной графитовой арматуры (ГМЗ, МПГ-6 и И-3). Полученные поликристаллические пленки карбида титана (структурный тип NaCl) характеризовались ростовой аксиальной текстурой [111] и наличием «температурных» механических напряжений, зависящих от марки графита, вследствие разности температурных коэффициентов линейного расширения между карбидом титана и графитовой основой. Типовые толщины покрытий составляли 10–20 мкм. Графитовые компоненты с покрытием TiC успешно протестированы в условиях высокотемпературного процесса синтеза монокристаллов карбида кремния. Проведена оценка трибологических свойств покрытий. Использование наиболее плотных разновидностей изостатического графита (И-3) является предпочтительным вследствие формирования двумерной плотной структуры защитного слоя на поверхности графита.

Ключевые слова: оксид титана, карбид титана, защитное покрытие, структурные характеристики

Благодарности: Авторы выражают благодарность сотрудникам Международного научно-образовательного центра «BaltTribo-Polytechnic», Института машиностроения, материалов и транспорта Санкт-Петербургского политехнического университета им. Петра Великого за трибологические исследования образцов.

Для цитирования: Афанасьев А.В., Быков Ю.О., Лебедев А.О., Марков А.В., Шаренкова Н.В., Латникова Н.М. Покрытие из карбида титана для графитовой арматуры высокотемпературных процессов. *Известия вузов. Порошковая металлургия и функциональные покрытия*. 2025;19(5):70–79. https://doi.org/10.17073/1997-308X-2025-5-70-79

Introduction

Single-crystal silicon carbide is currently in demand for manufacturing components of power, high-frequency, and high-temperature electronic devices [1]. Single-crystal SiC ingots are typically grown by the sublimation method (modified Lely process), developed by Tairov and Tsvetkov at LETI Institute, on their own seeds, in vacuum or in an inert atmosphere (usually argon) at a temperature of about 2000 °C, using high-purity silicon carbide powder as the source material. The graphite components used in the standard process of the modified Lely method are exposed to an aggressive vapor–gas environment containing volatile species Si, SiC_2, and Si_2C, which causes corrosion and leads to contamination of the crystal ingot with graphite particles [2].

To protect the surface of graphite assemblies, tantalum carbide films are typically used [3]. They remain stable at $t > 2000$ °C and can be produced by various methods. However, tantalum carbide coatings are relatively expensive, particularly when applied to components intended for single use. Therefore, it is necessary to search for more cost-effective coating materials that can serve as efficient protective barriers to prevent corrosion of graphite assemblies. Their surface can also be protected using other high-temperature carbides such as TiC, WC, VC, and others [4; 5]. Among them, titanium carbide is of greatest interest, as it provides an optimal balance of high hardness (up to 2400 HV and higher), corrosion resistance, and thermal stability.

The properties of TiC depend on the synthesis method [6]. Chemical vapor deposition (CVD) methods [7–9] are widely used industrially for corrosion-resistant materials; the resulting coatings exhibit high adhesion and uniformity on flat surfaces. However, these methods are costly (due to equipment and large consumption of carrier gases) and characterized by low growth rates (typically producing coatings

about 2–3 μm thick), as well as by the use of toxic or pyrophoric precursors [9]. The use of plasma enables coating of substrates and surfaces sensitive to high temperatures; such coatings are distinguished by high adhesion and low surface roughness [10].

The family of physical vapor deposition (PVD) methods includes thermal evaporation, ion sputtering, cathodic arc deposition, and electron-beam evaporation [11–13]; the most common heating method among them is indirect resistive heating. The coatings produced by these methods exhibit high hardness and wear resistance but insufficient adhesion to the substrate. Moreover, nonuniform coating thickness is observed inside cavities or on components with complex geometry.

The use of magnetron sputtering systems, including reactive and radio-frequency sputtering [14–17], enhances process efficiency by enabling deposition of uniform films over large areas. Additional annealing of coatings [14] improves the crystallinity of TiC films and increases the grain size. The actual coating thickness achieved and applied in practice remains small (a few micrometers), yet such films have a dense structure without cavities or cracks. The challenge of coating sidewalls and complex profiles is addressed using advanced magnetron control mechanisms.

Laser cladding of titanium carbide–reinforced composite coatings is effectively employed for surface passivation or surface hardening [18], but it cannot be used for large-area deposition. Pulsed laser deposition (PLD) involves the use of a laser to ablate material from a target [19]. The disadvantages of this method include its limited suitability for mass production, the dependence of ablation on laser energy, and nonuniform coating formation on complex surfaces.

Titanium carbide coatings can also be produced by several other methods. In [20], a TiC-containing coating was produced by plasma transferred arc welding (PTAW), which increased the corrosion potential of the substrate and significantly reduced the corrosion current density. Methods based on in-situ carburizing of titanium in a $CaCl_2$–CaC_2 molten salt – the salt-thermo-carburizing route [21] – or on anodic polarization–accelerated TiC coating formation in molten salt [22] are also applicable. These approaches are simple and provide high coating growth rates (over 100 μm in 8 h [21] and about 15 μm in 0.7 h [22]).

Overall, none of the methods reviewed combines all the required characteristics for producing low-cost functional corrosion-resistant TiC-based coatings for graphite components used in high-temperature processes of silicon carbide and aluminum nitride synthesis. Therefore, there is a need to identify the most economical coating techniques that do not require expensive equipment and can yield dense protective layers tens of micrometers thick.

Experimental procedure

In this study, a titanium carbide (TiC) film coating was produced by applying a reaction mixture containing powdered titanium dioxide TiO_2 (OSCh 7–3), an adhesive, and a solvent onto graphite components. Various phenol–formaldehyde resins were used as adhesives, and ethyl alcohol served as the solvent. The mixture was applied at room temperature to the surface of graphite components made of different graphite grades. The coated components were dried in air at t = 80÷100 °C, followed by annealing of the applied coating in forevacuum at temperatures up to 1900 °C for 4–5 h.

Graphite parts of commonly used domestic grades were employed as substrates for titanium carbide coating deposition, namely low-ash extruded graphite GMZ [23], fine-grained dense pressed graphite MPG-6 [24], and isostatic graphite I-3 [25].

The resulting coatings were examined by *X*-ray diffraction (XRD) for structural and phase composition analysis, scanning electron microscopy (SEM), optical microscopy (OM), energy-dispersive spectroscopy (SEM–EDS), profilometry, and tribometry.

The phase composition of the products at different stages of synthesis was studied using a D2 Phaser *X*-ray diffractometer (Bruker AXS, Germany) equipped with a copper anode *X*-ray tube and a nickel β-filter. The phase identification was carried out using the EVA software package (Bruker AXS, Germany) with the ICDD PDF-2 diffraction database, release 2014 (PDF-2 Powder Diffraction File-2, ICDD, 2014). To calculate the unit cell parameters of TiC, sodium chloride (NaCl) was used as an internal standard, certified with the XRD powder standard Si640f (NIST, Gaithersburg, Maryland, USA). The calculations were performed using the Rietveld refinement method implemented in Topas-5 (Bruker). The error did not exceed ±0.0001 Å.

XRD analysis was used to determine the lattice parameters, texture, crystallite size, and second-order microstrain.

Second-order stresses (microstresses within crystallite or mosaic block volumes) and the size of the coherent scattering regions (CSR) were estimated from the broadening of *X*-ray reflections obtained from θ/2θ scans on the diffractometer. The observed line broadening generally includes the following contributions: instrumental broadening, size broadening due to small crystallite size (i.e., CSR dimension), and

strain broadening caused by lattice microdeformation [26]. The size–strain separation was performed using the Williamson–Hall method [26], which considers the dependence of reflection broadening on the reflection order (for the first and third orders – 111 and 333 – of the cubic titanium carbide lattice). The instrumental contribution was determined from peak widths of nearly perfect single crystals (Si and Ge) measured at similar diffraction angles.

For Bragg angles corresponding to the 111 and 333 reflections of TiC, high-quality single-crystal silicon and germanium standards were used to evaluate the instrumental broadening. For the 111 reflection at $2\theta \approx 35.9°$, the instrumental component was

$$\beta_{instr} = 1.9 \cdot 10^{-4} \text{ rad},$$

and for the 333 reflection ($2\theta \approx 135.1°$) it was

$$\beta_{instr} = 7.0 \cdot 10^{-4} \text{ rad}.$$

The diffraction profiles followed a Gaussian distribution; therefore, the total line broadening was calculated by summing the squared components from different sources as follows:

$$\beta_{\Sigma}^2 = \beta_{instr}^2 + \beta_{\varepsilon_n}^2 + \beta_{L_n}^2 = \beta_{instr}^2 + \beta_{phys}^2,$$

where β_{Σ} is the total broadening; β_{instr} is instrumental broadening; β_{ε_n} is the broadening caused by lattice strain along the diffraction vector; β_{L_n} is the size broadening due to the finite CSR dimension; β_{phys} is the physical broadening. It is known that

$$\beta_{\varepsilon_n} = 4\varepsilon_n \operatorname{tg}\theta, \quad (1)$$

$$\beta_{L_n} = \frac{\lambda}{L_n \cos\theta}, \quad (2)$$

where $\varepsilon_n = \Delta d/d$, d is the interplanar spacing.

The coating thicknesses were determined by SEM, SEM–EDS, and OM from polished cross-sections of the "titanium carbide – graphite substrate" structures. Cross-sections were prepared from the end faces of the structures by breaking or cutting samples, followed by facing, grinding, and polishing operations.

The tribological properties of the TiC coating (10 μm thick) on a graphite substrate (grade I-3) were evaluated using counterbodies made of structural steel (ShKh-15) and zirconia (ZrO_2) on an FMT-5000 tribometer according to the standard disk–ball test configuration. The disk rotation speed was 60 rpm (linear speed 0.03 cm/s), the wear track radius was 5 mm, and the applied load range was 10–200 N.

To assess the chemical stability, graphite components with TiC protective coatings were held at 2100 °C for 10 h in the presence of SiC powder.

Results and discussion

Synthesis mechanism. According to estimates reported in [27], the chemical reaction between titanium oxide and carbon powders starts at $t = 1300$ °C, and a single-phase titanium carbide is formed at about 1500 °C It was also noted in [28] that the degree of conversion of titanium dioxide to titanium carbide approaches unity in the temperature range of 1500–3340 K. XRD phase identification of the product obtained by holding the TiO_2-based reaction mixture applied to graphite components at 1500 °C for 1 h in forevacuum (<1 Pa) (Fig. 1, *a*) revealed a mixture of the oxides Ti_2O_3 and TiO together with the titanium carbides $TiC_{0.957}$ and TiC.

Thus, it can be assumed that the transformation proceeds through intermediate stages involving the formation of lower oxides (TiO and Ti_2O_3), in accordance with the principle proposed by A.A. Baykov [29]:

$$TiO_2 \rightarrow Ti_2O_3 \rightarrow TiO \rightarrow TiC.$$

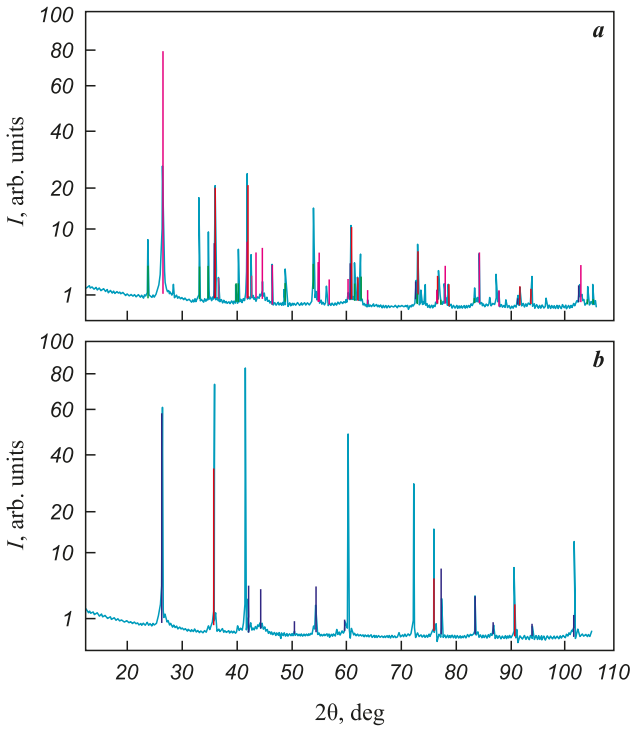

Fig. 1. *X*-ray diffraction patterns (CuK_α radiation) of TiO_2–carbon reaction products
a – $t = 1500$ °C, $\tau = 1$ h; ***b*** – 1900 °C, 1 h

Рис. 1. Рентген-дифрактограмма (CuK_α-излучение) продуктов взаимодействия TiO_2 с углеродом
a – $t = 1500$ °C, $\tau = 1$ ч; ***b*** – 1900 °C, 1 ч

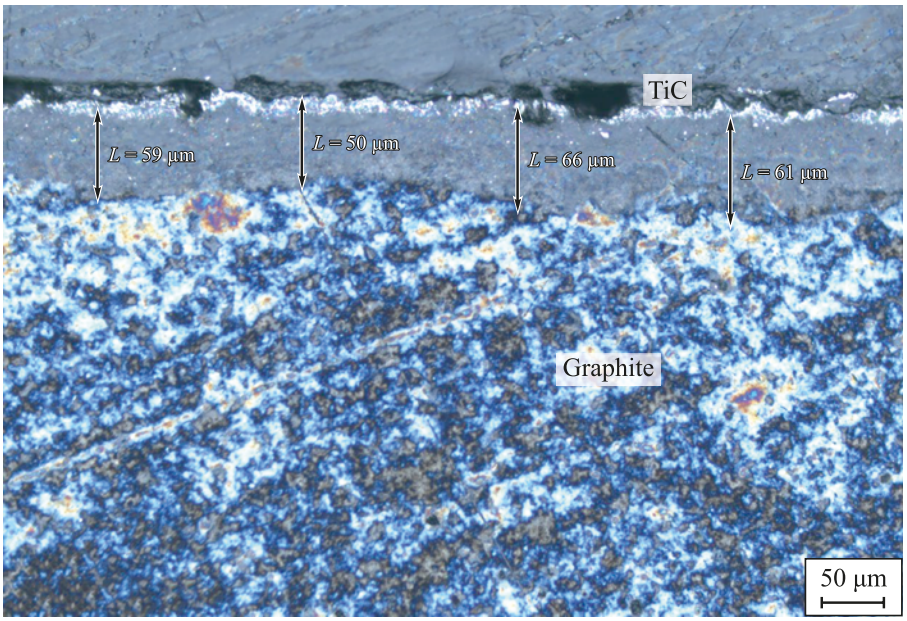

Fig. 2. Optical micrograph of a polished cross section

Рис. 2. Оптическая микрофотография участка шлифа

After holding at t = 1900 °C for 1 h under forevacuum conditions (Fig. 1, *b*), the reaction of carbide formation was complete for all graphite grades. The main phase was cubic $TiC_{0.957}$ (hamrabayevite, NaCl-type structure) with a small amount of graphite, which apparently resulted from carbonization of the adhesive.

As noted in [30], the high rate of solid-state carbothermal reactions of oxide carburization can be explained by the formation of a vapor phase that adsorbs onto carbon surfaces. In this study, in addition to vapor-phase transport, we observed redistribution of the reaction mixture along the graphite surface via flows of a liquid phase (likely TiO_2).

Coating thickness. In fracture cross-sections of the TiC-on-graphite structure, the coating thickness could not be determined by optical microscopy (OM) because of insufficient contrast. After polishing, a strong optical contrast appeared due to the substantial difference in mechanical properties between titanium carbide and graphite, enabling thickness estimation (Fig. 2). Since graphite is highly porous and the transformation of oxides into carbide occurs via participation of a liquid phase, OM observations of polished sections may overestimate the coating thickness.

SEM–EDS mapping of the same structure (Fig. 3) yielded significantly smaller thickness values – 20–25 μm compared to 50–60 μm in Fig. 2.

Penetration of the liquid oxide into graphite pores and its reaction with the substrate lead to blurring of the TiC–graphite interface and to the formation of an extended composite interlayer beneath the TiC coating, composed predominantly of graphite. This interfacial blurring is evident in Fig. 4.

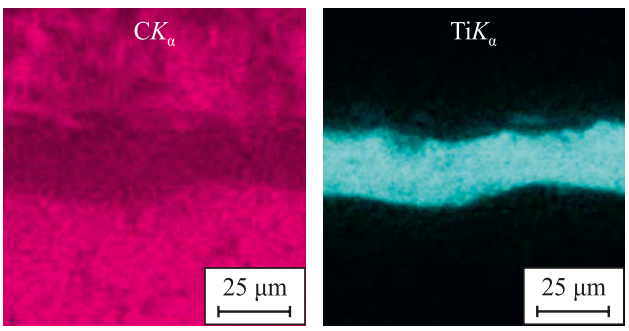

Fig. 3. SEM–EDS image of a polished cross section (see Fig. 2)

Рис. 3. РЭМ ЭДС-изображение участка шлифа (см. рис. 2)

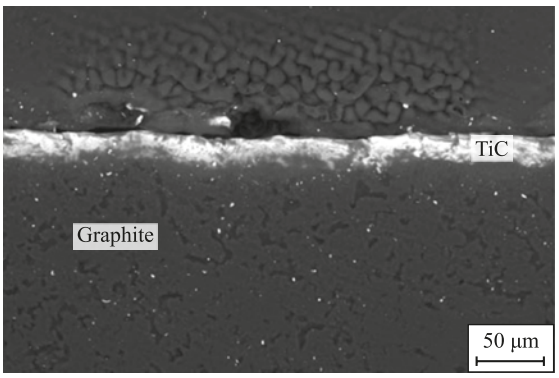

Fig. 4. SEM image of a polished cross section in backscattered electron (BSE) contrast

Рис. 4. РЭМ-изображение шлифа в упругоотраженных электронах (BSE контраст)

Morphology. On isostatic graphite, the titanium carbide coating generally exhibited a dense, flat surface composed of fused crystallites with sizes of 10–30 μm (Fig. 5, *a*). For less dense graphite grades, the surface appeared more developed, consisting of columnar crystallites poorly bonded to each other (Fig. 5, *b*).

Structural defects. In thicker coatings (>30 μm), local cracking was observed, evidently caused by the difference in the linear coefficients of thermal expansion (CTE) between the coating and the substrate for all graphite grades (Fig. 6). First-order (macroscopic) stresses were confirmed by XRD (see Table 2).

Texture analysis. Protective coatings obtained on graphite components by chemical vapor deposition (CVD) methods usually exhibit a pronounced axial growth texture oriented normal to the graphite surface (for example, this is noted for tantalum carbide coatings in [31]).

For protective applications, the most favorable state is texture-free, as it is associated with the absence of through cracks [31]. However, a weak growth texture contributes to improved crystallite bonding and enhances the smoothness and continuity of the coating layer.

To evaluate the growth texture, XRD (θ–2θ) reflection intensities were measured after background subtraction for TiC films deposited on graphite plates made from the selected grades (sample *1* – GMZ, *2* – MPG-6, *3* – I-3). A polycrystalline TiC reference from the ASTM card No. 35-0801 [32] and a TiC powder synthesized in-house (without a graphite substrate) were used for comparison. The reflection intensities normalized to the intensity of the (111) reflection of the corresponding sample are presented in Table 1.

According to Table 1, samples *1–3* are, with high confidence, characterized by a pronounced axial [111] growth texture.

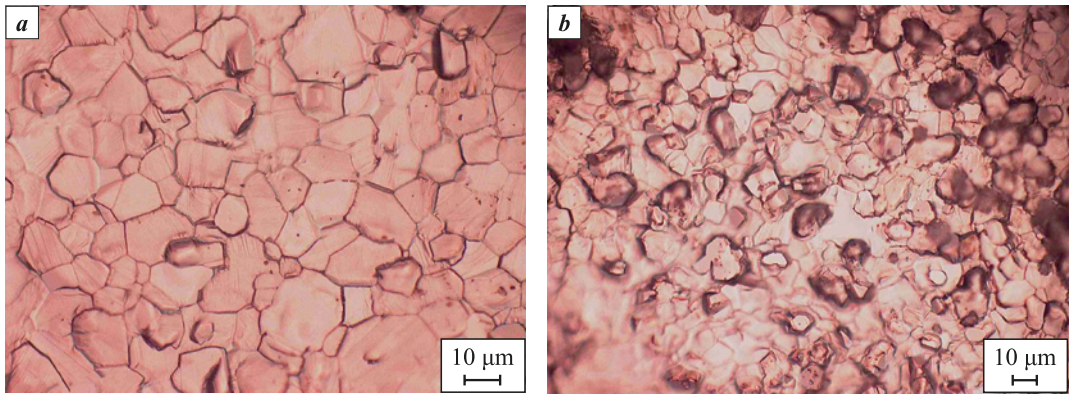

Fig. 5. Surface morphology of the protective coating (optical microscopy image)
a – on I-3 graphite; ***б*** – on MPG-6 graphite

Рис. 5. Морфология поверхности защитного покрытия (ОМ)
а – на графите И-3; ***б*** – на графите МПГ-6

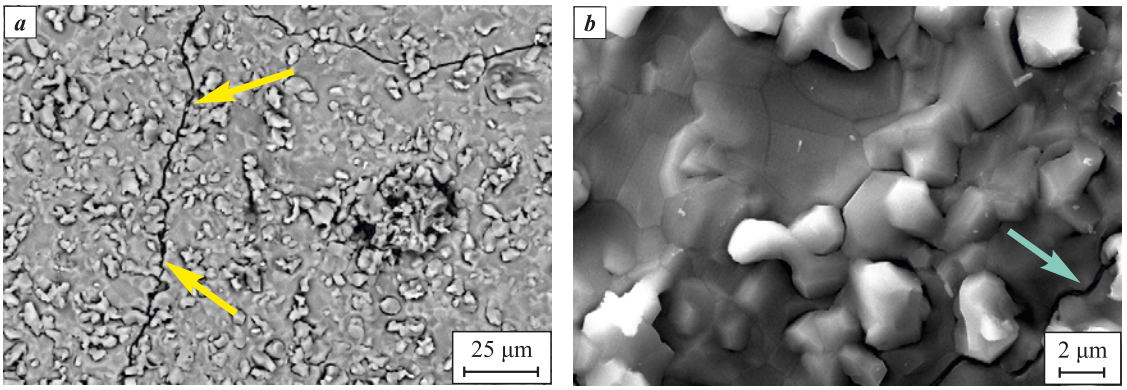

Fig. 6. SEM image of the coating surface on GMZ graphite at different magnification
The arrows indicate surface crack

Рис. 6. РЭМ-фотографии поверхности покрытия на графите ГМЗ с разным увеличением
Стрелки указывают на трещины на поверхности

Table 1. **Intensities of *X*-ray diffraction peaks for TiC samples**

Таблица 1. **Интенсивности рефлексов обзорных дифрактограмм образцов TiC**

Reflection	Intensity, arb. units				
	Sample			ASTM, 035-0801	TiC powder
	1	*2*	*3*		
111	100	100	100	100	100
200	64	86	52	137	110
220	37	42	18	82	82
311	19	22	16	41	65
222	16	16	22	23	47
400	4	5	5	14	30

Determination of the lattice period and first-order stresses. The measured lattice parameters of TiC are presented in Table 2 (the measurement uncertainty was ±0.0001 Å). According to the ASTM database, the equilibrium lattice parameter of titanium carbide is a_{eq} = 4.3274(2) Å. The values of TiC lattice strain on graphite substrates of different grades, listed in Table 2, are of the same sign in all cases, which suggests the presence of thermal stresses at the TiC–graphite interface. As is well known, graphite grades exhibit high anisotropy and a wide range of linear coefficients of thermal expansion (CTE); however, literature data on CTE values for specific graphite grades are scarce [33–36]. An exception is represented by isostatic graphites, which are characterized by isotropic physical properties. The CTE values of the graphite grades used are also given in Table 2. For comparison, the CTE of titanium carbide is $(7.0\div8.0)\cdot10^{-6}$ K^{-1} [29; 37].

As can be seen from Table 2, the strain values are not only of the same sign (positive) but also correlate with the differences between the CTE of TiC and that of the corresponding graphite substrate. Note also that isostatic graphite is not the best substrate for a TiC film owing to the high stress level generated in the coating.

Measurement of crystallite size and inhomogeneous lattice microstrain. The calculated results are summarized in Table 3.

It is well known that, according to Eqs. (1) and (2), the ratio β_{333}/β_{111} lies within the bounds

$$\left(\frac{\cos\theta_{111}}{\cos\theta_{333}} = 2.49\right) < \frac{\beta_{333}}{\beta_{111}} < \left(\frac{tg\theta_{333}}{tg\theta_{111}} = 7.48\right).$$

When β_{333}/β_{111} approaches the cosine ratio, the line broadening is governed primarily by the finite crystallite size (i.e., the limited coherent scattering region, CSR). Conversely, when the ratio approaches the tangent ratio, microstrain provides the dominant contribution to broadening. As seen from Table 3, for all graphite substrates the principal contribution arises from the limited CSR (crystallite) size, which – within the measurement uncertainty – is on the order of 10^3 Å.

Tribological testing. During wear testing of the TiC coating (Vickers hardness 3000 HV, thickness 10 μm) deposited on a graphite substrate (500 HV) in disk configuration and tested against a ShKh15 steel ball (1900 HV), no coating wear was observed. When the TiC coating was tested against zirconium dioxide (ZrO_2, 12,000 HV), coating wear occurred, and it was

Table 2. **Lattice parameter a of TiC and related characteristics on graphite substrates of different grades**

Таблица 2. **Параметры решетки TiC на деталях из различных марок графита**

Graphite grade	TiC lattice parameter *a*, Å	TiC lattice strain (first-order), $(a - a_{eq})/a_{eq}$	Graphite CTE, 10^{-6} K^{-1}	ΔCTE (TiC – graphite), 10^{-6} K^{-1}
GMZ	4.3305	$+7.2\cdot10^{-4}$	4.5	2.5–3.5
MPG-6	4.3290	$+3.7\cdot10^{-4}$	6–8	0–1.0
I-3	4.3340	$+1.5\cdot10^{-3}$	3–5	2.0–5.0

Table 3. **Analysis of *X*-ray peaks broadening factors**

Таблица 3. **Анализ факторов уширения рентгеновских линий**

Graphite grade	Reflection	β_{phys}, 10^{-3} rad	β_{333}/β_{111}	ε_n	L_n, Å
GMZ	111	2.15	2.06	–	750–900
	333	4.44			
MPG-6	111	1.39	2.84	–	1000–1150
	333	3.95			
I-3	111	2.08	2.33	–	750–850
	333	4.84			

four times greater than the wear of the ZrO_2 ceramic ball. In this case, the TiC coating began to fail at loads ≥90 N, accompanied by a sharp increase and scatter (instability) in the friction force and an exponential increase in the penetration rate of the ZrO_2 ball into the coating during sliding as the load increased.

In the initial state, the profilometric parameters of the coating were, μm: R_a = 1.973; R_q = 2.550; R_z = 14.096; and R_t = 17.547. After testing, the surface roughness increased approximately 1.2-fold.

Testing under SiC single-crystal growth conditions. After holding the coated graphite components in contact with SiC powder at 2100 °C under an argon atmosphere (200 Pa) for 10 h, no changes in the coating's morphology or phase composition were observed.

Conclusion

A simple and inexpensive two-stage liquid-phase process for depositing titanium carbide from a TiO_2-based mixture can be used to produce passivating layers on graphite assembly components operating in high-temperature processes under aggressive gaseous environments. Isotropic graphites with minimal porosity are preferable as structural materials for graphite assemblies, as they exhibit a more favorable morphology of the protective coating. The resulting coatings are characterized by a [111] texture and by thermal stresses whose magnitude depends on the graphite grade.

References / Список литературы

1. Tairov Yu., Lebedev A., Avrov D. The main defects of silicon carbide ingots and epitaxial layers. Saarbrucken: Lambert Academic Publishing, 2016. 76 p.
2. Avrov D.D., Bulatov A.V., Dorozhkin S.I., Lebedev A.O., Tairov Yu.M. Defect formation in silicon carbide large-scale ingots grown by sublimation technique. *Journal of Crystal Growth*. 2005;275(1–2):e485–e489. https://doi.org/10.1016/j.jcrysgro.2004.11.112
3. Nakamura D., Shigetoh K. Fabrication of large-sized TaC-coated carbon crucibles for the low-cost sublimation growth of large-diameter bulk SiC crystals. *Japanese Journal of Applied Physics*. 2017;56(8):085504. https://doi.org/10.7567/JJAP.56.085504
4. Sun X., Zhang J., Pan W., Wang W., Tang C. Research progress in surface strengthening technology of carbide-based coating. *Journal of Alloys and Compounds*. 2022;905:164062. https://doi.org/10.1016/j.jallcom.2022.164062
5. Dahotre N.B., Kadolkar P., Shah S. Refractory ceramic coatings: processes, systems and wettability/adhesion. *Surface and Interface Analysis*. 2001;31(7):659–72. https://doi.org/10.1002/sia.1092
6. Kavishwar S., Bhaiswar V., Kochhar S., Fande A., Tandon V. State-of-the-art titanium carbide hard coatings: a comprehensive review of mechanical and tribological behaviour. *Engineering Research Express*. 2024;6(4): 042401. https://doi.org/10.1088/2631-8695/ad7fb7
7. Gong Y., Tu R., Goto T. High-speed deposition of titanium carbide coatings by laser-assisted metal-organic CVD. *Materials Research Bulletin*. 2013;48(8):2766–2770. https://doi.org/10.1016/j.materresbull.2013.03.039
8. Uhlmann E., Schröter D. Process behaviour of micro-textured CVD diamond thick film cutting tools during turning of Ti–6Al–4V. *Procedia CIRP*. 2020;87:25–30. https://doi.org/10.1016/j.procir.2020.02.014
9. Azadi M., Sabour Rouhaghdam A., Ahangarani S. Effect of temperature and gas flux on the mechanical behavior of TiC coating by pulsed DC plasma enhanced chemical vapor deposition. *International Journal of Engineering. Transactions B: Applications*. 2014;27(8):1243–1250. https://doi.org/10.5829/idosi.ije.2014.27.08b.10
10. Shanaghi A., Rouhaghdam A.R.S., Ahangarani S., Chu P.K., Farahani T.S. Effects of duty cycle on microstructure and corrosion behavior of TiC coatings prepared by DC pulsed plasma CVD. *Applied Surface Science*. 2012;258(7):3051–3057. https://doi.org/10.1016/j.apsusc.2011.11.036
11. Dan A., Bijalwan P.K., Pathak A.S., Bhagat A.N. A review on physical vapor deposition-based metallic coatings on steel as an alternative to conventional galvanized coatings. *Journal of Coatings Technology and Research*. 2022;19(2):403–438. https://doi.org/10.1007/s11998-021-00564-z
12. Baptista A., Silva F., Porteiro J., Míguez J., Pinto G. Sputtering physical vapour deposition (PVD) coatings: a critical review on process improvement and market trend demands. *Coatings*. 2018;8(11):402. https://doi.org/10.3390/coatings8110402
13. Fenker M., Balzer M., Kappl H. Corrosion protection with hard coatings on steel: Past approaches and current research efforts. *Surface and Coatings Technology*. 2014;257:182–205. https://doi.org/10.1016/j.surfcoat.2014.08.069
14. Aihaiti L., Tuokedaerhan K., Sadeh B., Zhang M., Shen X., Mijiti A. Effect of annealing temperature on microstructure and resistivity of TiC thin films. *Coatings*. 2021;11(4):457. https://doi.org/10.3390/coatings11040457
15. Sidelev D.V., Pirozhkov A.V., Mishchenko D.D., Syrtanov M.S. Titanium carbide coating for hafnium hydride neutron control rods: *In situ X*-ray diffraction study. *Coatings*. 2023;13(12):2053. https://doi.org/10.3390/coatings13122053
16. Ogunlana M.O., Muchie M., Swanepoel J., Adenuga O.T., Oladijo O.P. Numerical modelling and simulation for sliding wear effect with microstructural evolution of sputtered titanium carbide thin film on metallic materials. *Coatings*. 2024;14(3):298. https://doi.org/10.3390/coatings14030298
17. Xie Q., Sun G., Fu G., Kang J., Zhu L., She D., Lin S. Comparative study of titanium carbide films deposited by plasma-enhanced and conventional magnetron sputtering at various methane flow rates. *Ceramics International*. 2023;49(15);25269–25282. https://doi.org/10.1016/j.ceramint.2023.05.061

18. Chen L., Guan C., Ma Z., Cui Z., Zhang Z., Yu T., Gu R. Modeling and simulation of grinding surface morphology for laser cladding in situ TiC reinforced Ni-based composite coatings. *Surface and Coatings Technology*. 2025;498: 131831. https://doi.org/10.1016/j.surfcoat.2025.131831

19. Shepelin N.A., Tehrani Z.P., Ohannessian N., Schneider C.W., Pergolesi D., Lippert T. A practical guide to pulsed laser deposition. *Chemical Society Reviews*. 2023;52(7): 2294–321. https://doi.org/10.1039/D2CS00938B

20. Zhao T., Zhang S., Zhou F.Q., Zhang H.F., Zhang C.H., Chen J. Microstructure evolution and properties of *in-situ* TiC reinforced titanium matrix composites coating by plasma transferred arc welding (PTAW). *Surface and Coatings Technology*. 2021;424:127637. https://doi.org/10.1016/j.surfcoat.2021.127637

21. Zhao M., Ma Y., Zhang Y., Liu X., Sun H., Liang R., Yin H., Wang D. An efficient salt-thermo-carburizing method to prepare titanium carbide coating. *Surface and Coatings Technology*. 2023;465:129546. https://doi.org/10.1016/j.surfcoat.2023.129546

22. Zhao M., Tang M., Shi H., Sun H., Li X., Yin H., Wang D. Anodic polarization accelerated titanium carbide coating formation in molten salt. *Surface and Coatings Technology*. 2024;483:130803. https://doi.org/10.1016/j.surfcoat.2024.130803

23. Grafit-Garant LLC, Chelyabinsk. Coarse and medium grained graphite: GMZ, 3OPG, PPG. URL: https://grafit-garant.ru/grafit/grafit-gmz-zopg-ppg/ (accessed: 07.02.2025). (In Russ.).

24. LLC PC Grafit-Region, Chelyabinsk. Graphite grades used at the Graphit–Region plant. URL: https://graphite-r.ru/info/marki/?ysclid=m35je0yhbq68035288 (accessed: 07.02.2025). (In Russ.).

25. Grafit-Garant LLC, Chelyabinsk. Isostatic grades of graphite I-1, I-3. URL: https://grafit-garant.ru/grafit/izostaticheski-grafit/ (accessed: 07.02.2025). (In Russ.).

26. Gorelik S.S., Skakov Yu.A., Rastorguev L.N. *X*-ray and electron-optical analysis. Moscow: MISIS, 2002. 360 p. (In Russ.).

Горелик С.С., Скаков Ю.А., Расторгуев Л.Н. Рентгенографический и электронно-оптический анализ М.: МИСиС, 2002. 360 с.

27. Elyutin V.P., Pavlov Yu.A., Polyakov V.P., Sheboldaev S.B. Interaction of metal oxides with carbon. Moscow: Metallurgiya, 1976. 360 p. (In Russ.).

Елютин В.П., Павлов Ю.А., Поляков В.П., Шеболдаев С.Б. Взаимодействие окислов металлов с углеродом. М.: Металлургия, 1976. 360 с.

28. Rosin I.V., Tomina L.D. General and inorganic chemistry. Modern course. Moscow: Yurait, 2012, 1338 p. (In Russ.).

Росин И.В., Томина Л.Д. Общая и неорганическая химия. Современный курс. М.: Юрайт, 2012. 1338 с.

29. Kiparisov S.S., Levinskii Yu.V., Petrov A.P. Titanium carbide: production, properties, application. Moscow: Metallurgiya, 1987, 216 p. (In Russ.).

Кипарисов С.С., Левинский Ю.В., Петров А.П. Карбид титана: получение, свойства, применение. М.: Металлургия, 1987. 217 с.

30. Wang L., Li Q., Zhu Y., Qian Y. Magnesium-assisted formation of metal carbides and nitrides from metal oxides. *International Journal of Refractory Metals and Hard Materials*. 2012;31:288–292. https://doi.org/10.1016/j.ijrmhm.2011.10.009

31. Nakamura D., Shigetoh K., Suzumura A. Tantalum carbide coating via wet powder process: From slurry design to practical process tests. *Journal of the European Ceramic Society*. 2017;37(4):1175–1185. https://doi.org/10.1016/j.jeurceramsoc.2016.10.029

32. ASTM Diffraction Data File. ASTH, Philadelphia, 1969–2025.

33. Ostrovskii V.S., Virgil'ev Yu.S., Kostrikov V.I., Shipkov N.N. Artificial graphite. Moscow: Metallurgiya, 1986. 272 p. (In Russ.).

Островский В.С., Виргильев Ю.С., Костриков В.И., Шипков Н.Н. Искусственный графит. М.: Металлургия, 1986. 272 с.

34. Stankus S.V., Yatsuk O.S., Zhmurikov E.I., Tekchno L. Thermal expansion of artificial graphites in the temperature range 293–1650 K. *Thermophysics and Aeromechanics*. 2012;19(5):637–642. (In Russ.).

Станкус С.В., Яцук О.С., Жмуриков Е.И., Текчно Л. Тепловое расширение искусственных графитов в интервале температур 293–1650 К. *Теплофизика и аэромеханика*. 2012;19(5):637–642.

35. Zhmurikov E.I., Bubnenkov I.A., Dryomov V.V., Samarin S.I., Pokrovskii A.S., Kharkov D.V. Graphite in science and nuclear technology. Novosibirsk, 2023. 193 p. (In Russ.).

Жмуриков Е.И., Бубненков И.А., Дремов В.В., Самарин С.И., Покровский А.С., Харьков Д.В. Графит в науке и ядерной технике. Новосибирск, 2023. 193 с.

36. NPP Grafit–Pro, Chelyabinsk. Graphite products of various brands. URL: http://grafitpro.ru/izdeliya-iz-grafita (accessed: 13.02.25). (In Russ.).

37. Kim J., Kang S. Elastic and thermo-physical properties of TiC, TiN, and their intermediate composition alloys using *ab initio* calculations. *Journal of Alloys and Compounds*. 2012;528:20–27. https://doi.org/10.1016/j.jallcom.2012.02.124

Information about the Authors

Aleksey V. Afanas'ev – Cand. Sci. (Eng.), Associate Professor, Director of the Center for Microtechnology and Diagnostics, Leading Research Scientist, Saint Petersburg State Electrotechnical University "LETI"
ORCID: 0000-0001-7511-7463
E-mail: a_afanasjev@mail.ru

Сведения об авторах

Алексей Валентинович Афанасьев – к.т.н., доцент, директор Центра микротехнологии и диагностики, вед. науч. сотрудник Санкт-Петербургского государственного электротехнического университета (ЛЭТИ) им. В.И. Ульянова (Ленина) (СПбГЭТУ)
ORCID: 0000-0001-7511-7463
E-mail: a_afanasjev@mail.ru

Yuri O. Bykov – Leading Engineer, LETI
E-mail: bykov@list.ru

Andrey O. Lebedev – Dr. Sci. (Phys.-Math.), Chief Research Scientist, LETI and Ioffe Physical-Technical Institute of the Russian Academy of Sciences (Ioffe Institute)
ORCID: 0000-0003-3476-1783
E-mail: aswan61@yandex.ru

Alexandr V. Markov – Engineer, LETI
E-mail: sanmarkov@gmail.com

Natalia V. Sharenkova – Cand. Sci. (Eng.), Senior Research Scientist, Ioffe Institute
ORCID: 0000-0001-6471-6233
E-mail: natasha.sharenkova@gmail.com

Natalia M. Latnikova – Cand. Sci. (Eng.), Senior Research Scientist, Central Research Institute of Materials named after D.I. Mendeleev
E-mail: LatnikovaN@cniim.spb.ru

Юрий Олегович Быков – вед. инженер, сотрудник СПбГЭТУ (ЛЭТИ)
E-mail: bykov@list.ru

Андрей Олегович Лебедев – д.ф.-м.н., гл. науч. сотрудник, сотрудник СПбГЭТУ (ЛЭТИ) и Физико-технического института им. А.Ф. Иоффе РАН (ФТИ РАН)
ORCID: 0000-0003-3476-1783
E-mail: aswan61@yandex.ru

Александр Владимирович Марков – инженер, сотрудник СПбГЭТУ (ЛЭТИ)
E-mail: sanmarkov@gmail.com

Наталья Викторовна Шаренкова – к.т.н. ст. науч. сотрудник ФТИ РАН
ORCID: 0000-0001-6471-6233
E-mail: natasha.sharenkova@gmail.com

Наталья Михайловна Латникова – к.т.н. ст. науч. сотрудник Центрального НИИ материалов им. Д.И. Менделеева
E-mail: LatnikovaN@cniim.spb.ru

Contribution of the Authors

A. V. Afanas'ev – wrote the manuscript.
Yu. O. Bykov – conducted annealing experiments on the protective coating.
A. O. Lebedev – defined the study objectives.
A. V. Markov – prepared and applied coating mixtures.
N. V. Sharenkova – performed *X*-ray phase analysis.
N. M. Latnikova – performed SEM-EDS analysis and sample sectioning.

Вклад авторов

А. В. Афанасьев – написание статьи.
Ю. О. Быков – проведение экспериментов по отжигу защитного покрытия.
А. О. Лебедев – определение цели работы.
А. В. Марков – приготовление и нанесение смесей.
Н. В. Шаренкова – проведение рентгеновского фазового анализа.
Н. М. Латникова – выполнение РЭМ ЭДС, шлифы.

Received 28.11.2024
Revised 09.04.2025
Accepted 21.04.2025

Статья поступила 28.11.2024 г.
Доработана 09.04.2025 г.
Принята к публикации 21.04.2025 г.

Materials and Coatings Fabricated Using the Additive Manufacturing Technologies
Материалы и покрытия, получаемые методами аддитивных технологий

UDC 66.046.44
https://doi.org/10.17073/1997-308X-2025-5-80-93

Research article
Научная статья

Densification of porous SLS SiC preforms through polymer infiltration, pyrolysis, and liquid silicon infiltration

B. B. Bubnenkov[1], A. S. Zharmukhambetov[1], I. A. Ivanov[1], I. S. Sharapov[2], S. N. Veselkov[2]

[1] **JSC "Scientific and Production Association "Central Research Institute of Mechanical Engineering Technology (CRIMET)"**
4 Sharikopodshipnikovskaya Str., Moscow 115088, Russia
[2] **JSC "Scientific Research Institute and Scientific Production Association "LUCH"**
24 Zheleznodorozhnaya Str., Podolsk, Moscow region 142103, Russia

bogis13@yandex.ru

Abstract. This article continues the research on α-SiC powder preforms produced by selective laser sintering (SLS) [1]. The study examines the hydrostatic density and microstructure of the surface and internal cross sections of both the porous preforms and the densified specimens obtained through post-processing. Two post-processing routes were tested to increase the density of porous SLS preforms. The first method involved densification by silicon infiltration (liquid silicon infiltration, LSI). The second method was hybrid, combining polymer infiltration and pyrolysis followed by silicon infiltration (PIP + LSI). For conventionally pressed materials, this hybrid treatment forms a higher fraction of silicon carbide in the structure compared to LSI alone, which has a beneficial effect on mechanical and thermophysical properties. The study established the dependence of SiC, Si, and C phase contents and the relative density on the number of infiltration and pyrolysis cycles and on the post-processing route. Specimens were fabricated with different single-layer thicknesses (30 and 50 μm). Specimen with a 30 μm layer thickness had a higher initial density than those with 50 μm layers and required only 2–3 infiltration cycles for carbon saturation, compared with 4–5 cycles for the 50 μm specimens. The final density of the specimens with both layer thicknesses was approximately the same – no higher than 2.88 g/cm^3. The density of specimens subjected only to silicon infiltration was 2.52–2.65 g/cm^3, which is lower than that of the fully post-processed specimens. This density difference was not due to porosity; in fact, the porosity was lower in the LSI specimens. According to quantitative microstructural analysis, the lower density resulted from nearly twice the content of free silicon, which has a lower density than SiC and thus decreases the overall density of the LSI specimens.

Keywords: selective laser sintering, silicon carbide, densification, siliconization, reaction sintering, liquid silicon infiltration (LSI), high-temperature ceramics, porous ceramics, post-processing

For citation: Bubnenkov B.B., Zharmukhambetov A.S., Ivanov I.A., Sharapov I.S., Veselkov S.N. Densification of porous SLS SiC preforms through polymer infiltration, pyrolysis, and liquid silicon infiltration. *Powder Metallurgy and Functional Coatings*. 2025;19(5):80–93. https://doi.org/10.17073/1997-308X-2025-5-80-93

Повышение плотности пористых СЛС-заготовок из карбида кремния пропиткой, пиролизом и силицированием

Б. Б. Бубненков[1], А. С. Жармухамбетов[1], И. А. Иванов[1], И. С. Шарапов[2], С. Н. Веселков[2]

[1] **АО «НПО «Центральный научно-исследовательский институт технологии машиностроения (ЦНИИТМАШ)»**
Россия, 115088, г. Москва, ул. Шарикоподшипниковская, 4
[2] **АО «НИИ НПО «ЛУЧ»**
Россия, 142103, Московская обл., г. Подольск, ул. Железнодорожная, 24

bogis13@yandex.ru

Аннотация. Данная статья является продолжением работы по исследованию образцов из порошка α-SiC, получаемых по технологии селективного лазерного спекания (СЛС) [1]. Рассматриваются гидростатическая плотность, а также микроструктура поверхности и внутренних сечений пористых заготовок и уплотненных с помощью постобработки. Проведена апробация двух способов постобработки для повышения плотности пористых заготовок. Первый способ – уплотнение за счет силицирования, так называемой пропитки расплавом кремния (LSI), или жидкофазной пропитки. Второй способ уплотнения является гибридным из-за сочетания метода пропитки полимером пористой заготовки с последующим пиролизом и силицированием – так называемый PIP метод, совмещенный с LSI. Для стандартных методов прессования гибридная обработка PIP + LSI позволяет сформировать повышенную долю карбида кремния в материале по сравнению со способом LSI, что благоприятно сказывается на механических и теплофизических свойствах. По результатам исследований установлена зависимость содержания фаз SiC, Si, C в материале и относительной плотности от количества циклов пропитки, пиролиза и способа постобработки. Образцы изготавливались с различной высотой единичного слоя – 30 и 50 мкм. Образцы с высотой слоя 30 мкм имели бóльшую начальную плотность, чем образцы со слоем в 50 мкм, а также требовали 2–3 пропитки для насыщения углеродом, в отличие от 4–5 пропиток во втором случае (50 мкм). Финальная плотность образцов при высоте слоя 30 и 50 мкм находилась примерно на одном уровне – не более 2,88 г/см^3. Для образцов, прошедших только стадию силицирования, плотность составила 2,52–2,65 г/см^3, что меньше, чем у образцов после полного цикла постобработки. Разница плотности образцов не связана с пористостью – напротив, пористость меньше в образцах после LSI. По результатам количественного микроструктурного анализа разница плотности обусловлена в 2 раза бóльшим содержанием свободного кремния, который имеет плотность ниже, чем у SiC, снижая тем самым общую плотность LSI-образцов.

Ключевые слова: селективное лазерное спекание, карбид кремния, уплотнение, силицирование, реакционное спекание, пропитка расплавом кремния, высокотемпературная керамика, пористая керамика, постобработка

Для цитирования: Бубненков Б.Б., Жармухамбетов А.С., Иванов И.А., Шарапов И.С., Веселков С.Н. Повышение плотности пористых СЛС-заготовок из карбида кремния пропиткой, пиролизом и силицированием. *Известия вузов. Порошковая металлургия и функциональные покрытия*. 2025;19(5):80–93. https://doi.org/10.17073/1997-308X-2025-5-80-93

Introduction

Porous ceramic materials are widely used in industry for a range of functions, including heaters, filters, catalysts, and thermal insulators. Silicon carbide (SiC) in a porous form is commonly employed as a filtration element in metal casting operations. Porous architectures can also be used as catalyst supports for depositing a catalytice coating; for such applications, porosity typically ranges from ~70 to ~20 %. In preforms produced by selective laser sintering (SLS), achievable porosity is ~55 to ~15 %, which is suitable for manufacturing such components. A further advantage of SLS is the ability to design hierarchical porous structures within a part – useful for heat-exchange and thermal-management elements, gas and liquid filters, catalysts, sensors for aggressive environments, and medical implants.

During SLS, laser exposure sinters SiC powder via a high-rate evaporation–condensation mechanism: SiC partially decomposes upon sublimation and then recondenses. The surfaces of the starting powder particles undergo this process, which causes spheroidization of angular fragments and the formation of submicrometer particles of nonstoichiometric SiC_{1-x} and Si (average size <1 μm). These decomposition products appear on the particle surfaces as spherical inclusions. Owing to laser heating, lower-melting surface phases of Si and nonstoichiometric SiC_{1-x} form on the SiC powder particles. These phases promote particle sliding and rearrangement, leading to local densification within the sintering zone; upon crystallization, the par-

ticles bond to one another, thereby building the porous skeleton of the SLS preform [1].

It should be noted that, to impart additional strength to the porous SLS framework, an extra manufacturing cycle in the form of pressureless sintering at a temperature typical for such processes (usually above 1800 °C) with a short dwell (3–5 h) may be required. This operation is warranted because the interparticle bonds formed during high-rate sintering via the evaporation–condensation mechanism are relatively weak and contain a fraction of free silicon, as shown in our previous study [1]. During pressureless sintering, stronger bonding develops owing to more complete and extensive diffusion at interparticle contacts under the sintering temperature with a longer time at temperature than in the SLS process.

Combining SLS with conventional pressureless sintering enables the fabrication of parts and porous structures with tailored, controlled porosity and complex geometries for high-tech, emerging industrial sectors that require such components.

However, despite a certain industrial demand for porous SiC components of complex shape, the greater share of demand is for high-density products. This is driven by their superior mechanical and thermophysical properties, which broaden the range of applications.

It is well established that, across various additive manufacturing (AM) methods for SiC, the as-built relative density of SiC parts typically lies in the 40–85 % range; therefore, porous SLS preforms require post-processing to increase material density and meet the property requirements of dense parts [2; 3].

To increase the density of porous α-SiC preforms produced by conventional and additive manufacturing methods, both chemical vapor infiltration (CVI) – first tested in the 1910s [4] – and siliconization by liquid silicon infiltration (LSI), known since the 1960s [5], can be employed [5].

Densification methods for porous SiC preforms

Possible implementations of densification methods for porous SiC preforms are shown in Fig. 1.

Chemical vapor infiltration (CVI) involves the infiltration of silane compounds from the gas phase into porous compacts. According to [6], this method yields additively manufactured parts with a bulk density of up to 92 % and a flexural strength of 300 MPa. The residual porosity results from isolated pores that are not accessible from the surface [6].

Siliconization, or liquid silicon infiltration (LSI), is a conventional powder-metallurgy technique used to increase the density of porous graphite and SiC components, thereby minimizing production costs – either by avoiding the need for initially denser compacts or by replacing more time-consuming densification processes. The resulting microstructure contains an increased amount of free silicon, which limits the use of this method by the compositional requirements of the material. During siliconization, pores are filled by molten silicon through capillary action, which increases the density and, consequently, enhances the mechanical properties of the material. Since the mechanical and thermophysical properties of silicon are lower than those of SiC, a drawback of this post-processing method is the reduced overall property set caused by the presence of residual free silicon in the regions formerly occupied by pores.

An important advantage of siliconization is that the process causes virtually no shrinkage. Solidification of molten silicon is accompanied by a volumetric expansion of up to 10.8 % [7], which helps prevent cracking during cooling. This allows the densification of not only simple shapes but also complex-profile parts, where thermal stresses upon cooling are much higher. However, this volume expansion also means

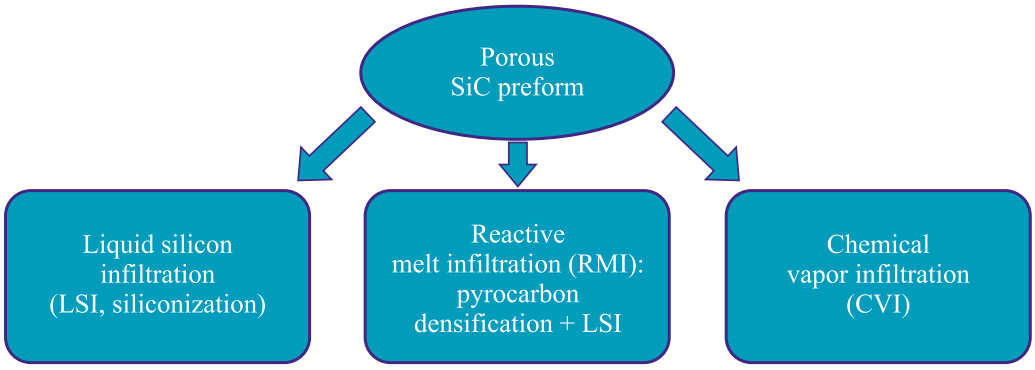

Fig. 1. Variants of densification routes for porous SiC preforms

Рис. 1. Варианты реализации уплотнения пористых заготовок деталей из SiC

that an excess volume is generated during solidification. As the solidification front moves toward the surface, the final freezing of the silicon melt occurs near the surface and is accompanied by expulsion of free silicon outward. This makes mechanical removal of the excess silicon necessary and represents a specific limitation of the method.

Another densification route is the formation of reaction-bonded SiC (RB-SiC) ceramics via reactive wetting of pyrolytic/free carbon by molten silicon within the pores – reactive melt infiltration (RMI) – with the pore space being progressively filled by secondary SiC formed *in situ*. The process flow is illustrated in Fig. 2. At the first stage, the preform is impregnated with a high-char-yield, low-impurity polymer (e.g., phenolic resin) to fill the pores. The polymer is then thermally decomposed – pyrolyzed – to form pyrolytic carbon in the regions previously occupied by the polymer. Alternatively, a carbon source can be incorporated during the initial preform fabrication, for example by using a mixture of SiC powder with carbon powder.

Thermal pyrolysis of the polymer binder phase generates internal pressure within the SiC preform due to the active gas evolution associated with the decomposition of organic components in the binder composition. As a result, a thermal cycle with a slow heating rate (about 1–2 °C/h) is required to prevent thermal deformation and cracking during pyrolysis. In this context, geometric limitations are imposed on the resulting components, particularly on the wall thickness. Typically, the binder phase is converted into residual carbon after thermal debinding, but it can directly transform into SiC when a silicon-containing polymer precursor, such as polycarbosilane or allylhydridopolycarbosilane, is used [8].

After binder burnout, a preliminary sintering step is performed to form new and strengthen existing necks between particles, thereby imparting mechanical integrity to the porous body, similar to conventional porous ceramics fabrication.

At the next stage – siliconization – densification occurs through the reaction between the pyrolytic carbon and molten silicon, resulting in the formation of secondary silicon carbide:

$$Si(l) + C(s) = SiC(s). \quad (1)$$

The liquid silicon infiltration (LSI) process is typically carried out at 1500–1600 °C. During the exothermic reaction (cementation) between molten silicon and pyrolytic carbon, β-SiC is formed and remains stable upon cooling. It is known that the transformation of β-SiC into α-SiC occurs at temperatures above 2000 °C, although a local thermal spike caused by the exothermic reaction may induce partial conversion to the α modification [9; 10]. Densification is gradually completed during cooling with the formation of a new secondary SiC phase, which coexists with the initial α-SiC, residual free silicon, and, in some cases, unreacted carbon. Depending on its volume fraction, the pyrolytic carbon is either completely or partially converted to SiC during siliconization.

After additional polymer infiltration and pyrolysis (PIP) cycles, the volume fraction of SiC after LSI increases due to the growth of the β-SiC phase on the initial α-SiC particles. The amount of carbon particles decreases as they dissolve in the silicon melt, starting with the smaller ones. The pyrolytic carbon acts as the nucleation center for the formation of the β-SiC phase [11]. The reaction leading to the formation of secondary β-SiC is accompanied by a volumetric expansion of approximately 53 % [12; 13], which exceeds the expansion occurring during the crystallization of silicon in the LSI process.

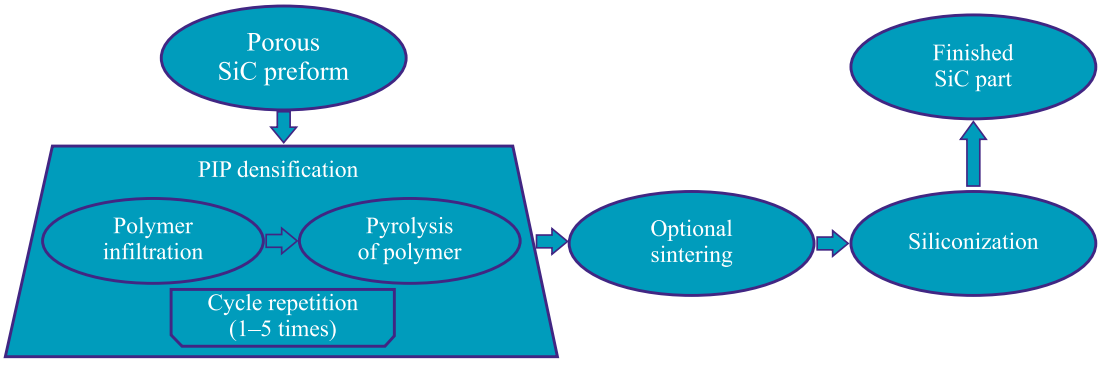

Fig. 2. Flow diagram of densification of porous SiC part preforms by reactive melt infiltration (RMI)

Рис. 2. Схема реализации уплотнения пористых заготовок деталей из SiC методом реакционной пропитки (RMI)

A variation of the Reactive Melt Infiltration (RMI) method involves using a porous carbon preform instead of SiC for silicon-based densification. The mechanical strength of such products is significantly lower because of the high content of unreacted free carbon (matrix) remaining after siliconization [14].

In the PIP + LSI method, an important parameter affecting the anisotropy of properties is the uniformity of carbon distribution within the pores across the section. This factor determines the completeness of the reaction between free silicon and carbon and, consequently, the residual amount of free silicon. In regions with a higher carbon concentration, the local temperature is elevated, accelerating the C + Si reaction. This, in turn, leads to a pronounced increase in the rates of phase formation and gas evolution (CO and SiO_2), as well as a rise in the material's porosity [15].

Another important factor is the carbon content within the pores, defined as the average fraction of a pore's volume filled with carbon. This parameter determines the infiltration capacity of the pore network during siliconization – that is, how long the molten silicon can penetrate through the system of capillary channels before they become sealed by newly formed SiC. It is crucial to minimize the residual free silicon and porosity to achieve the desired combination of mechanical properties. At the same time, this aspect of the process can be deliberately utilized to fabricate graded materials by varying the porosity, carbon concentration, and free silicon content across the section. The number of PIP cycles directly influences the concentration and distribution of pyrolytic carbon, as well as the amount of residual free silicon. Moreover, the number of infiltration cycles can be optimized to reduce residual porosity and obtain the required mechanical strength characteristics [16].

With an increase in the carbon content of the preform before siliconization, both the strength and density initially rise, reach a maximum, and then decrease. This behavior is explained by the fact that at low carbon contents, a large amount of free silicon remains in the structure, whereas at high carbon contents, free carbon persists, and the pores become sealed, hindering the penetration of silicon into the bulk of the preform. As a result, the interfacial strength between large SiC particles and the residual silicon weakens.

At an optimally adjusted carbon concentration, with appropriate reactivity and pore channel size, the residual pore volume surrounding the pyrolytic carbon can be completely filled with secondary silicon carbide. Thus, the secondary and primary SiC phases can be bonded without residual components in the structure. Reducing the amount of free silicon directly decreases the total area of weak SiC/Si interfaces and the number of regions with localized residual stress concentrations. Consequently, the likelihood of crack initiation along the SiC/Si boundary decreases, while both the density and mechanical strength of the material increase.

The LSI process can also be applied to composites (e.g., C_f/SiC), but it has certain specific features. Since LSI is carried out at a temperature above the melting point of silicon, the carbon fibers (C_f) eact with molten Si to form SiC [17–19]. This reaction significantly reduces the carbon fiber content in the composite, thereby diminishing the reinforcing effect.

In [20], the CVI method was used to produce a protective SiC interphase coating on the surface of the C_f, preventing their reaction with molten silicon. After LSI processing, the fibers were well protected, and the composite exhibited a flexural strength of 274 ± 13 MPa and a fracture toughness of 5.82 ± 0.25 MPa·m$^{1/2}$. The authors of [21] fabricated C_f coated with SiC by a hydrothermal method. The SiC coating successfully protected the fibers from erosion and significantly improved the flexural strength and fracture toughness of the C_f/SiC composite by 32.6 and 26.3 %, respectively. However, both of these protective approaches are relatively low in productivity and resource-intensive.

Another study [22] demonstrated that the PIP method can be used to protect fibers prior to siliconization by forming a pyrolytic carbon layer on their surface. This approach is considerably faster and more cost-effective, while increasing the fraction of secondary SiC and reducing the content of free silicon.

The use of various siliconization approaches in combination with SLS offers new opportunities for component fabrication, enabling the production of complex SiC parts with near-net shapes, thereby eliminating the need for costly final machining by additive methods and subsequent densification of porous preforms [23].

The objective of this study was to evaluate the effect of post-processing parameters – polymer infiltration, pyrolysis, and siliconization – on the density of porous SiC preforms produced by the SLS method.

Materials and methods

Porous cubic SiC preforms (10×10×10 mm; Fig. 3) were produced by selective laser sintering in the vertical build direction on mesh supports using a MeltMaster3D-160 system (NPO TsNIITMASH, Moscow) equipped with an ytterbium fiber laser (up to 200 W). The laser energy density used to form the porous SLS preforms was maintained at approxi-

mately 100 J/mm^3 while varying the layer thickness from 30 to 50 µm according to the following relation:

$$E = \frac{P}{Vhd}, \quad (2)$$

where E is the laser energy density, P is the laser power, V and d are the scanning speed and scanning pitch, respectively, and h is the layer thickness.

The starting material for sintering was a single-component SiC powder (grade F320), pre-dried at 100 °C. The powder had poor flowability, an average particle size of 48 ± 0.5 µm, a bulk density of 1.11 ± 0.01 g/cm^3, and a vibrated density of 1.36 ± 0.01 g/cm^3. No sintering aids or other additives were introduced. Layer-by-layer sintering of the SiC powder was carried out in an argon flow atmosphere to prevent oxidation and the formation of SiO_2. The synthesis procedure is described in more detail in [1].

The post-processing of the SLS-fabricated SiC preforms consisted of three main stages:

1. Polymer infiltration – filling the open porosity with a carbon-rich polymer (furan resin). The process was repeated until complete saturation, which was determined by the absence of further mass increase after each infiltration stage.

2. Pyrolysis – thermal decomposition of the polymer with a high carbon yield. After this stage, the infiltrated polymer decomposed within the pore network, leaving free carbon behind. The combined process of polymer infiltration and pyrolysis is referred to as PIP (*Polymer Infiltration and Pyrolysis*).

3. Siliconization (LSI) – infiltration of the preforms through open porosity with liquid silicon. The process was carried out in a chamber under excess pressure, promoting melt penetration into the pores. The molten silicon reacted with the previously formed free carbon, resulting in the formation of secondary silicon carbide, which crystallized upon cooling. A portion of excess silicon also remained and solidified within the pores, filling them.

The post-treatment aimed at increasing the density and strength of the preforms was carried out using two different methods:

– Liquid Silicon Infiltration (LSI) without preliminary polymer infiltration;

– PIP + LSI, combining polymer infiltration, pyrolysis, and subsequent siliconization.

Polymer infiltration with a carbon-rich precursor

Polymer infiltration was performed in furfurylidene diacetone under vacuum, followed by drying at 150 °C to cure the polymer inside the pores. After each infiltration and curing stage, the preforms were subjected to carbonization (pyrolysis).

Carbonization was carried out in a muffle furnace in air, using a graphite-chip carburizer bed as the protective medium according to the following temperature schedule:

– heating to 240 °C at a rate of 220 °C/h;

– heating to 450 °C at a rate of 20 °C/h;

– heating to 850 °C at a rate of 220 °C/h;

– holding for 1 h;

– cooling to room temperature.

Carbonization of the resin at 850 °C was not complete but sufficient for performing the subsequent operations.

The infiltration procedure was repeated n times until the network of inter-pore channels within the preform volume was saturated. Saturation was evaluated by measuring the specific mass gain after each infiltra-

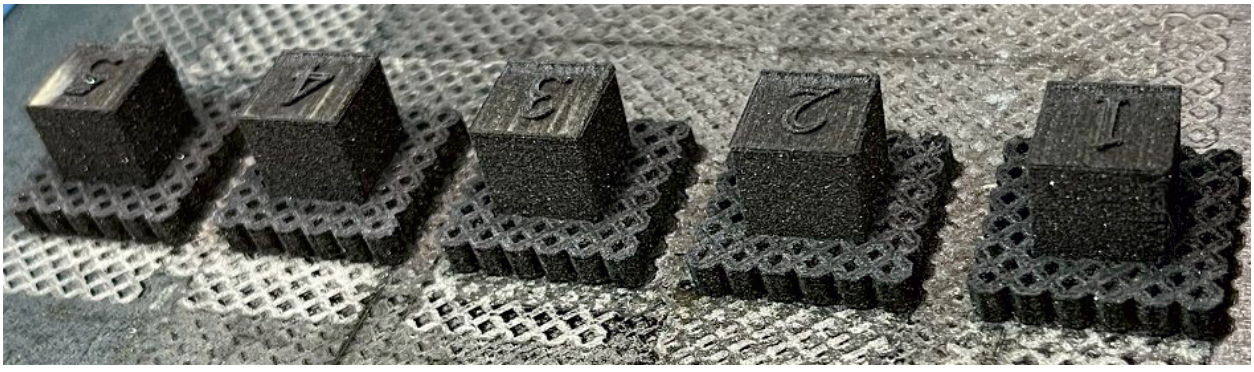

Fig. 3. Initial porous SLS SiC preforms

Рис. 3. Исходные пористые СЛС-заготовки

tion cycle. The absence of further weight increase indicated complete saturation of the preform, after which it was subjected to liquid silicon infiltration (LSI). For different preforms, the number of infiltration cycles ranged from 2 to 6.

Siliconization in a vacuum furnace

After completing the infiltration and carbonization cycles, the SLS- preforms were placed in a vacuum thermal furnace for LSI. The preforms were positioned in a crucible on a technological support assembly composed of composite materials and spacer elements. The crucible was placed on a separate stand, taking into account the temperature-field gradient of the furnace hot zone. Pre-prepared silicon was loaded into the crucible. Its quantity was determined by calculation based on the mass of the SLS preform, their free-carbon content, and porosity. LSI was conducted at 1450 °C. Capillary infiltration was used as the mechanism for melt penetration. The temperature was monitored with a pyrometer and visually through the furnace viewing ports. The total process time was about 10 h. After LSI, a small amount of silicon remained on the preform surfaces; the excess was removed mechanically during the finishing step.

Hot mounting of specimens

For metallographic preparation, the specimens were hot-mounted in phenolic resin using a CitoPress-1 mounting press (Struers, Denmark). Mounting was carried out in both longitudinal and transverse orientations relative to the SLS build direction.

Preparation of metallographic specimens

Metallographic specimen preparation was performed in several stages using a TegraPol-11 grinding and polishing system (Struers) equipped with the TegraForce-1 semi-automatic specimen rotation unit (Struers). The preparation sequence included grinding, fine grinding, diamond polishing, and oxide polishing. For grinding, diamond disks with abrasive grain sizes from 54 to 18 μm were used. Running water was supplied continuously to the grinding area as a cooling and lubricating medium. Fine grinding was carried out using composite single-step fine-grinding disks with diamond suspensions of 15–6 μm particle size. Polishing was performed on a hard polishing cloth with 3 μm diamond suspension, followed by final polishing on a soft cloth using an alumina suspension with a particle size of 0.04 μm.

Microscopy

Optical microscopy. Microstructural constituents and their relative proportions in the specimens were examined using an Olympus PNG-3 optical microscope (Japan) equipped with the Vestra Imaging System (NPO LATEMI, Moscow) for image analysis. Quantitative analysis was performed by assigning distinct colors to individual phases and calculating the number of colored pixels using software-based image segmentation.

Because the structural constituents exhibited different etching behavior, chemical etching for microstructure revelation was not performed.

Scanning electron microscopy. SEM studies were conducted using a Tescan Vega 3XMU analytical system (Czech Republic) equipped with an Oxford Advanced AZtec Energy EDS unit (UK) based on an X-Max80 detector (Oxford Instruments, UK). Observations were performed in high-vacuum mode at an accelerating voltage of 20 kV.

Density measurement by hydrostatic weighing

The density of the specimens was determined after SLS fabrication, during post-processing, and after the final LSI stage using the hydrostatic weighing method in accordance with GOST 18898-89. The density was calculated as

$$\rho = \frac{M_1 \rho_c \rho_l}{(M_2 - M_3)\rho_c - M_4 \rho_l}, \qquad (3)$$

where M_1 is the mass of the specimen without protective coating, g, M_2 is the mass of the coated specimen weighed in air, g, M_3 is the mass of the coated specimen weighed in liquid, g, M_4 is the mass of the protective coating, g; ρ_l is the density of the working liquid, g/cm^3, ρ_c is the density of the coating material, g/cm^3.

Results and discussion

Post-processing

As a result of post-processing, final SiC specimens were obtained from the porous SLS preforms (Fig. 4). Their outer surface exhibited a characteristic metallic sheen, which can be attributed to the presence of free silicon segregated on the surface. During infiltration, silicon penetrates into the porous SLS preform by a capillary mechanism. It reacts both with the sintered SiC skeleton of the preform and with the free carbon present in the pore channels introduced through the PIP process. Upon crystallization, silicon undergoes

Fig. 4. Cubic specimens – porous SLS SiC preforms after PIP densification and LSI treatment

Рис. 4. Кубические образцы – бывшие пористые СЛС-заготовки, прошедшие стадии пироуглеродного уплотнения и силицирования

volumetric expansion, which causes the residual melt to be expelled toward the surface of the specimens.

It should be noted that the depth of melt penetration into the bulk is limited by the presence of closed porosity, the pore size, and the reactivity of carbon. Fig. 5 shows a fracture surface of a specimen demonstrating limited melt infiltration to a depth not exceeding 1.0–1.5 mm. In this case, the shallow penetration was associated with an excessive number of PIP cycles, which led to over-saturation with carbon and, consequently, a reduction in pore size and blockage of most pore channels, preventing molten silicon from penetrating into the interior of the porous SLS preform.

The reaction between molten silicon and carbon occurred only in the near-surface zone on all sides of the specimen, since the entire outer surface was in contact with the melt. However, the observed infiltration pattern indicates that the melt penetrated the specimen volume only within this peripheral region, uniformly distributed over the entire cross-section.

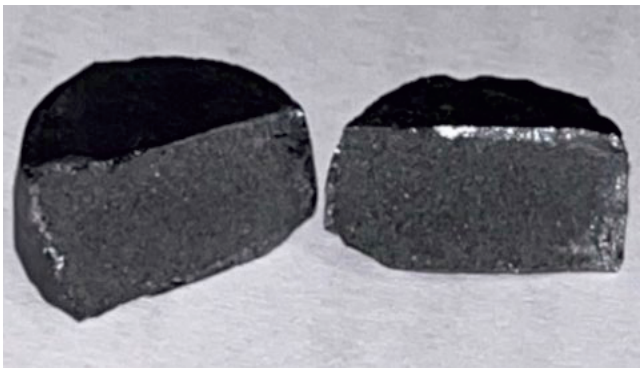

Fig. 5. Cross-sectional fracture of a specimen subjected to an excessive number of PIP densification cycles after LSI

Рис. 5. Поперечный излом образца с избыточным количеством циклов пироуглеродного уплотнения после силицирования

Density measurement

The initial density of the specimens fabricated with a layer thickness of 50 µm (hereinafter referred to as "50 µm" specimens) ranged from 1.28 to 1.37 g/cm^3, whereas specimens produced with a layer thickness of 30 µm ("30 µm" specimens) exhibited densities 13–16 % higher, in the range of 1.46–1.63 g/cm^3. This difference suggests denser layer packing and more complete sintering in thinner layers.

The porous SLS preforms were subjected to PIP densification, which included vacuum infiltration with furfurylidene diacetone followed by carbonization. Carbonization, representing the thermal decomposition (pyrolysis) of the polymer, resulted in the formation of free carbon. After each PIP densification cycle, all specimens were re-weighed to evaluate their density.

The density data were used to plot density variation curves as a function of the number of PIP cycles (Fig. 6) for preforms fabricated with different technological parameters – namely, layer thicknesses of 50 and 30 µm.

As seen in Fig. 6, *a*, the initial density increase for the "50 µm" specimens after the first PIP infiltration –from 1.28–1.37 to 1.58–1.67 g/cm^3 – amounted to 16–24 %. After the second infiltration, their density rose further to 1.68–1.80 g/cm^3, i.e., an additional 7–12 % compared to the first cycle. During subsequent infiltration and pyrolysis cycles, a stable density increase of 2–5 % per cycle was observed.

According to the graphs for the "30 µm" specimens (Fig. 6, *b*), their density after the first infiltration either remained nearly unchanged or slightly decreased, most likely due to moisture retained in the pores. However, after the second infiltration, the density increased to 1.76–1.85 g/cm^3, i.e., by approximately 11–16 % compared to the previous cycle.

A noticeable mass increase for the "30 μm" specimens ceased after the second PIP cycle, while for the "50 μm" specimens it leveled off after the fourth cycle, indicating complete saturation. Thus, the limit of PIP densification was reached after 4–5 cycles for the "50 μm" specimens and after 2–3 cycles for the "30 μm" specimens. Based on the difference in the number of cycles required to achieve saturation for specimens fabricated with different layer thicknesses, it can be inferred that these specimens possess different free volumes and, consequently, different porosities and initial densities, which is consistent with the density measurements. It is also reasonable to assume differences in pore and channel sizes, which could affect pore permeability and infiltration efficiency during polymer infiltration. The final density of the "50 μm" specimens after the last infiltration cycle was 1.88–1.94 g/cm^3, while that of the "30 μm" specimens ranged from 1.73 to 1.85 g/cm^3.

Subsequently, the densified specimens were subjected to liquid silicon infiltration (LSI). Fig. 7 shows the relationship between the density of the "30 μm" specimens after LSI, the number of PIP cycles, and the density after the final PIP cycle.

In addition, a comparative analysis of the density of specimens fabricated under identical SLS parameters but subjected to different post-processing routes – LSI only and the combined PIP + LSI treatment – was carried out (Fig. 8). According to the resulting diagram, the specimens after LSI exhibited a density of 2.52–2.65 g/cm^3, while those that underwent the complete PIP + LSI cycle reached 2.77–2.88 g/cm^3. The average density difference between the specimens after LSI and PIP + LSI treatments was approximately 10 %.

Microstructural studies

A detailed microstructural analysis was performed on the "50 μm" specimens after both PIP + LSI and LSI treatments to determine the relative contents and distribution characteristics of the SiC, Si, and C phases, as well as residual closed porosity. In the optical micrographs (Fig. 9), the initial SiC powder particles appear as dark gray, irregularly shaped grains, including fragmented and needle-like morphologies. Silicon is observed as light gray regions, while carbon particles appear darker than SiC.

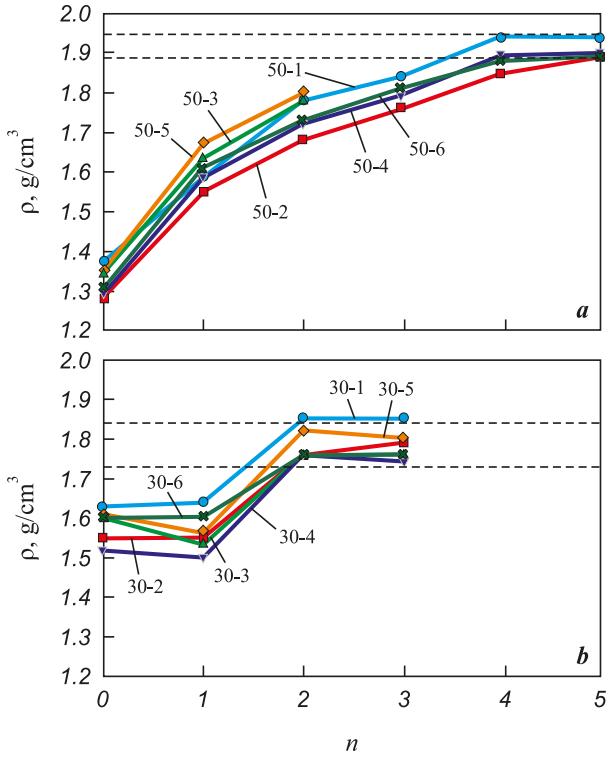

Fig. 6. Variation in the density (ρ) of specimens treated by PIP + LSI as a function of the number of infiltration cycles *n*

Layer thickness – 50 μm (***a***) and 30 μm (***b***)

Рис. 6. Изменение плотности (ρ) образцов, подвергнутых обработке PIP + LSI, в зависимости от количества пропиток (*n*)

Толщина слоя – 50 мкм (***a***) и 30 мкм (***b***)

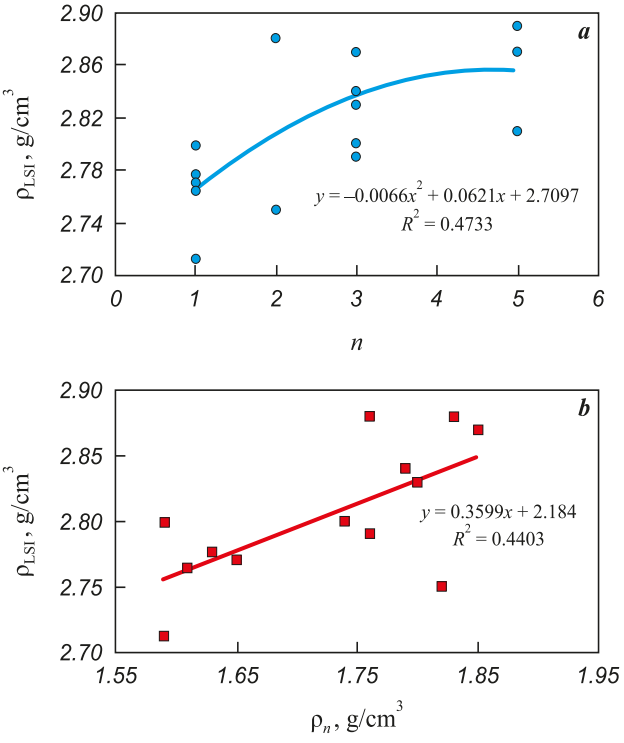

Fig. 7. Density of the "30 μm" specimens after silicon infiltration (ρ_{LSI}) as a function of (***a***) the number of prior infiltration cycles *n* and (***b***) the density after the last infiltration (ρ_n)

Рис. 7. Зависимость плотности образцов «30 мкм» после силицирования (ρ_{LSI}) от количества предварительных пропиток (*n*) (***a***) и от плотности после последней пропитки (ρ_n) (***b***)

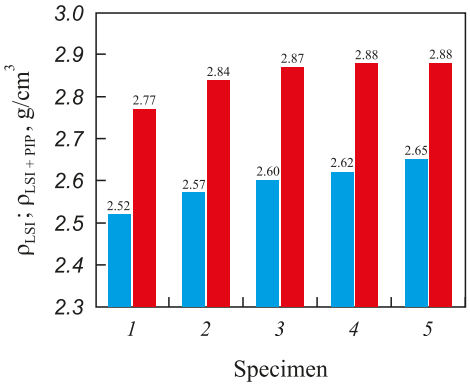

Fig. 8. Comparative density chart of the "50 μm" specimens after silicon infiltration (LSI) and after the complete PIP + LSI treatment

– LSI, – PIP + LSI

Рис. 8. Сравнительная диаграмма плотности образцов «50 мкм», прошедших только стадию силицирования (LSI), и образцов после полного цикла (PIP + LSI)

– LSI, – PIP + LSI

Pores are displayed as black areas. The secondary SiC exhibits an intermediate gray tone between the original SiC and silicon – that is, lighter than SiC grains but darker than free silicon. According to the analysis, the secondary SiC phase is identified similarly to the primary SiC. This is most likely due to the β-SiC → α-SiC transformation, since the resulting α-SiC has a morphology comparable to that of the initial powder.

The specimen subjected to the PIP + LSI treatment exhibits a banded structure formed by the distribution of carbon and silicon phases of different shapes and sizes. Carbon and pores are uniformly distributed throughout the specimen cross-section, while silicon is distributed nonuniformly. Relatively large silicon inclusions are localized in regions with high carbon concentration. Evidence of reaction between silicon and carbon with the formation of secondary SiC along the perimeters of these inclusions is observed (Fig. 10). The specimen exhibits both a regular, ordered structure, consisting of repetitive rhombohedral SiC cells surrounded by carbon, and a disordered structure with locally misoriented phases.

Large carbon inclusions separated by thin silicon veins were concentrated in the peripheral region of the specimen, near the surface, which is likely associated with solidification structure formation under heat dissipation conditions. The specimen also contained numerous continuous, parallel microcracks extending through the structure.

According to the examination of the specimens after LSI, their structures were found to be similar, consisting of uniformly distributed SiC grains embedded in a silicon matrix. The SiC crystals exhibit a regular but non-equiaxed morphology with well-defined grain boundaries. In some regions near the boundaries of SiC grains and within the silicon matrix, fine, diffuse SiC precipitates were observed.

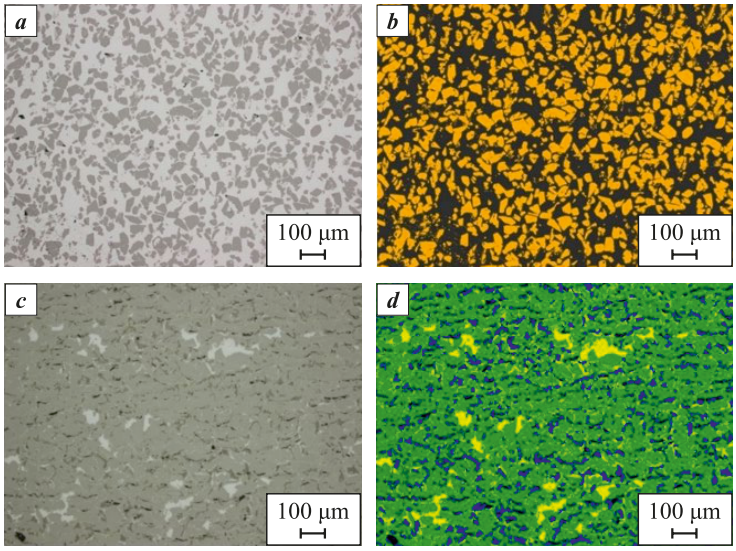

Fig. 9. Microstructure of cross-sections of "50 μm" specimens

a – original image after LSI; ***b*** – the same LSI specimen with phase-colored constituents; ***c*** – original image after PIP + LSI; ***d*** – the PIP + LSI specimen with phase-colored constituents

Рис. 9. Микроструктура поперечных сечений образцов «50 мкм»

a – исходное изображение образца после LSI; ***b*** – изображение LSI-образца с окрашенными структурными составляющими; ***c*** – исходное изображение образца после PIP + LSI; ***d*** – изображение образца после PIP + LSI с окрашенными структурными составляющими

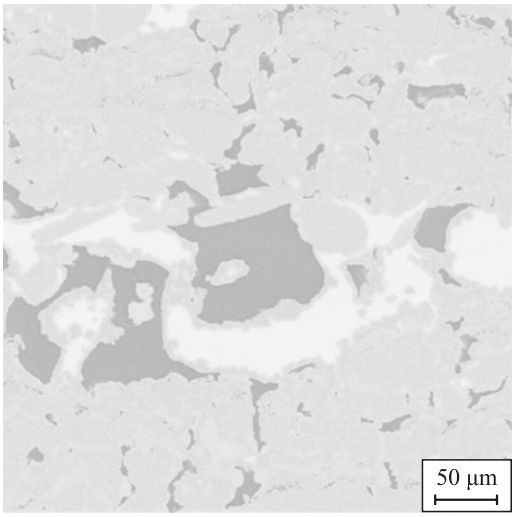

Fig. 10. Formation of secondary silicon carbide from the reaction of free silicon with free carbon in a PIP + LSI-treated specimen

Рис. 10. Взаимодействие свободного кремния и углерода с образованием вторичного карбида кремния в образце, прошедшем обработку PIP + LSI

The structure of all LSI specimens is dense, containing only isolated pores located mainly within the SiC phase. Across all specimens, sharp-edged recesses of regular shape were found. These features likely originated from the pull-out of SiC or other hard-phase crystallites during metallographic preparation.

Detailed SEM analysis of the SiC phase revealed the presence of graphitic inclusions within individual SiC grains (Fig. 11). These inclusions appear as chains of point-like features localized along the grain boundaries of the carbide crystals.

The Table below presents the quantitative contents of SiC, free Si, and carbon phases in the specimens after PIP + LSI and LSI treatments. The contents of pores and the carbon phase in the LSI-treated specimen were not considered in the calculation because of their negligibly small amount (<1 %).

Based on the data in the Table, it can be concluded that the specimens without preliminary PIP treatment contain approximately 50 % less SiC phase than those subjected to the full PIP + LSI cycle. This difference may be attributed both to the lower density of the initial preforms and to the absence of secondary SiC formation. From the difference in the SiC content between the LSI and PIP + LSI specimens, it can be inferred that the secondary SiC phase (SiC_{II}) forms in the amount of 25–37 %, increasing the total SiC content in the material from 43–45 to 70–80 %. This increase likely enhances both the mechanical and thermophysical properties of the material. At the same time, the porosity of the LSI specimens was found to be quantitatively lower, which can be explained by better capillary penetration of the silicon melt into the bulk due to larger pore sizes and the absence of pore-channel blockage by carbon. According to the microstructural images, the additional porosity observed in the PIP + LSI specimens may be associated with incomplete wetting of large residual carbon inclusions and the formation of voids at the interface with the free silicon phase, resulting in localized porous zones.

Based on the obtained quantitative phase composition, it can be assumed that the LSI specimen, with a SiC content of 43–45 %, would be expected to have a theoretical density of 2.70–2.73 g/cm^3 instead of the actual 2.52–2.65 g/cm^3, while the PIP + LSI specimen, containing 70–80 % SiC, should theoretically reach 2.94–3.03 g/cm^3 instead of the measured

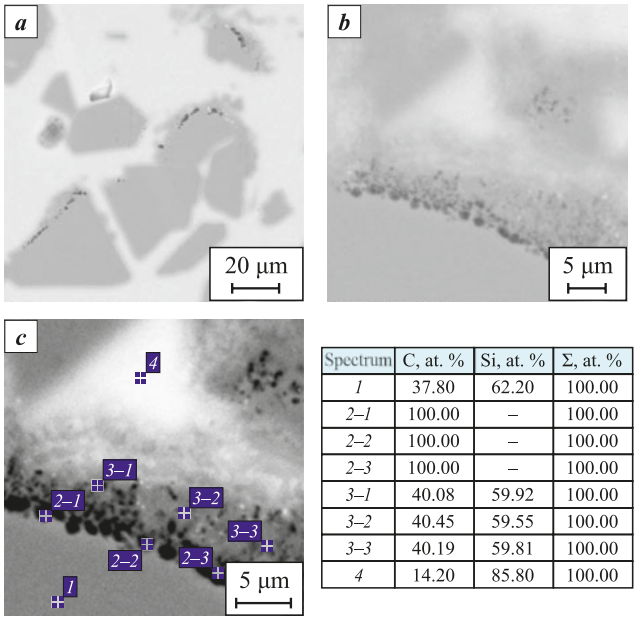

Spectrum	C, at. %	Si, at. %	Σ, at. %
1	37.80	62.20	100.00
2–1	100.00	–	100.00
2–2	100.00	–	100.00
2–3	100.00	–	100.00
3–1	40.08	59.92	100.00
3–2	40.45	59.55	100.00
3–3	40.19	59.81	100.00
4	14.20	85.80	100.00

Fig. 11. Carbon-phase inclusions within the SiC phase in a PIP + LSI-treated specimen
a – 1500×; ***b***, ***c*** – 5000×
Local chemical composition analysis

Рис. 11. Включения углеродной фазы в SiC-фазе в образце после обработки PIP + LSI
a – 1500×; ***b***, ***c*** – 5000×
Локальный анализ химического состава

Proportions of structural constituents in "50 μm" specimens after PIP + LSI and after LSI

Соотношение структурных составляющих в образцах «50 мкм» после обработок PIP + LSI и LSI

Specimen	Phase fraction, %				Density, g/cm^3
	Pores	Si	C	SiC	
PIP + LSI	1–2	6–17	9–13	70–80	<2.88
LSI	<1	55–57	<1	43–45	<2.65

2.77–2.88 g/cm^3. However, the lower actual density values indicate the presence of additional low-density phases and residual porosity, both of which affect the overall result – findings that are consistent with the quantitative microstructural analysis.

Further research aimed at optimizing the post-processing parameters to achieve maximum densification of SLS SiC preforms and evaluating the mechanical properties will help establish a correlation between the mechanical strength and the quantitative phase composition of the final specimens after different post-processing routes. Planned future studies also include mechanical testing to determine the fracture mechanisms of specimens fabricated along different build directions, in order to assess the possible anisotropy of mechanical properties.

Conclusions

1. The initial density of the specimens fabricated by SLS was 15–30 % higher than the bulk density of silicon carbide. For the "50 μm" specimens, the density was comparable to that of vibratory-compacted powder, while the "30 μm" specimens exhibited densities 10–15 % higher than that of vibratory-compacted powder. The SiC powder particles had irregular (elongated) shapes. To achieve higher final density, it is necessary to increase the initial preform density, for example, by using more spherical SiC powder.

2. The increase in the initial density of the SLS preforms with decreasing layer thickness is likely associated with improved vertical heat transfer in thinner layers (30 μm). This thermal profile promotes particle sliding/rearrangement, reduces interparticle pore size, and improves adhesion to the previously sintered layer. In contrast, for 50 μm layers the packing density may decrease because of a double-layer effect: two needle-like SiC particles can stack vertically, leading to additional heat absorption (thermal shielding) and difficulty achieving full, uniform heating during laser sintering. Consequently, interlayer sliding and consolidation proceed less efficiently than in the "30 μm" specimens, where each layer is approximately one particle thick. In the "50 μm" specimens, the initial density was 1.3–1.4 g/cm^3, whereas in the "30 μm" specimens, it reached 1.5–1.6 g/cm^3.

3. The SLS specimens can be densified by polymer infiltration and pyrolysis (PIP) to a density of 1.85–1.94 g/cm^3, indicating a carbon mass uptake of up to 0.62 g/cm^3 – sufficient for the subsequent formation of secondary SiC within the pores, thereby increasing the overall density toward the theoretical value.

4. Comparison of the densities of specimens subjected to PIP + LSI treatment shows a linear correlation, indirectly confirming a high degree of carbon conversion into secondary SiC and demonstrating the potential for further material quality improvement. The quantitative microstructural analysis directly supports this conclusion, showing that the secondary SiC (SiC_{II}) accounts for 25–37 % of the total SiC content.

5. It is necessary to optimize both the amount and reactivity of carbon introduced into the SLS preforms, as well as the method of its incorporation, to achieve maximum final density with minimal porosity. Introducing excess carbon (to generate more than ~35 % of secondary SiC) results in high residual carbon content and significant closed porosity due to pore-channel blockage during infiltration and pyrolysis. Improved results may be obtained by modifying the polymer precursor or by using alternative infiltration polymers.

6. The "30 μm" specimens achieved maximum carbon densification after only 2–3 infiltration cycles, while the "50 μm" specimens required 4–5 cycles. This difference can be attributed to variations in total porosity and pore-channel cross-section size, which affect the saturation efficiency during infiltration.

7. The final density after siliconization (LSI) was insufficient for both the "50 μm" and "30 μm" specimens. The maximum achieved density was 2.88 g/cm^3. The specimens subjected to only one PIP infiltration showed the lowest post-LSI density (2.62–2.80 g/cm^3). To reach maximum densification, 4–5 infiltrations are required for the "50 μm" specimens, and 2–3 for the "30 μm" specimens.

8. The results demonstrate that SLS-fabricated specimens subjected to LSI without preliminary PIP treatment exhibit lower density (2.52–2.65 g/cm^3) compared to those that underwent the full PIP + LSI process (2.62–2.88 g/cm^3). In earlier experiments with infiltration, visible voids and delaminations were observed, whereas in the present specimens no delaminations or large pores were detected, confirming improved structure integrity.

References / Список литературы

1. Bubnenkov B.B., Zharmukhambetov A.S., Ivanov I.A., Yudin A.V., Taktashov A.E., Starkov A.M., Sharapov I.S., Alekseeva E.M. Investigation of influence of technological parameters on the properties of SiC samples fabricated by selective laser sintering. Part 1. *Powder Metallurgy and Functional Coatings*. 2024;18(3):71–84. https://doi.org/10.17073/1997-308X-2024-3-71-84

Бубненков Б.Б., Жармухамбетов А.С., Иванов И.А., Юдин А.В., Такташов А.Е., Старков А.М., Шарапов И.С., Алексеева Е.М. Исследование влияния технологических параметров на свойства образцов из SiC, получаемых методом селективного лазерного спекания. Часть 1. *Известия вузов. Порошковая металлур-*

гия и функциональные покрытия. 2024;18(3):71–84. https://doi.org/10.17073/1997-308X-2024-3-71-84

2. Bubnenkov B.B., Zharmukhambetov A.S., Ivanov I.A. Methods of additive technologies for the manufacture of silicon carbide products. Part 1. *Tyazheloe mashinostroenie*. 2024;(10):2–9. (In Russ.).

   Бубненков Б.Б., Жармухамбетов А.С., Иванов И.А. Методы аддитивных технологий для изготовления изделий из карбида кремния. Часть 1. *Тяжелое машиностроение*. 2024;(10):2–9.
3. Bubnenkov B.B., Zharmukhambetov A.S., Ivanov I.A. Methods of additive technologies for the manufacture of silicon carbide products. Part 2. *Tyazheloe mashinostroenie*. 2024;(11-12):2–11. (In Russ.).

   Бубненков Б.Б., Жармухамбетов А.С., Иванов И.А. Методы аддитивных технологий для изготовления изделий из карбида кремния. Часть 2. *Тяжелое машиностроение*. 2024;(11-12):2–11.
4. Hutchins O. Method of producing silicon-carbide articles: Patent 1266478 (USA). 1918.
5. Popper P., Davies D.G.S. The preparation and properties of self-bonded silicon carbide. *Powder Metallurgy*. 1961;4(8):113–127. https://doi.org/10.1179/pom.1961.4.8.009
6. Terrani K., Jolly B., Trammell M. 3D printing of high-purity silicon carbide. *Journal of the American Ceramic Society*. 2020;103(3):1575–1581. https://doi.org/10.1111/JACE.16888
7. Faes M., Valkenaers H., Vogeler F., Vleugels J., Ferraris E. Extrusion-based 3D printing of ceramic components. *Procedia CIRP*. 2015;28:76–81. https://doi.org/10.1016/j.procir.2015.04.028
8. Baux A., Goillot A., Jacques S., Heisel C., Rochais D., Charpentier L., David P., Piquero T., Chartier T., Chollon G. Synthesis and properties of macroporous SiC ceramics synthesized by 3D printing and chemical vapor infiltration/deposition. *Journal of the European Ceramic Society*. 2020;40(8):2834–2854. https://doi.org/10.1016/j.jeurceramsoc.2020.03.001
9. Baumann H.N. The relationship of alpha and beta silicon carbide. *Journal of the Electrochemical Society*. 1952;99(3):109. https://doi.org/10.1149/1.2779671
10. Seo Y.K., Eom J.H., Kim Y.W. Process-tolerant pressureless-sintered silicon carbide ceramics with alumina-yttria-calcia-strontia. *Journal of the European Ceramic Society*. 2018;38(2):445–452. https://doi.org/10.1016/j.jeurceramsoc.2017.09.011
11. Oh J-W., Park J., Nahm S., Choi H. SiC–Si composite part fabrication via SiC powder binder jetting additive manufacturing and molten-Si infiltration. *International Journal of Refractory Metals and Hard Materials*. 2021;101:105686. https://doi.org/10.1016/j.ijrmhm.2021.105686
12. Logan R.A., Bond W.L. Density change in silicon upon melting. *Journal of Applied Physics*. 1959;30(3):322. https://doi.org/10.1063/1.1735159
13. Zhou H., Singh R.N. Kinetics model for the growth of silicon carbide by the reaction of liquid silicon with carbon. *Journal of the American Ceramic Society*. 1995;78(9):2456–2462. https://doi.org/10.1111/j.1151-2916.1995.tb08685.x
14. Markov M.A., Krasikov A.V., Kravchenko I.N., Erofeev M.N., Bykova A.D., Belyakov A.N. Development of new structural ceramic materials based on silicon carbide for products with complex geometry. *Problemy mashinostroeniya i nadezhnosti mashin*. 2021;(2):81–87. (In Russ.). https://doi.org/10.31857/S0235711921020097

   Марков М.А., Красиков А.В., Кравченко И.Н., Ерофеев М.Н., Быкова А.Д., Беляков А.Н. Разработка новых конструкционных керамических материалов на основе карбида кремния для изделий сложной геометрии. *Проблемы машиностроения и надежности машин*. 2021;(2):81–87. https://doi.org/10.31857/S0235711921020097
15. Xu H., Liu Y., Che Y., Chen Z. Combination of direct ink writing and reaction bonded for rapid fabrication of SiC_w/SiC composites. *Ceramics International*. 2023;49(1):392–402. https://doi.org/10.1016/j.ceramint.2022.09.002
16. Cramer C.L., Elliott A.M., Lara-Curzio E., Flores-Betancourt A., Lance M.J., Han L., Blacker J., Trofimov A.A., Wang H., Cakmak E., Nawaz K. Properties of SiC–Si made via binder jet 3D printing of SiC powder, carbon addition, and silicon melt infiltration. *Journal of the American Ceramic Society*. 2021;104(11):5467–5478. https://doi.org/10.1111/JACE.17933
17. Hozer L., Lee J.-R., Chiang Y.-M. Reaction-infiltrated, net-shape SiC composites. *Materials Science and Engineering: A*. 1995;195:131–143. https://doi.org/10.1016/0921-5093(94)06512-8
18. Narayan J., Raghunathan R., Chowdhury R., Jagannadham K. Mechanism of combustion synthesis of silicon carbide. *Journal of Applied Physics*. 1994;75:7252–7257. https://doi.org/10.1063/1.356660
19. Tang J., Liu M., Wei Y., Yang Y., Huang Z. An efficient and low-cost liquid silicon infiltration method to prepare SiC-coated carbon short fiber for fiber protection of C_f/SiC ceramic matrix composites. *Ceramics International*. 2021;47(9):13235–13241. https://doi.org/10.1016/j.ceramint.2021.01.115
20. Lu Z., Xia Y., Miao K., Li S., Zhu L., Nan H., Cao J., Li D. Microstructure control of highly oriented short carbon fibres in SiC matrix composites fabricated by direct ink writing. *Ceramics International*. 2019;45(14):17262–17267. https://doi.org/10.1016/j.ceramint.2019.05.283
21. Zhang H., Yang Y., Liu B., Huang Z. The preparation of SiC-based ceramics by one novel strategy combined 3D printing technology and liquid silicon infiltration process. *Ceramics International*. 2019;45(8):10800–10804. https://doi.org/10.1016/j.ceramint.2019.02.154
22. Hu S., Feng K., Wang Q., Sun J., Yuan J., Mao Y., Cai D., Jiang W., Ye C., Wei Q. Lightweight C_f/SiC composites with high fiber content fabricated by binder jetting additive manufacturing and liquid silicon infiltration. *Additive Manufacturing Frontiers*. 2024;3(1):200116. https://doi.org/10.1016/j.amf.2024.200116
23. Zocca A., Lima P., Diener S., Katsikis N., Günster J. Additive manufacturing of SiSiC by layerwise slurry deposition and binder jetting (LSD-print). *Journal of the European Ceramic Society*. 2019;39(13):3527–3533. https://doi.org/10.1016/j.jeurceramsoc.2019.05.009

Information about the Authors

Bogdan B. Bubnenkov – Research Scientist, Institute of Metallurgy and Mechanical Engineering (IMME), JSC "SPA "Central Research Institute of Mechanical Engineering Technology (CRIMET)"
ORCID: 0009-0001-4963-4229
E-mail: bogis13@yandex.ru

Alps S. Zharmukhambetov – Head of the Laboratory of Additive Technologies, IMME of JSC "SPA "CRIMET"
ORCID: 0009-0002-1977-2492
E-mail: alps98@mail.ru

Ivan A. Ivanov – Cand. Sci. (Phys.-Math.), Associate Professor, Director of IMME, Deputy General Director of JSC "SPA "CRIMET"
ORCID: 0000-0001-9083-1059
E-mail: ivalivanov@rosatom.ru

Ilya S. Sharapov – Deputy Director of the Department, JSC "SRI SPA "LUCH"
ORCID: 0009-0005-7449-6517
E-mail: SharapovIS@sialuch.ru

Sergey N. Veselkov – Leading Engineer, JSC "SRI SPA "LUCH"
ORCID: 0009-0003-3567-7644
E-mail: VeselkovSN@sialuch.ru

Сведения об авторах

Богдан Борисович Бубненков – науч. сотрудник Института металлургии и машиностроения (ИМиМ) АО «НПО «Центральный научно-исследовательский институт технологии машиностроения (ЦНИИТМАШ)»
ORCID: 0009-0001-4963-4229
E-mail: bogis13@yandex.ru

Алпс Савырович Жармухамбетов – зав. лабораторией аддитивных технологий ИМиМ, АО «НПО ЦНИИТМАШ»
ORCID: 0009-0002-1977-2492
E-mail: alps98@mail.ru

Иван Алексеевич Иванов – к.ф-м.н., доцент, директор ИМиМ, зам. генерального директора АО «НПО ЦНИИТМАШ»
ORCID: 0000-0001-9083-1059
E-mail: ivalivanov@rosatom.ru

Илья Сергеевич Шарапов – зам. директора отделения АО «НИИ НПО «ЛУЧ»
ORCID: 0009-0005-7449-6517
E-mail: SharapovIS@sialuch.ru

Сергей Николаевич Веселков – вед. инженер АО «НИИ НПО «ЛУЧ»
ORCID: 0009-0003-3567-7644
E-mail: VeselkovSN@sialuch.ru

Contribution of the Authors

B. B. Bubnenkov – conducted experiments and investigations, processed the results, and wrote the manuscript.
A. S. Zharmukhambetov – conducted experiments and investigations, processed the results, and wrote the manuscript.
I. A. Ivanov – defined the research objectives, supervised the study, and participated in the discussion of the results.
I. S. Sharapov – defined the research objectives, supervised the study, and participated in the discussion of the results.
S. N. Veselkov – conducted experiments and investigations, processed the results, and wrote the manuscript.

Вклад авторов

Б. Б. Бубненков – проведение экспериментов и исследований, обработка результатов, написание статьи.
А. С. Жармухамбетов – проведение экспериментов и исследований, обработка результатов, написание статьи.
И. А. Иванов – определение цели работы, курирование исследований, участие в обсуждении результатов.
И. С. Шарапов – определение цели работы, курирование исследований, участие в обсуждении результатов.
С. Н. Веселков – проведение экспериментов и исследований, обработка результатов, написание статьи.

Received 25.02.2025
Revised 22.04.2025
Accepted 24.04.2025

Статья поступила 25.02.2025 г.
Доработана 22.04.2025 г.
Принята к публикации 24.04.2025 г.

Приглашаем вас стать авторами научно-практических журналов Университета науки и технологий МИСИС

МИСИС УНИВЕРСИТЕТ

https://portal-journals.misis.ru/

ПОРТАЛ НАУЧНЫХ ЖУРНАЛОВ

Университета науки и технологий МИСИС

Журналы платформы

Горные науки и технологии / Mining Science and Technology

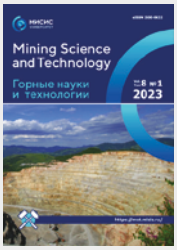

- Основан в 2016 г.
- Учредитель журнала: НИТУ «МИСИС».
- Является одним из основных научно-технических журналов, освещающих междисциплинарные направления, которые способствуют прогрессу в горном деле.
- Целевая аудитория – исследователи, специалисты в области горного дела, представители академического и профессионального сообществ.
- В журнале публикуются оригинальные статьи, описывающие результаты исследований, опыт реализации проектов в горнопромышленном комплексе, обзорные публикации.
- Индексируется в РИНЦ, Scopus, GeoRef, Dimensions, электронной базе Реферативных журналов ВИНИТИ РАН.
- Включен в международные Базы данных: CAS, EBSCO, J-Gate, Jisc Library Hub Discover, Ulrich's Periodicals Directory.

https://mst.misis.ru/

Известия высших учебных заведений. Черная Металлургия

- Основан в 1958 г.
- Учредители журнала: НИТУ «МИСИС», СибГИУ.
- Основная задача журнала – обобщение научных и практических достижений в области черной металлургии и материаловедения.
- В журнале публикуются научные сотрудники РАН и отраслевых научных центров, специалисты-практики, профессорско-преподавательский состав вузов, соискатели ученых степеней, другие специалисты России, стран СНГ и зарубежных стран.
- Журнал индексируется в Scopus, RSCI, Chemical Abstracts, РИНЦ, РЖ/БД ВИНИТИ.

https://fermet.misis.ru/

Известия вузов. Порошковая металлургия и функциональные покрытия / Powder Metallurgy and Functional Coatings

- Основан в 2007 г.
- Учредитель журнала: НИТУ «МИСИС».
- Один из основных российских журналов по актуальным научным проблемам порошковой металлургии и инженерии поверхности, порошкового материаловедения, синтеза неорганических материалов в режиме горения, технологий покрытий и модифицирования поверхности, наноструктурных материалов и нанотехнологий, керамики и композитов, пористых и биоматериалов.
- В журнале публикуются научные сотрудники РАН и отраслевых научных центров, специалисты-практики, профессорско-преподавательский состав вузов, соискатели ученых степеней, другие специалисты России, стран СНГ и зарубежных стран.
- Журнал индексируется в Scopus, RSCI, РИНЦ, БД/РЖ ВИНИТИ.
- Включен в Перечень ВАК (категория К1)

https://powder.misis.ru/

Известия вузов. Цветная металлургия / Izvestiya. Non-Ferrous Metallurgy

- Основан в 1958 г.
- Учредитель журнала: НИТУ «МИСИС».
- Один из основных научно-технических журналов по актуальным научным проблемам цветной металлургии и материаловедения. Отражает новые результаты фундаментальных, проблемно-ориентированных, поисковых научных исследований в аналитических статьях, обзорах и кратких сообщениях.
- В журнале публикуются научные сотрудники РАН и отраслевых научных центров, специалисты-практики, профессорско-преподавательский состав вузов, соискатели ученых степеней, другие специалисты России, стран СНГ и зарубежных стран.
- Журнал индексируется в RSCI, РИНЦ, РЖ/БД ВИНИТИ.
- Включен в Перечень ВАК (категория К1).

https://cvmet.misis.ru/

Известия высших учебных заведений. Материалы электронной техники

- Основан в 1998 г.
- Учредитель журнала: НИТУ «МИСИС».
- Один из основных российских научно-технических журналов, освещающих проблемы получения и исследования свойств полупроводниковых, магнитных и диэлектрических материалов для микро- и наноэлектроники.
- В журнале публикуются специалисты – ученые и аспиранты ведущих высших учебных заведений и научных организаций России, стран ближнего и дальнего зарубежья.
- Журнал индексируется в Chemical Abstracts (CAS), EbscoHost, РИНЦ, РЖ/БД ВИНИТИ.
- Включен в Перечень ВАК (категория К2).

https://met.misis.ru/

Экономика промышленности / Russian Journal of Industrial Economics

- Основан в 2008 г.
- Учредители журнала: НИТУ «МИСИС», ОМК.
- Журнал сфокусирован на инновационном развитии индустрии производственно-потребительского цикла. Представляет собой дискуссионную площадку для обсуждения новейших достижений экономической науки, практики реализации передовых технологий и индустриального стратегирования.
- В журнале публикуются специалисты – стратегические лидеры, высший и средний управленческий персонал, ученые, инженеры, экономисты и практики всех отраслей промышленности и науки.
- Журнал индексируется в РИНЦ, РЖ/БД ВИНИТИ.
- Включен в Перечень ВАК (категория К2).

https://ecoprom.misis.ru/

Modern Electronic Materials

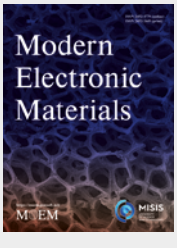

- Основан в 2015 г.
- Учредитель журнала: НИТУ МИСИС.
- Язык публикаций: английский.
- Размещается на издательской платформе ARPHA (PenSoft, Болгария).
- Журнал освещает фундаментальные и практические вопросы в области материалов для микро- и наноэлектроники, изучения их структуры и свойств.
- В журнале публикуются специалисты – ученые и аспиранты ведущих высших учебных заведений и научных организаций России, стран ближнего и дальнего зарубежья.
- Журнал индексируется в Scopus, RSCI, РИНЦ, Chemical Abstracts, DOAJ, Altmetric, ASOS Indeks, CNKI, CrossRef, EBSCO Essentials и др.

https://moem.pensoft.net/

- ☑ **Публикация бесплатная после процедур двойного слепого рецензирования**
- ☑ **Все журналы с 2023 г. размещаются в открытом доступе**
- ☑ **Занимают высокие места в рейтингах своих тематических групп в РИНЦ и Перечне ВАК**
- ☑ **Индексируется в реферативных базах данных (Scopus, RSCI, CAS, GeoRef, РЖ/БД ВИНИТИ и др.)**
- ☑ **Всем публикациям присваиваются DOI с регистрацией в CrossRef**

Рады видеть вас в числе авторов наших журналов!

Зарегистрирован Федеральной службой по надзору
в сфере связи, информационных технологий
и массовых коммуникаций.
Свидетельство о регистрации ПИ № ФС77-79230

Журнал распространяется агентством «Урал-Пресс»
Подписной индекс: 80752 (печатная версия)
05108 (электронная версия)